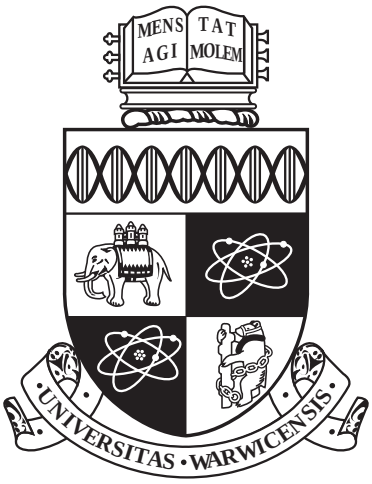

Local Analogues to $z \sim 5$ Lyman Break Galaxies

by

Stephanie M L Greis

Thesis

Submitted to the University of Warwick

for the degree of

Doctor of Philosophy

Physics

Oct 2017

THE UNIVERSITY OF
WARWICK

Contents

List of Tables

List of Figures

Acknowledgments

First and foremost I would like to thank my supervisor, Elizabeth Stanway, for her continuous support and guidance. I am very grateful for the knowledge of galaxies which she has imparted to me, and - maybe more importantly - for helping me learn to ask the right questions. And I realise that as her first PhD student, I may have been responsible for the odd sleepless night - not counting the nights we spent observing in La Palma - but overall, I can honestly say that I could not have asked for a better supervisor. Thank you!

I would also like to thank my co-supervisor, Andrew Levan, for helpful feedback on papers, practice talks, and proposals, as well as for general life and career advice.

A big thank you goes to my Mum, who has encouraged me to explore the world since I was little: I remember standing on top of a mountain with her, in the freezing cold with a telescope she had given me, and seeing the rings of Saturn with my own eyes, and another time when the beautiful band of the Milky Way was stretching above us. And I am very excited to note that this love for astronomy seems to be rubbing off on her: she's been attending evening classes for a few years now. [Und, zur Sicherheit auch noch auf Deutsch: Ganz vielen Dank für deine Unterstützung, sowohl während der letzten vier Jahre meiner Doktorarbeit, als auch in den fast zehn Jahren davor als Auswanderer auf dieser kleinen Insel - und natürlich in den Jahren davor (mit Planetariumsbesuchen und immer diesen "wieso, weshalb, warum" Fragen). Danke!]

A further big thank you goes to my colleagues and fellow PhD students, who have shared the ups and down of PhD life over the past four years, and whose (often

rather interesting, weird, at times very scientific or philosophical) conversations have helped tremendously in keeping me sane. In particular, my thanks go to Charlotte, for being a good friend (who also makes very yummy cake, gives good book recommendations, can sanity check my maths and physics, and patiently listens to the occasional rant that might have happened during four years of PhDing). To Greg, for helping me out with my (1+z) factors, for reassuring me when I got stuck, and for getting me involved with the planetarium and general outreach activities which helped me realise how much I enjoy sharing my passion for astronomy and science. To Mark for allowing me to call white dwarfs 'contaminants', for reminding me of my artistic side, and for final-few-months-of-PhD compassion. To Tom, for making me think about morality (often through conversations which might have included considerations of genocide and/or cannibalism), and introducing me to some great thinkers. To Dave, for helping me become an author with the astrobites blog, and for organising our cinema trips (and only losing a few people along the way). To Matt, for good chats that almost made me forget that I should be working (that's the best kind). To George, for sharing my outrage of the news of 2016 and 2017 (though, really, all those mentioned here did), and for being my fellow non-drinker. To Kirk, for being a great desk neighbour for two years, and for great conversations about life.

And lastly, though most definitely not least, I would like to thank my best friend and husband of almost 5 years. Thank you for bearing with me throughout all of this! Thank you for reminding me that I could do it, for believing in me when I was doubting myself, for going for walks around the beautiful Warwickshire countryside with me, and for your premium hugs.

Declarations

This is a declaration of the extent of the original work within this thesis and of the work published/submitted for publication. This thesis has not been submitted in part or full to any other institution for any other qualification.

The work presented in chapter 2 on spectral energy distribution fitting is based on a paper published by the Monthly Notices of the Royal Astronomical Society (MNRAS) with the title 'Physical properties of local star-forming analogues to $z \sim 5$ Lyman-break galaxies' [Greis et al., 2016]. The analysis shown in Fig. 2.18 was undertaken by Elizabeth Stanway.

The radio observations and their analysis, presented in chapter 3, has also been published by MNRAS under the title 'Radio observations confirm young stellar populations in local analogues to $z \sim 5$ Lyman break galaxies'. The APEX sub-millimetre observations in that chapter were reduced by Elizabeth Stanway, who also calculated synthetic stellar populations (using BPASS) for a system with a constant star formation rate of 1 $M_{\odot}yr^{-1}$, processed the output stellar spectrum through the radiative transfer code CLOUDY, calculated [O II] and Hα fluxes, made predictions for the core-collapse SN rate, and corrected this for Type I SNe.

In chapter 4, Elizabeth Stanway provided the final catalogue of (uncalibrated) line fluxes. The work presented in this chapter has not yet been published.

Analyses and interpretations from Stanway et al. [2014] are included throughout the thesis. For this publication I provided the galaxy catalogue, but the main body of work was undertaken by Elizabeth Stanway and collaborators.

Abstract

Lyman break galaxies (LBGs), characterised by the eponymous spectral break at the electron transition energy of neutral hydrogen, are young, intensely star-forming, compact galaxies in the distant Universe. Due to the presence of hot, young stars within them, these galaxies are ideal candidates for the types of sources which contributed ionizing flux during the Epoch of Reionization by $z \sim 6$. Not only can their study help us to learn more about the process of reionization, but LBGs are also primary sources for our understanding of the formation and evolution of galaxies. However, due to their large luminosity distance, and hence their apparent faintness and small projected sizes, they are difficult to study directly. A local analogue population, selected to reproduce the observed properties within their distant cousins, can be used to greatly improve the interpretation of distant LBGs. Such local Lyman break analogue (LBA) populations have been established for $z \sim 3$ LBGs; however, there is significant evolution in the physical properties within galaxies between $z \sim 3$ and $z \sim 5-7$ (representing a difference of over one billion years in the age of the Universe), hence making it inappropriate to use the same analogue sample for both epochs. The establishment and study of an analogue sample of $z \sim 5-7$ is described in this thesis.

Building on the work of Stanway & Davies [2014], I selected an LBA candidate sample of 180 local ($0.05 < z < 0.25$) galaxies whose ultraviolet luminosity and colours matched those observed in the distant $z \sim 5-7$ LBG population. I fit the spectral energy distribution (SED) of the candidates, deriving their stellar masses, dominant population ages, dust reddening, metallicities, star formation rates, and star formation rate densities. Comparing these properties with those found in the distant LBG sample, and depending on the age and mass cuts applied, approximately $\sim 40-70\%$ of candidates are good local analogues. This confirms that galaxies exist in the local Universe whose physical properties are akin to those found in the distant cosmos.

I have reduced and interpreted radio observations of a subset of the LBA candidates, confirming them to be young, star formation driven systems that do not host AGN. In fact, their stellar populations appear to be so young that in most sources no significant supernovae-driven radio continuum has been established. Their low ages also indicate that commonly used star formation rate (SFR) indicators, typically calibrated for stellar populations at ages > 100 Myr, are likely to underestimate their true SFRs.

In order to determine the projected density of genuine LBA, I analysed low-resolution AAOmega spectroscopy for a sample of ~ 230 photometrically selected LBA candidates. Combining this with the results of the SED fitting, the spatial density of genuine local Lyman break analogue galaxies lies between 24 and 40 per square degree.

These findings have important implications for the distant LBG population, suggesting that galaxies with comparable star formation rate densities exhibit similar physical properties, and indicating that both LBAs and the distant LBG sources are undergoing bursty episodes of star formation (as opposed to a continuous star formation rate). From the high ionization parameters found in the local LBA sources, predictions can be made about potentially observable emission lines in the $z \sim 5-7$ LBG population. Future surveys, such as the *JWST* and the LSST, are likely to shed further light on both this local analogue populations and their distant cousins.

Chapter 1

Introduction

The study of the heavens appears to be as old as humanity itself, with some of the earliest artefacts charting the motion of the stars, the Moon or the equinoxes tracing back thousands, if not tens of thousands, of years. With its apparently bottomless chasm stretching across the night sky, it is no wonder that it has evoked feelings of awe, as well as posing one of the most human questions of all: where did we - the stars and galaxies, and eventually our little planet with its inhabitants looking back into the cosmos - come from?
To a very small extent, the work of my PhD attempts to shed light on this question. In this thesis I will be presenting my research into local analogues to high redshift galaxies, which were likely the progenitors of our own Galaxy, the Milky Way.

In this introductory chapter I will start with a general introduction to the formation and evolution of the first galaxies, and the impact they had on the Universe, particularly during the Epoch of Reionization. I will explore what is currently known about the evolution of star forming galaxies' physical properties throughout cosmic history, and aim to show that - while many advances have been made in recent years - a local analogue population to those galaxies which existed during the Epoch of Reionization is necessary in order to study the properties of, and make inferences about, some of the most distant galaxies. I will also introduce some existing analogue populations to distant galaxies, and comment on the reasons why they are not suitable as analogues to the $z \sim 5-7$ Lyman break galaxy population.

there's a hell
of a good universe next door; let's go

---

e e cummings

1.1 The First Galaxies & The Epoch of Reionization

According to the standard cosmological model, the ΛCDM model in which the Universe contains both a cosmological constant (Λ) and cold dark matter (abbreviated CDM), the first stars in the Universe formed some tens to hundred of millions of years after the Big Bang, at a redshift of around $z \sim 65$ [Naoz et al., 2006; Fialkov et al., 2012], followed by the first dwarf galaxies when the Universe was approximately 100 million years old. Since no elements heavier than helium (and small amounts of lithium) had yet been formed through stellar nucleosynthesis, the only available cooling mechanism for the collapsing gas clouds was molecular hydrogen. This resulted in the gas cloud fragmenting into relatively massive clumps which continued to collapse to form the first generation of stars (known as Population III stars), with characteristic masses significantly higher than those of present-day stars. Additionally, due to the relationship between mass, temperature and luminosity, this meant that the first stars produced a lot of highly energetic ultraviolet and X-ray radiation during their short lifecycles, before ending their lives in supernova explosions, enriching the surrounding medium with heavier elements (commonly referred to as metals). Due to the presence of these heavier elements, the interstellar medium was then able to cool to lower temperatures, making it possible for lower-mass clumps to form - resulting in the second generation of stars (known as Population II stars). The ionizing ultraviolet radiation emitted by these firsts stars leaked out of the young galaxies and into the intergalactic medium (IGM) where it ionized the previously neutral hydrogen far outside the reaches of individual galaxies, causing the second major change in the ionization state of hydrogen in the Universe (after recombination around $z \sim 1100$ in which electrons and protons formed the first hydrogen atoms). As bubbles of ionized gas around galaxies grew and merged, the cosmos started to become transparent, marking one of the most crucial transitions in the history of the Universe: the Epoch of Reionization. According to the hierarchical model of galaxy formation, the earliest dwarf galaxies merged and grew into bigger galaxies, constructing, through mergers of hundreds of small building blocks [see e.g. Press & Schechter, 1974; Lacey & Cole, 1993; Cole et al., 1994; Heyl et al., 1995; Cole et al., 2000; Carilli et al., 2001], galaxies like the Milky Way. A schematic history of the Universe is shown in Fig. 1.1.

When exploring the first stars and galaxies, it is important to note that due to the finite speed of light and the expansion of the Universe, photons emitted by the first galaxies have taken a finite amount of time to reach our telescopes. Additionally, the light has lost energy, being 'stretched' or redshifted by the expanding cosmos.

z	light travel time [Gyr]	age of the Universe [Gyr]	1" corresponds to [kpc]	Lyα (1216 Å rest-frame) [Å]
5	12.3	1.2	6.3	7296
3	11.4	2.1	7.7	4864
0.25	2.9	10.5	3.9	1520
0.15	1.9	11.6	2.6	1398

Table 1.1: Table showing the light travel time (in Gyr), corresponding age of the Universe (in Gyr), and the distance which subtends one arcsecond at redshifts relevant to this work. In particular, $z \sim 0.15$ and $z \sim 0.25$ correspond to the mean and maximum redshift of the local analogue population to $z \sim 5$ Lyman break galaxies, which forms the bulk of my thesis, while $z \sim 3$ is the redshift at which the Lyman break dropout technique was pioneered. The standard ΛCDM cosmology with $H_0 = 70\,\mathrm{km\,s^{-1}\,Mpc^{-1}}$, $\Omega_M = 0.3$ and $\Omega_\Lambda = 0.7$ is assumed.

Thus by assuming some cosmology (here, the standard ΛCDM cosmology with $H_0 = 70\,\mathrm{km\,s^{-1}\,Mpc^{-1}}$, $\Omega_M = 0.3$ and $\Omega_\Lambda = 0.7$ is assumed throughout) and measuring the amount of redshift (z),

$$\lambda_{observed} = (1 + z)\lambda_{emitted}$$

it is not only possible to determine the light travel time (and hence the distance between the telescope and the distant object), but also the age of the Universe at the time at which the light was emitted. Table 1.1 provides this information for some of the most important redshifts mentioned in my thesis: the redshift at which the galaxies reside whose local analogues I will explore in the remainder of this thesis ($z \sim 5$); the redshift at which the Lyman break dropout technique described below was pioneered ($z \sim 3$); and $z \sim 0.25$ and $z \sim 0.15$, the highest and median redshift of the sample of 180 local Lyman break analogues which forms the basis of my thesis (see chapter 2 for the description of sample selection).

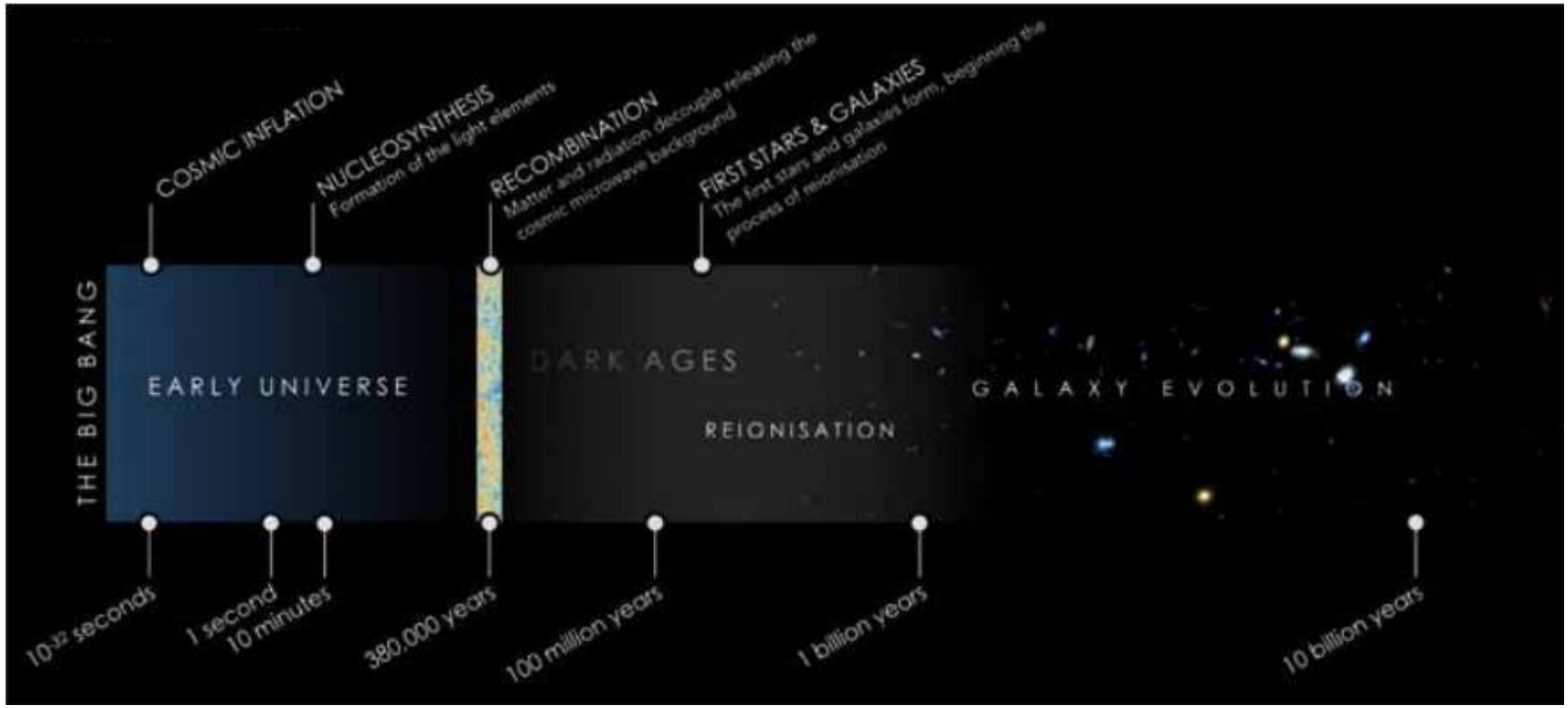

Figure 1.1: The history of the Universe [image by Wilkins & Stanway, 2015]. Following recombination when the Universe was approximately 380,000 years old and the cosmic microwave background was released, the second major phase transition occurred after the first stars and galaxies formed. Releasing large amounts of ionizing radiation into the IGM, these first galaxies are thought to have driven the process of reionization, during which most of the hydrogen in the cosmos became ionized. This process was mostly completed by the time the Universe was ~ 1 Gyr old, corresponding to a redshift of $z \sim 5$. Hence, in order to understand what drove this process, it is crucial to study the typical galaxies present at that epoch. However, due to their large distance and apparent faintness, direct observations of the $z > 5$ star-forming galaxy population is complicated, demonstrating the need for a sample of local analogue sources whose physical properties mimic those of their distant cousins, but whose relative nearness makes it possible to study them in greater detail.

1.2 How to Identify High-Redshift Galaxies

The first galaxies which formed in the history of the Universe are very rare objects in the night sky. Prior to the observation of the Hubble Deep Field (HDF) in December 1995 only a handful of galaxies at $z > 1$ (corresponding to a lookback time of about half the current age of the Universe) were known. The HDF, however, opened up a new frontier, containing numerous highly redshifted galaxies out to $z > 6$, observed less than one billion years after the Big Bang. Some method of distinguishing these distant galaxies from faint red foreground sources thus needed to be developed.

1.2.1 The Lyman Break, or Dropout, Technique

The Lyman break technique uses adjacent filters to identify objects whose flux abruptly drops out in the shorter wavelength band, hence also making this technique known as the dropout technique. It was first pioneered by Steidel et al. [1996], and makes it possible to estimate an object's redshift by assuming that the observed spectral break corresponds to the Lyman break in a distant galaxy. The abrupt spectral break is then taken to occur at 1216 $(1+z)$Å (the Lyman-α line) due to absorption by galactic and intergalactic neutral hydrogen along the line of sight. A second break at the redshifted Lyman-limit wavelength of 912 $(1+z)$ Å can also sometimes be observed. Few objects show similar intrinsic colours since such abrupt spectral breaks cannot occur due to emission. Using two or more filters, the spectral region in which the galaxy's flux drops out can be identified, hence constraining the object's photometric redshift. A veto filter shortwards of the bluer filter, or a continuum slope filter longwards of the redder filter would also be desirable. Fig. 1.2 illustrates the technique for a galaxy at redshift $z \sim 7$.

For example, in order to identify a galaxy at $z \sim 5$, where the Lyman-α break is redshifted to $(1+5) \times 1216 = 7296$Å, one might use the r-band of the *Sloan Digital Sky Survey* [SDSS Abazajian et al., 2009] (centred at 6200 Å) and i-band (centred at 7600 Å) and would expect the sources to be visible in the i-band, but to have dropped out in the r-band. In distant galaxies and quasars, the spectral region shortwards of the Lyman-α break exhibits multiple absorption line features due to absorption of light by intervening clouds of neutral hydrogen at different redshifts, and is known as the Lyman-α forest. Between redshifts $\sim 2 < z < 6$, the transmitted fraction of the Lyman-α forest shows a smooth evolution with redshift, indicating that the fraction of ionized hydrogen decreases smoothly in the distant Universe [Songaila, 2004]. Hence, broadly speaking, at intermediate redshifts ($z \sim 2-4$), it is possible to observe flux down to the Lyman-limit at 912Å, corresponding to the

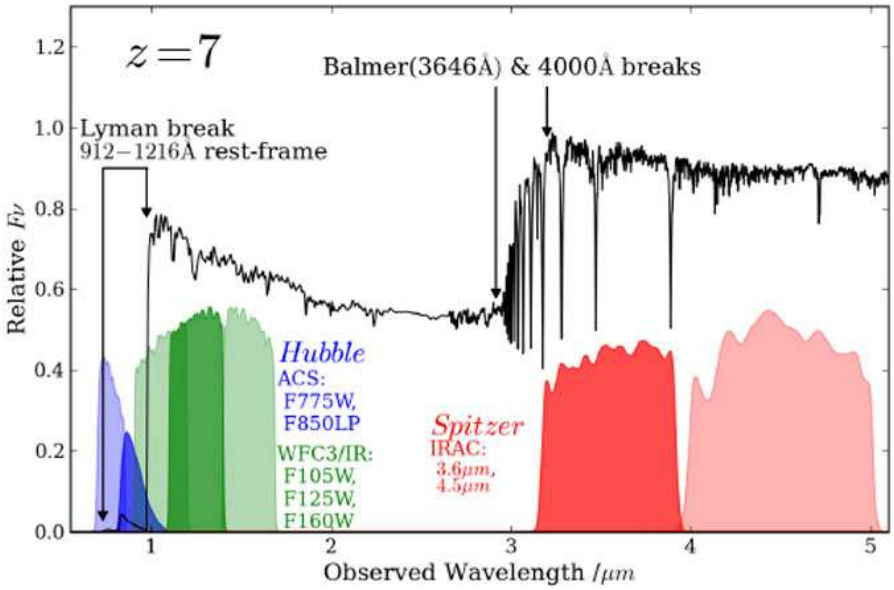

Figure 1.2: Illustration of the Lyman break dropout technique used to identify high-redshift galaxies. As the redshift of an observed source increases, the Lyman break is shifted to longer wavelengths. Thus, by observing adjacent filters, and detecting in which filter the drop in flux occurs, an approximate redshift can be calculated. Reproduced from `https://ned.ipac.caltech.edu/level5/Sept14/Dunlop/Figures/figure1.jpg`.

energy above which the ground state of neutral hydrogen may be ionized, while, at higher redshifts, the flux between the Lyman-α line and the Lyman-limit is absorbed by neutral hydrogen in the IGM. Thus more nearby systems exhibit a steep increase in flux between 912 Å and 1216 Å rest-frame.

When the Lyman break technique was pioneered, optical UGR filters were used to select dropout galaxies, thus typically selecting $z \sim 3$ LBGs which drop out in the U filter, giving rise to the naming of these galaxies as 'U-band dropouts'. With improved filter capabilities and CCD sensitivities at longer wavelengths, research into yet more distant systems became possible. Some of the most distant LBG candidates to date have been found to occur at less than $\sim$ 500 Myr after the Big Bang [see e.g. Bouwens et al., 2011; Barone-Nugent et al., 2015; Bouwens et al., 2016, for photometrically selected galaxies up to $z \sim 10$] [and Oesch et al., 2015; Tilvi et al., 2016, for spectroscopically confirmed LBGs at $z > 7.5$].

When selecting distant galaxies using only the photometric dropout technique, it is crucial to be aware of potential local contaminants which can mimic the colour selection used. The colours of M class stars can make them look like V- or R-band dropouts, while L and T stars can reproduce I-drop objects [Stanway et al., 2008]. Additionally intermediate redshift ($z \sim 1$) galaxies which are strongly line-emitting or have strong Balmer breaks can be mistaken for high-redshift sources.

Since this contamination is redshift dependent, more observed filterbands can help to clarify the situation, and can provide photometric redshift estimates. Despite these potential contaminants, Steidel et al. [2004] find a success rate of 78% for photometrically identifying $z \sim 3$ LBGs using this method. For a more robust identification, it is ideal to use a spectroscopically confirmed redshift.

1.2.2 Other techniques

Another method used to select high redshift galaxies makes use of narrow-band imaging in order to identify galaxies with a strong Lyman-α emission line, known as Lyman-α Emitters (LAEs). Using photometric bandpasses, this type of galaxy can be relatively easily detected if one narrow band contains the strong emission line while the object remains undetected or relatively faint in nearby bands. Since ionizing photons are absorbed and reprocessed into Lyman-α photons by the interstellar medium (ISM) in distant galaxies, the Lyman-α line is (by definition) very strong in these sources. However, while one advantage of this technique is that both the redshift and location of the observed galaxy can be readily determined, it has disadvantages when used as an identifier for the distant galaxy population. One drawback is that the Lyman-α photons can be absorbed and scattered by dust particles present within the source galaxy, reducing the observed flux from the object and complicating the interpretation. Another disadvantage is that potential ambiguity remains due to other strong emission lines within galaxies, such as e.g. Hα, [OIII], Hβ or [OII]. However, spectroscopic observations with high enough signal-to-noise of the source should be able to resolve this confusion. Lastly, due to absorption by the Earth's atmosphere, as well as night sky emission lines in the infrared bands, only certain spectral 'windows' can be observed unambiguously, restricting observations to particular redshift ranges. While infrared satellites exist which can overcome atmospheric constraints, their use is costly and time-consuming compared to ground-based observations.

Another tool to study some of the most distant galaxy populations is through the use of massive foreground structures as gravitational lenses which magnify the observed flux from faint background sources. Acting much like other types of lenses, a distribution of matter in the foreground bends the light from a distant object as it travels towards the observer (though another method, such as one of the ones described above, is still required to identify the source as a high-redshift object). Using this method, it has been possible to study some of the galaxies during the Epoch of Reionization [e.g. Schmidt et al., 2014]. Some of the major disadvantages of this method, however, are its reliance of favourably aligned foreground sources,

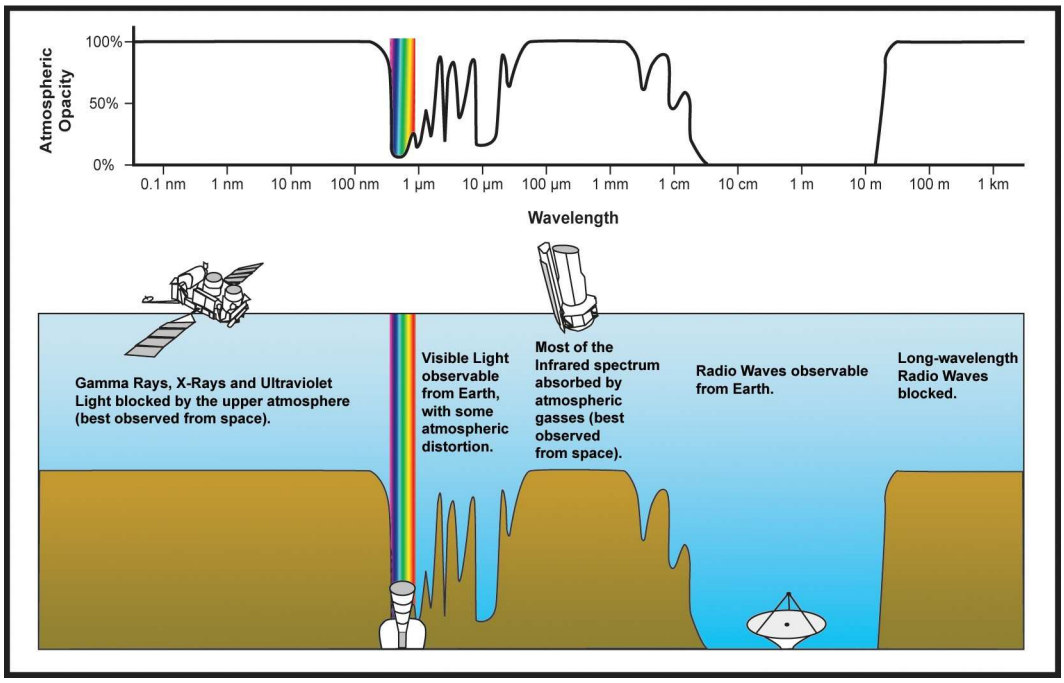

Figure 1.3: Atmospheric absorption spectrum, illustrating the need for space-based observations in the ultraviolet and infrared part of the spectrum where the Earth's atmospheric opacity is high. With the development of sensitive infrared detectors, it has become possible to identify Lyman break galaxies at increasingly higher redshifts (i.e. galaxies whose spectral break occurs in the infrared). Image reproduced from `http://gsp.humboldt.edu/olm_2015/Courses/GSP_216_Online/lesson2-1/atmosphere.html`.

and hence the very small volumes probed, as well as difficulties in modelling accurately the matter distribution within the foreground sources in order to determine a map of the magnification effect, leading to morphological distortion of the distant galaxy.

Both of the methods described have helped significantly to extend our understanding of the distant cosmos and have led to discoveries in their own right. They are mentioned for completeness, but do not form part of my analyses.

1.3 Lyman Break Galaxies

1.3.1 Properties of Distant Lyman Break Galaxies

The Lyman break galaxy population constitutes a significant, and possibly the dominant, fraction of the population of star-forming galaxies at high reshifts [de Barros et al., 2014]. Using the dropout technique described above, it has been possible to identify this type of galaxy throughout cosmic time, and to begin to study the physical conditions within them. Amongst the most readily discernible properties, at least for relatively nearby objects, is their physical size and morphological features, which allows measurements of any clumpiness or asymmetry of the source, as well as the

possibility of determining any clustering of similar sources nearby. Using spectroscopic or multi-waveband photometric observations, it is possible to determine the spectral energy distribution of a galaxy (more on this in chapter 2). From the colours and relative luminosities it is possible to determine the amount of dust attenuation and emission, providing a measure of the amount of light absorbed and re-emitted by non-luminous particles within the galaxy. Additionally, several wavebands and emission lines can be used as tracers of the total amount of stellar mass and star formation activity within the systems. Furthermore, spectroscopic measurements make it possible to not only constrain the metallicity within the sources, but also to calculate the ionization parameter (a measure of the hardness of ionizing radiation), and hence to determine whether the galaxy is powered primarily through star formation or contains an active galactic nucleus (AGN). Finally, by constraining the proportion of stars of certain ages, it is possible to place limits on the age of the galaxy itself.

While much can be learned in this way about the characteristics of galaxies, it is essential to note that many of these physical properties have underlying processes which significantly influence each other. For example, the dust in a galaxy is formed as stellar populations age, become asymptotic giant branch (AGB) stars and explode in supernovae, thereby enriching the interstellar medium with both dust and metals. The presence of these metals, in turn, will influence what kinds of stars can form from the now more strongly enriched ISM. Both the dust and metallicity content, as well as stellar populations of different ages, contribute to the bolometric output of a galaxy.

It can thus be complicated to break observational degeneracies between various observed characteristics. For example, as the blue part of a galaxy's spectrum is absorbed by dust in the ISM, the galaxy's spectral distribution will appear redder. However, a similar observed effect could be produced by an older stellar population whose hot, blue stars are no longer present.

In the following sections I provide a brief overview of the evolution of the main physical characteristics of (Lyman break) galaxies, how they are measured and what they can tell the observers, while also highlighting where degeneracies might occur between the properties. It should be noted that many of the very distant sources do not have spectroscopically confirmed redshifts, and that results at those redshifts are therefore tentative and subject to uncertainties due to potential contaminants.

Size and Morphology

Understanding the morphology evolution of galaxies can help shed light on questions such as whether galaxies form 'bottom up' or 'top down', i.e. whether structure first formed on small scales with subsequent mergers, or in larger clumps which then split into smaller objects. As indicated in table 1.1, even at high redshifts, galaxies can theoretically be resolved to a few kiloparsecs. Advances in ground-based adaptive optics and high-resolution space-based imaging have made it possible to resolve galaxies out to redshifts of $z \sim 8$ [see e.g. Akiyama et al., 2008; Conselice & Arnold, 2009], making it possible to study the compactness, clumpiness, size distributions and morphologies of galaxies throughout cosmic time, and revealing that structure formation differed significantly in the early Universe from what is observed locally.

In particular the compactness of a galaxy has implications for the physical processes within it: a more compact galaxy has a higher ionizing photon density, resulting in higher dust and ISM temperatures than would be expected in less dense star-forming regions. This increase in temperature, in turn, affects the way gas clouds collapse into stars, thus resulting in a different physical environment than in a less compact galaxy. In order to understand the evolution of galaxies' physical characteristics, it is thus crucial to investigate the change in morphology with cosmic time. Several studies have found that galaxies become less compact as the Universe becomes older, i.e. with decreasing redshift [see e.g. Daddi et al., 2005; Ferguson et al., 2004; Trujillo et al., 2007; Buitrago et al., 2008; van Dokkum et al., 2008, 2010; Weinzirl et al., 2011; Williams et al., 2014]. For example, Oesch et al. [2010] find that at $z \sim 7-8$ galaxies are very compact with typical sizes of 0.7 ± 0.3 kpc. This can be contrasted with galaxies at $z \sim 5$, which have mean half-light radii of ~ 0.9 kpc [Douglas et al., 2010; Jiang et al., 2013]. By redshifts $z < 2$ and in the local Universe, the relative abundance of such ultra-compact galaxies has declined significantly [Buitrago et al., 2008; Cassata et al., 2013], such that higher redshift galaxies of comparable masses have sizes a factor of 2-5 smaller than corresponding galaxies today.

It has been found that a strong relationship between morphology and stellar mass exists in both local and relatively distant galaxies [see e.g. Mosleh et al., 2012, and references therein], such that up to at least $z \sim 3$ the most massive galaxies tend to have elliptical morphologies and little or no star formation. Additionally, observations have shown that, at a fixed stellar mass, the sizes of galaxies decrease significantly with increasing redshift. This correlation has been confirmed up to at least $z \sim 5$ [Mosleh et al., 2012], and may extend as far as $z \sim 7$ [Allen et al., 2017, though these sources are medium-band selected and are not all Lyman break galax-

ies]. One caveat for the mass-size relations is that for these very distant galaxies, the sizes and masses are measured in different filters (rest-frame UV for sizes, and rest-frame optical for stellar masses), i.e. that star-forming regions may be more compact than the average distribution of stars in the galaxy, hence potentially making the observed correlation less robust. The evolution of the masses of galaxies throughout cosmic time will be described below in more detail.

Using high-resolution HST imaging, Douglas et al. [2010] find that more than half of $z \sim 5$ galaxies have irregular morphology and multiple components, ranging from 2 - 4 components with a mean distance between them of 5.3 kpc (ranging between 1 and 16 kpc), while noting that additional fainter components may be present that were not detectable above the surface brightness limits of their observations. This poses the interesting question of whether a recent merger history can be inferred in these galaxies. Some studies have found a large merger fraction for $z \sim 6$ LBGs of around 50% [Conselice & Arnold, 2009; Jiang et al., 2013; Ferguson et al., 2004]. For $z > 4$ LBGs, Conselice & Arnold [2009] find that a substantial fraction of these sources are currently either undergoing a merger or rapid assembly phase as indicated by tidal features, which are conceivable indicators for mergers.

Both locally and in the distant Universe, galaxies undergoing active star formation have different structures and morphologies from passive quiescent ones, with the former displaying clumpy structures, knots of star formation, or even galaxy-wide starbursts [Shibuya et al., 2015; Allen et al., 2017; Conselice, 2014]. Interestingly, star-forming galaxies display similar morphologies in their rest-UV, optical and near-infrared, suggesting that all these wavelengths are tracing the distribution of star formation directly, and that the youngest and most massive stars dominate the galaxy's spectral energy distribution at all wavelengths.

While studies of galaxy morphologies at high redshift are shedding light on the evolution of these properties, it is important to note that there is uncertainty about whether the high-redshift systems are truly representative of the entire collapsed mass within their galactic halo, or are simply high surface brightness regions with strong star formation, embedded within larger lower surface brightness systems. Obtaining a more nearby laboratory whose physical characteristics mimic those found in the distant Universe would make it easier to interpret the results of these high redshift observations.

Star Formation, Masses, and Ages

The star formation rates of an unresolved stellar population can be measured using conversions of emission line and photometric filter fluxes, which trace stellar pop-

ulations at different evolutionary stages after a star formation event. A recently formed stellar population, containing many O and B type stars, is strongly emitting in the ultraviolet and blue part of the (rest-frame) spectrum (unless the light is absorbed by intervening dust). Similarly, Hα emission lines can provide insights into the photoionization rates due to OB stars, and hence also trace massive star formation directly. However, for a normal initial mass function (IMF), low-mass stars dominate the integrated mass of the stellar population, but not the UV or Hα emission. In the absence of significant amounts of interstellar dust which absorbs UV light and re-radiates the energy in the infrared region, the red optical and near-infrared emission of a galaxy can be used as a mass proxy. Alternatively, fitting the synthetic stellar population templates to the observed spectral energy distribution of a galaxy makes it possible to calculate the stellar mass-to-light ratio of the source, and to calculate the total stellar mass within it; this is described in more detail in chapter 2. At the longest wavelengths, radio emission traces the rate of supernova explosions and hence also traces star formation (see chapter 3). One caveat to bear in mind is that star formation rate indicators are calibrated for stellar populations with ages of at least 100 Myr, and that they are likely to underestimate the true SFR of younger populations. This is particularly relevant to consider for radio SFR indicators since supernovae can be offset from the original star formation event by several tens of Myr. This problem, as well as a suggested solution, is discussed further in section 3.4.2.

Combining the findings on the evolution of the star formation rate and the typical sizes of galaxies, the comoving star formation rate density (star formation rate per unit area of volume) can be calculated, and has been found to peak at $z \sim 2.5$, declining rapidly at both higher and lower redshifts [see e.g Lilly et al., 1996; Madau et al., 1996; Shapley, 2011; Madau & Dickinson, 2014; Oesch et al., 2014]; see Fig. 1.4. Locally, this means that the bulk of the stellar mass in nearby galaxies was produced at $1 < z < 3$. At high redshifts, between $z \sim 10$ and 8, corresponding to a time interval of ~ 170 Myr, stellar mass is thought to have increased by approximately an order of magnitude [Oesch et al., 2014].

As would be assumed, higher redshift galaxies have been found to contain younger stellar populations and to be less massive than lower redshift sources. Interestingly, a differential mass growth of galaxies has been observed in photometrically selected high redshift sources, with the number density of the most massive galaxies increasing more rapidly than that of lower-mass galaxies, suggesting that, while the number density of low-mass galaxies remains relatively constant, there is a buildup of more massive galaxies [Song et al., 2016]. This is characteristic of 'downsizing'

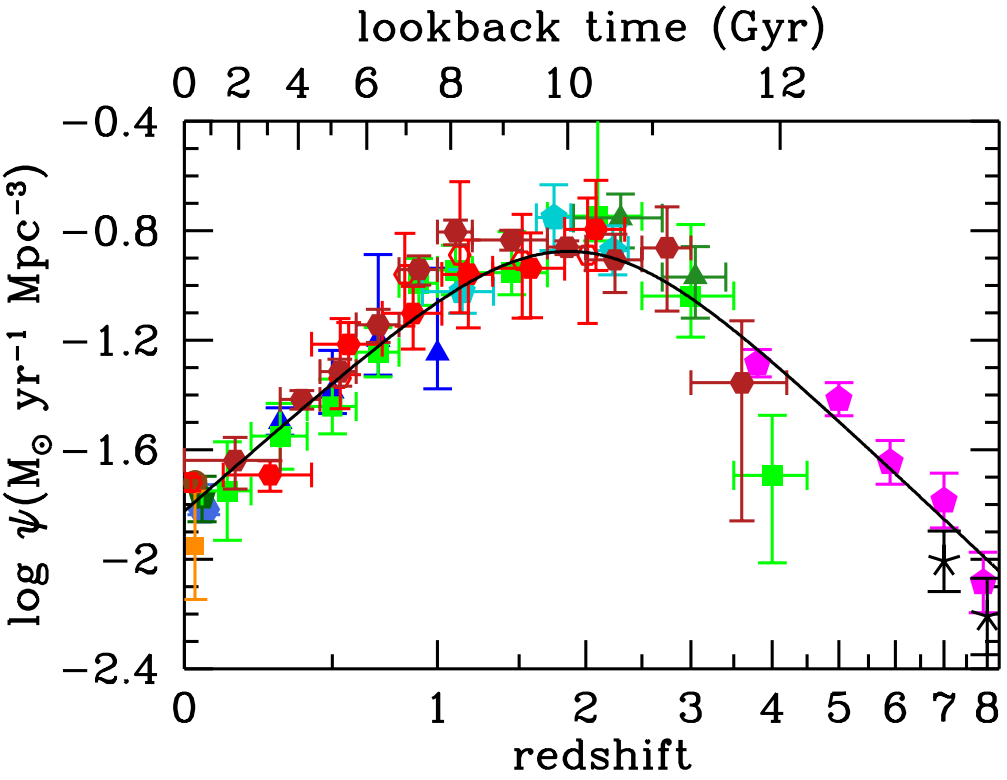

Figure 1.4: Evolution of the cosmic star formation rate density (SFRD) using (uncorrected) FUV and IR rest-frame measurements and assuming a Salpeter IMF; from Madau & Dickinson [2014]. The different shapes and colours refer to samples from different studies; e.g. the magenta pentagrams at $z \sim 4-8$ are taken from Bouwens et al. [2012b,a], while the black crosses at $z \sim 7-8$ are from Schenker et al. [2013]. It should be noted that both of these used photometric selection criteria, and hence there is potential uncertainty in the photometric redshifts.

observed with decreasing redshift. In the local Universe ($z < 4$), low mass galaxies are building their mass most rapidly, while this changes with increasing redshift [Neistein et al., 2006].

An alternative to determining a galaxy's stellar population would be to integrate its star formation history from its earliest instance of star formation to the observed epoch. However, several open questions remain about typical star formation histories: are stars formed continually in a smooth process, or does star formation follow bursty episodes of intense activity, interspersed with times of little or no star formation? If galaxies assembled their mass smoothly over timescales comparable to the Hubble time, they would be expected to form a tight sequence on a star formation to stellar mass plot, while a more bursty star formation history would result in significant scatter about the mean relation. So far, different studies are producing conflicting results: Brinchmann et al. [2004]; Noeske et al. [2007]; Elbaz et al. [2007]; Daddi et al. [2007]; Lee et al. [2011]; Sawicki [2012] find a strong tight correlation at $0 < z < 4$, while others determine no such correlation with a large amount of scatter [e.g. Franx et al., 2008; Mannucci et al., 2009]. Another possible interpretation of the observed discrepancies between the observed SFRs and the stellar mass in lower redshift galaxies might be that at each epoch studied, high redshift galaxies, which have only recently formed their most UV luminous stars, are dominating the observations [Stark et al., 2009]. This interpretation would give weight to an episodic, rather than smooth, star formation history within high redshift sources.

Comparing specifically the SFRs, ages and masses of $z \sim 5$ and lower redshift Lyman break galaxies, the trends mentioned above continue to exist: $z \sim 5$ LBGs are typically much younger (< 100 Myr) and have lower stellar masses ($\sim 10^9$ $M_\odot$) than those at $z \sim 3$, which have typical ages of 10^9 years and masses of 10^{9-11} $M_\odot$ [Verma et al., 2007]. This comparison also makes it apparent that $z \sim 5-7$ LBGs are not simply $z \sim 3$ LBGs at a higher redshift, and that therefore the findings for lower redshift populations likely can not easily be extrapolated to more distant galaxies. The high redshift sources appear to be experiencing their first (few) generations of large-scale star formation in what can be thought of as a galaxy-wide super-starburst with an extremely high star formation rate density [Verma et al., 2007; Douglas et al., 2010]. Given their young ages and high star formation rates, their implied formation redshifts may be as recent as $z \sim 6-7$.

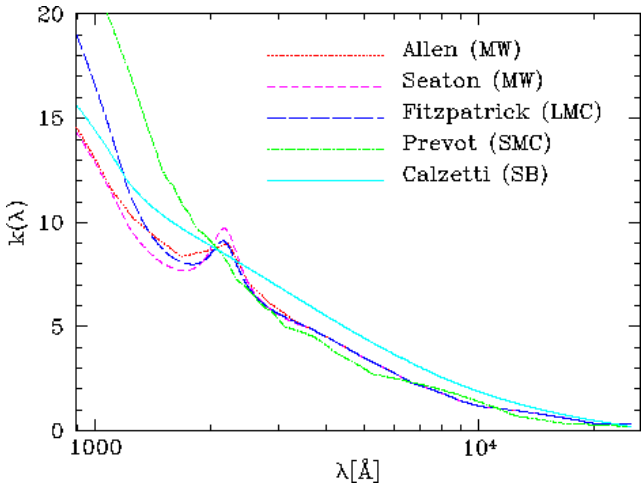

Figure 1.5: Extinction curves k(λ) for different reddening laws. Both the SMC and Calzetti et al. [2000] laws lack the graphite bump at 2175Å , suggesting an underabundance of carbon in systems described by these laws. For high-redshift studies, the Calzetti et al. [2000] law, which was empirically derived from a sample of nearby starburst galaxies, is most commonly used. However, more recently, a mixture between SMC-like and Calzetti et al. [2000] laws has been suggested for the dust treatment in distant galaxies [Bouwens et al., 2016]. Image from `http://webast.ast.obs-mip.fr/hyperz/hyperz_manual1/node10.html`.

Dust Absorption and Emission

The most commonly used star formation rate estimate for LBGs is the rest-frame ultraviolet luminosity, which measures the contribution of recently formed O and B type stars in a galaxy, whose luminosity peaks in the UV. However, one major uncertainty in this estimate is the amount of dust present within the source. Dust particles present in the interstellar medium of a galaxy absorb and scatter light away from the line-of-sight, and re-emit it as thermal grey-bodies in the infrared. The amount of extinction at a given wavelength, A_λ, depends on both the grain size distribution and composition: smaller grains tend to scatter shorter wavelengths more, while the presence of graphite can lead to a bump in the reddening curve at 2175Å . Extinction is related to the observed reddening of the spectrum as $A_\lambda = k_\lambda \cdot$E(B-V), where k_λ describes the reddening curve as a function of wavelength (see Fig. 1.5 for some commonly used dust extinction curves). Thus, if spectroscopic measurements are available, dust extinction in the optical can also be derived from observed line ratios whose intrinsic ratio is known, such as the Balmer decrement.

Locally, and in the $z < 3$ Universe, the amount of dust within a galaxy is well-described by the Meurer et al. [1999] relation according to which the amount of dust in a galaxy can be inferred from the relative fluxes in UV and infrared (known as

the infrared excess or, IRX) [see e.g. Álvarez-Márquez et al., 2016; Fudamoto et al., 2017; To et al., 2014]. Specifically, it indicates that the rest-frame UV continuum can be approximated by a power law of the form $F_\lambda \propto \lambda^\beta$, where for normal star-forming galaxies the exponent β, also known as the UV spectral slope, is assumed to take take intrinsic values of $\beta \sim -2$, corresponding to a flat spectrum in F_ν, though observed UV spectral slopes of $z \sim 3$ LBGs have been found in the $-3 < \beta < 0$ range. Fig. 1.6 indicates the redshift evolution of the IRX-β relation at different redshifts. Meurer et al. [1999] indicate that the standard IRX-β relation would only be applicable to high-z star-forming galaxies under the assumption that they are analogous to local starbursts, with the absorbing dust co-located with the young stars, hence ensuring the UV slope is directly associated with the re-processed thermal dust emission. In this case, it would be possible to determine the dust absorption in high-redshift galaxies [see e.g. Ouchi et al., 2004; Stanway et al., 2005; Bouwens et al., 2009]. However, as described above, in high-redshift star-forming systems star formation is likely to be more compact clumpy, resulting in a complex dust geometry relative to the stars. It should also be noted that this method is sensitive not only to assumptions on the intrinsic UV spectral slope of the galaxy but also the shape of the extinction curve itself. These properties are, in turn, related to the dust properties and stellar population characteristics, such as age and metallicity, within the galaxy. While originally calibrated to $z \sim 3$ LBGs in the Hubble Deep Field, deviations from the Meurer et al. [1999] relation have been found in both studies of local star forming galaxies [see e.g. Takeuchi et al., 2010; Overzier et al., 2011; Takeuchi et al., 2012] and high-redshift UV selected systems [see e.g. Wilkins et al., 2013; Capak et al., 2015, for $z \sim 5$ LBG]. Hydrodynamic simulations of high-redshift systems suggest that the intrinsic UV spectral slope varies significantly with redshift, and, at $z > 4$ is bluer than the β-value in the Meurer relation [Wilkins et al., 2013].

Two of the most commonly used extinction curves for high redshift galaxies are the SMC and Calzetti et al. [2000] laws. The most noticeable difference between them and other dust extinction laws is the absence of the graphite bump at 2175Å , suggesting that systems which are well-described by the SMC or Calzetti et al. [2000] laws are underabundant in carbon relative to the Milky Way. For high-redshift studies, the Calzetti et al. [2000] law, which was empirically derived from a sample of nearby starburst galaxies, is most commonly used, since galaxies with stellar masses above $10^{9.75}$ $M_\odot$ have been found to have observed IRX-β relations following that of Calzetti et al. [2000]. However, there are also suggestions that an intermediate dust treatment between the SMC law and the Calzetti et al. [2000] one may be more

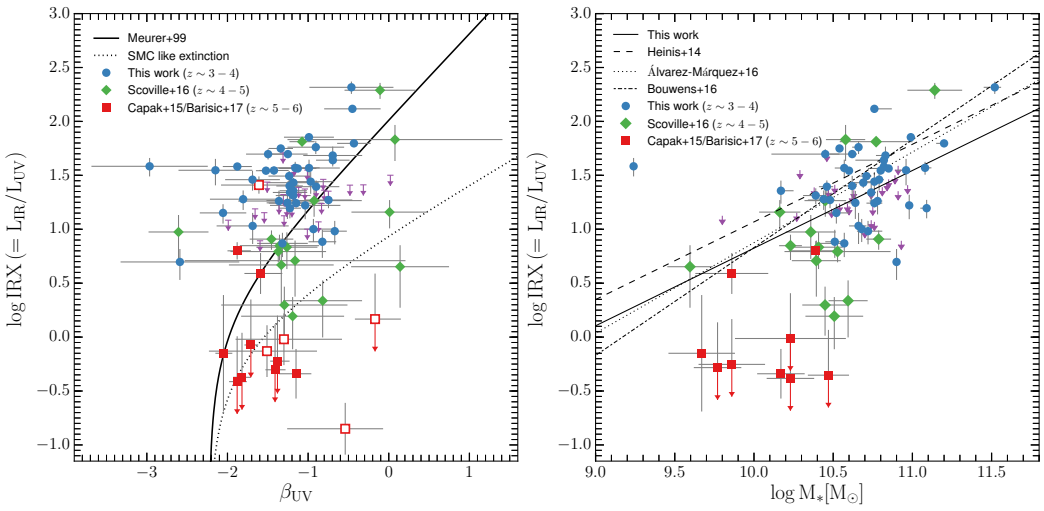

Figure 1.6: IRX-$\beta_{\rm UV}$ and IRX-M$_\star$ diagrams for galaxies at $z = 3-6$; plots reproduced from Fudamoto et al. [2017] who used ancilliary data from Scoville et al. [2016]; Capak et al. [2015]. **Left panel:** IRX-$\beta_{\rm UV}$ diagram. The solid line indicates the Meurer et al. [1999] relation, while an SMC like extinction curve is shown by the dotted line. **Right panel:** IRX-M$_\star$ plot of the same samples. Considered together, these figures suggest a significant redshift evolution of the IRX-$\beta_{\rm UV}$ relation between $z \sim 3$ and $z \sim 6$, even when taking into account the IRX-M$_\star$ correlation.

appropriate [Bouwens et al., 2016; Capak et al., 2015].

Measuring the sub-millimetre properties of $z \sim 3$, 4, and 5 Lyman break galaxies, a slight increase in 850 μm flux with redshift can be seen [Coppin et al., 2015]. Due to the negative k-correction in the sub-millimetre, an increase in flux with redshift corresponds to an increased intrinsic luminosity in the sources. The luminosity evolution of the LBGs is found to be broadly consistent with model predictions for the expected contribution of (ultra-)luminous infrared galaxies (or (U)LIRGs; with infrared luminosities $L_{IR} \sim$ 3-11$\times10^{11}$ L$_\odot$) at these epochs. The most distant sources, however, are also found to be increasingly unlikely to be sub-millimetre luminous [Coppin et al., 2015; Ho et al., 2010], potentially indicating that they contain very little dust which could absorb and re-radiate in the sub-millimetre regime.

Since galaxies are known to evolve through cosmic time, and since the interstellar processes in the Universe may be different from those in the local cosmos, it is reasonable to assume that their dust composition would also evolve with the age of the galaxy. In galaxies with stellar populations of < 400 Myr, mostly found at $z > 5$, asymptotic giant branch (AGB) stars have not yet evolved away from the main sequence, and hence supernovae are likely the only sources of condensed dust in these systems. On the other hand, in older (> 1 Gyr) galaxies, mostly found in the more nearby Universe, AGB stars may be the dominant source of dust production.

In observations of $z \sim 5$ LBGs, significantly lower infrared excess values are found than in typical local galaxies. Stanway et al. [2010] obtain non-detections in 870μm observations of a field known to host an overdensity of $z \sim 5$ LBGs. Stacking nine spectroscopically confirmed sources also yields a non-detection, hence constraining the typical sub-millimetre flux of these sources to < 0.85 mJy. These limits imply that the mass of thermal dust within $z \sim 5$ LBGs is likely less than a tenth of their typical stellar mass [Stanway et al., 2010]. Even with ALMA, the thermal dust continuum emission is only detected in four out of nine $z \sim 5$ LBG sources [Capak et al., 2015]. The thermal emission is less than a tenth of that in similar systems at $z \sim 3$, confirming strong evolution of the ISM properties between $z > 5$ and $z \sim 3$.

Until the advent of ALMA in 2011, our understanding of the far-infrared properties of UV-selected galaxies had mostly been restricted to the $z \sim 0$ to $z \sim 3$ range. *Herschel* observations of $0.95 < z < 2.2$ galaxies observed in both the rest-UV (with *Hubble*) and infrared indicate that the dust attenuation increases with stellar mass [Buat et al., 2012]. The presence of the graphite bump is detected in 20% of the overall sample, but is heavily concentrated at the lower redshift end, with 90% occurring at $z < 1.5$ [Buat et al., 2012]. ALMA observations of ten $z \sim 3$ LBGs result in the detection of one source at 870 μm. By combining the rest-frame infrared detection with rest-UV data, the detected galaxy is found to lie a factor of ~ 10 below the IRX-β relation of Meurer et al. found in local starbursts [Koprowski et al., 2016]. This might be due to the complex relative morphology between dust and UV emitting regions within the sources.

Several important questions thus remain: what causes the evolution in the observed dust properties of high-redshift galaxies? Do they contain a different dust composition to more nearby galaxies? Do they follow a different dust attenuation curve than typical local sources? Or both?

Spectroscopic Observations and Metallicity

Stars undergoing nuclear fusion in their interiors not only produce helium, but also heavier elements, known as metals. Since stars evolve and these metals are released into the interstellar medium in the form of stellar winds and supernova explosions, the metallicity of a galaxy gradually increases with time and a new generation of stars then forms from the enriched gas. Hence, a relation between the metal content and age of a system can be determined, with older systems typically having a lower metal abundance than younger ones, which in turn formed from metal-enriched gas. The chemical history of the Universe thus provides a record of past generations of

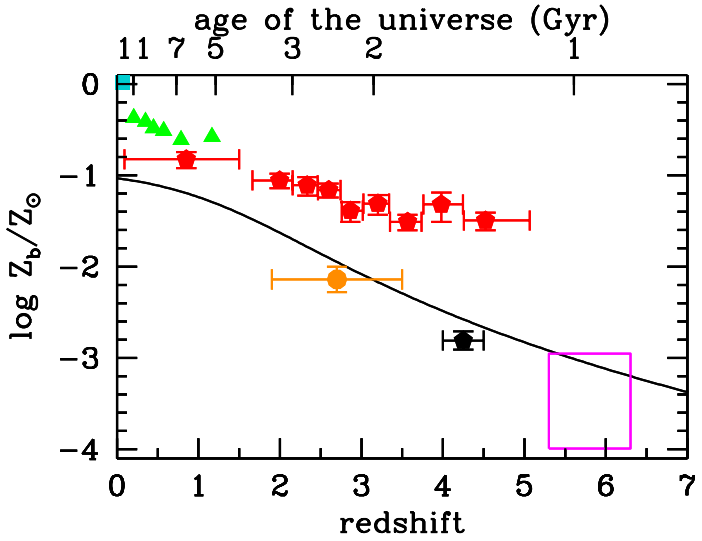

Figure 1.7: Mean metallicity evolution of the Universe, relative to Solar metallicity [from Madau & Dickinson, 2014]. The turquoise square (top left corner) indicates the stellar metallicity in the nearby Universe, while green triangles are used to show the mean iron abundances in central regions of galaxy clusters. The red pentagons indicate the metallicities of damped Lyα absorption systems, and the metallicity of the IGM as probed by O VI absorption in the Lyα forest is indicated by the orange dot. The black pentagon and magenta rectangle show the metallicity of the IGM as probed by C IV, and C IV and CII absorption respectively. It can also be seen that the available observations of the high redshift Universe are sparse and subject to large uncertainties.

star formations within galaxies. Its evolution is shown in Fig. 1.7.

Since the presence or absence of metals influences the available cooling mechanism in a galaxy, it has a direct impact on the types of stars that can form within the system and their evolution. This, in turn, influences the ionizing photon output and spectral energy distribution. It is therefore crucial to understand the evolution of metallicity with redshift. Studies of galactic abundances at high redshift have, however, often been plagued by observational and measurement uncertainties, with the commonly used metal calibrations disagreeing by more than an order of magnitude [Kewley et al., 2006]. A major difficulty is that current high-redshift metallicity calibrators assume conditions of the interstellar medium (ISM) to be similar to local sources. However, recent studies show that both the ISM pressure and ionization parameters evolve with redshift. Galaxies at $z \sim 3$ have been found to have significantly higher [OIII]/Hβ ratios than present day ones [Hainline et al., 2009; Bian et al., 2010; Kewley et al., 2013; Steidel et al., 2014], likely due to a change in

both the ISM pressure and ionization parameter due to intense star forming activity. More locally, Kewley et al. [2015] show that ionization parameter changes systematically in galaxies between $0 < z < 0.6$, resulting in an increase of the [OIII]/Hβ ratio, and a fall in the [NII]/Hα one. Hence, in order to accurately determine a system's chemical abundance, a metallicity calibrator should take these changes into account, or ideally be independent of both the ionization parameter and the ISM pressure. Dopita et al. [2016] propose such a metallicity measure, but which depends critically on the N/O ratio and its evolution.

Direct measurements of $z \geq 5$ metallicities in LBGs remain largely unexplored by current observations since direct observations of multiple optical lines are required. The observations which have been made at $z \sim 5$ indicate that these sources have estimated metallicities in the range 0.1-0.2 $Z_{\odot}$, about a factor of 3 lower than their $z \sim 3$ counterparts. Spectroscopy of $z \sim 4-8$ galaxies suggests that they have high rest-frame emission line widths above 30Å in Lyα, pointing to unusual properties in distant star forming galaxies [Holden et al., 2016; Oesch et al., 2015; Ono et al., 2012; Finkelstein et al., 2013]. While the presence of neutral hydrogen in the IGM leads to a suppression in flux shortwards of the rest-frame Lyα line known as the Gunn-Peterson trough, the observed Lyα emission line widths suggest that distant galaxies likely have different ISM properties than those seen in local galaxies. While not necessarily requiring very low metallicities, the high [OIII]/Hβ ratios indicate high ionization parameters. Possible physical mechanisms proposed to explain such high ionization parameters may include binary stellar populations [Stanway et al., 2014].

Studying the ISM within local analogues with comparable physical properties to the $z \geq 5$ LBG population might shed light on the physical processes driving the high ionization parameters, and could help to explore the metallicity evolution at $z > 5$.

In summary, Lyman break galaxies at $z \sim 5$ are less luminous [see e.g. Bouwens et al., 2007], younger and less massive [see e.g. Verma et al., 2007; Oesch et al., 2013], and have lower metallicities [Douglas et al., 2010] than $z \sim 3$ LBGs. The star-formation rate density within the LBG samples increases by a factor of $\sim 4-5$ from $z \sim 5$ to $z \sim 3$ [van der Burg et al., 2010]. They are also significantly more compact than their $z \sim 3$ counterparts [Wilkins et al., 2011; Mosleh et al., 2012], which has implications for the physical processes within the galaxies. The compactness modifies star formation since a higher UV-photon density causes higher dust and ISM temperatures, than would be present in more distributed star forming regions, which thus affects the collapse of molecular clouds into stars, the ionization

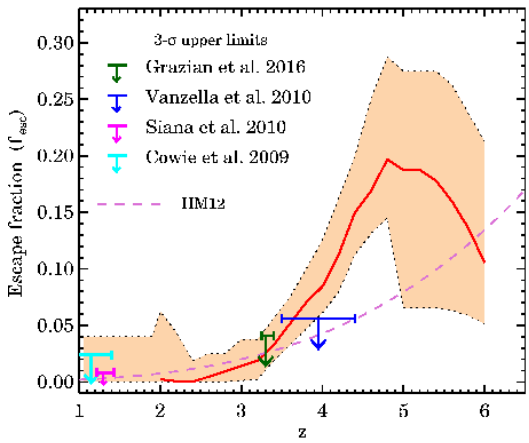

Figure 1.8: Evolution of the escape fraction through cosmic time. Image reproduced from Khaire et al. [2016].

of the intergalactic medium and potentially the mode of star formation itself [see e.g. Stanway et al., 2014].

1.3.2 The Role of Galaxies during the Epoch of Reionization

In order to determine the contribution of LBGs to the reionization of the Universe, the amount of ionizing radiation leaving a galaxy has to be determined. Measuring this quantity, known as the escape fraction (f_{esc}), remains a challenge at the highest redshifts. Fig. 1.8 indicates the evolution - and uncertainty - of measurements of f_{esc} through cosmic time. In addition, the relationship between a galaxy's properties and the escaping ionizing radiation is not well understood, nor its evolution with redshift. This, however, is a crucial question, bearing on problems such as galaxy evolution, and the contribution of galaxies to cosmic reionization.

Recently, the Planck Collaboration et al. [2016a] provided the most robust constraints to date on cosmic reionization extracted from the *Planck* cosmic microwave background data. They find the average redshift at which reionization occurs to lie between $z = 7.8$ and 8.8, depending on the reionization model adopted. Above $z \sim 10$, the Universe is found to be ionized at less than 10%, suggesting that an early onset of reionization is strongly disfavoured by the *Planck* data. However, by $z \sim 6$, the intergalactic gas has become almost fully ionized. Hence, the current conventional picture indicates that early galaxies progressively reionized hydrogen throughout the Universe between $z \sim 12$ and $z \sim 6$, before being overtaken by quasars at $z \sim 6$ to $z \sim 2$.

Since measuring the fraction of ionizing flux both inside and outside a galaxy during the Epoch of Reionization is almost impossible (due to the increasing neutral intergalactic gas fraction at $z > 4$, which would absorb any emitted ionizing flux), the evolution of the escape fraction has been studied in lower redshift systems up

to $z \sim 3-4$. This can be done using two main strategies: Using very deep UV imaging and/or spectroscopic observations, it is potentially possible to put direct constraints on even a small amount of escaping flux shortward of ~ 900Å . Such surveys are, however, very time consuming, requiring tens of hours of integration time. An alternative method is to measure escaping ionizing flux via shallower UV images for a very large sample of galaxies, and to stack the sources to obtain an average escape fraction.

Additionally, indirect methods of determining the escape fraction exist. For example, Alexandroff et al. [2015] find that the residual flux in the cores of saturated interstellar low-ionization absorption lines (such as Si II transitions), the relative amount of blue-shifted Lyα line emission, and the relative weakness of the [SII] optical emission line are good tracers of escaping UV flux. The strongest correlations are found in galaxies with highly compact star-forming regions and those with high outflow speeds, suggesting that high intensity ionizing radiation and strong radiation and wind pressures combine to drive high escape fractions. These indirect observational f_{esc} indicators can be used in observations of high-redshift systems where direct measurements are impossible.

However, exploring the amount of ionizing radiation escaping galaxies at even these lower redshifts yields contradictory results, with some studies claiming values as high as 50% [Steidel et al., 2001], while most indicate that less than 10% of the ionizing radiation escapes [Vanzella et al., 2010; Giallongo et al., 2002; Inoue et al., 2005; Shapley et al., 2006; Boutsia et al., 2011], calling into question whether these types of galaxies could have contributed significantly to the process of reionization.

It has, nevertheless, been found that f_{esc} appears to increase with redshift from $\sim 0\%$ at $z \sim 0$ to $\sim 10\%$ at $z \sim 3$ [Vanzella et al., 2010]. Additionally, there are indications that the escape fraction increases in fainter galaxies [Japelj et al., 2017] and in less massive systems [Xu et al., 2016]. This highlights the importance of small, faint galaxies as sources of ionizing radiation. However, these types of galaxies are notoriously difficult to study directly in the very distant Universe.

More nearby systems which mimic the properties seen in distant galaxies may therefore be helpful in in determining the likely escape fraction of $z \geq 5$ LBGs.

1.4 The Need for Local Analogues

Lyman break galaxies are selected for their spectral break, UV luminosity, and UV slope, the first of which is an extrinsic feature due to the interaction with neutral hydrogen along the line of sight, while the latter two are intrinsic to the system. Due

to their great luminosity distances, high-redshift galaxies are very difficult to study directly, requiring long integration times or, in the case of lensed systems, lucky alignment with foreground galaxies. They have small angular sizes and appear faint in the sky, making it near-impossible to explore their constituents in greater detail. Since the dropout technique selects galaxies above a certain luminosity threshold, there might also be a bias towards identifying the brightest galaxies, hence making it difficult, if not impossible, to guarantee the completeness and representativeness of a chosen high redshift population. For example, an $L_\star$ galaxy with an absolute magnitude of $M_{AB} = -21$ in the rest-frame UV, would have apparent magnitudes of $m_r = 26$ at $z \sim 3$, and $m_i = 27.4$ at $z \sim 5$, but $m_{NUV} = 18.3$ at $z \sim 0.15$. With a resolution of 0.1 arcsec, HST would be able to resolve structures down to ~ 0.8 and 0.6 kpc at $z \sim 3$ and 5 respectively, but down to 0.3 kpc at $z \sim 0.15$ (though this is a less compelling argument).

Hence, a possible solution to these problems is the use of more nearby galaxies as analogues or local laboratories to study their more distant cousins. Such local systems are selected to reproduce the observed properties of the distant sample, such as their luminosities, spectral slope, or emission line strengths. Due to the analogue population's more nearby location it is then possible to explore the physical properties in greater detail; properties such as ISM properties, gas kinematics, star formation rates and surface densities, and, in the case of the most nearby objects or with sufficiently powerfulS telescopes, even their morphologies.

One of the more extensively studied types of local analogues are Lyman break analogues to $z \sim 3$ LBGs. These local ($z < 0.3$) UV-bright systems are selected to reproduce the observed luminosities of $z \sim 3$ LBGs, with typical masses of $\sim 10^{9-11}$ $M_\odot$, metallicities between a third and 1.5 times Solar, and star formation rates of a few tens to hundreds $M_\odot$ yr^{-1} [Heckman et al., 2005; Hoopes et al., 2007; Gonçalves et al., 2010].

Another interesting sample of local analogues is the 'Green Pea' or 'Extreme Emission Line Galaxies' (EELGs) population established by Cardamone et al. [2009] and constituting galaxies originally identified by the general public in the Galaxy Zoo project. These sources are characterised by strong optical [OIII] emission lines, giving them their green appearance, and have small projected sizes. Identified as low mass ($10^{8.5-10}$ $M_\odot$) galaxies with high star formation rates (~ 10 $M_\odot$ yr^{-1}), very high specific star formation rates (up to $\sim 10^{-8}$ yr^{-1}), moderately sub-Solar metallicities (typically more than 0.5 $Z_\odot$), and low dust reddening ($E(B-V) < 0.25$), these galaxies are thought to provide good local laboratories to study the properties of distant Lyman-α emitters (LAEs).

A further example of local analogues are Blue Compact Dwarf (BCD) galaxies. First identified by Zwicky [1965], these sources are faint, compact, gas-rich star-forming galaxies. With metallicities below a tenth $Z_{\odot}$, they are some of the most metal-poor objects in the local Universe, making them good candidates for local analogues to the most distant $z > 8$ galaxy population. However, they are often dusty and can have older underlying stellar populations.

It is thus clear that analogue populations for distant galaxies exist in the local Universe. However, significant evolution occurs between different redshifts, even within galaxies selected using the same method, and therefore local analogues for one epoch of galaxies cannot be used as local analogues for galaxies at a significantly different redshift. Additionally, none of the samples presented above reproduce the spectral break, UV luminosity and UV spectral slope seen in the $z \sim 5-7$ LBG population. The ultraviolet-luminous galaxies (UVLGs) established by Heckman et al. [2005] and Hoopes et al. [2007] come closest; however, their selection uses the UV-optical slope instead, which is sensitive to the 4000 Å break, and these types of galaxies have been found to be more massive and older than $z \sim 5$ systems.

The distant galaxy population at $z \sim 5-7$ is of particular interest as these sources are likely to have contributed significantly to the ionizing radiation driving the observed phase transition during the Epoch of Reionization, and are therefore an important population in the Universe's history. As shown above, no satisfactory dedicated local analogue population for these distant sources existed at the time of the start of my PhD. The establishment, confirmation, and study of such an analogues samples hence constitutes the work of my PhD.

1.4.1 A Dedicated $z \sim 5$ Analogue Sample

As shown in section 1.3, there is significant evolution of Lyman break galaxies between $z \sim 5$ and $z \sim 3$ which must be taken into account when determining the appropriate selection criteria for local analogues to $z \sim 5$ LBGs. Stanway & Davies [2014] present a pilot sample of 21 compact star-forming galaxies in the local ($0.05 < z < 0.25$) Universe, whose ultraviolet luminosities match those of $z \geq 5$ LBGs. The candidates were selected using DR7 of the Sloan Digital Sky Survey (SDSS) [Abazajian et al., 2009] and *GALEX* (GR6) [Martin et al., 2005] photometry, as well as spectroscopic measurements by SDSS. Analysing the optical emission lines within these sources, the galaxies are found to be metal-poor with typical metallicities of a few tenth Solar, consistent with the distant $z \sim 5$ LBG population. Additionally, radio continuum observations at 5500 and 9000 MHz of 13 sources indicate radio spectral slopes which preclude the presence of strong dust-obscured

AGN in all radio-observed sources. The sample established by Stanway & Davies [2014] forms the basis of the work described in the following chapters. By comparing the star formation densities of the Hoopes et al. [2007] sample of $z \sim 2-3$ Lyman break analogues with those of typical values for LBGs at higher redshifts, Stanway & Davies [2014] indicate that only $\sim 3\%$ of the Hoopes et al. [2007] sample of UVLGs have a star formation density comparable to that observed in distant Lyman break galaxies. This discrepancy only becomes exacerbated as the Lyman break samples are pushed to higher redshifts. It is also worth noting that, while such an analogue sample is selected to produce similar physical conditions in both low ($z < 0.25$) and high ($z \sim 5$) galaxies, the nature of these galaxies is likely to be very different. The $z \sim 5$ LBGs are presumably among the first structures to collapse in the Universe, and thus likely reside in massive, though rare, dark matter haloes. Due to this dark matter overdensity, these galaxies begin star formation only a Gyr after the Big Bang. On the other hand, the collapse of, and star formation in, the $z < 0.25$ sources has been delayed for a further ~ 10 Gyrs, suggesting that they reside in much lower mass dark matter haloes. It may also be that star formation in these younger galaxies was surpressed by photoionization by the IGM, which might explain the observed lack of large numbers of dwarf galaxies compared to ΛCDM predictions.

1.4.2 Data Mining for LBAs

In order to select a sample of local analogues, one would ideally want to obtain deep multi-wavelength imaging and spectroscopy of the entire sky to a sufficient depth, which includes high-resolution UV coverage. This is, sadly, not yet a real possibility. In the meantime, all-sky surveys and those which cover a large area of the sky can be used. In particular, ultraviolet, optical and infrared fluxes need to be measured, so that both the UV spectral slope can be measured, and further information can be gleaned, e.g. through SED fitting (see chapter 2 for more).

Some of the surveys which can be used for this include, but are not limited to the following. The only available ultraviolet survey with sufficient depth and area is the *Galaxy Evolution Explorer* (*GALEX*) whose medium imaging survey (MIS) (in *GALEX* release 6) undertook single orbit exposures of ~ 1000 sq. deg., resulting in a depth of 22.6(FUV)/22.7(NUV) mag. In addition to the MIS, *GALEX* also carried out an all-sky imaging survey (AIS); this, however, only reached a 5σ limiting magnitude of 19.9 (FUV)/20.8(NUV) [Bianchi et al., 2011]. Several optical surveys exist whose catalogues can be data mined for potential local Lyman break analogues (assuming that matching UV data exists). The Sloan Digital Sky

Survey (SDSS) covered $\sim 12,000$ deg^2 (in its 7th data release) in the *ugriz* filter bands, with typical magnitudes of 22, 22.2, 22.2, 21.3, and 20.5 respectively. In addition to these photometric observations which cover $\sim 30\%$ of the sky, $\sim 9,400$ deg^2 have spectroscopic measurements in the wavelength range $3800 - 9200$ Å, yielding 1.6 million spectra in total, and including 930,000 galaxies. While the SDSS observations (as well as the VST ATLAS survey) are mostly targeting the Northern sky, the VISTA Hemisphere Survey is undertaking similar observations of the Southern hemisphere, making use of the *ugriz* filters and aiming for comparable depth to SDSS. The catalogues of both optical surveys, as well as the *GALEX* database can be queried using the Structured Query Language (SQL).

Published in 2003, the Two Micron All-Sky Survey [2MASS, Skrutskie et al., 2006], observed $\sim 70\%$ of the sky in three wavebands centred at 1.25μm (J), 1.65μm (H) and 2.17μm (K_S). Its descendent, the UKIRT Infrared Deep Sky Survey [UKIDSS, Lawrence et al., 2007], surveyed ~ 7500 deg^2 in the Northern sky to a depth 3 magnitudes deeper than 2MASS, making it the near-infrared counterpart to SDSS. Imaging the near- and far-infrared, the *Wide-field Infrared Survey Explorer* [WISE, Wright et al., 2010], undertook all-sky observations at 3.4μm, 4.6μm, 12μm and 22μm, achieving 5σ photometric sensitivities of 19.3, 18.9, 16.5, and 14.6, respectively.

Cross-matching and combining the data from ultraviolet, optical and infrared surveys (and applying redshift, luminosity, size and declination constraints), it is possible to fit the spectral energy distribution of the candidates and hence to learn about their physical properties, as will be described in chapter 2.

1.5 Scientific Objectives and Overview of the Thesis

The goal of my PhD has been the establishment, confirmation, and study of a dedicated sample of local analogues to $z \sim 5$ Lyman break galaxies whose physical properties can be studied in greater detail in order to make possible the interpretation of results for their distant cousins.

In chapter 2, I present the work previously published in Greis et al. [2016] in which I extended the pilot sample of local Lyman break analogues candidates established by Stanway & Davies [2014] to 180 objects and derived their physical properties through SED fitting. Following the confirmation that most of the candidate galaxies successfully reproduce the mass ranges, ages, dust contents, star formation rates and metallicities seen in the distant $z \sim 5$ LBG population, I analysed 1.5 GHz VLA observations of a subsample of 32 confirmed Lyman break analogues, provid-

ing further insights into their dust and star formation properties, as well as placing stronger constraints on the absence of active galactic nuclei within these sources, and confirming that their stellar populations are younger than $\sim$ 100 Myr. This work forms chapter 3 of this thesis and has been published in Greis et al. [2017]. In the final science chapter I explore the efficiency of the photometric selection criteria used to select local Lyman break analogues. Using AAOmega spectroscopy of a purely photometrically selected sample of $\sim$ 230 LBA candidates, I determine what fraction of photometric candidates fulfill the spectroscopic LBA criteria. Combining this with the results from chapter 2 in which I determined what fraction of spectroscopic candidates are genuine good local analogues, it becomes possible to estimate the fraction of good analogues in a purely photometric sample - and hence the number density of LBAs on the sky. The final chapter of my thesis focuses on the conclusions that can be drawn from my work, and looks forward towards the advent of future observational facilities and their impact upon the field of the studies of distant galaxies and their local analogues.

Throughout this thesis, magnitudes are given in the AB system. In line with results by Planck Collaboration et al. [2016b], I adopt a standard ΛCDM cosmology with $H_0 = 70\,\mathrm{km\,s^{-1}\,Mpc^{-1}}$, $\Omega_M = 0.3$ and $\Omega_\Lambda = 0.7$, taking the cosmological parameters to 1 significant figure to account for the continual evolution of the field.

1.6 Summary

- Due to the Universe's expansion, light is stretched, or redshifted, as it traverses the cosmos. Since light travels at a finite speed, the redshift of a galaxy can be used to determine the distance to the galaxy. Hence a given redshift corresponds to a specific look-back time, and thus a specific epoch, or age, of the Universe is observed. The redshifts most relevant to my thesis are: $z \sim 5$, corresponding to a time when the Universe was approximately 1 Gyr old, and $z \sim 0.15$ which corresponds to a look-back time of 2 Gyr, i.e. when the Universe was about 11 Gyr old.

- During the Epoch of Reionization the intergalactic medium in the Universe underwent a phase change from a previously neutral state to an ionized one. This occurred, at least partly, due to the ionizing radiation emitted by hot stars in recently formed galaxies. In order to better understand how this process occurred, it is therefore important to learn more about the types of galaxies which contributed to the Epoch of Reionization.

- Distant galaxies can be selected in several ways, including the Lyman break or dropout technique. As clouds of neutral hydrogen in the line of sight absorb the flux emitted by a distant galaxy, an abrupt break occurs shortwards of the redshifted Lyman-α line (at 1216Å in the galaxy's rest-frame), and a second break occurs at the Lyman limit (at 912Å in a galaxy's rest-frame), corresponding to the ionization energy of hydrogen. By making use of (ideally, several) adjacent photometric filters, the dropout technique identifies galaxies whose flux abruptly drops out in one of the filters, indicating where the redshifted Lyman break has been detected. From this, the redshift of the observed source can be determined with some level of accuracy.

- Using the dropout method, as well as spectroscopic surveys, it has been possible to observe and infer the physical properties of galaxies at many redshifts; some up to $z > 6$. A clear evolution with redshift can be seen in the typical physical characteristics, such that the more distant galaxies are typically less massive, less luminous, less metal rich, and less dusty than more nearby sources.

- Due to their large distances and low apparent brightnesses, it is difficult to study high redshift galaxies directly. Using local analogues, which reproduce many of the observed physical characteristics of the distant samples as more nearby laboratories, can help interpret distant galaxies' observed properties.

- Such local analogue samples have been established for several distant galaxy populations, but so far no dedicated sample has been developed to reproduce the properties of $5 \leq z \leq 7$ LBGs which are likely to have been among the sources driving the ionization of the Universe during the Epoch of Reionization.

- The aim of my PhD is the establishment, confirmation, and study of a dedicated sample of local ($z < 0.25$) analogues to $5 \leq z \leq 7$ LBGs.

Chapter 2

Modelling the Spectral Energy Distributions of Lyman Break Analogue Candidates

> Man must rise above the Earth – to the top of the atmosphere and beyond – for only thus will he fully understand the world in which he lives.
>
> Socrates

2.1 Introduction

A galaxy's spectral energy distribution (SED) can, in principle, provide detailed information about its physical properties, including stellar mass, past and current star formation rate, metallicity, and dust content. In this chapter I will present the results of fitting the SEDs of 180 local galaxies selected to reproduce the observed ultraviolet properties of $z \sim 5$ Lyman break galaxies to confirm whether they can be used as local analogues to the distant galaxy population. However, before describing the sample, its selection, and the derived and inferred properties, I want to briefly introduce the key ingredients needed for the SED-fitting.

2.1.1 The Origin of a Galaxy's Spectral Energy Distribution

A galaxy's observed spectrum is made up of a mixture of stellar spectra, dust absorption and re-emission, emission and absorption due to the interstellar medium

within it, as well as any radio components. Additionally, for distant objects, any redshifting of the spectrum or absorption due to intervening gas clouds needs to be taken into account.

The stellar spectra in a galaxy's SED can be crudely approximated as a series of black-body energy distributions (together with atomic or molecular absorption features) spanning the range of stellar temperatures within the system; it is thus best to use empirical or theoretical stellar templates. The hottest and most massive stars in a stellar population are those of O and B types, whose spectra peak at very short wavelengths. Due to the inverse relationship between stellar mass and typical main-sequence lifetime, these ultraviolet-bright stars have relatively short lifetimes of a few to some tens or hundreds of Myr. This explains why the rest-frame ultraviolet spectral region of a galaxy is dominated by such recently formed O and B type stars. The most striking spectral feature in the ultraviolet is the abrupt spectral break at the Lyman limit, 912Å in a galaxy's rest-frame, corresponding to the ionization energy of hydrogen. As photons with higher energies are absorbed by hydrogen in the galaxy's ISM, this leads to a suppression of flux shortwards of the Lyman limit.

Less massive, and hence cooler, stars dominate the rest-frame optical emission of a galaxy. Since these less massive spectral types have longer lifetimes, the rest-frame optical light can be used as a good tracer for the total stellar mass within the galaxy. Their combined luminosity, however, can be entirely outshone by bright O and B type stars following a starburst event. Additionally, the spectral break at $\sim$4000Å arising from the combination of the Balmer break and metal line absorption, can be used as age indicators for a stellar population.

Moving on to longer wavelengths, dust emission dominates the infrared part of a galaxy's spectrum. Having absorbed the energy emitted by stars in the UV and optical, dust particles heat up and eventually emit the reprocessed energy at far-infrared (FIR) and sub-millimetre wavelengths. Polycyclic aromatic hydrocarbons (PAHs), organic compounds consisting exclusively of carbon and hydrogen which follow a more complex emission spectrum, fluoresce at $\sim 6 - 8$ μm. Dust in the ISM is an important component in almost all galaxies, particularly those undergoing active star formation. Since dust absorption is most strongly influenced by a galaxy's geometry, whereas dust emission depends strongly on the radiation field within the galaxy [Conroy, 2013], it is reasonably to model these two aspects separately in SEDs.

In order to fully understand a galaxy's spectrum, it is crucial to consider the evolution of the stars within it. As mentioned above, young, massive stars dominate in the ultraviolet, while less massive stars peak in the optical part of

the spectrum. As the stellar population ages, the emission from the most massive stars disappears first, creating an increasingly redder spectrum. Furthermore, the distinctive 4000 Å break, due to the absorption of high-energy radiation by metals in stellar atmospheres, becomes more prominent in an older stellar population.

Another important factor influencing the SED of a galaxy is the amount of dust absorption. As dust particles absorb ultraviolet radiation, reprocess and emit it as black-body radiation peaking in the infrared, the overall spectrum of the galaxy becomes redder. Since both dust absorption and old stellar populations can create red spectra, it is important to break this degeneracy.

One way to distinguish a galaxy reddened by dust absorption from one reddened due to an older stellar population, is to use spectroscopic measurements of emission and absorption lines in the observed spectrum and to compare the observed line ratios to predictions from atomic physics. These spectral line features arise from atoms or molecules undergoing transitions between different energy levels, producing an emission line when the system transitions from a higher to a lower state, and absorption features when the inverse process occurs. Stellar absorption lines are caused by atoms in a star's atmosphere which absorb specific wavelengths. The ISM can also cause absorption lines when stellar light passes through cold interstellar gas, while nebular emission lines arise from the gas being heated and ionized, and then re-radiating at specific wavelengths. Typical emission line features relevant in my thesis are e.g. the Balmer series of hydrogen emission lines (e.g. Hα at 6564Å Hβ at 4863Å Hγ at 4342Å etc., which are caused by the transition of a hydrogen electron to the second lowest energy level), and oxygen lines (such as the forbidden [O II] doublet lines at $\lambda\lambda$3726, 3729Å , and the forbidden [O III] line at $\lambda\lambda$4959, 5007Å). For a more in-depth discussion of spectroscopy, see chapter 4.

In addition to the spectral features and ranges mentioned here, galaxies also emit in the radio - observations at radio frequencies will form the basis of chapter 3.

In the absence of available spectroscopy, multi-band photometric observations of galaxies can be used to determine the spectral energy distribution.

2.1.2 How to Build a Synthetic Galaxy

To derive the physical properties of an observed galaxy, the shape of its observed SED, found by measuring its flux in several filters, is compared to a template, usually a synthetically constructed spectrum. Such a synthetic spectrum has several key ingredients described in the paragraphs below and shown in Fig. 2.1. The process of creating SED models begins by modelling a coeval stellar population (i.e.

one which formed at the same time) which evolves according to a set of specified stellar evolutionary tracks. This creates a simple stellar population (SSP), which can then be combined with an assumed star formation history to produce a composite stellar population (CSP). Modifying the CSP by incorporating the effects of dust attenuation and nebular emission thus creates the final synthetic SED at a given age and for specific input parameters.

The Initial Mass Function The initial mass function (IMF) provides a measure of the initial distribution of stellar masses along the main-sequence. It has been studied extensively for decades, with the canonical Salpeter [Salpeter, 1955] IMF taking the form $dN/dM \propto M^{-2.35}$ for stellar masses of up to $\sim$ 100 $M_{\odot}$. Other IMF models, such as the Kroupa [2001] and Chabrier [2003] models, have a shallower distribution at sub-Solar masses, hence producing fewer low-mass stars than the Salpeter IMF. By indicating how many stars of a given mass are present within a galaxy, the IMF determines the overall normalisation of the mass-to-light ratio of the synthetic stellar population. Knowing the IMF of a stellar population also makes it possible to calculate the luminosity evolution of the population, assuming that star-formation has ceased. When modelling the SED of a composite stellar population, the IMF affects the integrated light of the system. While, for a coeval population, the integrated light is dominated by stars at the turnoff mass, a composite population contains a range of turnoff masses which all contribute to the bolometric luminosity of the galaxy. While low-mass stars do not make a significant contribution to a galaxy's luminosity, they dominate the stellar mass within it.

The Interstellar Medium Emission and absorption due to atoms and molecules in the ISM needs to be taken into account. There are two components to nebular emission, the continuum emission due to free-free, free-bound, or 2-photon emission, and recombination lines. The effect of nebular emission on the spectral energy distribution of a system is particularly important at low metallicities and in young stellar populations, where the contribution from nebular emission can be as high as 20 - 60 % [Anders & Fritze-v. Alvensleben, 2003]. Nebular emission is also an important aspect to consider in high redshift systems where a fixed rest-frame equivalent width (EW) will occupy a larger fraction of the filter bandpass. This occurs due to the redshifting of the emission line, which is observed stretched by a factor of (1+z), hence providing flux in a larger fraction of a given filter band than an equivalent line would in a low-redshift observation. Additionally, the absorption and re-emission of stellar light by dust particles has a strong influence on the shape of an SED, and

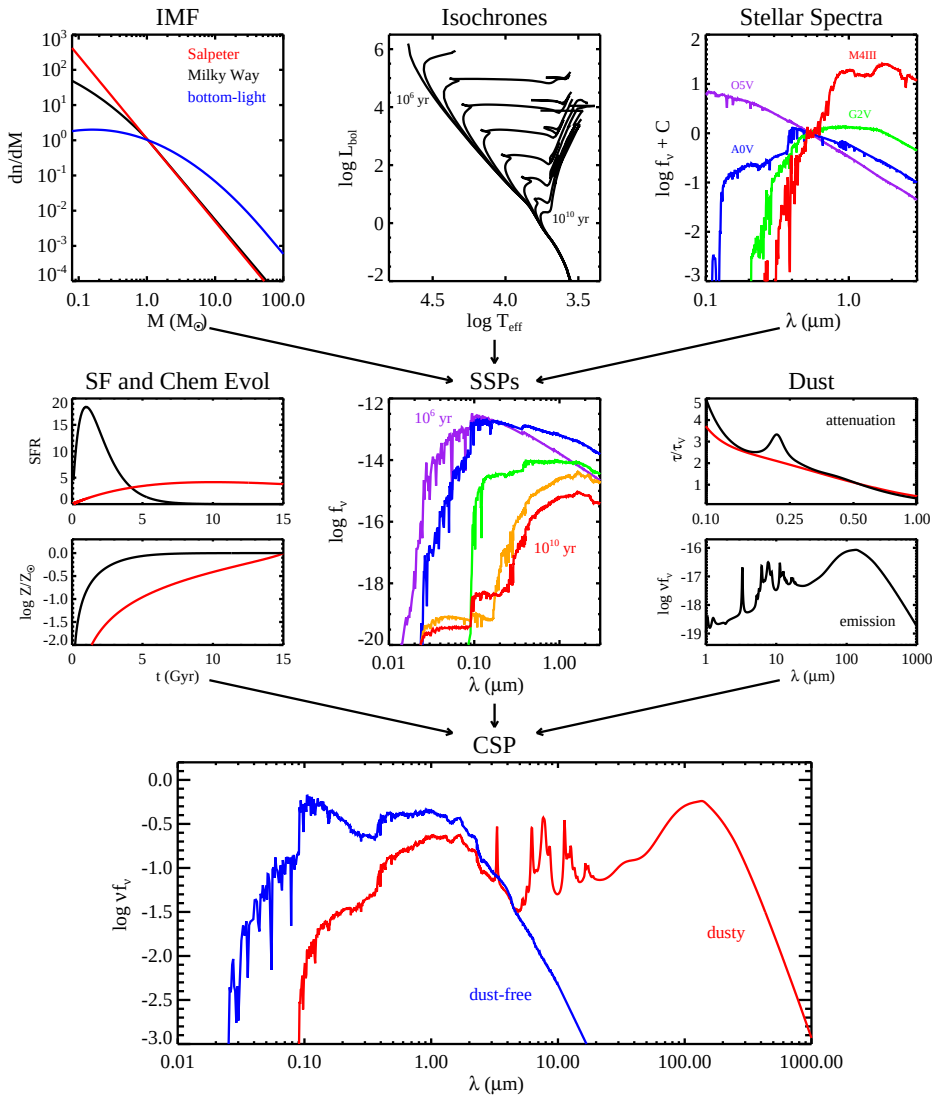

Figure 2.1: The key ingredients needed to construct a composite stellar population, reproduced from Conroy [2013]. The initial mass function, together with stellar evolution tracks and spectra creates the single stellar population models. Convolving these with star formation histories, metallicity enrichment, and dust attenuation and emission produces the final model (bottom panel, showing a composite stellar population both before and after the application of dust models).

needs to be considered when building a synthetic galaxy.

Composite Stellar Population Simple stellar populations are the building blocks for more complex stellar systems, with the main differences between CSPs and SSPs being that the former contain stars of different ages according to the assumed star formation history (SFH), that the stars can have different metallicities, and that CSPs contain dust. Theoretically, the assumed SFH can be arbitrarily complex. However, one of the most popular models is the exponential SFR, or τ-model, in which SFR $\propto e^{-t/\tau}$, where τ gives the typical timescale over which the SFR decreases. The τ-model arises naturally out of star formation models where the rate of star formation depends linearly on the gas density in a closed-box model [Schmidt, 1959]. In the models used in my thesis, one single metallicity is assumed for the entire stellar population of a galaxy.

SED Combining the elements described above, a synthetic model spectrum can be created. The flux observed from a source in different wavebands is then compared to synthetic spectra created from a library of either empirical or stellar population synthesis (SPS) model templates, making it possible to constrain physical parameters such as the mass-to-light ratio, the specific star formation rate (sSFR≡SFR per unit stellar mass), dust attenuation, and metallicity.

While much progress has been made over the past few decades in the implementation of SED fitting codes, many substantial uncertainties remain. These include, among others, the treatment of the thermally-pulsating asymptotic giant branch (TP-AGB) phase in stellar evolution, the effects of binarity, particularly on massive star evolution, the importance of rotation and the interdependence of the IMF on ISM properties such as metallicity or pressure. How a certain model implements these properties can have dramatic impact on the resulting spectra, and hence on the inferred physical properties of the stellar population to be fitted. Some popular SED codes include e.g. the Maraston [2005] ('M05') models, the Binary Population and Spectral Synthesis SPS code [BPASS, Eldridge & Stanway, 2009, 2012], Starburst99 [Leitherer et al., 1999], the Bruzual-Charlot models [BC03 and CB07 see e.g. Bruzual & Charlot, 2003; Bruzual, 2007], CIGALE [Burgarella et al., 2005; Roehlly et al., 2014], and others. Out of these BPASS is the only one which incorporates the stellar evolution due to binary interactions. Comparing Starburst99 with BPASS and others, Wofford et al. [2016] find that Starburst99 yielded higher dust reddening values for the most reddened sources than the other stellar evolutionary tracks probed. They additionally found that for young stellar populations

with ages < 10 Myr, both the single rotating Starburst99 and BPASS model with interacting binaries yield systematically larger ages than the rest of the models. Overall, Wofford et al. [2016] conclude that the observations of young massive star clusters are slightly better reproduced by models implementing binary interactions (BPASS), and least well reproduced by models with single rotating stars, such as Starburst99. Comparing BC03, M05 and others, Conroy & Gunn [2010] determine that for low metallicities and older ages these models predict similar colours, but that M05 colours are too red and their age-dependence is incorrect. They additionally find that BC03 better reproduces the optical and near-infrared colours of post-starburst systems than M05. The latter, however, include stellar evolutionary tracks for TP-AGB stars and good agreement between intermediate-redshift ($z \sim 2.5 - 3$) observations and model-predicted fluxes has been found (see e.g.Maraston [2005], though also Kriek et al. [2010] who find only a low contribution of TP-AGB stars in post-starburst galaxies).

2.1.3 Overview of Chapter

In this chapter I will present the process and results of fitting the spectral energy distributions of a sample of 180 local galaxies using the Binary Population and Spectral Synthesis SPS code [BPASS, Eldridge & Stanway, 2009, 2012], as well as the Maraston [2005] ('M05') models. I will compare the results from my SED fitting with those found using other independent models (such as CIGALE) and analyses [such as Salim et al., 2016] (in Section 2.8) before commenting on the suitability of this sample as a local analogue population to $z \sim 5$ LBGs, and comparing its properties to those of other local and distant galaxy populations.
The core of the results presented in this chapter is based on my published paper [Greis et al., 2016], with additional comparisons to the Salim et al. [2016] sample, published after the submission of Greis et al. [2016].

2.2 UV and Optical Sample Selection

Building on the pilot sample of twenty-one compact star-forming galaxies established by Stanway & Davies [2014], I extended it by lifting the declination constraint originally imposed on it. This constraint had originally been imposed to facilitate observations with Southern telescopes, such as ATCA. By lifting it, the number of candidate objects was increased significantly, hence making the results of this study more statistically robust. Potential candidates were identified from data release six

(GR6) of the publicly available *GALEX* survey[1] [Martin et al., 2005] and DR7 of the Sloan Digital Sky Survey[2] [SDSS, Abazajian et al., 2009], providing ultraviolet and optical data respectively. The candidates were selected such that their UV colours satisfy $-0.5 < FUV - NUV < 0.5$ or $-0.5 < FUV - r < 1.0$, where FUV and NUV correspond to the observed frame *GALEX* far- and near-ultraviolet bands at ~ 1500Å and ~ 2300Å respectively, while r indicates the *SDSS* red band at ~ 6200Å. We set this restriction to ensure that the rest-frame UV slope is close to flat, indicative of a recently formed population of young stars with ages < 200Myrs. A further colour selection is made such that $NUV - r < 2$ since no plausible candidate has been found to have colours redder than $NUV - r \sim 2.2$. The latter colour criterion is somewhat generous in order to allow for variations in the stellar population's age, as well as moderate dust extinction.

In addition to these colour constraints, the luminosities of the potential analogue galaxies are matched to those of high redshift LBGs. Bouwens et al. [2007] find that the absolute magnitude of galaxies becomes 0.7 mag brighter between $z \sim 7$ and $z \sim 4$, primarily due to hierarchical coalescence and merging of galaxies; I thus selected candidate galaxies such that their FUV absolute magnitudes are equivalent to those of the existing $z > 5$ LBG populations, by requiring that $L_{UV} = 0.1-5L^{\star}_{z=6}$ where $M^{\star}_{UV} = -20.24$ at $z \sim 6$ [Bouwens et al., 2007]. Neither the luminosities of the high redshift population nor those of this analogue sample are corrected for dust extinction. In order to select comparable star formation rate densities to the high redshift LBG population, candidates are required to have a projected half-light radius < 2kpc. This is not always possible to determine reliably in ground-based SDSS imaging. We thus allow for unresolved sources, so that objects are selected which subtend $< 1.2''$ or $r_{1/2} < 3.5\,\mathrm{kpc}$ in the galaxy's rest-frame where this can be measured [see Stanway & Davies, 2014]. It should be noted that these constraints are applied using optical (g and r bands) rather than ultraviolet images as available *GALEX* images do not offer sufficient resolution.

We require the candidates to have SDSS spectroscopy, which both identifies the precise redshift of the galaxies and confirms the source of their UV luminosity as most likely arising from star formation instead of AGN activity. I exclude galaxies with an identified AGN component since AGN are known to be rare in the distant galaxy population; see Douglas et al. [2007] for $z \sim 5$ or Nandra et al. [2005] for $z \sim 3$ observations of AGN. Additionally, we perform an initial, by eye, assessment of the reliability of these sources to exclude sources with clearly inaccurate photometry,

[1] http://galex.stsci.edu/GR6/
[2] http://www.sdss.org/

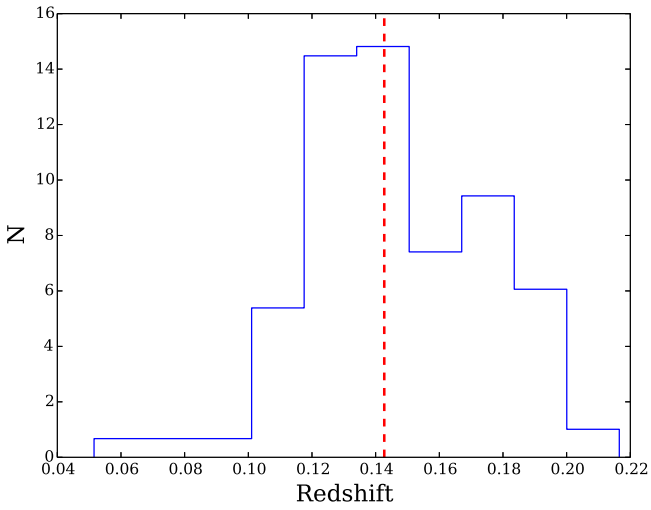

Figure 2.2: The distribution of (SDSS) spectroscopically-determined redshifts z of the sample of 180 candidate galaxies. The median redshift of 0.14 is indicated by the dashed vertical line.

e.g. due to artefacts or bright neighbours, or multicomponent sources in which only a small region satisfies our criteria (see Section 2.4). Using Galactic foreground reddening values determined by Schlafly & Finkbeiner [2011], all galaxies in the sample are found to have very low mean Galactic foreground reddening ranging between $0.007 \leq E(B-V)_{SFD} \leq 0.088$, with a mean Galactic extinction of 0.025. When fitting the galaxies' spectral energy distributions, I adjust their photometry for this using the Milky Way extinction law of Allen [1976] (see Section 2.5 for a description of the SED Fitting procedure).

The redshift distribution of the resulting sample of 180 candidate galaxies at $0.05 < z < 0.25$ is shown in Fig. 2.2.

2.3 Infrared photometry

All candidates have *GALEX FUV/NUV* and SDSS *ugriz* photometry. In order to extend the range of wavelengths, I determined photometry for the sample from the *Widefield Infrared Space Explorer* [WISE, Wright et al., 2010] and 2-Micron All Sky Survey [2MASS, Skrutskie et al., 2006] images, resulting in photometric data spanning a combined wavelength range of approximately 1500Å to 22μm. For consistency I determined either measurements or limits on the galaxies' magnitudes from the infrared imaging using fixed aperture photometry at the SDSS locations

Band	wavelength (μm)	reference aperture (arcsec)	zero-point (Vega)	magnitude correction Δm	AB conversion
J	1.235	4	20.9	0.05363	0.89
H	1.662	4	20.5	0.0572	1.37
K_s	2.159	4	20.0	0.0556	1.84
W1	3.4	8.25	20.5	0	2.683
W2	4.6	8.25	19.5	0	3.319
W3	12	8.25	18.0	0	5.242
W4	22	16.50	13.0	0	6.604

Table 2.1: The wavelength, reference aperture used, zero-point (in Vega magnitudes), magnitude correction Δm, and conversion between Vega and AB magnitudes for the 2MASS and *WISE* measurements. For 2MASS, the zero-point magnitude was found in the FITS header for each object individually, the quoted number gives the mean value.

and the recommended aperture sizes appropriate to point sources. Using IRAF I measured the flux interior to a series of apertures with 3, 4, 5, 7, 9, 11, 13, 15, and 20 arcseconds radius centred on the object location, and from this calculated the curve of growth correction for each source. The final magnitude in each infrared band was determined as $m_{AB,final}$ = measured flux in reference aperture + magnitude zero-point - magnitude correction + AB conversion; the values for the last three quantities are shown in Table 2.1. By using a series of aperture sizes, it was possible to ensure that any potential nearby neighbours could be excluded. However, the sources had been selected to have no nearby neighbours in the optical or ultraviolet, and so did not require model-dependent deblending. In $\sim$10% of the sample, however, 2MASS photometry at the source location was unreliable due to blended sources or insufficient depth of the survey compared to the objects' relative faintness. Approximately a third of the candidate objects are individually undetected above a 2σ detection limit in one or more infrared bands, where this limit is determined locally in each band.

2.4 Outliers

Having established a large sample of potential Lyman break analogue candidates, we performed an initial visual inspection of the SDSS images for each source in order to identify any obvious outliers whose photometry was unsatisfactory for the purposes of the planned analysis. We also inspected all candidates again to confirm that their visible features confirmed them to be suitable candidates. Five sources

(shown in Fig 2.3), which had passed the initial inspection, were identified in the second inspection and subsequently excluded from the analysis. One possible reason why these sources passed the initial selection process is that their SDSS-recorded sizes were in agreement with the compactness required of the candidate objects. However, it is likely that due to the SDSS spectroscopic fibre size of 3 arcseconds, only the brightest knots of star formation were catalogued. Hence, through visual inspection it was possible to determine that the actual size of these objects was larger, making them unsuitable analogue candidates. Another reason is likely to be that several of the outliers have very nearby neighbours or are undergoing merging processes. Since we initially selected based on the *GALEX*-determined location and due to this survey's larger point spread function, confusion may have arisen between the sources and their neighbouring systems. Hence, while these objects fulfil the photometric and spectroscopic selection criteria, they are clearly unsuitable analogues to high-redshift Lyman break galaxies as they form part of larger systems, which in some cases appear to be undergoing merger-driven starburst events. It is therefore important to conduct a visual inspection to ensure such systems are excluded from further analysis.

Figure 2.3: SDSS images of the five systems excluded following visual inspection. From left to right: Object 48621 appears to be a bright knot of star formation in a larger galaxy, while Objects 59660 and 01529 are part of much larger, merging systems. Similarly Objects 32955 and 13847 are clearly extended systems.

2.5 SED Fitting Procedure

Having established a sample of 180 potential local Lyman break analogue galaxies, I developed code to fit each object's spectral energy distribution (SED). Given that the relatively new BPASS models are not integrated into most existing fitting codes, and in order to retain physical insight into the input parameters, I construct my own SED fitting code, making use of the BPASS stellar population synthesis (SPS) code models as well as the Maraston [2005] (M05) models.

Both SPS codes are derived from models of the evolution of a stellar population at

different ages, and list the flux expected at a certain wavelength for a given stellar population age. Comparing the measured fluxes of the LBA candidate sources to a synthetic model spectra makes it possible to constrain the age, mass, dust content and other physical characteristics of the stellar population. To create such synthetic spectra I thus modified the SPS templates by implementing dust reddening with a range of possible $E(B-V)$ values, and systematically varying the input model's ages and metallicities. For each synthetic spectrum thus created, the synthetic magnitudes and fluxes were calculated using the filter profiles of the observed bands. The model magnitudes and fluxes were then compared to the observed ones, and the χ^2 parameter was calculated for each configuration. The best-fitting model with the lowest χ^2 parameter could thus be determined from which the best-fitting physical properties could be found. In addition the range of properties displayed by models whose χ^2 value lay within 1σ of the best-fitting minimum value was recorded. An alternative method could involve marginalising over the Bayesian priors for this sample; however since the priors are poorly constrained, and the data is sparse, this is unlikely to produce a stronger or more reliable constraint in this circumstance.

Maraston models: As described in Maraston [2005], the Marastron models generate composite stellar populations (CSP) with a Salpeter IMF and star formation rates which decline exponentially with time, such that $\dot{M} \propto e^{-t/\tau}$, where τ is the e-folding timescale. These models are built by combining simple single-age stellar population models which have been calibrated against globular cluster data for which ages and element abundances are independently known, so that various generations of stars can be modelled [Maraston, 2005]. Unlike the 'isochrone synthesis' technique used in most SPS models, the M05 models adopt the fuel consumption theorem. In this approach, post-Main Sequence evolution is determined by the amount of so-called 'fuel': the amount of hydrogen and/or helium that can be consumed via nuclear burning during a given post-MS phase [see Maraston, 2005, and references therein]. This has the advantage of being able to model short-lived evolutionary stages, such as the bright Red Giant Branch phase, or those whose theoretical modelling is uncertain due to mass loss or the lack of complete stellar tracks (relevant e.g. for Thermally Pulsing Asymptotic Giant Branch, or very hot old stars). The parameters of the physical inputs in the models, such as convection, mass loss, and mixing, which could not be derived from first principles, are thus fixed by observations. The M05 models is available as simple and composite stellar populations[3].

[3]see `http://www-astro.physics.ox.ac.uk/~maraston/Claudia's_Stellar_Population_Models.html` for M05 models

The former models a single, instantaneous burst at various chemical compositions and ages, while the latter describes various exponentially-declining star formation rates at different metallicities. Both SSP and CSP models are available with Salpeter or Kroupa initial mass functions.

BPASS **models:** The Binary Population and Spectral Synthesis code, or BPASS[4], was developed to address the effects of massive star evolution on the SEDs of galaxies [Eldridge & Stanway, 2009, 2012; Stanway et al., 2016, Eldridge et al submitted]. While in young stellar populations a galaxy's spectrum is dominated by the radiation emitted by massive hot stars, a more aged population shows a spectrum which is strongly influenced by the evolution of moderately massive stars that live for longer than the most massive population. This evolution is often modified by processes such as angular momentum transfer, and mass transfer due to a binary companion, allowing evolved secondary stars to extend their highly luminous phase, and to boost the population of rapidly rotating H-depleted Wolf-Rayet stars [Stanway et al., 2014]. Recent studies suggest that up to 70% of massive stars form in multiples, highlighting the importance of including binary evolution when modelling stellar populations.

The standard BPASS distribution provides model spectra for instantaneous starbursts, which are constructed with a distribution of binary periods, hence affecting the evolution of binary systems. From these model spectra, we construct exponentially declining star formation history models, to match those available in the Maraston models.

The stellar flux output in the BPASS model is processed to estimate the nebular emission component using the radiative transfer code Cloudy [Ferland et al., 1998]. We select an electron density of $10^2\,\mathrm{cm}^{-3}$, a covering fraction of 1, and a spherically symmetric gas distribution with inner radius of 1pc. These are appropriate for a H II region, as discussed in Eldridge & Stanway [2012] and Stanway et al. [2014]. For the SED fitting described in this chapter, BPASS v2.0 was used.

Dust modelling: The template M05 and BPASS spectra are modified using the Calzetti et al. [2000] dust extinction law, which was empirically derived for local infrared-luminous galaxies with active star formation. It takes the form

$$k(\lambda) = 2.659 \times (-1.857 + 1.040/\lambda) + R_V$$

[4]See `http://bpass.auckland.ac.nz` for BPASS models

for $0.63\mu\text{m} \leq \lambda \leq 2.20\mu\text{m}$; and

$$k(\lambda) = 2.659 \times (-2.156 + 1.509/\lambda - 0.198/\lambda^2 + 0.011/\lambda^3) + R_V$$

for $0.12\mu\text{m} \leq \lambda \leq 0.63\mu\text{m}$, where $R_V = 4.05 \pm 0.8$. In the Calzetti law the extinction in front of nebular line emission regions is higher than that on the stellar continuum such that $E_{\text{cont}}(B-V) = 0.44 \times E_{\text{line}}(B-V)$. For broadband photometry, the emission is dominated by stellar continuum.

At each model age, I modify the synthetic SED by a reddening curve corresponding to colour excesses in the continuum, $E_{\text{cont}}(B-V)$, between 0.0 and 0.6 mags (in steps of 0.05). An alternative method of constraining the dust within the sources would be the use of the Balmer decrement. This technique makes use of the the Hα/Hβ line ratio, which can, in the absence of dust, be calculated from first principles and depends only weakly on the gas temperature [Osterbrock, 1989]. However, I do not constrain the dust for the SED fitting using the Balmer break method since it is likely that the nebular emission regions are significantly smaller than the galaxy as a whole [Finkelstein et al., 2009; Scarlata et al., 2009], and so the dust measured by the Balmer decrement may well not be representative of the stellar continuum emission. I do, however, make comparisons between the SED-derived dust values and those inferred from the observed Balmer decrement in section 2.6.3.

Fitting Procedure: Initially, in both the M05 and BPASS models, the star-formation histories considered were an instantaneous burst of star formation, a constant star formation rate, and exponentially declining and increasing star formation rates with timescales τ, between 100 Myr and 20 Gyr. The increasing SFR model, however, did not produce reasonable fits and was thus disregarded for the remainder of the analysis. In addition, no significant constraints were found on the best-fitting value of τ, and in the final SED fitting only the following values of τ were considered: 100 Myr, 500 Myr and 1 Gyr for the M05 model, and 1 Gyr for the BPASS model. The age of the dominant stellar population was allowed to range from 1 Myr to 15 Gyr in the M05 model, and 1 Myr and 10 Gyr for the BPASS model. The metallicity could take values of 0.5 $Z_\odot$, $Z_\odot$ and 2 $Z_\odot$ in the M05 models, and 0.05 $Z_\odot$, 0.2 $Z_\odot$, 0.4 $Z_\odot$, $Z_\odot$, and 2 $Z_\odot$ in BPASS . In the M05 models, the canonical Salpeter [1955] IMF is used, while the BPASS models include a shallower lower-mass slope of -1.3 for stellar masses between 0.1 and 0.5 $M_\odot$, and the standard Salpeter [1955] slope of -2.35 between 0.5 and 100 $M_\odot$.

The SED fitting procedure was unable to place meaningful constraints on the best-fitting star formation history (SFH), and in the further analysis only the

exponentially declining star formation history is considered as it can be considered the most physically motivated for actively star-forming galaxies, which neither the instantaneous starburst model, nor the constant star formation rate model describe. Alternatively, the exponentially increasing SFH can also be justified as it reproduces the hierarchical assembly of systems through cosmic time.

In addition to the poorly constrained SED-derived metallicities, the metal abundance of the LBA candidate sample could be determined from their optical line ratios using the Dopita et al. [2016] metallicity diagnostics. This is shown in Fig. 2.4. In order to reduce the number of free parameters in fitting limited data, only the sample's median metallicity of $\sim 0.5\, Z_{\odot}$ is used in the following sections. One possible caveat arising from this is the question of whether the gas-phase metallicity of the sources is the same as the stellar metallicity. However, since the galaxies have been photometrically selected to have young stellar populations, it can be reasonably assumed that no significant amount of metal enrichment of the ISM (relative to the stars) has occurred yet. A plot of metallicity and redshift of the LBA candidates (Fig. 2.5) shows no strong correlation between the two properties.

A typical source in our sample is well detected in the optical and ultraviolet, but often weakly detected or undetected in the near-infrared. Their mid-infrared (*WISE*) properties vary significantly. Given the number of parameters required both to build a stellar population, and to be inferred from the resulting template, any SED-fitting procedure can be subject to substantial uncertainty and degenerate solutions. The number of extracted parameters can be comparable to the number of input data points. It is worth noting that at wavelengths longwards of K_S the effects of dust extinction are negligible and thus excluding the relatively shallow *WISE* bands does not impact the inferred extinction. Similarly, the reprocessing of extincted ultraviolet emission by thermal dust does not produce emission shortwards of 3 microns and so no dust emission component is required for modelling the stellar population. I thus excluded the *WISE* bands from the fitting procedure since these are most strongly dependent on the dust properties adopted, rather than on the input stellar spectra. However I evaluate the consistency of the *WISE* data with our best fit model spectra in section 2.7.4. Hence, I fit the observational data over the spectral range 0.12-2.16 μm, i.e. from *GALEX* FUV to *2MASS* K_S band inclusive, and excluded all four *WISE* bands. Where sources are undetected at the $2\,\sigma$ level in a given band, I took the $1\,\sigma$ flux in that band, and assigned an uncertainty equal to the flux.

In the remainder of this chapter, I use the M05 composite stellar population models with $0.5\, Z_{\odot}$ and a standard Salpeter IMF. I compare the results obtained

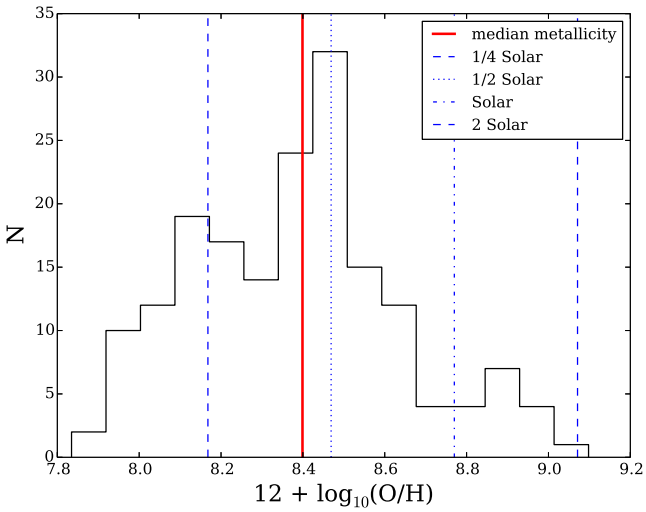

Figure 2.4: The oxygen abundance distribution of our sample as calibrated from strong emission line ratios in SDSS spectroscopy, using the line diagnostic of Dopita et al. [2016]. Dashed vertical lines indicate 0.25, 0.5, 1 and 2 times the local Galactic concordance value of 12+log(O/H)=8.77 which has been proposed as a better calibration than bulk Solar abundance [Nieva & Przybilla, 2012]. The solid vertical line indicates the sample median ~ 0.4 $Z_{\odot}$.

using the M05 model to those found using v2.0 of BPASS [Stanway et al., 2016] with $0.5\,Z_{\odot}$ models and an initial mass function with a typical Salpeter slope of -2.35 for stars between 0.5 and 100$M_{\odot}$, and a slope of -1.3 for stellar masses between 0.1 and 0.5 $M_{\odot}$.

2.6 SED-Derived Properties of the Sample

While presenting the results of M05 and BPASS SED fitting in the following sections, I also carried out SED fitting with the CIGALE code [Burgarella et al., 2005; Roehlly et al., 2014] in order to compare certain results from the different codes. This was done as an independent check of my SED fitting program since CIGALE, unlike my code, assumes Bayesian statistics. Additionally, I compare my results to those found in the analysis by the MPA-JHU collaboration [Brinchmann et al., 2004] [5] and the *GALEX*-SDSS-*WISE* Legacy Catalogue of Salim et al. [2016]. The results of the these comparisons are described in section 2.8.

[5] http://www.mpagarching.mpg.de/SDSS/DR7

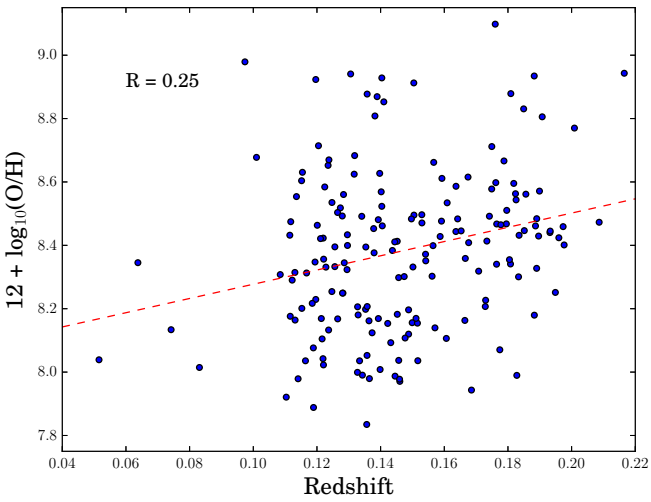

Figure 2.5: The distribution of metallicities in the LBA sample against the redshift of the sources. The correlation between the metallicity and redshift of the sample is $R = 0.25$, indicating that no strong correlation exists between the two.

2.6.1 Stellar Masses

The best-fitting stellar mass is one of the most robust outputs of an SED fitting procedure since it depends primarily on the optical/NIR normalisation of the spectrum (i.e. the galaxy luminosity at its known redshift) rather than the details of the spectral shape. However, there is modest dependence on the synthetic stellar population input, both in terms of that initial normalisation and since the mass to light ratio at any given wavelength depends on the stellar population.

The median stellar masses, M_*, of our sample were consistent between input templates, and found to be $\log(M_*/M_\odot) = 9.80 \pm 0.42$ for the standard BPASS model and $\log(M_*/M_\odot) = 9.31 \pm 0.34$ for the M05 model (where the uncertainty is given by the sample standard deviation). In Fig. 2.6 we compare the distributions of masses. As expected, the derived distributions are broadly similar between different input SPS models, with no catastrophic disagreements between them. The BPASS model produces slightly higher masses than the equivalent M05 model.

The independent galaxy template fitting procedure performed for star forming galaxies by the MPA-JHU collaboration [Brinchmann et al., 2004] shows good agreement with the SED model fits for our objects, as does a parallel fitting procedure using the M05 templates in the CIGALE SED fitting code, which I undertook. Testing seven widely-used stellar population synthesis models against young star clusters, the interacting binary treatment (as implemented in BPASS) has been

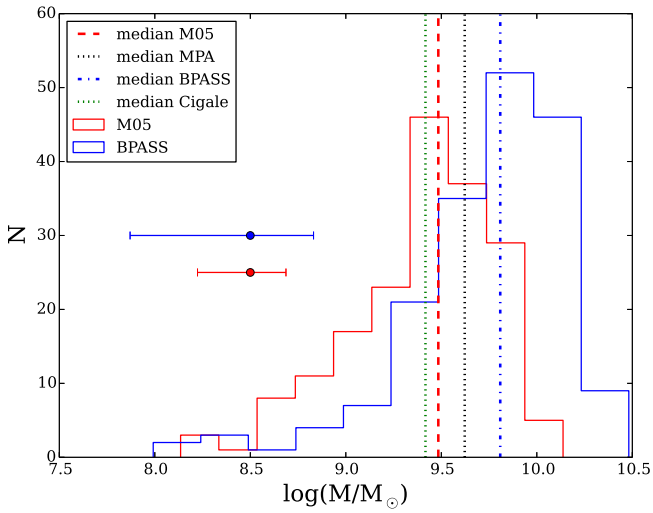

Figure 2.6: The distribution of derived stellar masses, comparing the M05 and BPASS models. The median fitted values are indicated by vertical dashed lines, as are those independently found by MPA-JHU and by fitting the data with the CIGALE code and M05 models. These all show good agreement. Representative uncertainties on individual masses are indicated by points and associated ranges. The uncertainty on the median is substantially smaller.

shown to best reproduce the observations [Wofford et al., 2016]. I will, therefore, be using the BPASS model results for further analysis in the remainder of the thesis.

2.6.2 Ages

For most galaxies the age of the stellar population in an SED is most strongly constrained by the strength of the spectral break at around 4000Å in the rest-frame. Our selection criteria required the break to be modest, with near-flat ultraviolet to optical colours, selecting young starbursts. The population as a whole shows a relatively narrow distribution of best fit ages as Fig. 2.7 illustrates. The uncertainty on individual galaxies is somewhat larger and typical values are indicated on the figure. This uncertainty is calculated as the range of values whose χ^2 statistic lie within 7.04 (the χ^2 value such that the right tail area is 1σ, or 68.3%, given 6 degrees of freedom: the number of wavebands to which the models are fit minus the number of parameters fit, in this case mass, age, dust, metallicity) of the best-fitting value.

The ages found using the M05 models were lower than the ones found from the BPASS models, with median ages of $\log(\text{age/yr}) = 7.78 \pm 0.49$ and $\log(\text{age/yr}) = 8.60 \pm 0.52$ respectively. The higher age found using BPASS τ mod-

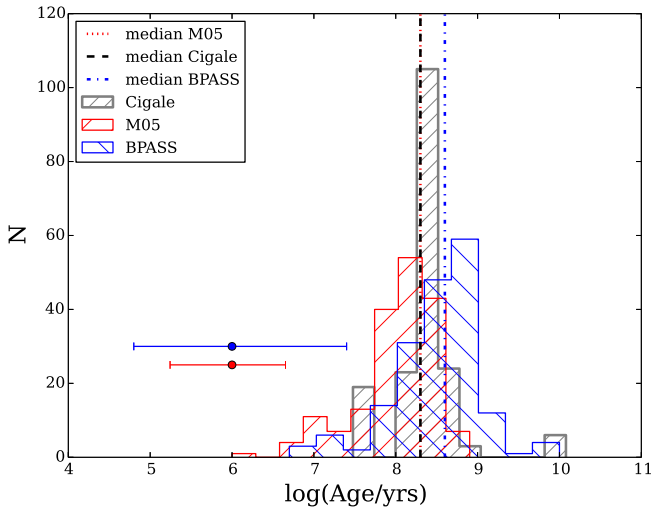

Figure 2.7: Distribution of the stellar population ages of the target galaxies found using SED fitting with the M05, CIGALE, and BPASS models. Indicative uncertainty ranges on individual galaxies are indicated by horizontal bars.

els is consistent with the more massive stellar populations found in section 2.6.1. The ages determined using the CIGALE SED fitting code are in agreement with both M05 and BPASS results. They do, however, span a smaller range of values, probably due to the larger number of parameters fit by the CIGALE code.

2.6.3 Dust Extinction

As mentioned in section 2.5 I fit an internal dust extinction component for each object, applied in the objects' rest-frame, in addition to the foreground absorption arising from line of sight extinction through the Milky Way. The best-fitting $E_{\rm cont}(B-V)$ values are in close agreement regardless of SPS templates adopted, giving mean $E_{\rm cont}(B-V)$ values of 0.16±0.10 for the M05 templates, 0.12±0.07 for the BPASS model as shown in Fig. 2.8.

I also calculate an estimate of dust extinction from the ratio of recombination line strengths in the objects' spectra. For this I assume an intrinsic Balmer decrement for case B recombination, at a temperature of 10^4 K and an electron density of n_e= 10^2 cm^{-3}, such that Hα/Hβ=2.86. For comparison with the stellar continuum derived extinctions, I adjust this $E_{\rm line}(B-V)$ value by a factor of 0.44, as required by the Calzetti et al. law. As Fig. 2.8 shows, the resultant $E_{\rm cont}(B-V)$ value distribution shows good agreement with those calculated from model SED fits.

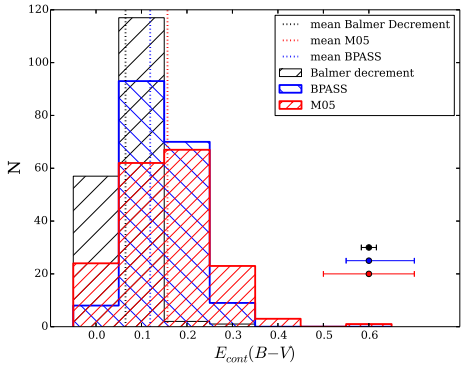

Figure 2.8: The distribution of $E_{\rm cont}(B-V)$ values obtained from model SED fitting (blue for BPASS, red for M05), and those calculated from the observed Hα/Hβ flux ratios (assuming case B recombination with a temperature of 10^4 K and an electron density of n_e= 10^2 cm^{-3}, multiplied by 0.44 to recover equivalent continuum extinction; black).

2.7 Inferred Properties

2.7.1 Excitation Measurements

The BPT diagram [Baldwin et al., 1981] indicates the origin of the ionizing radiation heating the nebular gas in a galaxy on the basis of its [O III], Hβ, [N II] and Hα flux ratios. This allows the classification of the ionizing spectrum into star-forming or AGN-driven. Using the BPT diagram as a diagnostic for the LBA candidate ionization (Fig. 2.9) it can be seen that the majority of sources fall below the proposed cut-off separating star formation and AGN activity [black dashed line, Kauffmann et al., 2003], thus confirming that these are indeed star-forming galaxies. Four objects fall into the 'composite' region, indicating that these sources may contain components of both star formation and AGN activity. While it is noteworthy that the sample typically lies well above the median relation seen in local galaxies [described by equation (8) in Steidel et al., 2014], none of the LBA candidate objects lie above the theoretical boundary line determined by Kewley et al. [2001] for a 'maximal' starburst. This forms the upper limit of theoretical pure stellar photoionization models, and galaxies lying above this maximum starburst line are likely to be AGN-dominated. Interestingly, high-redshift galaxies have also been found to lie above the local relation [Steidel et al., 2014].

The mass-excitation (MEx) diagnostic developed by Juneau et al. [2011] provides an alternative indication of the AGN contribution within a galaxy, similar to the BPT diagnostic but with the separation between star forming galaxies and

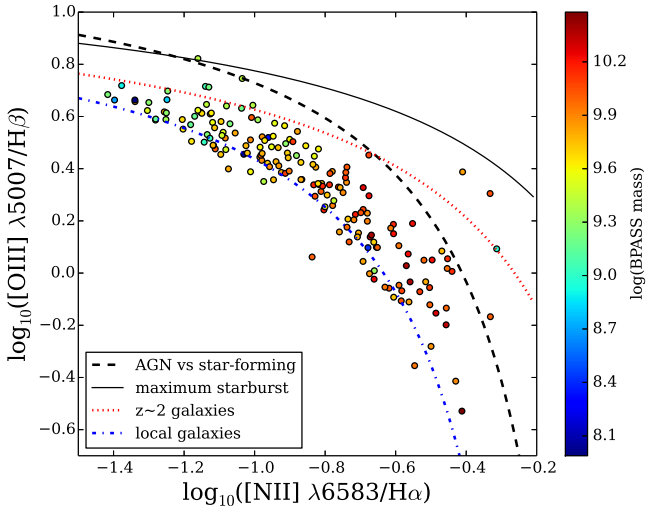

Figure 2.9: BPT diagram for our sample, with colour coding according to the masses determined by BPASS SED fitting. The blue dot-dashed line indicates the average value for local galaxies [Steidel et al., 2014], while the red dotted line shows the average of redshift $z \sim 2$ star-forming galaxies [Steidel et al., 2014]. The solid black line indicates the proposed maximal starburst [Kewley et al., 2001], and the black dashed line shows the standard criterion used to separate AGN from star-forming activity [Kauffmann et al., 2003]. Only a few targets fall above the dashed line, indicating that they might include an AGN component.

AGN-hosts enhanced by the effects of the mass-metallicity relation for local sources. Fig. 2.10 shows the [O III]/Hβ vs stellar mass plane for the objects in our sample. Again, the majority of candidate objects trace the starburst galaxy region of the parameter space, but, even more so than in the BPT diagram, an offset can be seen between our population and the local SDSS sample from which it was drawn, pushing our sample to straddle the border of AGN classification. Such a shift is likely indicative of a harder ionizing flux and associated higher ionization potential but not necessarily one arising from AGN [see Stanway et al., 2014]. This may indicate a difference in the galaxy mass-metallicity relation between our sample and more typical galaxy populations at the same redshift, with relatively little dependence of stellar metallicity on stellar mass for these intense starbursts.

2.7.2 Star Formation Rates

In the SED fitting analysis of the candidate LBA galaxies I allowed star formation rate to vary as this was defined by the combination of star formation rate timescale, mass, extinction and stellar population age. It is worth noting that while it might have been possible to pre-constrain this using nebular line emission, such constraints

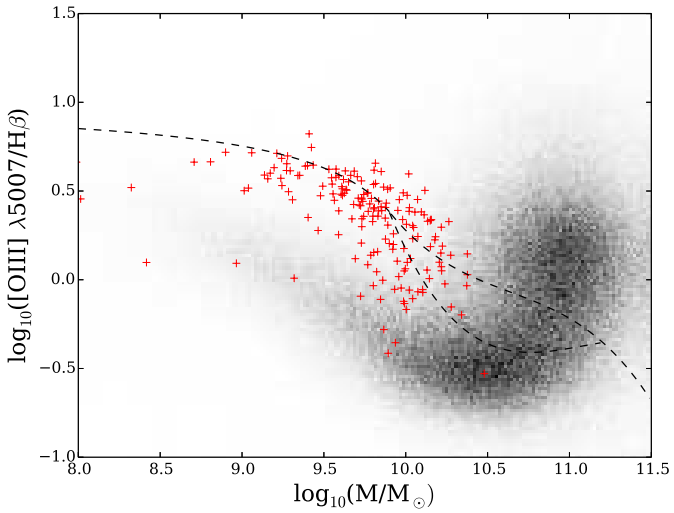

Figure 2.10: Mass-excitation diagram for our sample (red crosses) and SDSS galaxies (underlying grey distribution). The LBA candidate galaxies in our sample appear to be irradiated by a significantly higher ionizing potential than other local galaxies of comparable mass. The dashed lines indicate proposed classifications between AGN (above line), composite (bordered region), and star formation activity (below line) according to Juneau et al. As in the BPT diagram, the majority of our objects are found in the star-forming region.

would have been dependent on dust extinction and star formation history assumed in the calibration used, and would have underestimated obscured star formation. To explore the effect of such assumptions, and their appropriateness for this sample, I determine the star formation rates (SFRs) of our galaxies using a range of established star formation rate indicators, from UV to mid-infrared wavelengths.

UV: I calculate star-formation rates from dust-corrected FUV fluxes using the Madau et al. [1998] prescription at 1500 Å for a Salpeter IMF. For a stellar population with ongoing continuous star formation dominated by young stars, the UV luminosity is a good tracer of the stellar birth rate and independent of the star formation history if the age $t \gg t_{MS}$, where $t_{MS} \leq 2 \times 10^7$ yrs for late-O/early-B type stars [Madau et al., 1998]. For comparison, I also calculate SFRs based on the SDSS u-band photometry, after correcting for dust, using the calibration of Hopkins et al. [2003]. As Fig. 2.11 shows, this is associated with a relatively large uncertainty, but is comparable to the dust-corrected FUV-derived SFR.

Hα and [O II*]:* The star formation rates from Hα and [O II] fluxes are calculated using standard conversion factors (Kewley et al. [2004], see also Kennicutt [1998]). The SDSS fibre [O II] and Hα fluxes are not corrected for fibre losses since our targets are very compact, but are corrected for nebular dust extinction as described above. Both strong line indicators are very sensitive to instantaneous star formation, i.e. stellar ages $< 3 - 10$ Myr, but also sensitive to the ionization condi-

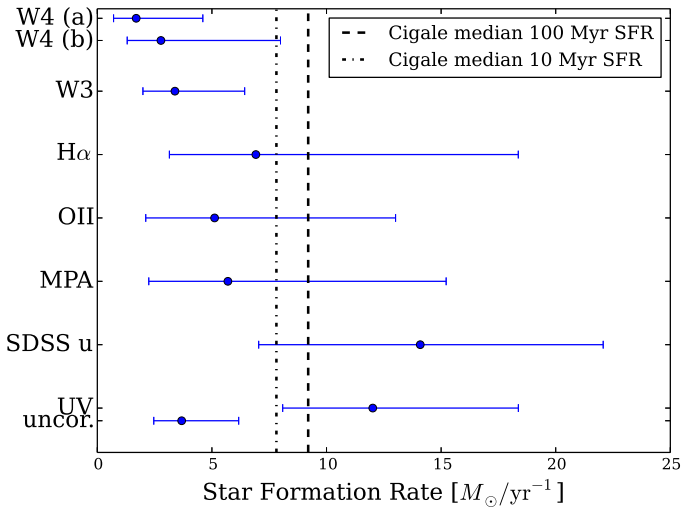

Figure 2.11: The median, upper and lower quartile dust-corrected star formation rates (SFRs) of the sample. All fluxes were corrected for Milky Way dust attenuation. Vertical lines indicate the median SFRs found by the CIGALE models, averaged over the past 10 and 100 Myrs, respectively. The [O II], and Hα fluxes were further corrected for the object-intrinsic dust extinction with $E_{\mathrm{line}}(B-V)$ values found using the (Milky Way dust-corrected) Balmer decrement. The U-band and UV corrected using $E_{\mathrm{cont}}(B-V)$ determined by SED fitting. The UV SFR found without applying an intrinsic dust correction is shown underneath the corrected value. We show two calibrations for the W4 band - that of Cluver et al. [2014] as (a) and Lee et al. [2013] as (b). The SFRs determined by MPA-JHU [Brinchmann et al., 2004] are shown as a comparison.

tions of the nebular gas and so the applicability of these calibrations in this sample has not been verified. The UV and the spectral line indicators agree within a factor of a few, and it can thus reasonably be assumed that the galaxies are experiencing an ongoing starburst on timescales of at least a few tens of Myr.

W3 and W4: The star-formation rates inferred from the infrared bands were found using the empirical Lee et al. [2013] prescription for *WISE* bands W3 and W4. These SFR indicators were calibrated for a large sample of local star-forming galaxies with SFR > 3 $M_\odot$ yr^{-1} and mid-infrared data. Galaxies with apparent AGN activity were excluded from the calibration. For W4, I also use the calibration of Cluver et al. [2014], which is based on the local GAMA galaxy survey. The median SFRs derived from W3 and W4 are 4.9 and 2.4 $M_\odot$ yr^{-1} respectively (based on the Lee et al calibration). The PAH emission region falls into the W3 and W4 bands, and can dominate the infrared luminosity of star-forming galaxies and hence this empirical calibration is somewhat redshift-dependent. Further, some of the W3 and W4 magnitudes in our sample were upper limits, these have been included in this median with a nominal SFRs equal to the 1σ flux limits. As a result, the derived median values may be skewed by these inferred limits on star formation rates.

The median, upper and lower quartile star formation rates derived for the entire sample are shown in Fig. 2.11. The different SFR indicators, as well as the independently determined MPA-JHU results, are in good agreement, with the median values of each indicator lying between ~ 2.5 and 14 $M_\odot yr^{-1}$. The highest SFRs are found from the dust-corrected UV fluxes, but are associated with considerable uncertainty on the dust extinction correction. The uncorrected UV SFRs are also shown as they provide a lower limit on the SFR in the objects. Given the sample's best-fitting ages (as described in section 2.6.2) of a few tens to a few hundreds Myrs, and the uncertain contribution of strong line emission to the *WISE* bands, the Hα and UV star formation rate indicators are most likely to provide accurate descriptions of the objects, subject to uncertainties in extinction. However, since both the UV and Hα fluxes are strongly affected by any dust within the galaxies, it is important to ensure the fluxes are dust-corrected. In the calculations described above I use Balmer break-derived dust corrections. It should be noted that since the dust reddening is inferred from nebular emission lines it might not be representative of the dust found in star forming regions from which the UV flux originated, and hence might not be truly applicable to these SFR indicators.

Further SFR indicators based on radio observations of a subset of these galaxies are discussed in section 3.3.1 below.

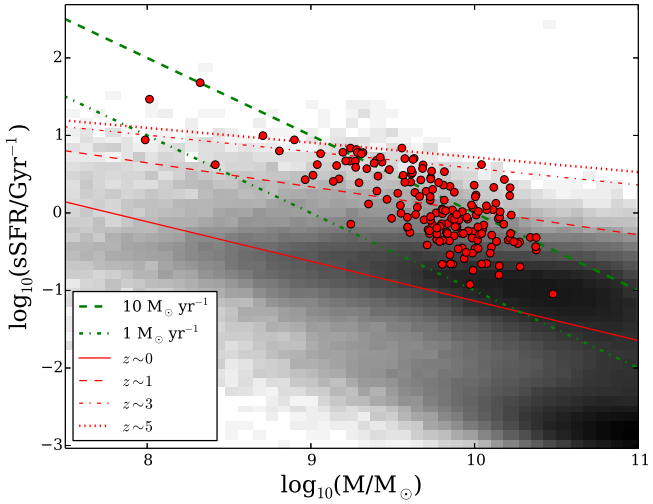

Figure 2.12: Specific star-formation rate (as $\log_{10}(\mathrm{sSFR/Gyr^{-1}})$) vs mass of the LBA candidate sample (red dots), using the Hα SFR conversion. The green dashed and dot-dashed lines represent constant star-formation rates of 10 $M_\odot$ yr^{-1} and 1 $M_\odot$ yr^{-1} respectively. The red lines show the star formation main sequence at different redshifts according to Leslie et al. [2016]. The underlying grey distribution gives the logarithm of the local SDSS galaxies' distribution. It is apparent that our objects lie significantly above the main sequence for local galaxies.

2.7.3 Specific Star Formation Rates and Timescales

From the star formation rates calculated from Hα in section 2.7.2 and the masses derived from BPASS SED fitting in section 2.6.1, I calculate the specific star formation rates (sSFR = SFR/mass) and star formation rate surface densities (Σ_{SFR} = SFR/area). The galaxies in our sample have $\log(\mathrm{sSFR/yr^{-1}}) \sim -9.00 \pm 0.47$. As shown in Fig. 2.12, these specific star formation rates indicate that the candidate LBA sample is more intensely star-forming at a given stellar mass than more typical local galaxies. The galaxies lie significantly above the star-forming galaxy main-sequence for $z \sim 0$ shown as a solid red line in the figure. While our galaxies show a mild evolution in sSFR with mass (consistent with their ultraviolet luminosity, and hence SFR, selection criteria), no correlation of sSFR with redshift could be found over the narrow redshift range spanned by the sample.

The inverse of the specific star formation rate, sSFR^{-1}, provides a measure of the time it would take to double the stellar mass of the system assuming constant star formation at the present rate. In order to calculate this mass doubling time scale, I again use the star formation rates derived from Hα and find that the mass

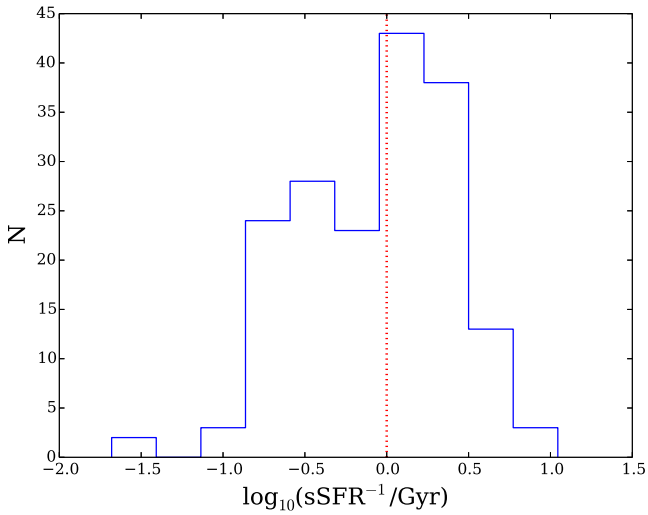

Figure 2.13: The distribution of the inverse specific star formation rate in log(Gyr). This corresponds to the mass doubling time scale of the galaxies. The median value of 1.0 Gyr is shown by the vertical red dotted line.

doubling time scales of our sample have a median of 1.0 Gyr as shown in Fig. 2.13. Given that the stellar population ages are $\ll$ 1Gyr, this implies high star formation rates in the past.

2.7.4 Dust Emission

The fit to the optical to near-infrared data is not sensitive to the reprocessing of radiation absorbed in the ultraviolet and re-emitted in the thermal infrared. However, the observed extinction and inferred stellar continuum can be used to predict the expected emission assuming there is no additional, heavily-obscured star forming or AGN component. To model the re-emission of thermal photons at long wavelengths, I adopt the energy-balance prescription of da Cunha et al. [2008]. While this is implemented in the MAGPHYS code, it represents a simple formulation in which the energy lost from UV-optical is re-emitted as a combination of grey-body and polycyclic aromatic hydrocarbons (PAH) emission components. I reproduce this in my SED fitting code, using identical black body parameters to those derived by da Cunha et al. [2008] as the MAGPHYS defaults. For the PAH emission component, I use the average luminosity-weighted composite template of Smith et al. [2007], which is based on low resolution mid-infrared *Spitzer Space Telescope* spectroscopy for nearby AGN and star-forming galaxies. The luminosity of intensely star-forming galaxies in the mid-infrared ($\sim 3 - 25$ μm) is dominated by strong

emission features attributed to PAHs, with up to 20% of the infrared flux emitted in the strong transition lines alone [Smith et al., 2007].

Comparing the measured infrared fluxes (or upper limits) with the best-fitting model SEDs, I find no significant discrepancy between these in the near-infrared shortwards of the K_S band. However, in the PAH-dominated region of $\sim 3 - 25\mu$m, an offset between model and observation can be seen. Figures 2.14 and 2.15 show this offset for the *WISE* W3 and W4 bands centred at 12 and 22 μm respectively. At 12 μm (observed) the models marginally under-predict the galaxy flux, based on SED-fitted extinction and assumed dust emission law. No significant difference in behaviour is observed between the M05 and BPASS models.

In the W4 band, however, predicted magnitudes derived from the BPASS model are in much better agreement with the observed values than those found using the M05 model. This suggests that, given the combination of BPASS stellar models and Calzetti et al. dust extinction, the Smith et al. composite luminosity-weighted average spectrum provides a reasonable estimate of the PAH component. However, if the M05 stellar population synthesis model better describes the population, a steeper PAH model with increased flux at higher wavelengths [see Fig. 18 in Smith et al., 2007] may be more appropriate. This would indicate that the most luminous sources have the warmest thermal SEDs, and might give clues about the ionization state and distribution of grain sizes of the sources' dust and ISM.

An extinction law which absorbs more flux at short wavelengths would also lead to stronger IR dust emission and hence stronger PAH features. My use of the Calzetti law was motivated by its description of intensely star-forming systems - exceeding the star formation rate of the Milky Way or other sites for which dust law formulations exist, and more akin to the galaxies in our sample. While it was originally developed for a small sample of UV and FIR-bright galaxies, Calzetti et al. also confirmed the applicability of the dust reddening law on a larger sample of starburst galaxies, and it is widely used for starbursts across a broad redshift range.

The thermal dust emission is modelled here as a series of single temperature grey-bodies. A change in the dust grain size or composition may modify these. We note that SED fitting using the CIGALE code (described in section 2.8), which scales a dust emission curve derived from Dale et al. [2014], but otherwise has identical input stellar populations to my fitting, overpredicts the median model flux by 40 per cent. However, in deriving this, I had to assume three default dust parameters to fit data essentially constrained by two points, and we would hence suggest that further investigation of the mid-infrared properties of this or similar samples may be required.

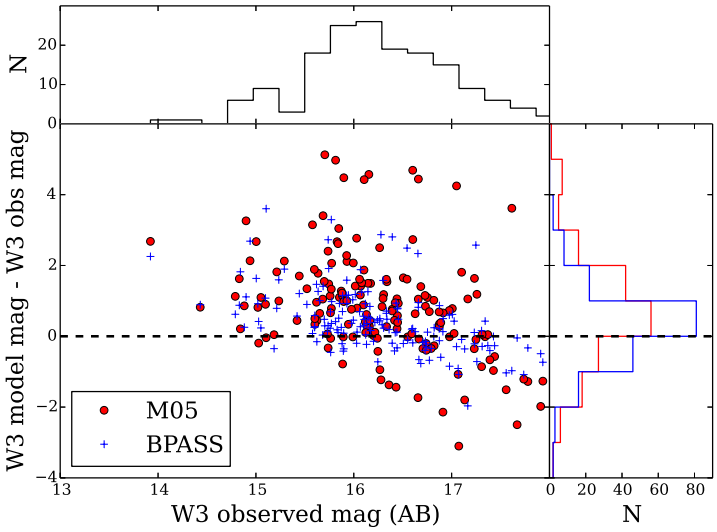

Figure 2.14: Comparing the observed W3 magnitude to the colour difference between the SED model and observations. The red dots indicate the M05 model results, while the BPASS model results are represented by blue crosses. The dashed line marks the magnitude line where model and observations coincide. For W3, at 12μm, no significant difference can be seen between the two models.

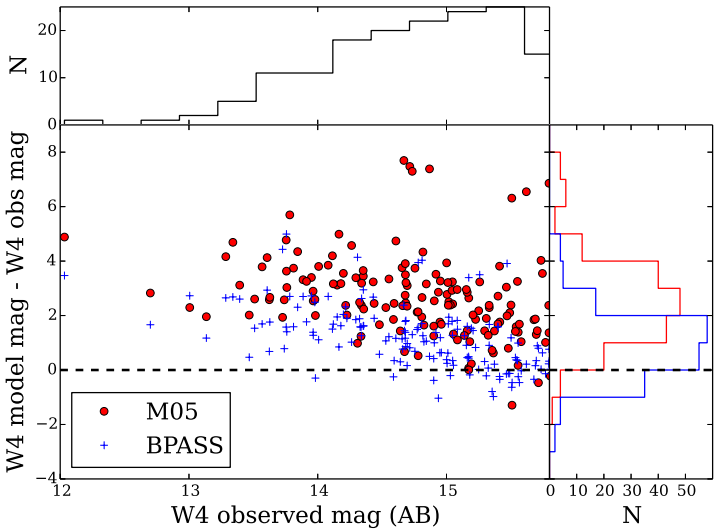

Figure 2.15: Same as Fig. 2.14 but for the W4 band at 22μm. Both model sets underpredict mid-infrared emission. A clear offset between the M05 and BPASS model can be seen with the BPASS (blue crosses) model's magnitudes in better agreement to the observed ones.

2.8 Analysis of Other Independent SED Fitting Procedures

Results from the MPA-JHU collaboration In order to evaluate the effectiveness and reliability of the spectral fit I also made comparisons to two additional fitting methods. For this, I made use of the enhanced spectroscopic catalogue publicly available from the MPA-JHU collaboration[6] [Brinchmann et al., 2004], containing SDSS photometric and spectroscopic data as well as inferred physical properties. These were derived from a narrower wavelength range than that which we considered, but make additional use of spectroscopic constraints. A small number (< 10) of our objects are not included in the MPA-JHU catalogues, but this has no significant effect on the comparisons.

CIGALE SED Fitting Code I also considered a parallel analysis using the Maraston models and the CIGALE fitting algorithm [Burgarella et al., 2005; Roehlly et al., 2014]. This incorporates stellar, nebular, and dust extinction components which were selected to range over the same values as our code. It also includes dust emission and performs a marginalisation analysis to determine the best fit. Configuring the CIGALE dust emission component requires three additional parameters and thus the number of constrained inputs is comparable to the number of photometric data points on a typical source. Nonetheless, I confirm that this method produces very similar results to those of my independent fitting code. I also confirm that there is no significant change in the SED-fitting results when the *WISE* bands are included in the fit, although several additional parameters are required to do this.

Results from the *GALEX*-SDSS-*WISE* Legacy Catalog Since the publication of the results described in this chapter, the *GALEX-SDSS-WISE Legacy Catalog* was published by Salim et al. [2016]. The catalogue lists the SED-derived physical properties of $\sim$ 700,000 galaxies with SDSS redshifts below 0.3. These properties were obtained from UV/optical SED fitting using Bayesian methodology [see Salim et al., 2007], and improved to include blending corrections, flexible dust attentuation laws, and emission line corrections. By comparing the LBA candidates' positions to those in the catalogue, I found 19 sources which had meaningful analyses in the Salim et al. sample. However, two of these sources had to be excluded as they had been identified as outliers in our sample. For the remaining good LBA candidates, Salim et al. [2016] find a median stellar mass of $\log(\text{mass}) = 10.06 \pm 0.07$,

[6] based on DR7, http://www.mpa-garching.mpg.de/SDSS/DR7/

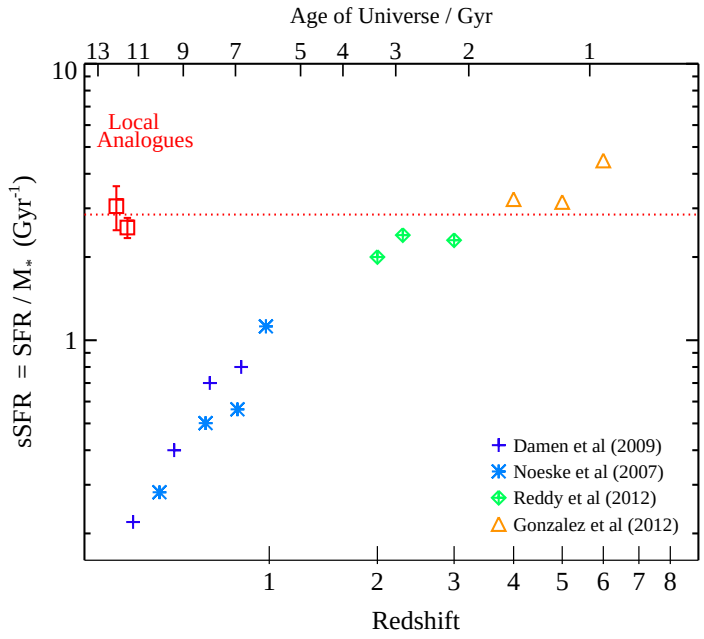

Figure 2.16: The specific star formation rate (sSFR) of our sample (red squares) compared to other galaxy populations at different redshifts. The sample is split into two redshift subsets, at $0.05 < z < 0.15$ and $0.15 < z < 0.25$, and the mean of the entire sample is indicated by a dotted line. The average sSFR of our sample is significantly higher than that of other local and low-redshift galaxies, but in very good agreement with the sSFRs found for $4 < z < 6$ LBGs.

and a UV-optical SFR of 9.9 ± 1.3 $M_{\odot}yr^{-1}$. This compares to a BPASS stellar population synthesis model derived stellar mass of log(mass)$= 10.13 \pm 0.16$, a UV (Hα) SFR of 16.2 ± 2.0 (7.2 ± 1.1) $M_{\odot}yr^{-1}$ for the same objects, indicating that our findings and those of Salim et al. [2016] are in good agreement.

2.9 Suitability as Lyman break analogues

2.9.1 Implications for the $z \sim$5 LBGs

Our sample was selected for their potential use as analogues to the most distant galaxy populations. In table 2.2 I summarise the inferred physical properties of our sample, and also those derived for the high redshift galaxy population. In many respects these are similar, with comparable dust extinction, stellar mass, stellar age, metallicities, star formation rates and sSFRs.

A small number of our larger, older galaxies may be inappropriate as analogues for the distant galaxy population. None of the objects in our sample have masses greater than 5×10^{10} $M_{\odot}$, and 132/180 objects satisfy a mass criterion of $M < 10^{10} M_{\odot}$. Further excluding all objects with ages greater than one Gyr leaves 124/180 sources, while only accepting those with ages $< 10^{8.5}$ years, produces a young subsample of 78/180 galaxies.

In Fig. 2.16 we consider the specific star formation rate of our sample in comparison to more typical galaxy populations as a function of redshift, derived from the Hα-inferred star formation rates and the SED-derived masses. At low redshifts our sample is very atypical of the bulk of the population. At high redshifts, LBGs constitute the majority of the observable galaxy sample. It is apparent that the sSFRs of our sample lie significantly above those for more typical local galaxies (also measured in Hα). In this respect they are more akin to those seen in $z \sim 4-6$ LBGs (as can also be seen in Fig. 2.12), which are also an extreme, ultraviolet-selected star forming population. The high sSFRs in this sample also provide a possible explanation for the high excitation parameters seen in them (see Fig. 2.10) and poses interesting questions such as: what is their escape fraction of ionizing radiation, and how does it compare to those inferred in high redshift galaxies?

I calculate the ultraviolet continuum mass to light ratio for our sources, using masses determined via SED fitting and dust-corrected 1500 Å FUV fluxes as shown in Fig. 2.17. This is compared to the theoretical predictions of Dayal et al. [2014, dashed black line] for $z \sim 5$ galaxies, and also with the ultraviolet luminosities of more typical low redshift star forming galaxies selected from the GAMA survey [Liske et al., 2015, greyscale]. For the latter, I apply the Calzetti law and the extinction reported by the GAMA team to correct for dust extinction. The Dayal models apply a prescription for supernova-driven wind quenching of star formation based on a semi-empirical galaxy evolution model. Our sources are offset from the local GAMA sample, but in very good agreement for the predicted $z \sim 5-9$ population, suggesting that the properties of this sample may be driven by the same evolutionary pressures and feedback constraints that apply in the distant Universe.

If the galaxies comprising our sample were redshifted to $z \sim 5$, corresponding to an age of the Universe of ~ 1.15 Gyr, their mean mass doubling time scale would place their formation redshift at $z \sim 22$. However, this assumes constant star formation over 1 Gyr, which would seem unlikely. The median age of the dominant stellar populations as derived from fitting the M05 models would indicate that they formed as late as $z \sim 5.2$, while the BPASS model would place their formation redshift at $z \sim 7$ (based on the population averages). The latter is in very good agreement with the formation redshifts inferred for $z \sim 5$ LBGs, which Lehnert et al. [2007] found to be $z \sim 6-7$.

2.9.2 Comparison to Other Galaxy Populations

A number of galaxy populations have now been proposed as local analogues to high redshift LBGs. While these share a common property - the presence of intense star

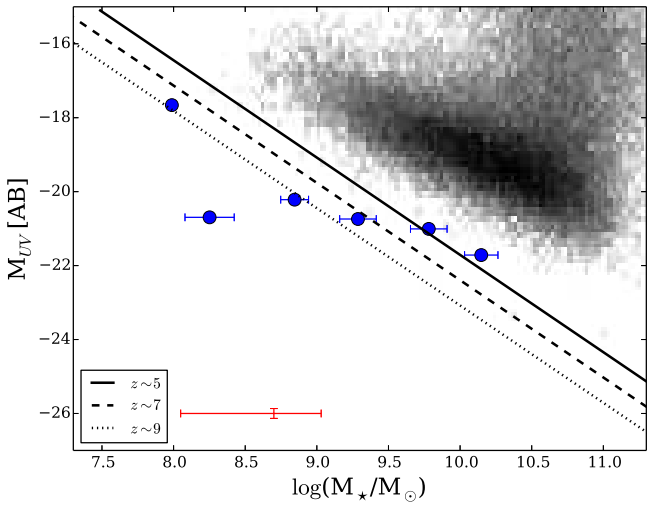

Figure 2.17: The absolute (dust-corrected) 1500 Å *FUV* magnitude vs mass distribution of our sample. The black solid line shows the theoretical prediction for $z \sim 5$ galaxies by Dayal et al. [2014]; lines for $z \sim 7$ and 9 are also shown on the plot. The blue circles give the mean values of our sample, binned in 0.5 dex mass increments, and their standard errors. The M_{UV} uncertainties are too small to be seen. The red error bars are indicative of the uncertainty on each individual data point contributing to a given bin. For comparison, the distribution for galaxies measured by the GAMA survey [Liske et al., 2015] at the same redshift as our sample is shown in grey.

formation - they vary significantly in their selection criteria and observed properties. In Table 2.2 we also contrast our sample with some of the other suggested local analogue populations.

z∼3 LBGs and LBAs

The most widely-used analogue sample is a selection of local ($z < 0.3$) UV-luminous ($L_{FUV} > 2 \times 10^{10} L_\odot$) galaxies (UVLGs) chosen to overlap the luminosity range of $z \sim 3$ LBGs [Heckman et al., 2005]. The selection criteria for the original Heckman et al. [2005] sample and ours are very similar. They aim to reproduce the properties of similar galaxy populations, albeit populations at different epochs in the evolution of the Universe. As a result the galaxies presented in Heckman et al. [2005], Hoopes et al. [2007], and Gonçalves et al. [2010] are significantly more massive than our sample, reflecting the evolution of mass and luminosity between $z \sim 5$ and $z \sim 3$ LBGs [see e.g. Verma et al., 2007]. Only one of our ~ 180 objects overlaps with the Hoopes et al. [2007] sample.

Blue Compact Dwarves

Similarly, blue compact dwarfs [BCDs, Zwicky, 1965] are characterised by compact and gas-rich regions of high star formation. However, unlike our sample, BCDs are

representative of the extremely low end of galaxy luminosity ($M_B = -18$ mag), mass, and metallicity functions. They are among the most metal-poor galaxies in the local Universe, with some objects having metallicities below a tenth Solar, below that inferred for our sample or for the high redshift population at $z \sim 5$. Thus, while both our sample and the BCD sample can be characterised as compact star forming galaxies, it is likely that the BCD sample provides a better match for galaxy populations at still earlier times ($z > 8$), when both typical metallicity and typical luminosity are expected to be rather lower than at $z \sim 5$. None of our sample would be classified as BCDs.

Green Peas

The 'Green peas' are a sample of local ($0.112 < z < 0.360$) SDSS galaxies with strong nebular emission lines, particularly the [O III] λ5007 Å line in the SDSS r-band giving rise to a green appearance [Cardamone et al., 2009; Amorín et al., 2015]. However, there are significant differences between our sample and these extreme emission-line sources. While most of the Peas/EELGs are identified as star-forming, some objects fall on the AGN or 'composite' regions of the BPT diagram. Their selection technique also differs in important respects from the LBG selection. They are required to show strong optical nebular features, particularly the [O III] line, and no constraint is placed on the ultraviolet continuum. This is effectively a selection on emission line equivalent width, more akin to Lyman-α emitter (LAE) selection than typical Lyman-break selection techniques.

To demonstrate the complementarity of our LBA sample and the EELGs, it is interesting to consider the Hydrogen recombination line strengths. High redshift ($z > 5$) galaxies are observed in the rest-frame ultraviolet and thus usually characterised by their Lyman-α emission line. Both the Pea/EELG sample and our own sample of LBAs are observed in the rest-frame optical and their properties therefore most easily quantified in the Balmer series. A comparison between the two is not entirely straightforward. Lyman-α is resonantly scattered and its radiative transfer can be complex. Nonetheless, it is possible to infer a predicted rest-frame Lyman-α equivalent width from the Hα feature in the low redshift samples. To do so we use stellar population synthesis models to model the scaling from Hα equivalent width to Lyman-α at the typical age of each sample. We also adjust the inferred Lyman-α emission to recover the predicted emission in the presence of dust, assuming a typical extinction $E_{cont}(B-V) = 0.1$, and account for the higher extinction of the emission lines relative to the stellar continuum according to the prescription of Calzetti et al. [2000].

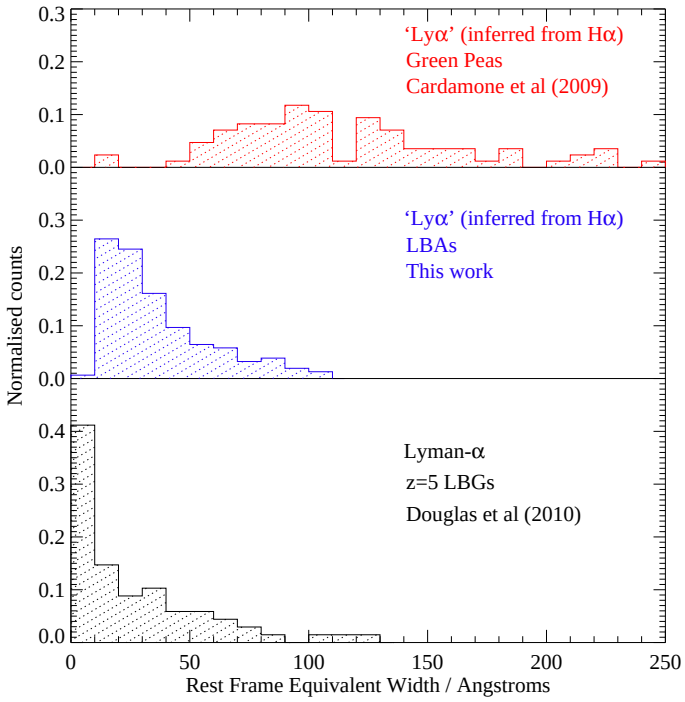

Figure 2.18: The equivalent width distributions of Lyman-α in the $z \sim 5$ Lyman break galaxy sample of Douglas et al. [2010], in the Green Pea sample of Cardamone et al. [2009] and in our sample. In the latter two cases, a predicted Lyman-α equivalent width has been inferred from their Balmer line emission as discussed in section 2.9.2.

Fig. 2.18 shows the comparison between the Green Pea sample of Cardamone et al. [2009], the $z = 5$ sample of spectroscopically-confirmed Lyman break galaxies from Douglas et al. [2010] and the sample presented in this paper, based on hydrogen line equivalent width. While neither analogue sample fully reproduces the observed $z \sim 5$ distribution, it is notable that only 22$\pm$4 per cent of the Douglas et al. sample had a rest-frame equivalent width exceeding 20 Å - quite unlike the distribution seen in the EELG sample. A significant difference in equivalent width distribution is indicative of a discrepancy in stellar population between samples since this is sensitive to the ratio of instantaneous star formation rate and its longer term average.

Local Galaxies

Lastly, our sample can also be compared to the typical population of local star forming galaxies, as shown in Figs. 2.9, 2.10, 2.12, and 2.17. In all of the diagnostics probed, a clear offset can be seen between our sample and the local SDSS or GAMA galaxy population, even when selected to be at the same redshift. The galaxies in our sample display higher ionization parameters and specific star formation rates, and lower stellar masses and ultraviolet mass-to-light ratios. This indicates that the galaxies selected here form a distinct population which, while residing at comparable

redshifts, is characterised by physical properties very unlike those found in typical nearby galaxies.

2.10 Summary and Conclusions

- Many of the physical properties of a galaxy can be determined by studying its spectral energy distribution (SED). Depending on the age of the dominant stellar population, initial mass function (IMF), star formation rate history (SFH), and amount of dust present within the system, the shape of a galaxy's SED changes, and can therefore give clues about these parameters. Stellar population synthesis codes provide a grid of models for stellar populations at different ages, metallicities and SFH (among other possible parameters), making it possible to find the best-fitting model and hence to determine the most likely physical properties of the system.

- I establish a population of 180 galaxies which resembles $z \sim 5$ LBGs in their observed properties by fulfilling the drop-out criteria of LBGs, and having UV-optical slopes indicative of young stellar populations. They lie in the $0.05 < z < 0.25$ redshift range.

- I performed SED fitting on this sample using the Maraston [2005] and BPASS [Eldridge & Stanway, 2009, 2012] stellar population synthesis codes. The analysis of the best-fitting models allowed me to determine the objects' best-fitting ages, masses, and dust content. In addition, I calculate star formation rates, metallicities, and excitation measurements. Both observed and inferred properties have been compared to those determined for different galaxy populations, including $z \sim 5$ LBGs.

- The main scientific findings include the following:

  - The median stellar mass for our sample of $\log(M_*/M_\odot) \sim 9.80 \pm 0.42$ is in agreement with the masses found for $z \sim 5$ LBGs. The median age of the sample is $\log(\text{age/yr}) = 8.60 \pm 0.52$, indicating that, if our sample was redshifted to $z \sim 5$, their formation redshifts would be $z \sim 6 - 7$. The $E_{\text{cont}}(B-V)$ values, found using the Calzetti et al. [2000] starburst extinction law, show little to moderate dust reddening with a median of 0.12 ± 0.07.

  - Using observed flux measurements as well as spectroscopic data, I determine median star formation rates between $\sim$ 2.5 and 14 $M_\odot$ yr^{-1},

depending on SFR indicator, and mean specific star formation rates of $\sim 10^{-9}$ yr^{-1}.

– Comparing these properties to those of $z \sim 5$ LBGs in table 2.2, there is good agreement between the properties of our sample, and the range of properties found in $z \sim 5$ LBGs. It is therefore reasonable to conclude that our sample can be used, with caution, as a local analogue population.

Sample	redshift	mass (median) $\log_{10}(M_\odot)$	dust extinction $E(B-V)$	age $\log_{10}$(yrs)	SFR $M_\odot$ yr^{-1}	sSFR log(yr^{-1})	metallicity $Z_\odot$
Our Sample	0.05 - 0.25	9.80 ± 0.42	$\sim 0.12 \pm 0.07$	$\sim 8.1 - 9.0$	~ 14 (UV)	$\sim -9.0 \pm 0.5$	~ 0.5
$z \sim 5$ LBGs[a]	~ 5	$8 - 11$ (~ 9)	~ 0.2	< 8	$\sim$ few 10s	~ -8.7[e]	~ 0.2
LBAs[b] to $z \sim 3$	$0 < z < 0.3$	~ 9.0 to 10.9	$A_{FUV} \sim 0 - 2$mag	~ 9[f]	few 10s- 100s	-9.8 to -8	$0 \sim 0.3 - 1.5$
Green Peas[c]	$0.11 < z < 0.36$	8.5 - 10	≤ 0.25	~ 8[f]	~ 10	up to -8	~ 1
Blue Compact Dwarfs[d]	$z < 0.01$	7-8	low	$\sim$6-10[g]	$\sim 10^{-3} - 1$	-	~ 0.1

Table 2.2: Comparison of physical properties in various galaxy populations. The superscripts indicate: a = from Verma et al. [2007]; Douglas et al. [2010]; Yabe et al. [2009]; b = from Heckman et al. [2005], Hoopes et al. [2007], Gonçalves et al. [2010]; c = Cardamone et al. [2009], d = Corbin et al. [2006], Zhao et al. [2011]; e = González et al. [2010]; f = doubling time; g = the younger (1-10 Myr) population dominates the light while older (10 Gyr) stars dominate the mass; solar metallicity is taken as $\log[O/H] + 12 \sim 8.7$.

Chapter 3

Radio Observations Confirm LBAs to be Young, Star-forming Systems

In the previous chapter I introduced the selection criteria for local analogue galaxies to $z \sim 5$ LBGs and described their ultraviolet to infrared SED fitting procedure. The results for this sample of 180 local galaxies indicate that a large fraction of these sources can be used as Lyman break analogues. In this chapter I describe the the results of radio and sub-millimetre observations, taken with the Karl G. Jansky Very Large Array (VLA) and the Large Apex BOlometer CAmera (APEX/LABOCA) respectively, of a subsample of the local analogues sample in order to shed further light on the physical processes taking place in these galaxies.

3.1 Introduction

3.1.1 The Origins of Radio Emission in Galaxies

All electromagnetic radiation is the result of accelerations of charged particles. While line emission occurs in processes which have quantised energy states, continuum emission arises from processes in which the energy of the resultant photon is not quantised and hence a continuous energy distribution can be emitted. Radio continuum emission in galaxies arises in two types: thermal emission which depends solely on the emitter's temperature, and non-thermal which arises from other processes. In particular, free-free thermal emission, or bremsstrahlung, is emitted when thermal electrons are absorbed in H II regions. As indicated by its name (which translates to 'braking radiation'), this type of emission occurs when charged parti-

cles are decelerated as they are deflected by another charged particle, such as an atomic nucleus. The kinetic energy lost in this interaction is released as a photon, thus conserving energy. Another common type of radio continuum emission, called non-thermal or synchrotron emission, occurs when high-energy charged particles encounter a magnetic field, causing the particles to spiral along the field lines. In galaxies, this type of radiation can arise from cosmic-ray electrons accelerated in supernova (SN) shock waves or active galactic nuclei (AGN). The latter case arises through the accretion of matter onto a supermassive black hole in the centre of its host galaxy, which can also launch jets. As mentioned in chapter 2, AGN form a potential contaminant to the LBA sample since they can mimic the colour selection and redshift ranges of the local analogues. Their emission line ratios, as shown in the BPT diagram (see Fig. 2.9), however, are distinct, making it possible to preclude them from the LBA sample. Additionally, radio observations can be used to confirm that no radio-loud AGN are present within the LBA sample, which is expected to be significantly radio-quieter. I further comment on the possibility of AGN contaminants in the radio sample in section 3.4.1 below. Not considering AGN, both the free-free thermal radio emission and synchrotron processes require massive stars, either to emit the ionizing ultraviolet radiation which heats the HII region, or to explode in supernovae. The radio continuum can thus be used as a tracer for the star formation rate (SFR) [see e.g. Davies et al., 2017]. While thermal radio emission traces star formation almost instantaneously, non-thermal emission is subject to a time delay corresponding to the lifespan of massive stars and hence takes several tens of Myr to rise to a steady level after the onset of star formation. A lack of synchrotron emission in presently star-forming systems is thus a good indication of a very young stellar population which has not yet attained a stable supernova-driven radio continuum. In such young galaxies, free-free thermal radio emission dominates the (radio) spectrum.

Unlike ultraviolet continuum or optical line emission, radio continuum flux is unaffected by dust attenuation in the source galaxy and thus provides an independent, and potentially more reliable star formation rate indicator.

Previous studies have found SFRs in stacked radio and submillimetre observations of $z \sim 3-5$ LBGs between 6 ± 11 $M_\odot$ yr^{-1} (see Ho et al. [2010]) and 31 ± 7 $M_\odot$ yr^{-1} (see Carilli et al. [2008]), comparable to their UV and Lyα SFRs, indicating very little, if any, obscured star formation and a very low fraction of AGN hosts. Given the relative insensitivity of metre-wave telescopes, observations at rest-frame frequencies of 1.5 GHz (in the L-band) are effectively limited to the low-redshift ($z < 0.25$) Universe with current facilities. However, a local LBA sample

like ours can be used to explore the radio properties of galaxies with known physical conditions, and thus to interpret high-redshift sources. Using green peas [GPs, Cardamone et al., 2009] as local analogues to $z \sim 2-5$ LBGs, Chakraborti et al. [2012] suggest that both GPs and LBGs have some non-thermal or synchrotron radio emission, but, as mentioned above, it is far from clear that all LBA samples share the same characteristics.

3.1.2 Overview of Chapter

The work presented in this chapter has been published as Greis et al. [2017]. In section 3.2 I describe the observations, before deriving radio star formation rates and star formation densities for the targets in section 3.3. The interpretation of the derived properties and their implications for high redshift sources are discussed in section 3.4. The properties of individual sources are presented in a section 3.5, before concluding with section 3.6.

3.2 Observations

3.2.1 Sample Selection

Targets were selected from the catalogue of 180 LBAs as presented in chapter 2 and Greis et al. [2016]. Slight preference was given to those objects which had already been observed with ATCA at 5.5 and 9.0 GHz [see Stanway & Davies, 2014], those whose SED-derived physical properties made them ideal local analogues to $z \sim 5$ LBGs in terms of their masses and ages, and those which are part of an approved ALMA programme. Additionally, the sources were chosen to be visible during the LST ranges allocated to the programmes, and such as to avoid nearby radio-loud sources. Their optically-derived properties are listed in Table 3.1. Figures 3.1 and 3.2 show the loci of the entire LBA sample (reproducing figures 2.9 and 2.10) as small circles on the BPT [Baldwin et al., 1981] and mass-excitation diagrams [Juneau et al., 2011] respectively. The red squares indicate the locations of the radio-observed sources, which can be seen to span the whole range of properties of the LBA sample, making them a representative subsample.

ObjID (SDSS DR7)	ra	dec	redshift	FUV AB mag	mass $\log_{10}(M_\odot)$	dust $E(B-V)$	age $\log_{10}$(yrs)	Hα SFR $M_\odot$ yr^{-1}	metal. $Z_\odot$	observed by
587727876380754061	355.41867	-8.71988	0.074	18.66	8.0	0.13	7.2	3.1	0.23	VLA & ATCA
587726877273227473	336.64663	-9.68499	0.083	20.39	9.2	0.05	8.7	1.3	0.18	VLA & ATCA
587730817902116911	344.79825	-8.77026	0.097	19.31	9.8	0.18	8.6	5.1	1.62	VLA & ATCA
587727226227523734	1.16389	-10.15264	0.108	19.80	8.3	0.26	7.2	10.4	0.34	VLA & ATCA
587734841741083073	115.62922	21.334231	0.110	20.60	9.6	0.09	8.8	2.6	0.14	VLA
587737827281076428	111.6581	39.766087	0.111	19.86	9.4	0.16	8.6	8.0	0.46	VLA
587727178464624784	35.15693	-9.48536	0.113	19.78	8.5	0.06	6.7	6.8	0.35	VLA & ATCA & APEX
587745540508680573	128.92412	10.299852	0.115	20.59	10.0	0.14	9.0	1.8	0.68	VLA
587730774950608959	332.01197	13.226264	0.116	19.55	9.3	0.11	8.1	7.6	0.18	VLA
587732703947653150	178.63296	8.5770854	0.117	18.72	9.4	0.11	8.4	10.9	0.35	VLA
587726877810360392	337.13304	-9.46809	0.120	20.29	10.3	0.2	9.8	4.0	0.88	VLA & ATCA
587730818439577821	346.21707	-8.6318	0.121	19.94	9.9	0.11	8.4	3.9	0.45	VLA
587739381531476079	235.02877	24.51249	0.122	19.46	9.7	0.15	8.6	8.1	0.22	VLA
588017979426537518	174.90376	39.982965	0.130	19.66	9.8	0.07	8.8	2.7	0.43	VLA
587727179534762100	26.84033	-9.27951	0.136	19.98	8.7	0.02	7.3	5.2	0.09	VLA & ATCA
587733431922327825	251.40989	28.985973	0.136	20.30	9.8	0.17	8.7	3.8	0.25	VLA
587739648346357993	143.6293	26.285418	0.138	20.44	9.7	0.13	8.5	3.2	0.40	VLA
587736542021091412	221.73053	7.7560733	0.142	19.27	9.6	0.05	8.3	9.5	0.24	VLA
587735431232356415	212.84126	47.48035	0.145	19.73	9.7	0.08	8.7	7.6	0.16	VLA
587737809027334524	112.65454	39.143992	0.145	20.73	9.9	0.14	8.9	2.8	0.44	VLA
588017949897523218	211.19882	40.646364	0.145	20.08	9.9	0.10	8.8	6.6	0.26	VLA
587727230523605083	27.9936	-9.38417	0.146	20.36	9.9	0.12	8.7	8.1	0.34	VLA & ATCA & APEX
587730816826671294	340.88031	-9.44735	0.146	19.96	9.2	0.11	7.7	8.3	0.16	VLA & ATCA

587739827674808586	238.20283	16.985618	0.149	20.48	9.9	0.10	8.7	5.2	0.27	VLA
587727178463772856	33.14848	-9.63883	0.150	20.06	9.4	0.11	8.0	4.9	0.24	VLA & APEX
587735430151929942	189.89012	49.909903	0.150	20.43	9.7	0.12	8.7	2.0	0.27	VLA
587727178997432420	25.70536	-9.60746	0.161	20.1	10.2	0.34	8.7	41.8	0.58	VLA & APEX
587727180071108755	25.58712	-8.76605	0.164	20.41	9.7	0.21	8.1	15.8	0.35	VLA & ATCA
587732771035938857	137.37213	6.5544124	0.181	19.73	9.7	0.14	8.0	19.6	0.28	VLA
587724240687792239	37.28071	-8.95727	0.183	20.00	9.8	0.06	8.5	10.4	0.17	APEX
587741601493155849	179.62691	27.123929	0.183	19.92	9.7	0.12	8.4	7.1	0.25	VLA
587728668808315004	128.45934	45.825978	0.188	20.18	9.6	0.15	8.3	21.9	0.26	VLA
588017704028995952	237.44271	7.9204591	0.198	20.18	9.6	0.10	8.2	10.4	0.43	VLA

Table 3.1: Some of the physical properties of the radio targets, derived from SDSS photometry and spectroscopy. Columns give the SDSS identification number, the object's sky position and redshift, and observed FUV magnitude from *GALEX*. The masses and ages for each object were determined using SED fitting described in chapter 2 of the BPASS spectral synthesis model set, while the dust continuum $E(B-V)$ value was calculated from the Balmer decrement. The star formation rates are based on extinction-corrected Hα line fluxes, and quoted metallicities use the Dopita et al. [2016] calibration. The last column indicates by which telescope(s) each object was observed. For brevity, only last 5 digits of the SDSS object identifier are used as an object designation in the remainder of this chapter.

Observing Intent	Typical time [min]
Bandpass Calibration, Flux Calibration, Delay Calibration	~ 5
Gain Calibration	~ 5
Target	~ 8
Gain Calibration	$\sim 1-2$
Target	~ 8
Gain Calibration	$\sim 1-2$
Target	~ 8
Gain Calibration	$\sim 1-2$

Table 3.2: The setup of all VLA scheduling blocks. Exact times varied due to slewing and wrapping constraints.

3.2.2 VLA

The observations were carried out with the Karl G. Jansky Very Large Array (VLA) in programmes 14A-130, 15A-134, and 16B-104 (PI: Stanway) between March and May 2014, July and September 2015, and September 2016 and January 2017 respectively (see Table 3.3). Each object was observed in a 45 minute long scheduling block with a typical on source time of $\sim$ 20 minutes, split into 3 independent scans of near-equivalent length. These short observations were optimised to make use of short gaps between the executions of observing programmes with higher priorities. All observing programmes used the 'A' configuration and identical setups with the exception of targets observed in September 2016 which were observed in a transitional 'BnA' configuration and those observed in January 2017, observed in the 'AnD' configuration. Observations were taken in the L-band, centred at 1.5 GHz, and making use of the 1 GHz bandwidth of the VLA. Radio frequency interference (RFI) reduces the effective frequency bandwidth to ~ 0.5 GHz but with substantial variation from source to source. One observation had to be excluded due a bright nearby source which rendered imaging of the faint target impractical. In no other cases was a sufficiently bright target in the field to preclude detection of the science target. As all targets have previously been detected in the ultraviolet and optical, their positions are well-constrained. For each target, therefore, the area to be searched for counterparts consistent with the optical location is very small and the possibility of the observed sources arising from chance alignment is minimal. The 32 observed sources span a redshift range of $0.07 < z < 0.20$.

For each source, phase and gain calibration was achieved using a well-established

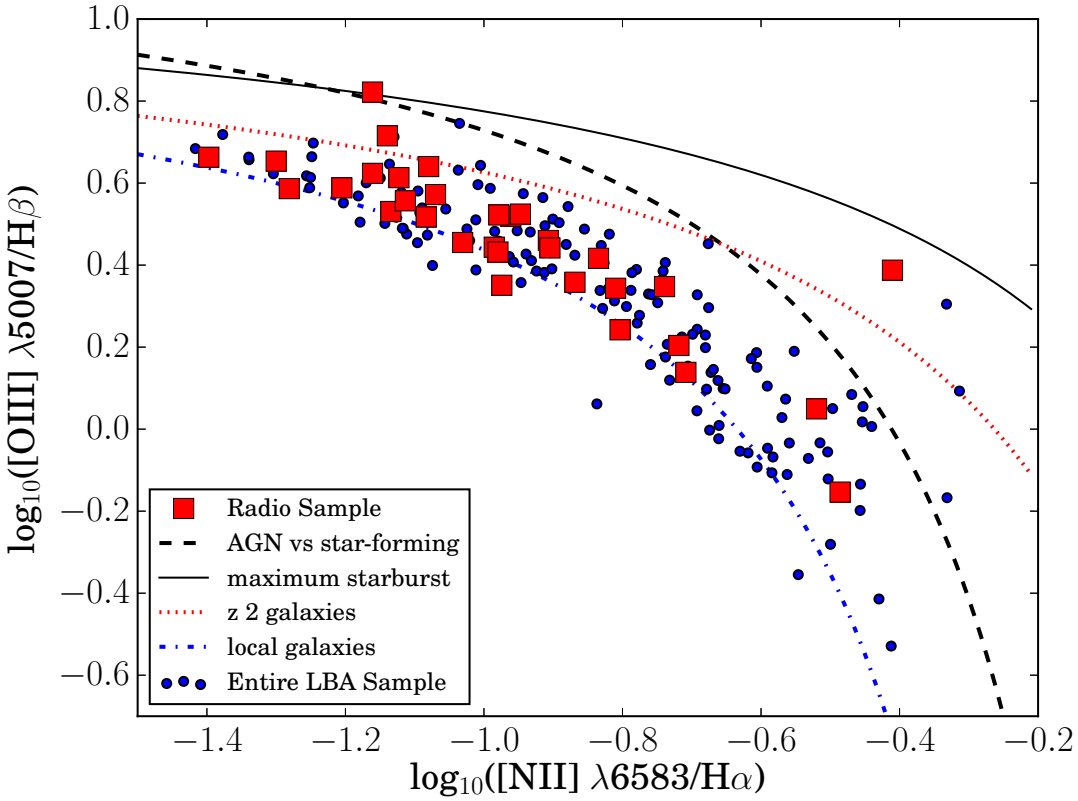

Figure 3.1: BPT diagram showing the loci of our large LBA sample [small circles Greis et al., 2016, and chapter 2], as well as those of the sources discussed in this chapter (red squares). Dashed and solid black lines indicate the AGN vs star forming criterion of Kauffmann et al. [2003] and the maximal starburst line of Kewley et al. [2001] respectively. The sources for which radio observations have been obtained span the entire range of the parent sample, making it plausible that the radio sources can be regarded as representative of the LBA sample. Note that one of the radio targets may have a substantial AGN contribution to its emission lines, though it lies below the maximal starburst line proposed by Kewley et al. [2001]. The locus representing $z \sim 2$ galaxies (red dotted line) is from Steidel et al. [2014] while the local galaxy population as detected by SDSS is shown with a dot-dash blue line.

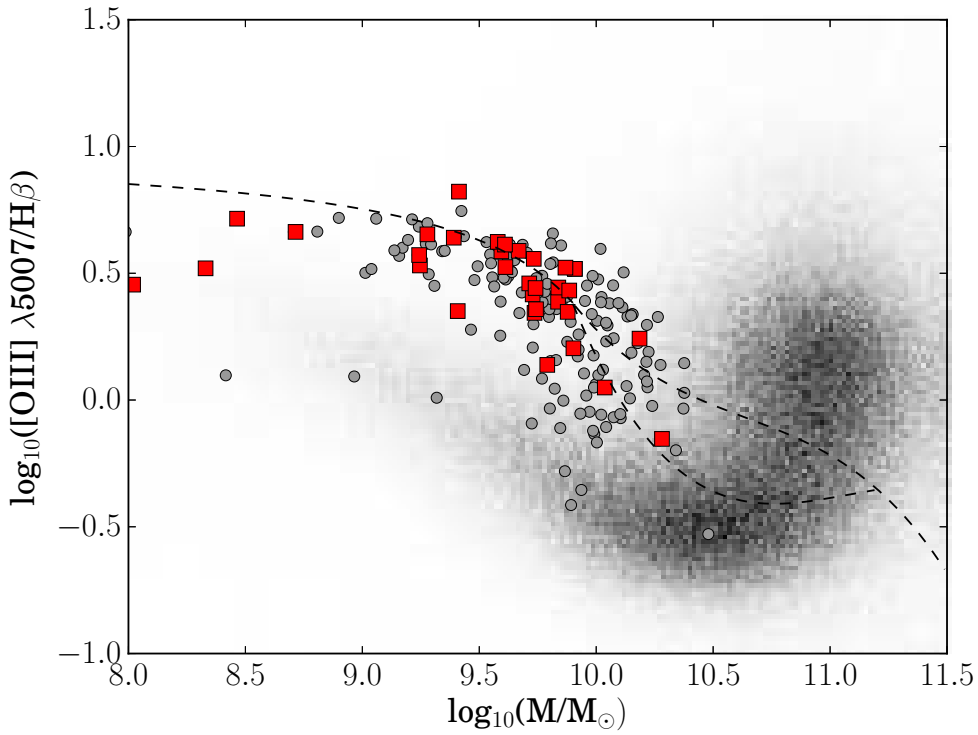

Figure 3.2: Mass-excitation diagram showing our LBA sample [small grey circles Greis et al., 2016, and chapter 2], overlaid on the local SDSS galaxy population (grey distribution). The locations of the galaxies described in this chapter are marked by red squares. There is a significant offset between our LBA sample and the bulk of the local galaxy population with a higher ionizing potential observed in the LBAs. The dashed line indicates the proposed separation between star formation (below) and AGN-driven (above) ionizing radiation according to Juneau et al. [2011]. Objects in the bordered region are classified as composites.

secondary phase calibrator from the VLA calibrator database[1]. The calibrator was observed for $\sim 1-2$ minutes between each ~ 8 minute on-source integration and was typically of order 1 Jy in flux and between 5 and 10 degrees from the science target. Absolute flux, delay and bandpass calibration was accomplished through observations of one of the standard VLA calibration sources, 3C48, 3C147, or 3C286 with the appropriate object chosen for the target RA. These sources are regularly monitored by the National Radio Astronomy Observatory (NRAO). For some sources, the wrapping direction of the antennae had to be considered: if observations are to be taken on opposite sides of the zenith, antenna unwrapping can be an issue. In particular, scheduling blocks which made use of a calibrator at zenith ($\sim 30^\circ$ N declination for VLA observations; i.e. calibrators 3C286 or 3C48), were required to have a specified antenna wrap[2]. To avoid loss of observing time due to unwrapping, I duplicated the relevant scheduling blocks, creating one with a clockwise and the other of a counter-clockwise wrap, and specified that only one of each pair of such scheduling blocks should be observed.

I initially analysed the available data in 2015, by manually flagging all fields (the two calibrators and the science target) and using the 'clean' image reconstruction algorithm of the currently available version of the Common Astronomy Software Application (CASA) package. In 2016, I updated CASA to v4.7.1 and (re)analysed the (previous and new) observations. During the course of these analyses, a calibration pipeline was implemented by NRAO. Each observing block was then pipeline-reduced using this pipeline[3], which is integrated into current versions of CASA. The pipeline is optimised for Stokes I continuum data and performs data-flagging and Hanning smoothing before calculating delay, gain, flux and bandpass calibrations. These are applied to the target data and diagnostic images of the calibrators are constructed.

Where necessary, I manually flagged the target data for any remaining RFI which is pervasive at the frequencies probed. Following flagging and pipeline calibration, the measurement sets were 'cleaned' interactively by the CASA software. For this the standard CASA 'clean' procedure to invert the visibility data was used. I used multi-frequency synthesis ('mfs') mode to create one image in the Stokes I (total flux) parameter for each object. This procedure can be problematic for datasets with a large fractional bandwidth, if there is spectral curvature. The standard procedure assumes that the source has a constant spectral index. For our most robust sources, I sub-imaged the data in different frequency bands and saw no evidence for

[1]VLA calibrator database: `http://www.vla.nrao.edu/astro/calib/manual/csource.html`
[2]`https://science.nrao.edu/facilities/vla/docs/manuals/obsguide/dynsched#antenna_wraps`
[3]VLA CASA calibration pipeline:`https://science.nrao.edu/facilities/vla/data-processing/pipeline`

significant flux variation with frequency. The CASA 'clean' algorithm is designed to deal with wideband multi-frequency synthesis imaging and I used the recommended parameters for low signal-to-noise data. 'Clean' creates a dirty image and primary beam pattern before iteratively reconstructing the sky image. After imaging test cases using different cell sizes, I found that a cell size of 0.5 arcsec produced the optimum signal-to-noise ratio. Our targets were too faint to consider polarimetric data. The imaging was done using 'Briggs' weighting which implements a flexible weighting scheme and a Briggs' robustness parameter of 0.5. 'Cleaning' was performed using the Clark cleaning algorithm and imaged with the phase centre at the pointing centre.

After successful 'cleaning' of both the calibrator and science target, I determined that each frame contained a number of mJy-level sources, although these were typically sparsely distributed through the field-of-view and did not affect flux measurement of the science target. In a few cases, a brighter target was present in the field and its sidelobe pattern apparent. In these cases, the image was carefully inspected and the local noise level used as an estimate of the rms. In no case was the science target detection consistent with a sidelobe detection of a brighter source. After verifying each detection through visual inspection, I split the targets' measurement sets into individual scans and imaged each scan independently to ensure that the object was detected in all three scans. Given the effects of RFI, the sensitivity varied substantially from scan to scan. Objects for which two out of the three scans yielded non-detections were considered to have a detection only if the source was detected in the scan with the lowest rms noise level. Measurements of the radio fluxes and object sizes were obtained from the images combining all 3 scans using CASA's 'imfit' routine with 3 to 5 arcsec radii around the source location (where imfit did not converge, I used 'imstat' to derive upper flux limits).

In five objects, the observations were not as intended: one object (at RA 31.21° Dec 15.24°) had a radio-loud nearby object, which made it impossible to obtain flux measurements from the target source. Another source (at RA 30.74° Dec 48.20°) could not be reduced because crucial information was missing from the measurement set file. A further object (Object 56425) could not be calibrated accurately since the radio source used as its gain calibrator was unsuitable for L-band calibrations. This meant that the calibrator does not correspond to a point source at the observed frequencies, hence making it impossible to construct a well cleaned image. A correct phase and gain calibrator not only needs to be a relatively bright source near the science target, but also suitable for the observed frequencies. While Object 56425 is included in the analysis presented here, only upper limits

on the source flux are given. Additionally, both objects 08959 and 62100 were observed twice due to inconsistent naming of the scheduling blocks. All of these issues illustrate the importance of checking my observations.

In early January 2017 the NRAO announced that a problem with the atmospheric delay calculation on the VLA had occurred, potentially affecting observations taken between August 9, 2016 and November 14, 2016, when some of our observations were taken. The effect of this issue was that sources would be displaced from their positions, as a function of their elevation, maximum projected baseline length, and distance from the complex gain calibrator, which are all functions of time. A fix to this was implemented into the CASA calibration pipeline used for the final analysis of the observations described here. According to the NRAO, the magnitude of this effect could be estimated as: offset $\sim 5ab$ milliarcseconds, where $a = sec^2(z)tan(z)$ for zenith angle z and b = separation of the target source from the calibrator in the elevation direction, in degrees. Using this, I estimated that the offset for the observations taken during the relevant period was negligible (generally of order a few tens milliarcseconds up to ~ 200 milliarcseconds in one source).

3.2.3 APEX

Five LBA targets were observed in the 870 μm (345 GHz) atmospheric window using the Large Apex BOlometer CAmera (LABOCA) at the Atacama Pathfinder EXperiment (APEX) as part of ESO programme ID 093.B-0414(A) (PI: Stanway). These observations used a compact spiral raster mode designed to optimise coverage in the central arcminute. While the allocated time was 11 hours, our observed programme totalled 6.8 hours of which approximately a third of the time was on source; further details are shown in Table 3.4. All observations used the same setup. Initial pointing and focus observations were obtained on a Solar System planet. The pointing was then refined and the flux scale determined using one of the standard APEX/LABOCA secondary flux calibrators: HLTAU, N2071IR, CRL618 and V883-ORI. Regular skydip observations were performed to calibrate for atmospheric opacity. Observations were reduced by my collaborator using v1.05-3 of the MiniCRUSH software suite[4] [Kovács, 2008], a minimalist version of the data reduction software CRUSH optimised for the APEX bolometers. This removes correlated noise in the time stream, which is then used to construct a source model using a maximum likelihood estimator. MiniCRUSH is a non-interactive software. The 'deep' pipeline option was selected for the reduction, which aggressively filters correlated noise and is optimally filtered (smoothed) to optimise signal-to-noise on point sources. This

[4]MiniCRUSH software: `http://www.astro.caltech.edu/~sharc/crush`

will underestimate extended structure, but none is expected on this scale. The pixel scale used was 4 arcsec. The APEX beam has a FWHM of 19.5 arcsec and the pipeline smooths the data to a FWHM of 27.58 arcsec.

At $z \sim 0.1 - 0.2$, the 870 μm band of LABOCA is close to the transition between the dust-dominated thermal black-body, which dominates the far-infrared, and the radio continuum emission that dominates at $\sim$1 GHz. Hence the flux density from both SED components is relatively small in the observed band.

3.3 Results

When imaging all three VLA scans combined, 27 objects out of the 32 observed with the VLA were detected at signal-to-noise ratios above 3. The remaining 5 were undetected above 3σ. Excluding the non-detections, the VLA observations were detected at a mean SNR of 6.3. No correlations were found between the SNR achieved and time of day at which the observations were taken, the temperature at the telescope, or the recorded wind speed (with p values of 0.78, 0.96 and 0.71 respectively, leading in all cases to the acceptance of the null hypothesis that the linear regression slope is zero). Of the sources observed with the VLA, 10 had previously been observed with ATCA, making it possible to determine their radio spectral slope (see Fig. 3.5 in section 3.3.3).
All APEX observations yielded non-detections and hence upper flux limits (see Fig. 3.6). These were consistent with expectations from their Hα-derived star formation rates and suggests none of these five sources contains a heavily obscured, powerful AGN. Given the sources' modest Balmer decrements, and hence low inferred dust extinction, is it not surprising that no evidence is found for heavily dust-obscured AGN.

ObjID	Observing date	Beam size arcsec^2	Exposure (min)	rms μJy
16911	2014 Mar 31	1.7 × 1.1	27.7	30
54061	2014 May 16	1.8 × 1.1	26.2	43
71294	2014 May 22	1.9 × 1.1	25.5	30
77821	2014 May 28	1.6 × 1.1	25.0	37
60392	2014 May 31	1.9 × 1.1	25.7	30
76428	2015 Jul 14	3.2 × 1.0	25.6	31
08959	2015 Jul 21 & Sep 07	1.4 × 1.2	2 × 24.6	38
80573	2015 Aug 01	2.3 × 1.1	24.0	40
23734	2015 Aug 11	1.6 × 1.1	25.6	72
24784	2015 Aug 13	2.0 × 1.2	25.6	34
27825	2015 Sep 01	1.5 × 1.1	25.6	25
15004	2015 Sep 16	1.4 × 1.1	25.6	31
27473	2015 Sep 20	1.8 × 1.1	25.6	28
34524	2016 Sep 18	2.2 × 1.2	24.5	19
57993	2016 Sep 19	2.2 × 1.1	24.6	27
83073	2016 Sep 22	2.4 × 1.1	24.5	32
37518	2016 Sep 23	2.9 × 1.2	24.5	30
08586	2016 Sep 23	1.7 × 1.2	24.6	23
53150	2016 Sep 24	3.9 × 1.2	24.5	54
76079	2016 Sep 24	1.7 × 1.1	24.6	31
95952	2016 Sep 24	2.0 × 1.3	24.6	17
91412	2016 Sep 28	1.6 × 1.2	24.6	60
23218	2016 Sep 29	2.2 × 1.0	24.6	44
56415	2016 Sep 29	1.9 × 1.7	24.6	45
55849	2017 Jan 18	1.2 × 1.2	24.6	15
29942	2017 Jan 23	1.9 × 1.0	24.6	15
38857	2017 Jan 24	1.4 × 1.11	24.6	28
05083	2017 Jan 24	1.7 × 1.1	24.6	29
08755	2017 Jan 24	1.6 × 1.2	24.6	27
32420	2017 Jan 24	2.5 × 1.0	24.6	39
62100	2016 Dec 15 & 2017 Jan 24	2.0 × 1.1	2 × 24.6	37
72856	2017 Jan 24	2.9 × 1.1	24.6	18

Table 3.3: VLA observations. Exposure time given is on-source.

ObjID	Observing date	Total Observing Time (hrs)	rms μJy
92239	2014 Mar 24	1.6	5.3
72856	2014 Mar 25	0.5	14.2
24784	2014 Mar 26	2.3	4.6
05083	2014 Jul 29	1.2	3.9
32420	2014 Jul 30	1.2	5.7

Table 3.4: APEX observations.

ObjID	1.5 GHz flux μJy	SNR	Angular size arcsec^2	1.5 GHz SFR $M_\odot$ yr^{-1}	Σ_{SFR} $M_\odot$ yr^{-1} kpc^{-2}
83073*	54 ± 17	3.2	(6.1 ± 2.8)×(1.9 ± 1.5)	1.18 ± 0.37	$0.03^{+0.3}_{-0.02}$
76428	90 ± 20	4.5	(3.08 ± 1.14)×(1.10 ± 0.15)	2.0 ± 0.4	$0.18^{+0.23}_{-0.09}$
80573*	113 ± 20	5.6	(2.77 ± 1.37)×(0.74 ± 0.48)	2.7 ± 0.5	$0.39^{+2.2}_{-0.26}$
08959*	131 ± 18	7.3	(2.28 ± 0.59)×(0.27 ± 0.42)	3.2 ± 0.4	$1.5^{+18.9}_{-1.1}$
53150*	132 ± 15	8.8	(2.78 ± 1.66)×(1.22 ± 0.67)	3.29 ± 0.37	$0.28^{+1.4}_{-0.18}$
77821*	246 ± 41	6.0	(1.9 ± 0.23)×(1.59 ± 0.17)	6.7 ± 1.1	$0.6^{+0.3}_{-0.2}$
76079*	113 ± 10	11.3	(2.11 ± 0.45)×(0.48 ± 0.45)	3.09 ± 0.27	$0.8^{+17.1}_{-0.5}$
37518*	76 ± 13	5.8	(3.41 ± 1.6)×(0.99 ± 0.87)	2.40 ± 0.41	$0.17^{+2.9}_{-0.12}$
27825	75 ± 17	4.4	(1.90 ± 0.54)×(1.20 ± 0.23)	2.7 ± 0.6	$0.25^{+0.29}_{-0.13}$
57993*	45 ± 9	4.7	(4.4 ± 1.3)×(3.3 ± 1.2)	1.62 ± 0.34	$0.02^{+0.04}_{-0.01}$
91412*	127 ± 21	6.0	(2.97 ± 0.6)×(2.75 ± 0.65)	4.96 ± 0.82	$0.12^{+0.11}_{-0.05}$
56415	<135	< 3	-	< 5.5	-
34524	< 57	< 3	-	< 2.5	-
23218*	79 ± 16	4.9	(3.6 ± 1.1)×(3.2 ± 1.3)	3.24 ± 0.66	$0.06^{+0.1}_{-0.03}$
08586*	62 ± 11	5.6	(2.17 ± 0.72)×(1.74 ± 0.9)	2.69 ± 0.48	$0.13^{+0.36}_{-0.08}$
72856	<54	< 3	-	< 2.4	-
29942	< 45	< 3	-	< 2	-
32420	211 ± 42	5.0	(2.39 ± 0.36)×(1.36 ± 0.13)	11.0 ± 2.2	$0.6^{+0.3}_{-0.2}$
38857*	175 ± 26	6.7	(1.17 ± 0.29)×(0.12 ± 0.52)	12.0 ± 1.8	$11.7^{+0.5}_{-10.2}$
55849	< 45	< 3	-	< 5.8	-
15004	147 ± 13	11.0	(1.4 ± 0.15)×(1.09± 0.09)	11.1 ± 1.0	$0.9^{+0.3}_{-0.2}$
95952	39 ± 12	3.3	(4.55 ± 1.91)×(1.47 ± 0.32)	3.30 ± 1.01	$0.06^{+0.11}_{-0.04}$

Table 3.5: Results for sources which were observed with the VLA only, giving their measured fluxes and signal-to-noise ratios. The angular sizes of the sources were estimated using CASA imfit. In most cases, CASA suggested that the objects were not resolved, and their estimated size measurements are hence upper limits. Objects for which 'imfit' provided a size measurement deconvolved from the beam are marked with an asterisk. Radio star formation rates use the Kennicutt & Evans [2012] conversion. Star formation rate densities Σ_{SFR} for our sample are derived from radio data alone. It should be noted again that since observed angular sizes are convolved with the beam, the values found for Σ_{SFR} are lower limits.

ObjID	1.5 GHz flux μJy	VLA SNR	5.5 GHz flux μJy	ATCA SNR	α	Angular size arcsec^2	1.5 GHz SFR $M_\odot$ yr^{-1}	Σ_{SFR} $M_\odot$ yr^{-1} kpc^{-2}
54061*	471 ± 70	6.7	215 ± 38	5.6	-0.60 ± 0.25	(4.12 ± 0.68)×(1.67 ± 0.46)	4.3 ± 0.6	$0.4^{+0.4}_{-0.2}$
27473†	70 ± 21	3.3	57 ± 23	2.5	-0.16 ± 0.57	(3.97 ± 1.96)×(0.97 ± 0.18)	0.8 ± 0.2	$0.1^{+0.2}_{-0.07}$
16911*	171 ± 26	6.6	91 ± 20	4.6	-0.49 ± 0.29	(1.31 ± 0.51)×(0.54 ± 0.44)	2.8 ± 0.4	$1.57^{+14.5}_{-1.0}$
23734*	283 ± 32	8.8	220 ± 34	6.4	-0.19 ± 0.21	(1.60 ± 0.43)×(0.35 ± 0.45)	6.0 ± 0.7	$3.5^{+5.6}_{-2.4}$
24784	132 ± 31	4.3	151 ± 27	5.6	0.10 ± 0.32	(2.00 ± 0.56)×(1.33 ± 0.26)	3.1 ± 0.7	$0.3^{+0.4}_{-0.2}$
60392* †	92 ± 13	7.1	54 ± 26	2.1	-0.41 ± 0.51	(1.81 ± 0.34)×(1.09 ± 0.12)	2.5 ± 0.4	$0.33^{+0.2}_{-0.12}$
62100†	19 ± 4.8	4.0	61 ± 25	2.4	0.90 ± 0.53	(1.39 ± 0.07)×(0.04 ± 0.00)	0.7 ±0.2	$2.6^{+0.8}_{-0.8}$
05083	149 ± 36	4.1	76 ± 22	3.5	-0.52 ± 0.42	(1.82 ± 0.31)×(1.4 ± 0.19)	6.1 ± 1.5	$0.5^{+0.2}_{-0.3}$
71294*	157 ± 38	4.1	72 ± 21	3.4	-0.60 ± 0.42	(1.36 ± 0.72)×(0.93±0.5)	6.5 ± 1.6	$1.0^{+4.7}_{-0.7}$
08755*	254 ± 33	7.7	159 ± 22	7.1	-0.36 ± 0.20	(2.10 ± 0.38)×(0.61 ± 0.37)	13.7 ± 1.8	$1.7^{+4.3}_{-0.9}$

Table 3.6: As in table 3.5 for those objects with both VLA and ATCA data. Objects marked with an asterisk have been resolved by the CASA software, and hence their deconvolved sizes, as determined by the software, are quoted. Objects marked with a † have ATCA observations with SNR$<$ 3 and their derived radio spectral slopes hence have large associated uncertainties. Since the ATCA observations effectively provide upper limits, the true spectral slopes of these sources are likely steeper than the values indicated here, see section 3.3.3 for discussion.

3.3.1 Star Formation Rate

Using the 1.5 GHz radio luminosity to SFR conversion of Kennicutt & Evans [2012], the mean star formation rate derived for the galaxies in our sample is $4.8 \pm 0.7\,M_\odot\,yr^{-1}$. This compares to a mean derived from Hα line emission in the same targets of $8.2 \pm 1.3\,M_\odot\,yr^{-1}$. Excluding any non-detections, the 1.5 GHz SFRs range from $0.7\,M_\odot\ yr^{-1}$ to $13.7\,M_\odot\ yr^{-1}$. These relatively low values are consistent with those inferred from the optical/ultraviolet and with previous work in the radio and sub-millimetre, both on high redshift targets directly, as well as on similar local analogue samples.

The Hα-derived SFR presented in chapter 2 and published in Greis et al. [2016] is very sensitive to the ionization conditions and metallicity of the nebular gas as well as potential dust obscuration. The most massive stars - and hence the most likely progenitors of supernovae and radio continuum flux - form in dusty molecular clouds and might therefore be missed when only considering the UV and optical emission of the galaxy. I dust-correct the Hα flux using the Balmer decrement and assuming case B recombination and a standard ratio of Hα to Hβ of 2.86. Having found LBAs to be generally dust-poor both from SED-fitting as well as via Balmer decrement measurements, obscured star formation is not expected to play a large part in this sample. However, if such star formation were present, it should lead to an *excess* in the radio emission relative to Hα predictions.

Fig. 3.3 shows the inferred 1.5 GHz radio star formation rates of the sample as well as those found from Hα. The red dashed line indicates a one-to-one relation, while the green dot-dashed one shows a radio SFR that is half as high as the one found in Hα. The majority of the sources lie well below the one-to-one line, indicating that the galaxies have significantly higher Hα-inferred SFRs than radio SFRs. These results remain unchanged when using the more recent Tabatabaei et al. [2017] radio-continuum to Hα SFR calibration. The only objects which display stronger radio than Hα SFRs are Objects 80573, 54061, 77821, and 29942. Apart from Obj 54061, these have all been found to be among the most massive sources in our sample and older than the typical source (see section 3.5 for more details). Thus it would be unsurprising if those sources were more likely to host dust-obscured star formation, since evolved AGB stars and supernovae are the main injectors of dust into the ISM [Dwek, 2005].

The *deficit* in emission relative to Hα in the bulk of the sample is, however, more surprising and is discussed in section 3.4.2.

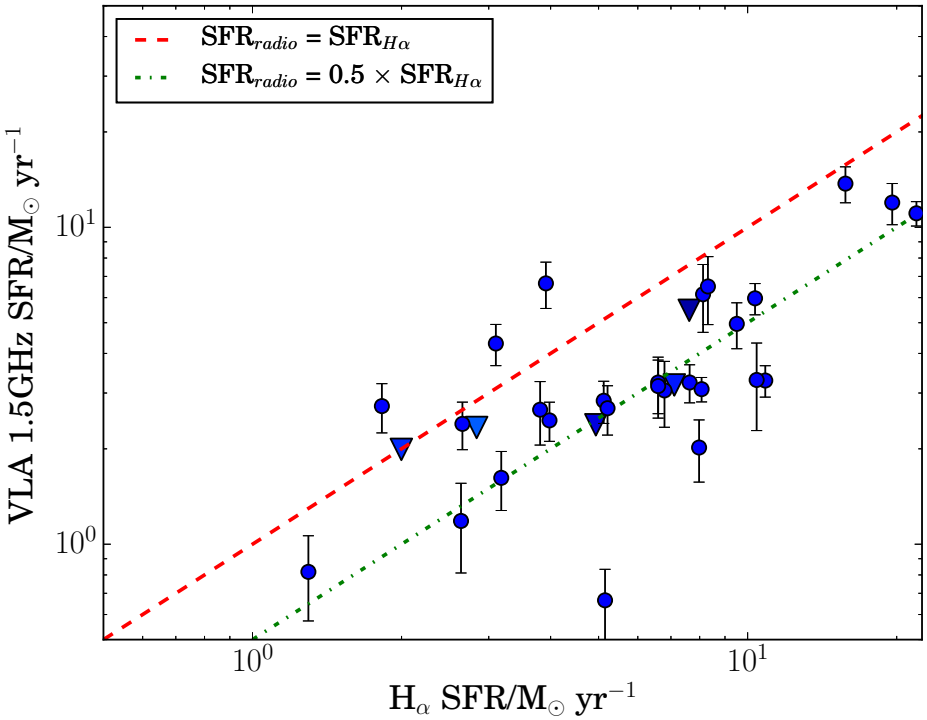

Figure 3.3: Comparison of the star formation rates calculated from radio (using Kennicutt & Evans [2012]) and (Balmer-decrement) dust-corrected Hα (using Kewley et al. [2004], see also Kennicutt [1998]) fluxes. Where it was only possible to determine upper limits, a triangle is shown, while in all other cases the errors on the inferred radio SFR are given. The red dashed line indicates the line of equality, while the green dot-dashed line shows radio SFR as half of the Hα. It can clearly be seen that most objects in this sample have lower radio- than Hα-inferred SFRs. The error bars on Hα are too small to be seen. Hα is not corrected for Milky Way dust.

3.3.2 Star Formation Rate Density

I determine measurements or upper limits on the angular sizes of the objects using CASA's 'imfit' procedure. This makes it possible to improve the size, and hence density constraints, of the sources compared to previous (unresolved) optical observations. In order to measure the objects' sizes, 'imfit' assumes an elliptical fit to the source, and provides major and minor axis measurements, as well as uncertainties on both. In about half of the sources (14 out of 32), the procedure is unable to deconvolve the source from the beam. In these cases, I use the measured value, which is likely a substantial overestimate of the true source size. In the remainder (18 out of 32), the radio source is resolved, and here I use the deconvolved size as reported by the software. The deconvolved measurements are approximately 10-30% smaller (in both minor and major axis) than the unresolved sizes quoted by 'imfit' for a given source. I use these size measurements to calculate an upper limit on the area of the source, and define an effective lower value of the star formation rate surface density as

$$\Sigma_{SFR} \equiv \frac{\mathrm{SFR}_{1.5\,GHz}}{\pi ab} \quad [\mathrm{M}_\odot\,\mathrm{yr}^{-1}\mathrm{kpc}^{-2}]$$

where a and b give the semi-major and semi-minor axis of the galaxy in kpc, and $SFR_{1.5\,GHz}$ is the 1.5 GHz radio-derived star formation rate discussed above. I also calculate stellar mass densities based on the SED-fitting derived masses presented in chapter 2.

In Fig 3.4 I compare the stellar mass density (in $\mathrm{M}_\odot/\mathrm{pc}^2$) and Σ_{SFR} (using size limits derived from 1.5 GHz observations) of our sample to those of local SDSS galaxies. The SDSS sample was selected to be in the same redshift range as our sample, and sizes, masses and SFRs are derived from the optical. AGN are excluded.

Two loci, representing passive and actively star forming galaxies, can be seen, with all of our sources lying well above the star-forming locus and displaying significantly higher Σ_{SFR} than other local galaxies. The sample clearly represents an extreme subsample of the larger population.

3.3.3 Spectral Slope

By measuring the radio spectral slope, $F_\nu \propto \nu^\alpha$, in the sources it is possible to consider the origin of their radio emission. A steeper slope is associated with non-thermal, or synchrotron, emission, while a flat spectrum is indicative of thermal radio emission arising from thermal electrons in HII regions. Emission associated with AGN and their jets can span a wide range of spectral indices.

A total of ten of our targets were observed at 5.5 GHz with ATCA [Stanway & Davies,

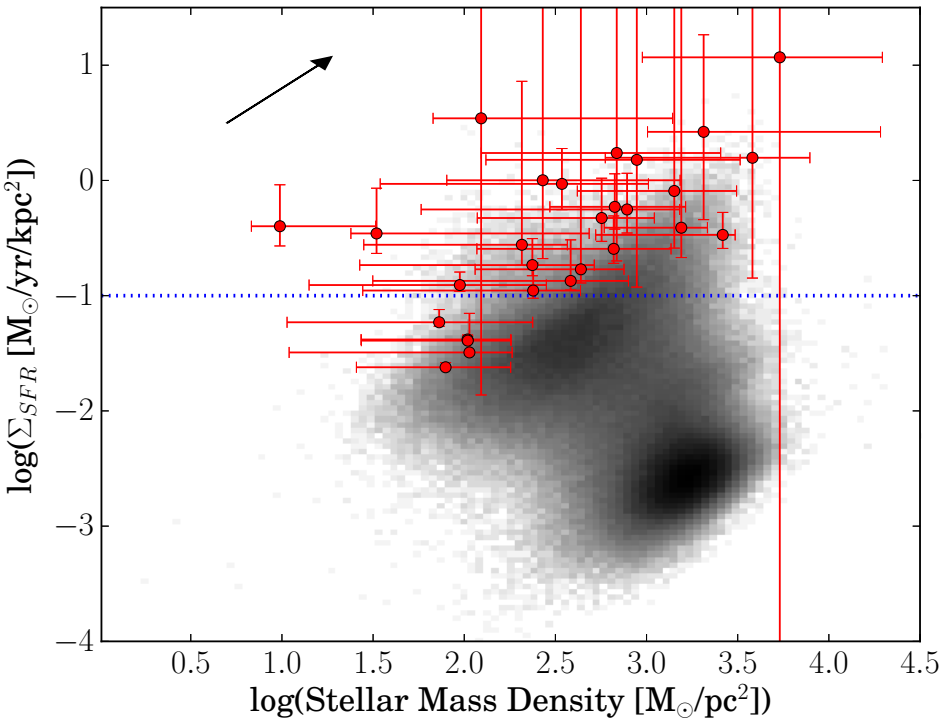

Figure 3.4: Lower limits on stellar mass density and the star formation rate density for our sample using the radio-derived SFRs. Since the sources are unresolved in both the optical and radio observations, the true sizes are likely smaller than the ones used here, and hence the derived densities are lower limits (the arrow in the top left corner of the figure indicates the direction in which the sample would move with decreasing size). The underlying grey-scale represents the local galaxy population as sampled by the SDSS in the same redshift range as our sample, and clearly separates into passive (low Σ_{SFR}) and star forming galaxies. The blue dotted line indicates the criterion of 0.1 $M_\odot$ yr^{-1} kpc^{-2}, suggested by Heckman [2002] as indicating the onset of starburst-driven galactic winds, or superwinds (see section 3.4.3).

2014]. Of these, three reported fluxes have a signal-to-noise ratio < 3, and are thus likely to represent upper limits, rather than robust detections. An additional three sources were detected at $3 <$SNR< 5. Given the extended beam of ATCA at this frequency for objects at these declinations, these detections might also be suspect in a blind field survey in which the false detection rate rises rapidly as signal-to-noise ratios fall below 5. However, Stanway & Davies [2014] inspected each source and found it to be coincident with the targeted optical galaxy, decreasing the likelihood of a false positive detection for the sources described here. The 5.5 GHz fluxes for these targets were also consistent with, or deficient relative to, the expected ultraviolet-inferred star formation rate in each case. If the low signal-to-noise detection, in fact, represents a misclassification of background noise, then the deficiency in radio flux seen in both the Stanway & Davies [2014] sample and the observations discussed here, is more dramatic still. In the following, sources with a SNR < 3 in the ATCA data are treated as upper limits, though I quote the measured value.

Comparing the fluxes in the ATCA and VLA radio bands, about half of the sources show spectral slopes, or upper limits, consistent with dominant thermal emission. The spectral slopes of the remainder suggest a mixture of thermal and star-formation driven synchrotron radiation (see Table 3.6 and Fig. 3.5). For comparison, the fluxes of galaxies taken from observations in the Extended Chandra Deep Field South by Miller et al. [2013] and Huynh et al. [2012] at 1.4 GHz and 5.5 GHz respectively are shown. These targeted sub-mJy, and hence predominantly star-forming, galaxies which are likely similar to our sample. The samples described here and in this previous work are consistent in both their distribution and the range of their spectral slopes.

A slight overdensity at $150 - 200\mu$Jy in 1.4 GHz sources can be seen in the E-CDFS observations by Miller et al. [2013]. This might potentially be due to the presence of radio-loud AGN. Bonzini et al. [2013] find that at $\sim 30 - 100\mu$Jy, the radio population in this field is dominated by star-forming galaxies ($\sim 60\%$) and radio-quiet AGN, while radio-loud AGN make up an increasing fraction at higher fluxes.

In normal star-forming galaxies with constant star formation rates, one would expect a radio spectral slope of ~ -0.7 to -0.8. However, the spectral slopes in our sources are significantly shallower, suggesting that they have a high fraction of thermal radio flux. Interestingly, this is what would be expected of a recent short-duration starburst, which produced thermal radio as well as Hα emission, but very little non-thermal synchrotron emission. Both the radio-derived results as well as the previously found stellar population ages are thus consistent with recent starbursts

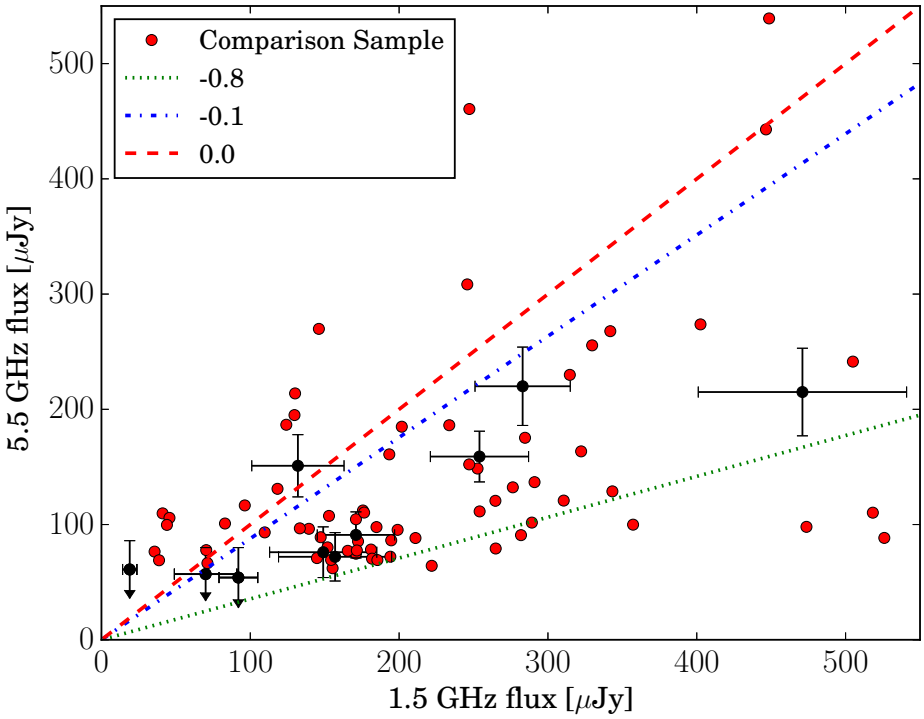

Figure 3.5: The fluxes and spectral slopes for objects observed with both VLA and ATCA. All spectral slopes are consistent with star formation driven synchrotron or non-thermal emission. Sources with 5.5 GHz measurements at less than 3σ are shown at the measured values with an upper errorbar indicating a 5σ limit, and the lower uncertainty unbounded. A comparison population is taken from observations of sub-mJy sources by Miller et al. [2013] and Huynh et al. [2012] at 1.4 GHz and 5.5 GHz respectively.

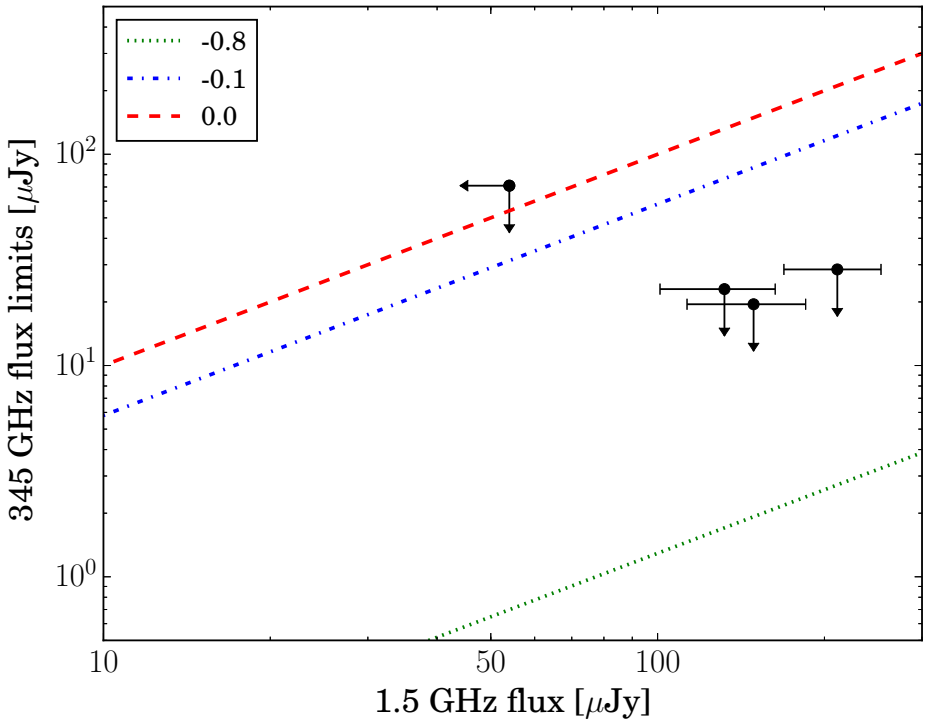

Figure 3.6: Like Fig. 3.5, showing 5σ upper flux limits for APEX 345 GHz non-detections and VLA 1.5 GHz fluxes (or 3σ limit on one source). The spectral slopes inferred for these sources are consistent with shallow slopes indicative of a large thermal fraction.

in the majority of our sources.

In addition to the spectral slopes derived from VLA and ATCA observations, I also plot upper limits for the 4 objects for which we obtained both VLA observations and APEX non-detections, assuming they would have been detected at 5σ above the rms noise (see Fig. 3.6). In agreement with the spectral slopes found above, the limits on their 1.5 - 345 GHz spectral fluxes are consistent with a combination of high thermal fraction and synchrotron emission due to recent star-formation.

Fig. 3.7 shows the ratio of Hα to 1.5 GHz radio SFRs against the spectral slopes found within them. A clear correlation between shallower (more positive) slopes and higher Hα to 1.5 GHz SFR ratios can be seen, indicating that systems with a recent starburst (those with high Hα to 1.5 GHz SFR ratios) are deficient in supernova-driven synchrotron emission which would give them steeper spectral slopes.

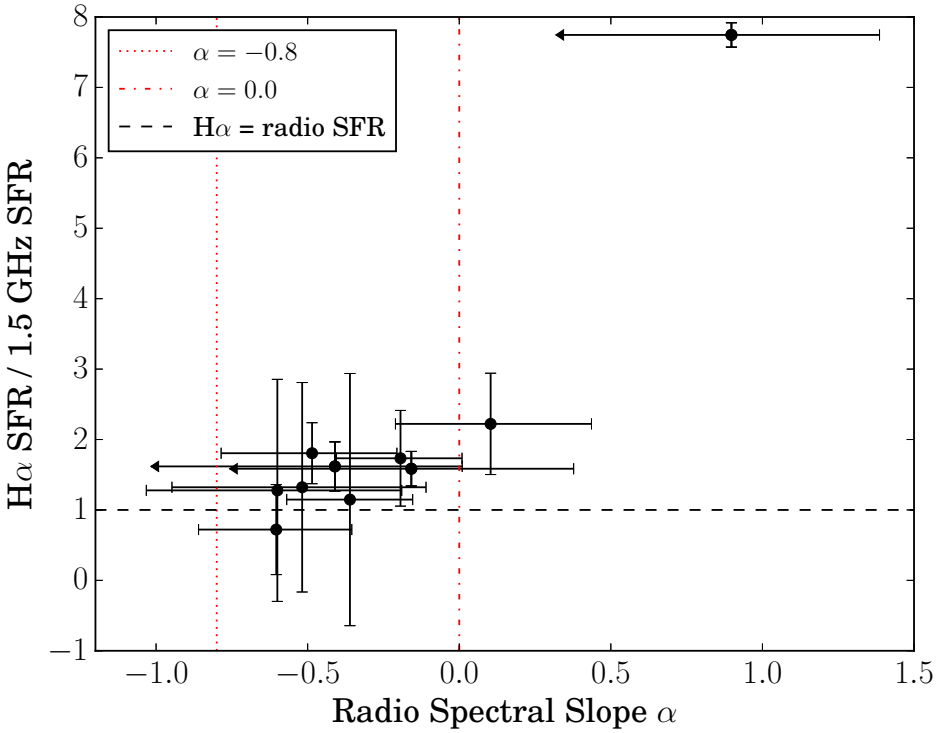

Figure 3.7: The spectral slopes and ratios of Hα to 1.5 GHz radio SFRs for objects observed with both VLA and ATCA. This provides further confirmation that these sources do not contain a strong non-thermal component. The systems with the highest Hα to 1.5 GHz ratio, indicative of a recent starburst, show a clear trend towards the flatter radio spectral slopes found in galaxies dominated by non-thermal radio emission. The most extreme system (Object 62100) has some of the least well constrained spectral slope measurements.

3.4 Discussion

3.4.1 Do these Sources Contain AGN?

At the typical luminosity of our sample, $L_{1.4GHz} \sim 5 \times 10^{21}\,\mathrm{W\,Hz^{-1}}$, star forming galaxies are an order magnitude more abundant than AGN powered sources [Condon et al., 2002; Sadler, 2016], hence very few such contaminants would be expected in this sample, even without our careful pre-selection based on optical and ultraviolet data. In Fig. 3.8, the luminosity distributions of star-forming galaxies and those identified as AGN within the Best & Heckman [2012] sample is illustrated, as well as that of our sources. By calculating the probability of AGN in each luminosity bin, and multiplying it by the number of our observed targets in each bin, the total expected number of AGN in our sample is found to be ~ 0.57. This prediction is, of course, subject to small number statistics and the associated Poisson uncertainty. Sadler [2016] suggest that compact accretion-powered radio sources may still be quite numerous at low luminosities, but, at $10^{24}\,\mathrm{W\,Hz^{-1}}$, uses a limit several orders of magnitude brighter than the target sample presented here. The AGN population is poorly constrained at the very low radio luminosities relevant here, with the best constraints coming from optically-selected samples [e.g. Best & Heckman, 2012], but the decline in the AGN luminosity function appears to be steep in current deep surveys, rendering it unlikely that there are significant numbers of concealed AGN in our sample. However, even adopting a conservative estimate of 1 ± 1 AGN contaminants entering our sample, the primary conclusions of these observations remain unchanged, with the bulk of our targets both powered by star formation and deficient in radio flux. In selecting the large LBA sample presented in chapter 2, any objects which were classified as AGN in SDSS were excluded (though a few lie in the overlap region, see Fig. 3.1). Thus, while it is conceivable that a small number of our targets might host a radio-quiet AGN, this seems unlikely given the optical properties of the sources, which indicate star-formation driven optical emission lines and low dust-obscuration.

Uncertainty arises for two objects; their strong lines place Objects 76428 and 16911 in or close to the AGN region of the BPT diagram. However, the line ratio diagnostic is sensitive to the object's redshift, star formation rate densities, and metallicity (among other factors), all of which are more extreme in our sample than in the normal galaxies for which the BPT diagnostics are calibrated. The validity of the BPT diagram for high-redshift sources - and hence potentially their local analogue populations - has been questioned [see e.g. Bian et al., 2016; Steidel et al., 2014], showing that the locus of high-redshift sources is shifted upwards compared to

local galaxies. Hence the location of Objects 76428 and 16911 on the BPT diagram may be an indication of their extreme physical properties, rather than AGN activity. The spectral slopes of AGN range from -1 to flat, showing a broad variety of behaviours with frequency. Therefore, the spectral slope has little diagnostic ability in this case. We note that, admittedly at brighter radio luminosities, AGN-dominated galaxies in the SDSS tend to show a far higher radio-to-Hα flux ratio than our targets. An AGN sufficiently obscured to not modify the optical emission line ratios in the BPT diagram typically adds to the radio continuum, providing an additional component on top of the host galaxy's star formation, while an unobscured AGN produces relatively little Hα for a given radio flux (and indeed relative to other optical emission lines, hence the location of such sources in the BPT diagram). Thus the presence of an AGN in one or more of our targets does not provide an explanation for the observed radio deficit. If the UV-optical emission represents star formation (as suggested by SED fitting and the emission line spectra), an AGN origin for any component of the radio emission would only increase the deficit in the remaining sources, as discussed in section 3.3.1.

3.4.2 Determining Ages

Most standard calibrations for SFR, including those of Kennicutt & Evans [2012] used here, assume star formation to have been continuous over the last 100 Myr. By contrast, only the stars formed in the last 10 Myr contribute to Hα flux, while stars over a much larger range of ages contribute to the supernova rate and hence power any 1.5 GHz radio synchrotron emission. Thus, a precise conversion from flux to star formation rate will be dependent on the stellar population age and star formation history. By using a stellar population synthesis model, it is possible to derive such conversions. It is important to note that for a given flux, the standard conversion rates underestimate the true rate of star formation in populations younger than a few hundred Myr.

Dr Stanway calculated the stellar population using the Binary Population and Spectral Synthesis [BPASS v2.0, Stanway et al., 2016, Eldridge et al submitted] population synthesis code for a system forming stars at a constant rate of $1\,\mathrm{M}_\odot\,\mathrm{yr}^{-1}$, but which has yet to stabilise at young ages. From this, the output stellar spectrum was processed through v13.04 of the radiative transfer code CLOUDY [Ferland et al., 2013, 1998] to calculate the [O II] and Hα fluxes. Additionally, the predictions of BPASS were used to calculate a core-collapse supernova rate. This is corrected for type Ia supernovae which contribute $\sim \frac{1}{3}$ of the SN rate at late times, and which track the overall star formation rate and thermal contribution with a de-

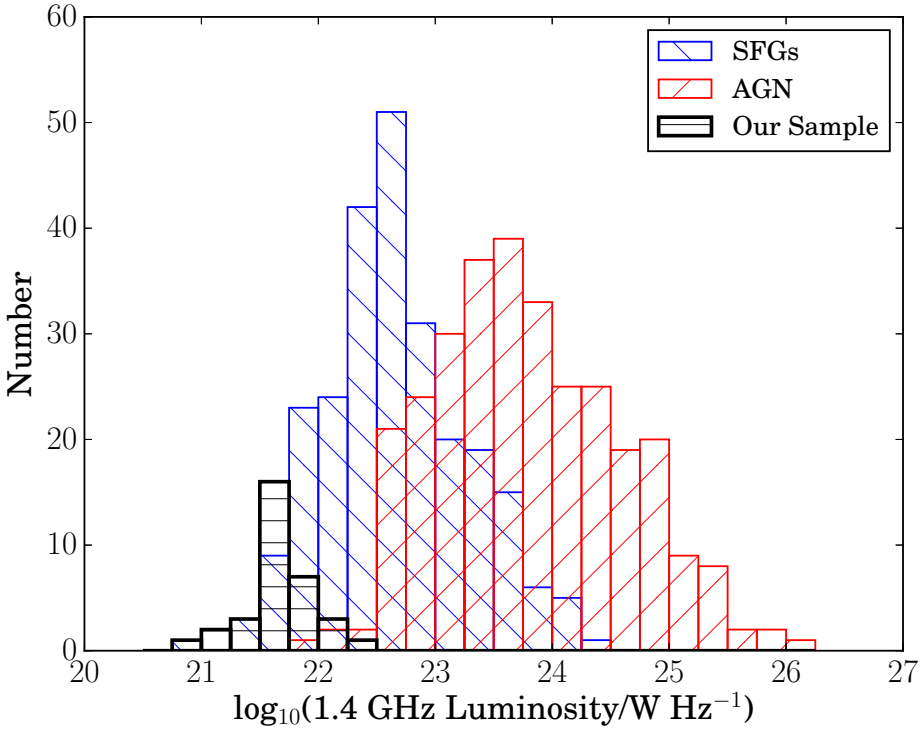

Figure 3.8: Comparing the observed luminosities of AGN (red) and star-forming galaxies (blue) in the Best & Heckman [2012] sample, cross-matched with the MPA-JHU catalogue, to the galaxies presented here (black). By calculating the fractional probability of AGN in each luminosity bin, and comparing it to the luminosity distribution of our sample, I predict that ~ 0.57 AGN may be present within our observations.

lay of 100 Myr. The radio-SFR calibration assumes $\sim 10-20\%$ thermal emission in a mature stellar population, with the remainder due to synchrotron emission which is proportional to the rate of core-collapse supernovae [Tabatabaei et al., 2017].

Given that the standard calibrations are calculated for a population age of 100 Myr, the outputs of the BPASS stellar population synthesis models are scaled by the values determined for populations at that age, to calculate a fraction of the steady-state line flux and supernova rate that will be measured at each age. By applying the standard calibrations to these outputs, the fraction of the 'true' SFR that would be inferred at a given age, were the standard calibration to be applied, is calculated. In Fig. 3.9, I illustrate this, and hence show the age dependence of each star formation rate indicator. As expected, the supernova rate (and hence the inferred synchrotron emission) only becomes significant at ages above $\sim$ 10 Myr, increasing steeply thereafter, while Hα and [O II] line emission rise more rapidly after the onset of star formation. While the (statistically unlikely) presence of an AGN in this sample would complicate the analysis presented here, the result would be to indicate still younger stellar populations: the nebular and radio flux from an AGN are both rapidly established and would act to increase the radio deficit relative to the optical emission lines.

In principle, finding the overlap region in which the calculated SFRs coincide makes it possible to constrain the age of the stellar population. In Fig. 3.10 I illustrate this technique for one of our targets, demonstrating good agreement with the young SED-derived age for this object. Caution should, however, be taken since uncertainties in dust correction of observed fluxes, star formation history and in handling of the thermal component of the radio continuum (discussed below) suggest that over-interpretation of these results at this stage is unwise.

As discussed in section 3.3.3, the spectral indices of this sample are largely consistent with the flat slopes indicative of thermal emission and star-formation driven synchrotron radiation. Thermal radio emission arises from H II regions and is proportional to the photoionization rate in the source. As such we might expect it to trace similar timescales to Hα and [O II]. This component typically contributes only $\sim 10-20\%$ to the radio continuum at 1.4 GHz and thus is often neglected in calculating calibrations.

Interestingly, Tabatabaei et al. [2017] present not only a calibration from total radio continuum to star formation rate, but also its decomposition into thermal and non-thermal components, calibrated against the local KINGFISH galaxy sample [Kennicutt et al., 2011]. Applying their derived calibration based only on thermal radio emission to our data, the inferred radio SFRs of our sample are found to

be consistent with the Hα expectation. In other words, for some cases we infer a thermal fraction in our observed sources of 100%, well above the typical fraction in local sources of 10% at 1.4 GHz, and higher than the maximum fraction in the KINGFISH sample (35%). It is worth mentioning that Tabatabaei et al. [2017] found that the thermal fraction was highest in dwarf irregular galaxies and at high star formation rates. If this trend holds, certain sources of our sample of very compact, irregular, starburst sources represent an extreme case. A thermal fraction of $\sim$100% in these objects would be consistent with the picture described above in which the non-thermal emission expected to be present simply has not yet had time to develop in these young galaxies. It is also in good agreement with the low gas-phase metallicities found in these sources (see Table 3.1), which indicate that relatively little metal-enrichment has occurred.

3.4.3 Leaky Box Model & Winds

An alternative explanation for the relative deficit of radio emission in this sample might be the 'leaky box' model in which the near-relativistic electrons providing the magnetic field of a galaxy are ejected from the galactic gravitational well, causing a decrement in observed radio emission compared to the true flux [Kaiser, 2005]. From the star formation rate densities found in section 3.3.2, one might expect that galaxy-wide superwinds are present in most of our sources. Such winds arise from the energy and momentum injected into the ISM by stellar winds and supernovae [Chevalier & Clegg, 1985; Heckman et al., 1990, see also discussion in Chen et al 2010]. While there are likely to have been supernovae in our sample, their stellar populations are not old enough to have produced a substantial number of Wolf-Rayet or AGB stars which drive strong stellar winds due to radiation pressure on dust in the stars' upper atmospheres.

There are conflicting studies correlating the velocity of outflows with related parameters such as star formation rate and its density. Heckman [2002] shows that outflow speeds with wind velocities of up to ~ 3000 km s^{-1} are ubiquitous in galaxies with SFRDs > 0.1 M$_\odot$ yr^{-1} kpc^{-2} and correlate with SFRD, while Rubin et al. [2014] find no such minimum threshold. Tanner et al. [2016] attempt to reconcile these findings with simulations that show correlations between SFR (and SFRD) and outflow velocity break down at a point dependent on the entrained cold gas component, which varies from galaxy to galaxy. These factors are also likely to be metallicity dependent and so, again, local correlations may not be entirely applicable to our sample.

Davies et al. [2017] find a sub-linear relation between the SFR and radio

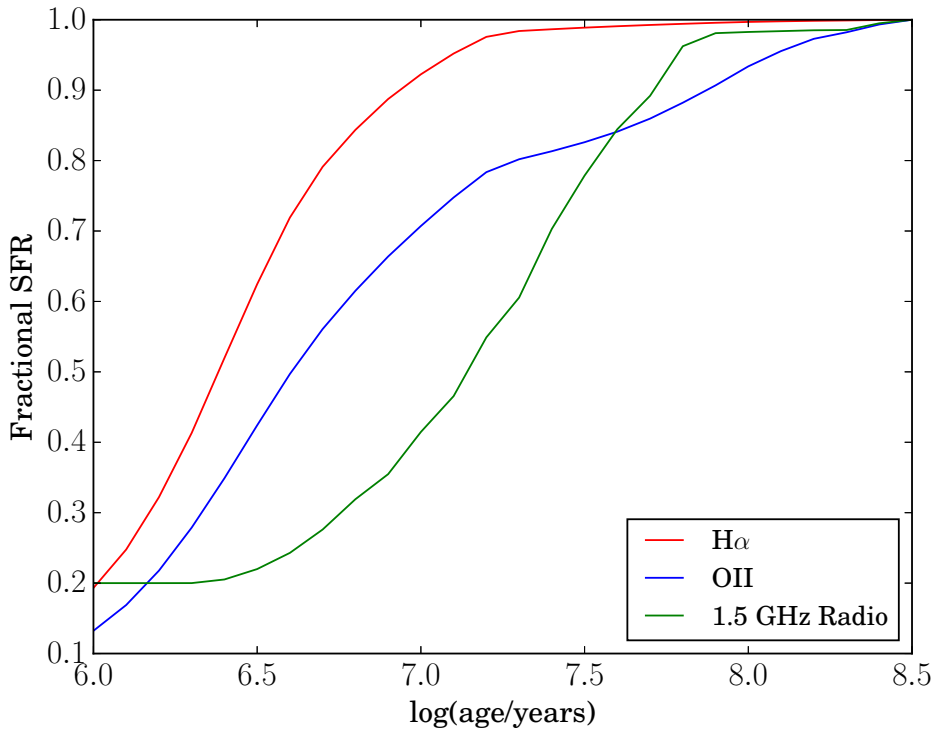

Figure 3.9: An estimate of the fraction of 'true' star formation rate that would be inferred given the standard calibrations, for young stellar populations. Fractions are calculated based on a population forming stars at a constant rate in the BPASS stellar population synthesis code, as described in section 3.4.2. Here, the fractional SFR is shown as a function of stellar population age for the Hα (red line), OII (blue line) and radio (green line) indicators. Radio continuum takes longer to establish than the nebular line emission leading to underestimates in the radio-derived star formation rate.

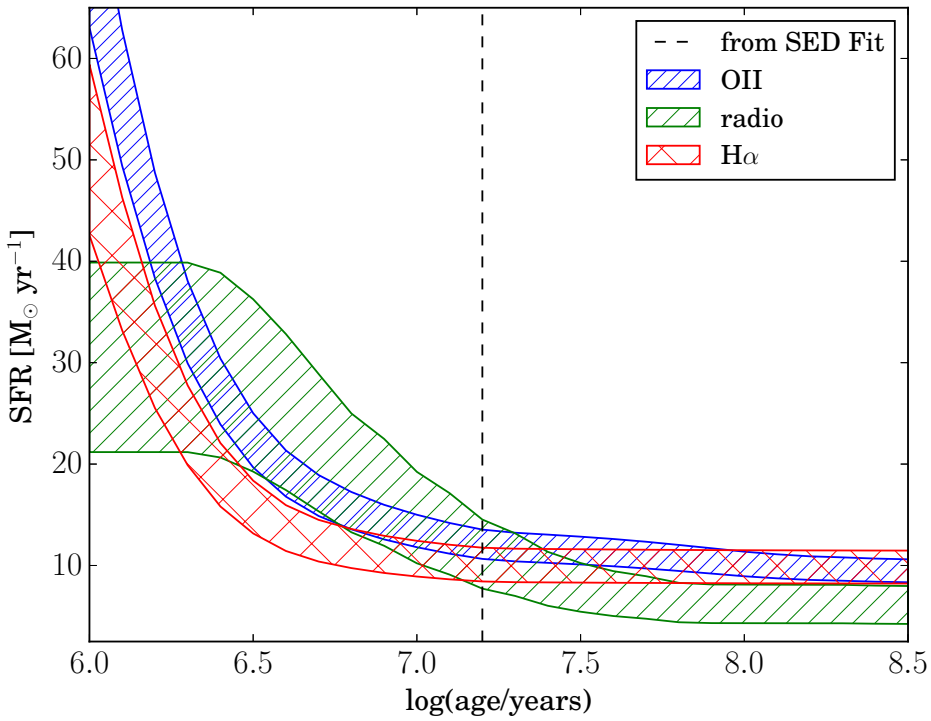

Figure 3.10: Using the conversion rates in Fig. 3.9, we show the inferred SFR for a given stellar population age for Obj 23734, assuming continuous star formation. The green dashed line indicates the radio SFR for a given age, while the solid blue and dotted red lines show the OII and Hα inferred SFRs respectively. As the standard calibrations assume a population of $\sim$ 100 Myr, a younger population with the same observed flux has a higher inferred SFR. The best-fitting age for this object, where the three SFR indicators intersect, is in good agreement with the SED-derived age of log(age)$\sim$ 7.2.

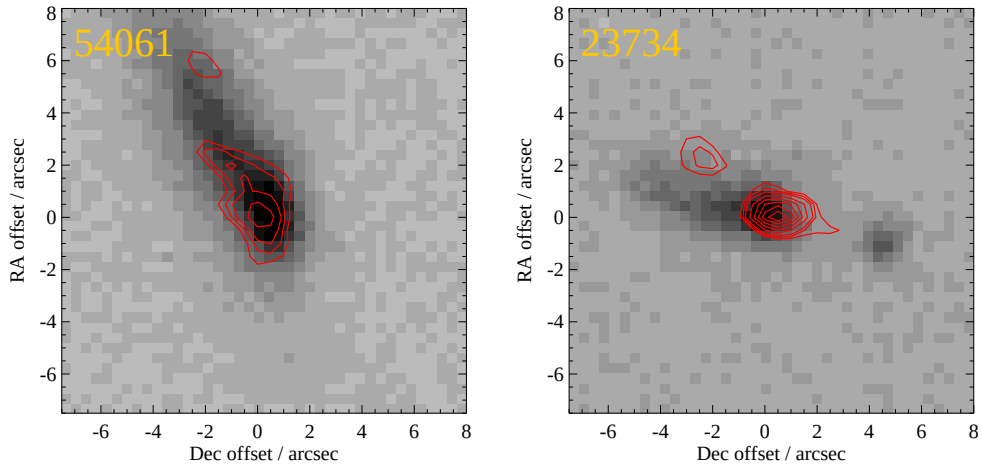

Figure 3.11: Radio contour plots overplotted on SDSS detections for the most extended optical sources in our sample. The contour levels are indicated at 2, 2.5, 3, 4, and 5σ.

luminosity of local galaxies. They interpret this as indicative of a leaky box model but note that this may conflict with their observed FIR-radio relation. A large thermal component may help reconcile this tension [Davies et al., 2017].

Spatially resolved morphological studies may provide insights into outflow structures and geometry. Such imaging, or resolved spectroscopy, of our sources would shed further light on the question of outflows, particularly by probing for an excess of ionized gas along the galaxy's minor axis (along which outflows may be more likely to escape), or broader emission line profiles (higher wind velocities) along the minor axis than the major axis. Such imaging would also provide a clear discriminator between distributed star formation occurring throughout the galaxy and a more localised event such as a nuclear starburst or any AGN contribution.

3.5 Descriptions of Individual Objects

The following provides brief descriptions of each of the 32 objects observed in VLA programmes 14A-140, 15A-134, and 16B-104, as well the five undetected APEX targets (4 of which were also observed by the VLA). The descriptions are ordered by increasing redshift of the source. Radio contours overplotted onto SDSS r-band images are shown in figures 3.11, 3.12 and 3.13.

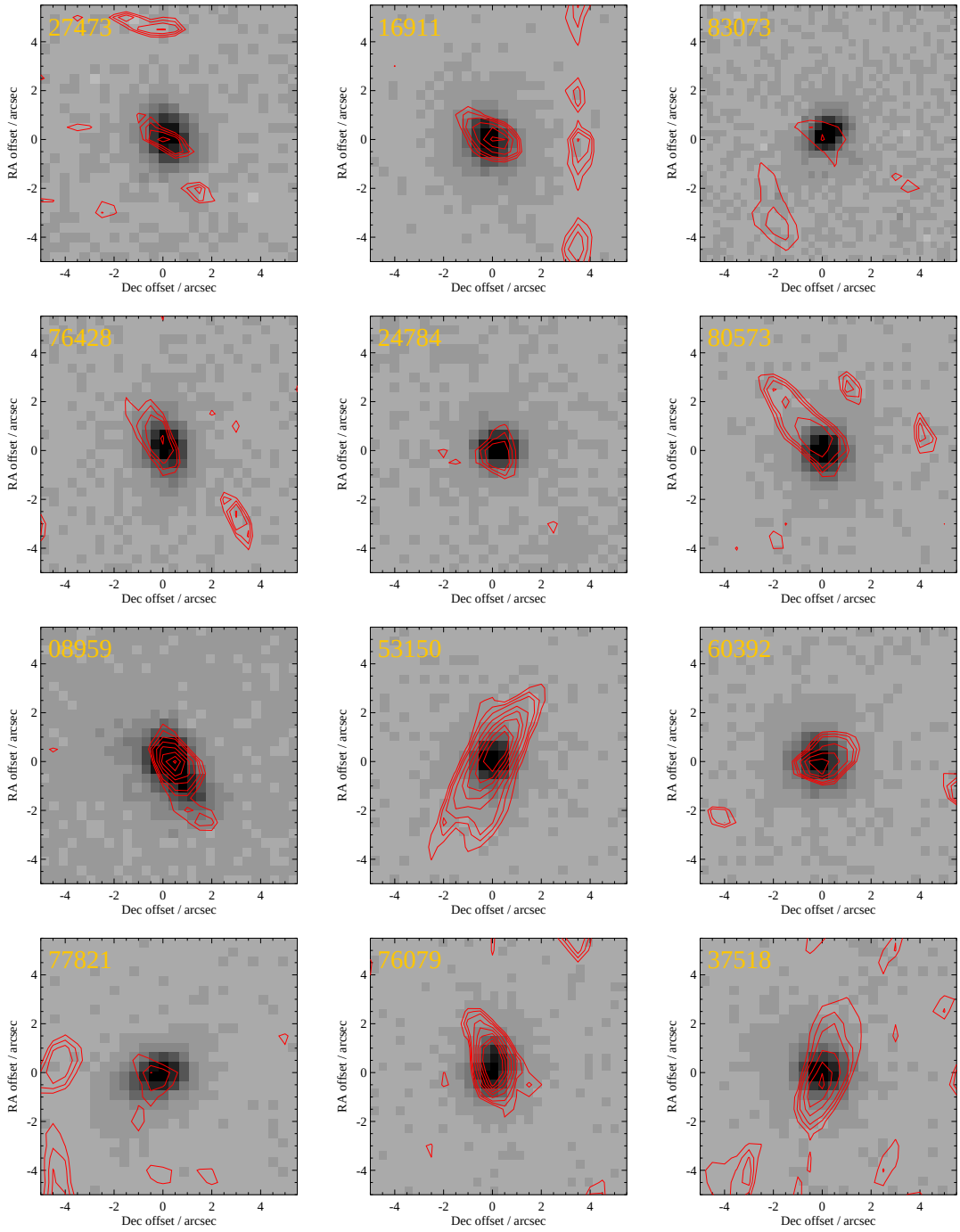

Figure 3.12: Radio contour plots overplotted on SDSS detections for objects with $0.08 < z < 0.18$. The contour levels are indicated at 2, 2.5, 3, 4, and 5σ.

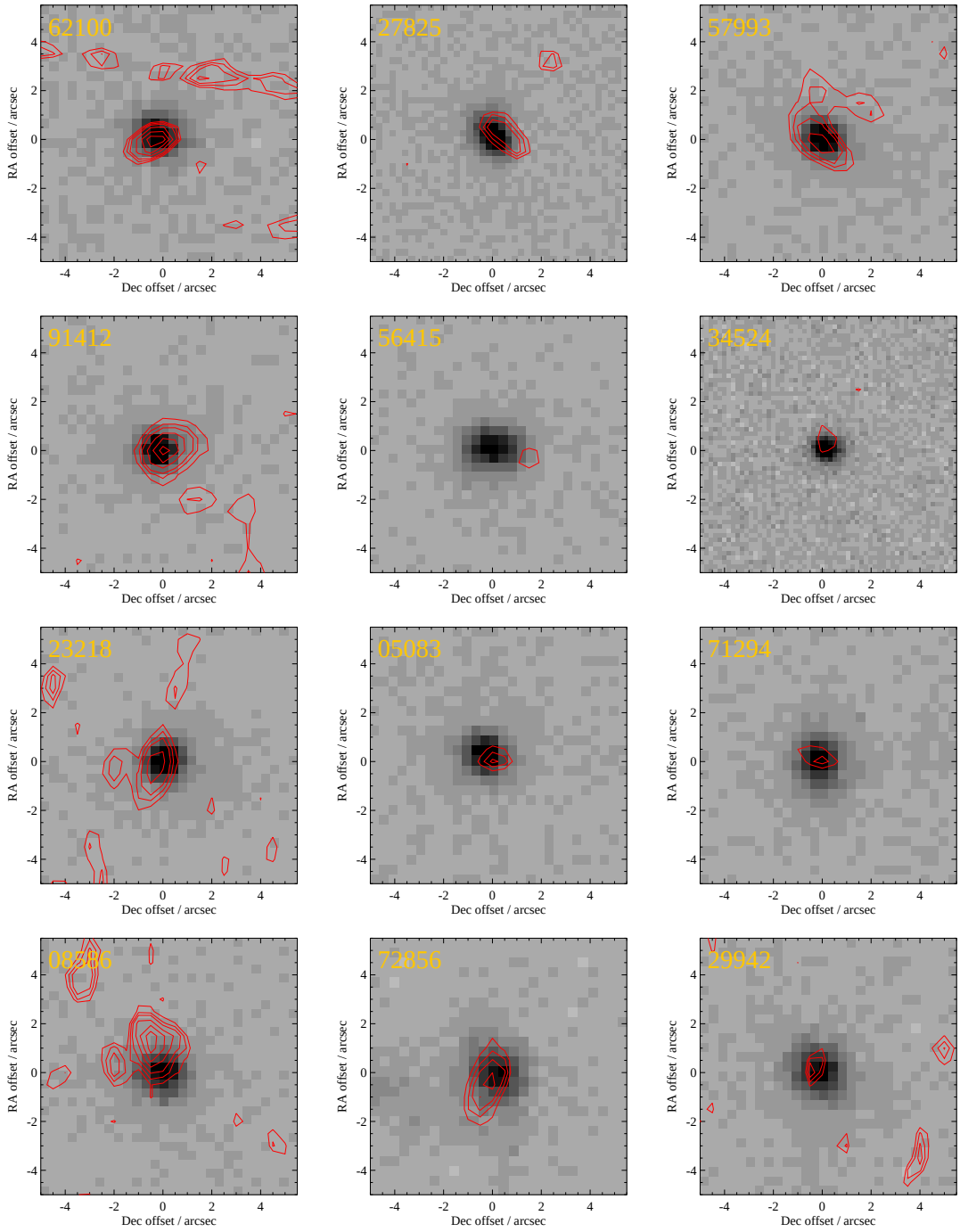

Figure 3.13: Same as 3.12 for objects with redshifts between 0.135 and 0.15. The contour levels are indicated at 2, 2.5, 3, 4, and 5σ.

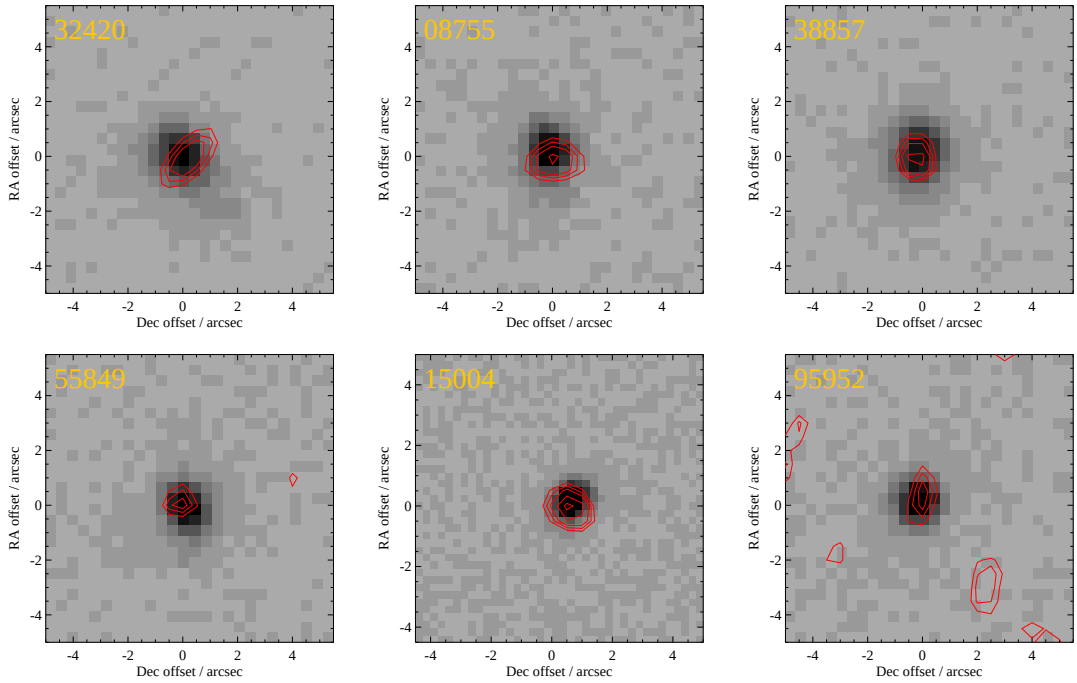

Figure 3.14: Same as 3.12 for objects with redshifts between 0.16 and 0.2. The contour levels are indicated at 2, 2.5, 3, 4, and 5σ.

Object 54061 is the most nearby object with $z = 0.074$ and the least massive of our radio sample with $\log(M/M_\odot) \sim 8.0$ from SED fitting. Additionally, it is among the youngest objects in this sample with a best-fitting age of $\sim$ 16 Myr and has a metallicity of 0.23 $Z_\odot$. These physical properties make it a good local analogue to high-redshift LBGs. It is the only source in our large LBA sample which is identified in FIRST radio source catalogue with an integrated flux of 570 μJy at 1.4 GHz (compared to our measurements of 470 ± 70 μJy). SDSS g-band imaging shows an elongated structure which is well traced by the radio contours (see figure 3.11). Having been observed by both the VLA and ATCA, its spectral slope is found to be $\alpha = -0.60 \pm 0.25$, consistent with star-formation driven synchrotron emission as well as a strong thermal component. CASA's 'imfit' routine measures an angular size of 4.12 $\times$ 1.67 arcsec (corresponding to $\sim$ 15 kpc^2). Its radio-derived SFR is 4.3 ± 0.6 $M_\odot$ yr^{-1}, resulting in a star formation rate density of 0.4 $M_\odot$ yr^{-1} kpc^{-1}. With a Σ_{SFR} above the critical value of 0.1 $M_\odot$ yr^{-1} kpc^{-1} [Heckman, 2002], it is thus likely that galaxy-wide superwinds exist in this object.

Object 27473 is both one of our most metal-poor sources with Z=0.18 $Z_\odot$, as well as one of the most dust-free objects in our radio sample with $E(B-V) = 0.05$ from Balmer decrement measurements using SDSS spectroscopy. Together with its SED-derived mass of $\log(\text{mass}/M_\odot) \sim 9.2$ and age of $\sim$500 Myr this makes this object an acceptable local analogue. It was observed by both the VLA and ATCA, with a measured radio slope of $\alpha = -0.16 \pm 0.57$. Its large measured projected size of 3.97 $\times$ 0.97 arcsec and low radio SFR of 0.8 $\pm$ 0.2 result in the lowest Σ_{SFR} of the radio sample of 0.1 $M_\odot$ yr^{-1} kpc^{-1}. However, it is worth noting that the measured sizes are upper limits, and hence the true Σ_{SFR} is likely higher than that derived here. Its radio contours coincident with its SDSS detection are shown in figure 3.12.

Object 16911 is an intriguing source and can be seen in fig. 3.12: despite fulfilling the optical and ultraviolet selection criteria, this source has by far the highest metallicity in our radio sample at 1.62 $Z_\odot$ (though it should be noted that the metallicity conversion used is unlikely to produce reliable results in such an extreme object). SED-fitting indicates a mass of $\log(\text{mass}/M_\odot) \sim 9.8$ and age of $\sim$400 Myr. These physical properties make Object 16911 an unlikely analogue to z $\sim$ 5 LBGs. It was observed by both the VLA and ATCA, producing one of the steepest of the observed radio slopes with $\alpha = -0.49 \pm 0.29$. Together with its position on the BPT diagram, this indicates the possible presence of an optically-obscured AGN.

However, while the VLA observation overall yielded a signal-to-noise ratio of 6.6, when splitting the measurement set into its three component scans, only one scan resulted in a detection with non-detections in the other two. We note that as figure 3.12 shows, this source has a nearby brighter object whose beam pattern passes close to the source. However, it does not appear to be affecting the source detection or flux measurement. Nonetheless, we conclude that the VLA detection of this source should be considered tentative.

Object 23734 was observed by both the VLA and ATCA with $> 6\sigma$ detections in both, giving rise to a radio spectral slope of α = -0.19 $\pm$ 0.21. It had previously been classified as a potential Seyfert 1 galaxy due to its strong emission lines; however, both its spectral slope and high radio star formation rate (SFR=6.0$M_\odot$ yr^{-1}), indicate a star-formation driven galaxy. Since it has one of the smallest projected areas of the sources in this sample (see figure 3.11 for its contour plot), the Σ_{SFR} determined for this source is among the highest in our sample at 3.5 $M_\odot$ yr^{-1} kpc^{-2}. Its SED-derived mass of $\log(\mathrm{mass}/M_\odot) \sim 8.3$ and young dominant stellar population (with an age of $\sim$ 16 Myr), as well as its low dust attenuation ($E(B-V) \sim 0.26$) and metallicity (0.34 $Z_\odot$) make Object 23734 a good local analogue to high-redshift LBGs. It is interesting to note that while the optical source is elongated, the radio source is spatially compact.

Object 83073 was detected at 3.2σ in our VLA observations. It is a very dust- and metal-poor galaxy with a Balmer-derived $E(B-V)$ value of 0.09, and $\sim$ 0.14 $Z_\odot$. With an SED-derived mass of $\log(M/M_\odot) \sim 9.6$, and a stellar population age of $\sim$ 600 Myr, it is an acceptable, though not ideal, local analogue. Its SDSS detection and radio contours are shown in figure 3.12.

Object 76428 was observed with the VLA, with an observed SNR of 4.5. It has a radio-derived SFR of 2 $M_\odot$ yr^{-1}, and one of the lowest Σ_{SFR} at $\sim$0.2 $M_\odot$ yr^{-1} kpc^{-2}. However, as the imfit-derived projected areas are upper limits, this Σ_{SFR} is a lower limit (its radio contours are shown in figure 3.12). As it lies above the critical value found by Heckman [2002], it is likely that the galaxy experiences strong superwinds. Using SED-fitting and spectroscopic analysis, its mass and age where found to be $\log(M/M_\odot)$ = 9.4 and 400 Myr, at half Solar metallicity. Since the Hα-derived SFR in the source is a factor of $\sim$ 4 higher, a recent starburst which has not yet had time to establish a strong radio continuum appears to be a reasonable

interpretation. These physical properties make Object 76428 an acceptable local analogue.

Object 24784 is one of two sources in this sample which were observed with VLA, ATCA, and APEX. It was detected at 4.3σ and 5.6σ in the VLA and ATCA data respectively, but undetected in APEX. Radio contours and its SDSS detection are shown in figure 3.12. The derived radio spectral slope is consistent with zero (see Table 3.6), and indicative of star-formation driven radio emission, with a stellar population that has not yet produced sufficient supernovae to establish a strong synchrotron emission spectrum. The SED physical properties derived in Greis et al. [2016] using ultraviolet to near-infrared photometry for this galaxy indicate a very young dominant stellar population at ~ 5 Myr, the youngest of our radio sources. Additionally it is also one of the most dust-free objects in our radio sample with $E(B-V) = 0.06$ from Balmer decrement. Together with an SED-found stellar mass of $\log(\text{mass}/\text{M}_\odot)\sim 8.5$, the physical properties of this source suggest that it can be considered a good local analogue to $z \sim 5$ LBGs.

Object 80573 is both one of the most massive of our radio sources with $\log(\text{M}/\text{M}_\odot)\sim 10$ from SED-fitting and one of the oldest objects with an SED-derived age of $\sim$1 Gyr. It was detected in our VLA observations with a SNR of 5.6 (see figure 3.12 for its contour plot), and is one of four objects in our sample whose radio SFR exceeds the Hα SFR at 2.7 ± 0.5 $\text{M}_\odot$ yr^{-1} and ~ 1.8 $\text{M}_\odot$ yr^{-1} respectively. This appears consistent with a massive galaxy whose dominant stellar populating is reaching an age at which a supernova-driven radio continuum has been established. It is hence unlikely that this object would make a good local analogue to $z \sim 5$ LBGs.

Object 08959 produced a 7.3σ detection in our VLA observations. It has one of the smallest projected areas derived from the radio observations, resulting in one of the highest Σ_{SFR} of our radio sample at 1.5 $\text{M}_\odot$ yr^{-1} kpc^{-2}. The radio detection is clearly coincident with the SDSS detection, as shown in figure 3.12. At an SED-derived age of $\sim$ 100 Myr and an Hα SFR of 7.6 $\text{M}_\odot$ yr^{-1} (a factor of $\sim$ 2 higher than its radio star formation rate), this source appears to show a recent starburst which has not yet established a strong radio continuum. Its stellar mass of $\log(\text{mass}/\text{M}_\odot)\sim 9.3$, very low dust content (with $E(B-V) \sim 0.11$), and very low metallicity of 0.18 $\text{Z}_\odot$ make this source a good local analogue to high-redshift LBGs.

Object 53150 was observed by the VLA, producing an 8.8σ detection with an observed radio flux indicating a SFR of ~ 3.3 $\text{M}_\odot$ yr^{-1}. With a best-fitting age of

$\sim$ 250 Myr and a stellar mass of $\log(M/M_\odot) \sim 9.3$, Object 53150 is a good local analogue to distant galaxies. It is very dust-poor with an $E(B-V)$ value of ~ 0.11 derived from Balmer-decrement measurements, and has a gas-phase metallicity of ~ 0.35 $Z_\odot$.

Object 60392 was observed by both the VLA and ATCA. SED-fitting indicates that this is both one of the most massive of our radio sources with $\log(M/M_\odot)\sim 10.3$, and the oldest one at log(age)=9.8. This suggests that it is unlikely to be a good local analogue galaxy.
Similarly to Object 16911, this source was well-detected with a SNR of 6.8 when combining all scans, but produced non-detections in two out of three scans when split into its three constituent scans. It produced the strongest radio SFR measured in our radio sample, but given the uncertainty on the reliability of the scans, this should be treated with caution. Additionally, it was not detected above 3σ in ATCA, making it difficult to put meaningful constraints on its radio spectral slope. We show its radio contours and SDSS detection in figure 3.12.

Object 77821 was observed with the VLA, producing a 6σ detection. Interestingly, it is, similarly to Object 80573, one of the most massive of our radio sources with $\log(M/M_\odot)\sim 9.9$ (from SED-fitting) while also having a higher radio SFR than that calculated from Hα, with 6.7 ± 1.1 $M_\odot$ yr^{-1} and ~ 3.9 $M_\odot$ yr^{-1} respectively. Given its SED-derived age of $\sim$ 250 Myr, this suggests that Object 77821 did not recently undergo a starburst, and might in fact have an established supernova-driven continuum. In addition, its high mass makes it a questionable LBA candidate. Its radio contours, coincident with SDSS detection, are shown in figure 3.12.

Object 76079 produced one of the highest signal-to-noise ratio of our VLA observations, with an 11.3σ detection (see figure 3.12 for its contour plot). CASA's 'imfit' procedure was able to deconvolve the source from the beam, measuring an angular size of $(2.11 \pm 0.45) \times (0.48 \pm 0.45)$ arcsec^2. SED-fitting indicates that the source has a dominant stellar population aged $\sim$ 400 Myr and a stellar mass of $\log(M/M_\odot)\sim 9.7$, making Object 76079 an acceptable local analogue galaxy. It is both dust- and metal-poor with an $E(B-V)$ value of ~ 0.15 derived from Balmer-decrement measures, and a metallicity $\sim 0.22 Z_\odot$.

Object 37518 was detected at $\sim 5.8\sigma$ in our VLA observations. The 'imfit' procedure was able to deconvolve the source from the beam, indicating an angular

size of $(3.41 \pm 1.6) \times (0.99 \pm 0.87)$ arcsec^2 (its radio contours and SDSS detection are shown in figure 3.12). At an age of ~ 630 Myr, this object is one of the oldest of our sample. This might explain why we find good agreement between the derived radio SFR of 2.40 ± 0.41 M$_\odot$ yr^{-1} and its Hα-derived SFR of ~ 2.7 M$_\odot$ yr^{-1}. Both its old age and high stellar mass of log(M/M$_\odot$)~ 9.8 make this galaxy an unlikely local analogue.

Object 62100 was observed with the VLA, producing a 4σ detection, and with ATCA, where it was marginally detected at 2.4σ. The resulting radio spectral slope of 0.90 ± 0.53 is an outlier in our sample, and should be considered tentative given the low SNR in the ATCA observations. With an SED-derived age of ~ 20 Myr, a stellar mass of log(M/M$_\odot$)~ 8.7, and a gas-phase metallicity of 0.09 Z$_\odot$, this is a good analogue to $z > 5$ LBGs. We find that it has a relatively low 1.5 GHz SFR of ~ 0.7 M$_\odot$ yr^{-1}; however, this does not take into account that the standard SFR calibrators assume a stable stellar population of > 100 Myr, making it likely that the true SFR within Object 62100 is substantially higher. Its radio detection is coincident with SDSS observations, and a contour plot of the source is shown in figure 3.13. We note that a beam residual from a neighbouring source passes close to the object and appears in figure 3.13, but does not affect its flux measurement.

Object 27825 was observed with the VLA with a 4.4σ detection (see figure 3.13 for its contour plot). At log(M/M$_\odot$)$\sim$9.8 and a dominant stellar population age of ~ 500 Myr (both from SED-fitting) it is both one of the most massive and oldest galaxies of our radio sources, making it unlikely to be a very good local analogue to the earliest galaxies, but a reasonable one for the $z \sim 3$ galaxy population.

Object 57993 was detected at 4.7σ in our VLA observations. CASA's 'imfit' procedure was able to deconvolve the source from the beam and derived one of the largest angular sizes in our sample, $(4.4 \pm 1.3) \times (3.3 \pm 1.2)$ arcsec^2, for it (see figure 3.13). With an SED-derived stellar mass of log(M/M$_\odot$)~ 9.7 and stellar population age of ~ 300 Myr, Object 57993 is a good local analogue galaxy. It has little dust extinction ($E(B-V) \sim 0.13$), and a metallicity of ~ 0.40Z$_\odot$.

Object 91412 was observed by the VLA and detected at 6σ. It is clearly coincident with its SDSS detection, as shown in figure 3.13. With a best-fitting stellar population age of ~ 200 Myr, and a stellar mass of log(M/M$_\odot$) ~ 9.6, this source is an acceptable local analogue to the earliest galaxies. It is a very metal- and dust-poor

galaxy with a gas-phase metallicity of ~ 0.24 $Z_\odot$ and a Balmer-decrement derived dust extinction of $E(B-V) \sim 0.05$. With a radio-inferred SFR of 4.96 ± 0.82 $M_\odot$ yr^{-1} and Hα inferred SFR a factor of ~ 2 higher, it is plausible that the deficit in radio flux in this source is due to its young stellar age.

Object 56415 was undetected in our VLA observations, putting an upper limit of < 5.5 $M_\odot$ yr^{-1} on its SFR. We show its SDSS detection in figure 3.13. At a dominant stellar population age of ~ 500 Myr and an SED-derived stellar mass of $\log(M/M_\odot) \sim 9.7$, this object would be an outlier of the typical $z \sim 5$ LBG population.

Object 34524 is one of the oldest and most massive sources in our sample with an SED-derived stellar population age of ~ 800 Myr and a mass of $\log(M/M_\odot) \sim 9.9$. This object would hence be an extreme outlier of the $z \sim 5$ LBG population, but might make a good analogue to the more nearby $z \sim 2-3$ galaxy population. The source is not detected above a 3σ limit in our VLA observations, indicating an upper 1.5 GHz radio SFR of < 2.5 $M_\odot$ yr^{-1}. Its SDSS detection is shown in figure 3.13.

Object 23218 was detected at 5σ in VLA observations. At $(3.6 \pm 1.1) \times (3.2 \pm 1.3)$ $arcsec^2$, its deconvolved angular size (according to CASA's 'imfit' procedure; see figure 3.13 for a contour plot) is one of the largest in the sample. Together with a radio-derived SFR of ~ 3.2 $M_\odot$ yr^{-1}, this indicates a low Σ_{SFR} of ~ 0.06 $M_\odot$ yr^{-1} kpc^{-2} for this source. Its SED-derived mass of $\log(M/M_\odot) \sim 9.9$, and stellar population age of > 600 Myr make Object 23218 an extreme object compared to the typical $z \sim 5$ LBG population.

Object 05083 is the second of our sources which was observed by VLA, ATCA, and APEX. It is one of the most massive and oldest of our radio sources with $\log(M/M_\odot) \sim 9.9$ and an age of ~ 500 Myr. It has low dust reddening with an $E(B-V)$ value derived from the Balmer decrement of 0.12, and a low metallicity of 0.34 $Z_\odot$, making it a potentially acceptable local analogue. It was observed, but not detected, using APEX, with a total observing time of 1.2 hours and an rms of 3.9 μJy. Interestingly, however, it was detected in both VLA and ATCA observations with a signal-to-noise ratio of 4.1, 3.4 and 2.5 at 1.5 GHz, 5.5 GHz and 9 GHz respectively. From these measurements, the spectral slope between 1.5 and 5.5 GHz could be constrained to be -0.52 ± 0.42. Together with its inferred 1.5 GHz star formation rate of ~ 6.1 $M_\odot$ yr^{-1}, this supports the interpretation of

this source as a recent starburst. Its radio detection is clearly coincident with its SDSS observation, as shown in figure 3.13.

Object 71294 was observed by both the VLA and ATCA, with detections in both bands, allowing us to constrain its radio spectral slope to -0.6 ± 0.42. This is consistent with a radio spectrum arising from thermal emission, as well as synchrotron radiation due to a recent starburst. This interpretation is given further support by the object's SED-derived age of $\sim$ 50 Myr. Being one of our most metal-poor objects in our radio sample with Z = 0.16 $Z_\odot$ makes this a good analogue galaxy to the distant LBG population. Its radio contours and SDSS detection are shown in figure 3.13.

Object 08586 was observed with the VLA, producing a 5.6σ detection and indicating a radio SFR of $\sim$ 2.7 $M_\odot$ yr^{-1}. CASA's 'imfit' procedure was able to deconvolve the object from the beam (see figure 3.13), determining an angular size of $(2.17 \pm 0.72) \times (1.74 \pm 0.9)$ $arcsec^2$. However, with an SED-derived stellar mass of $\log(M/M_\odot) \sim 9.9$, and a best-fitting stellar population age of $\sim$ 500 Myr, this source is likely to constitute an outlier of the typical $z \sim 5$ LBG sample.

Object 72856 is one of the most dust-poor objects in our radio sample with $E(B-V) = 0.09$ from Balmer decrement measurements. Its SED-derived age of 100 Myr, stellar mass of $\log(M/M_\odot)\sim9.4$, and metallicity of 0.24 $Z_\odot$ make it an acceptable LBA candidate. Both APEX and VLA observations of this source resulted in non-detections, producing an upper 1.5 GHz SFR limit of $< 2.4 M_\odot$ yr^{-1}. Figure 3.13 shows its radio contours overplotted on its SDSS detection.

Object 29942 is a relatively massive source in our sample with an SED-derived stellar mass of $\log(M/M_\odot)\sim9.7$. It is also among the older sources in this sample (with an SED-derived age of 500 Myr), making it an unlikely local analogue. It was undetected in VLA observations, producing an upper 1.5 GHz SFR limit of $< 2 M_\odot$ yr^{-1} (see figure 3.13 for a contour plot of this source).

Object 32420 is both one of the most massive of our radio sources with $\log(M/M_\odot)\sim10.2$ found using SED-fitting, and the most highly star forming galaxy in our radio sample with Hα SFR = $41.1 M_\odot$ yr^{-1}. Its stellar population age of $\sim$ 500 Myr, together with its other physical properties, makes it an unlikely LBA candidate. The galaxy was observed with both APEX and the VLA, resulting in a non-detection at 345 GHz,

but a 5σ detection at 1.5 GHz (see figure 3.14 for its radio contours and SDSS detection). Its 1.5 GHz flux indicates a SFR of 11.0 ± 2.2 $M_\odot$ yr^{-1}.

Object 08755 is our most distant source observed with both the VLA and ATCA, producing strong ($> 7\sigma$) detections in both (see figure 3.14 for its radio contours). From this, a radio spectral slope of -0.36 ± 0.20 could be determined. With a stellar mass of $\log(M/M_\odot) \sim 9.7$ and a dominant stellar population age of ~ 125 Myr, this source is an acceptable local analogue to the distant galaxy population. Its strong VLA-detected flux resulted in Object 08755 having the highest SFR of the sources in our radio sample.

Object 38857 was detected in our VLA observations, with one of the highest inferred radio SFRs (of 12.0 ± 1.8 $M_\odot$ yr^{-1}). Its stellar mass of $\log(M/M_\odot) \sim 9.7$, SED-derived age of ~ 100 Myr, low dust obscuration and ~ 0.28 $Z_\odot$ make this source an acceptable analogue to the distant galaxy population. It is clearly coincident with its SDSS detection, as shown in figure 3.14.

Object 55849 was not detected above the noise level in our VLA observations, producing an upper limit on the SFR within it of < 5.8 $M_\odot$ yr^{-1}. With a stellar mass of $\log(M/M_\odot) \sim 9.7$ and a stellar population age of ~ 250 Myr, this is an unlikely analogue to $z \sim 5$ LBGs. See figure 3.14 for its SDSS detection.

Object 15004 produced a very strong detection of 11σ in our VLA observations. In both Hα and radio, it is among the most star forming of our detected radio sources. We note that this source had been suggested to be a Seyfert 1 on SIMBAD due to its strong emission lines. Its stellar mass of $\log(M/M_\odot) \sim 9.6$ and population age of ~ 200 Myr make this a plausible local analogue galaxy with low dust ($E(B-V) = 0.15$) and metallicity (0.26 $Z_\odot$). Figure 3.14 shows the radio contours overplotted on the SDSS image. Both show a compact source with an upper limit on the projected area of 1.4×1.09 arcsec^2.

Object 92239 is one of our most metal-poor and dust-poor of our radio objects with $Z = 0.17_\odot$ and $E(B-V) = 0.04$ respectively, while also being one of the most massive of our radio sources with $\log(M/M_\odot) \sim 9.8$ as found from SED-fitting. Its dominant stellar population age of ~ 300 Myr, in conjunction with its high mass, makes this an unlikely local analogue for high-redshift LBGs. The source was observed, but not detected, using APEX.

Object 95952 is the most distant of our radio objects at z=0.198. It was detected, though not resolved, at $\sim 3\sigma$ in our VLA observations (see figure 3.14 for its SDSS detection and radio contours). Its SED-derived age of 150 Myr, stellar mass of $\log(M/M_\odot)\sim 9.6$, and ~ 0.4 $Z_\odot$ make it an acceptable local analogue. It has an above-average Hα SFR of 10.4 $M_\odot$ yr^{-1}, and a radio SFR of ~ 3.3 $M_\odot$ yr^{-1}. The dust extinction calculated from SDSS spectroscopy indicates a low extinction with $E(B-V) = 0.10$ from Balmer decrement measurements.

3.6 Summary and Conclusions

In this chapter I have presented the results of the analysis of radio and sub-millimetre observations of a sample of local analogues to $z \sim 5$ Lyman break galaxies, taken with the VLA at 1.5 GHz and LABOCA on APEX at 870 μm. The observed sources span the range of physical properties of the larger Lyman break analogue sample described in chapter 2 [and published in Greis et al., 2016] and can therefore be considered as representative of it. Out of 32 objects observed with the VLA, 27 were detected with a signal-to-noise ratio of at least 3 (when taking into account all three scans combined), while none of the 5 APEX observations yielded detections. The size measurements of the radio sources are improved, and hence star formation rate and stellar mass density within the sources are better constrained. The main results in this chapter are:

- There does not appear to be any strongly dust obscured star formation in these systems, agreeing with the Balmer decrement measurements and SED-derived dust values found previously in chapter 2.
- Given the radio luminosities of the targets, $\sim$0.6 contaminating AGN sources are predicted to be in the sample of 32 sources. This is consistent with their optical line ratios and the possibility that $\sim 1-2$ of the targets may show AGN-like characteristics. The possible presence of a single AGN would strengthen our conclusion that the radio luminosity is deficient in these sources.
- The mean star formation rate derived from radio observations of galaxies in our sample is $4.8 \pm 0.7\,M_\odot\,yr^{-1}$. This compares to a mean derived from Hα line emission in the same targets of $8.2 \pm 1.3\,M_\odot\,yr^{-1}$.
- The observed low radio fluxes and spectral slopes derived (where possible) are consistent with young stellar populations that have not yet established strong supernova-driven synchrotron emission. This is in good agreement with previously derived results from SED fitting.

- A method for constraining the age of a young stellar population using star formation rate indicators which traces stars at different timescales, such as OII, Hα, and radio continuum is presented.

Using the galaxies' SED-derived masses and radio-inferred star formation rate, together with (loose) constraints on their radio-derived physical sizes, it is possible to determine lower limits on the mass- and star formation rate densities within these sources. A moderate to significant offset between our radio LBA sample and more typical local SDSS star-forming galaxies selected at the same redshifts can be seen (Fig. 3.4). The star formation rate densities of the LBAs are potentially indicative of galaxy-wide superwinds typically found in local starbursts or high-z LBGs. If high redshift galaxies mirror their local analogues, this would have interesting consequences for the chemical enrichment of the surrounding intergalactic medium. However, their relatively low ages might preclude the existence of a strong AGB population which could drive such winds. Hence it is unclear whether such superwinds actually occur in these sources. In order to better understand the impact the galaxies in our sample are having on their surroundings, spatially resolved spectroscopy would be needed.

Chapter 4

Constraining the Spatial Distribution of LBAs using AAOmega Spectroscopy

Both the initial pilot sample by Stanway & Davies [2014] as well as my extended sample presented in chapter 2 [published in Greis et al., 2016] required the sources to have SDSS spectroscopy to make it possible to accurately determine their redshifts. However, this requirement also severely limited the candidate sample size. It would thus be desirable to be able to select LBAs via photometry alone. Additionally, it is plausible that the SDSS-selected spectroscopic sample (whose selection is described in chapter 2) introduces biases in its selection relative to a purely photometrically selected sample (e.g. since the SDSS DR7 spectroscopic survey predominantly targeted bright galaxies with r-band magnitudes < 18, Luminous Red Galaxies, and Quasars). In this chapter I present the justification, setup and results of spectroscopic observations of ~ 210 photometrically-selected Lyman break analogue candidates in order to determine how well such a selection reproduces spectroscopic samples, as well as to determine the spatial density and distribution of LBA sources, making it possible to estimate the likelihood of observing local Lyman break analogues within a photometrically selected sample.

4.1 Introduction

The importance of reliable photometric selection criteria of local Lyman break analogue galaxies becomes apparent when considering the cost of spectroscopic observations and surveys. While a genuine local analogue to $z \sim 5$ LBGs requires

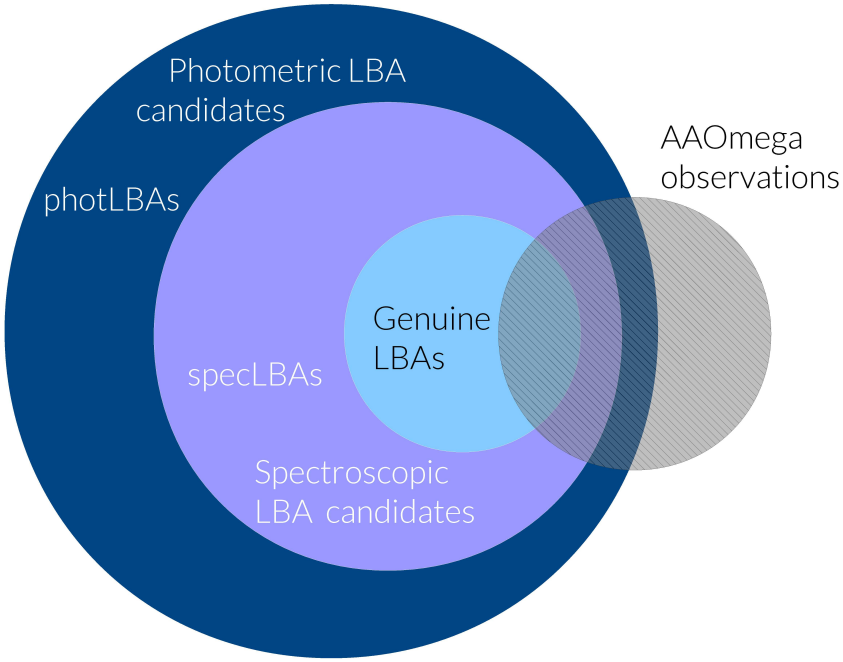

Figure 4.1: The different categories of LBA samples discussed in this chapter. The dark blue indicates the sample of objects which satisfy the photometric selection criteria (photLBAs), while the purple circle shows the subset of those which additionally fulfill the spectroscopic requirements for local analogues to $z \sim 5$ LBGs (specLBAs). A further subset of this, shown by the light blue circle, indicates the sample of genuine LBAs, which not only satisfy the photometric and spectroscopic selection criteria, but whose physical properties also make them suitable analogues to $z \sim 5$ LBGs. The fraction of spectroscopic LBA candidates which fulfill the physical requirements of genuine LBAs was explored in chapter 2. In this chapter, the fraction of spectroscopic candidates within a photometrically selected LBA sample will be explored. The hashed grey circle represents the AAOmega observations, which form the basis of this chapter. The relative sizes of the circles are not to scale.

spectroscopic confirmation of its redshift and emission-line features, as well as mass and age estimation, it should be possible to determine photometric selection criteria which maximise the probability of observing good analogues, and hence to calculate a more accurate estimate of both the spatial distribution and the global sky density of Lyman break analogues. Combining these, it should then be possible to constrain the total number of LBAs on the sky, as well as the volume which needs to be surveyed in order to find them.

Some estimates of the expected spatial density of LBAs are possible. From the analogue sample established in chapter 2 on spectral energy distribution fitting, the sky density of spectroscopically confirmed LBAs in the SDSS/*GALEX* overlap region can be found to be ~ 0.1 per square degree. Using only photometric selection criteria produces ~ 300 candidate objects within a 2-degree field, hence giving a spatial density of ~ 100 potential sources per square degree.

The different categories of LBA candidates and confirmed analogues described in this thesis are indicated in Fig. 4.1. The photometric LBA candidate sample, photLBAs (dark blue circle), fulfills only the photometric selection criteria, selecting for faint (17.5 <NUV< 23), blue, compact (projected radius < 4 arcsec, in order to include all sources with a physical size of ~ 3.5 kpc at the lowest LBA redshift of $z \sim 0.05$) objects with a steep spectral slope bluewards of NUV, such that $-0.5 <$ NUV - r ≤ 2. The spectroscopic LBA candidates sample, specLBAs (purple circle), is the subsample of photometric LBA candidates which are categorised as star formation-dominated emission-line galaxies in the appropriate redshift range of $0.05 \leq z \leq 0.25$, whose far-UV absolute magnitude is such that $M_{FUV} < -16.5$. The genuine LBA population (light blue circle) fulfills both the photometric and spectroscopic criteria, and has, additionally, been confirmed to have physical properties, such as mass, age, dust, metallicity and star formation rate, comparable to those found in the distant galaxy population. In chapter 2, I estimated that $\sim 45 - 70\%$ of spectroscopically selected LBA candidates are, indeed, genuine local analogues to $z \sim 5$ Lyman break galaxies, depending on the age and mass cuts made. In this chapter, I am attempting to answer the question of what fraction of photometric LBA candidates also satisfy the spectroscopic constraints, making it possible to estimate the sky distribution and total number density of local analogues to $z \sim 5$ LBGs (N_{LBA}):

$$N_{LBA} = N_{phot} \times f_{spec} \times f_{phys}/area$$

where N_{phot} is the number of objects which satisfy the photometric criteria, f_{spec} is the fraction of those which fulfill the spectroscopic requirements, and f_{phys} indicates the fraction which additionally reproduces physical characteristics plausible for $z \sim 5$ LBGs in a given area.

4.1.1 Overview of Chapter

The remainder of this chapter will be structured in the following way: first, I will present the photometric sample selection and AAOmega observational setup in section 4.2, before providing an outline of the reduction and preliminary analysis of the resulting spectra (section 4.3). Following this, I will present the results of this analysis. In particular, the question of how many photLBAs were observed will be answered in section 4.4, and more general results will be shown in section 4.5. Section 4.6 will explore how many specLBAs are present within the photometrically selected LBA sample. I will comment on potential contaminants in section 4.7. This is followed by a discussion of sources categorised as 'unknowns', whose types and

redshifts could not be confirmed. In section 4.9, the crucial question of how well LBA galaxies can be selected using photometric selection criteria only will also be discussed. Finally, I will present and summarise the conclusions of this analysis in section 4.10.

4.2 AAOmega Observations

4.2.1 Scientific Rationale

The primary goal of this investigation is to determine the reliability of the selection criteria used to characterise local Lyman break analogues by photometrically selecting a sample of suitable sources and obtaining spectroscopy for them. This makes it possible to not only determine which criteria are most relevant, but also to determine the spatial density and distribution of local analogues to $z \sim 5$ Lyman break galaxies. Further, this investigation seeks to overcome potential flaws in the follow-up classification of SDSS selection. Due to the sparse spatial density of spectroscopic LBA candidates and the high density of photometric candidates, a highly multiplexed spectrograph is needed to provide a statistically meaningful sample of observations.

4.2.2 Observational Setup

The observations were carried out July 2014 with the AAOmega spectrograph in programme AO181 (PI: Stanway) 'Finding Better Analogues for Galaxies in the Distant Universe'. The time on source was $(2100 + 2100 + 1800 =)6000$ seconds, or 100 minutes. The observations were taken in service mode.

The AAOmega Spectrograph is a dual-beam system, consisting of a blue and a red arm and spanning the spectral range between $3700 - 8500$Å , see Fig. 4.2. The observations presented in this chapter made use of the 580V (for the blue arm) and 385R grating (for the red arm), centred at 4800Å and 7250Å and with resolving power R= 1300 for both gratings, corresponding to central wavelength resolutions of $\Delta\lambda = 4$Å and 6Å respectively. Hence, velocity dispersions above ~ 230 km/s could be resolved. The gratings provide a dispersion of 0.1 and 0.16 nm/pix respectively.

The Two Degree Field system, also known as '2dF', is designed to simultaneously acquire 392 spectra of objects anywhere within a two degree diameter field on the sky. Of these 392 spectra, between 20 and 30 need to be allocated to blank regions of the sky and act as sky fibres to be used in sky subtraction. In addition to

Observed Field	Intent	Duration [s]
Quartz 75A	Flat	10
Quartz 20	Flat	3
CuAr, FeAr, He, Ne	Arc	45
LBA	science	2100
LBA	science	2100
LBA	science	1805
LTT 1020	Flux	50
LTT 1020	Flux	150

Table 4.1: Structure of the AAOmega observations.

the 392 fibres, 8 additional fibres are used as guide fibres which observe guide stars. These not only guide the telescope but also determine the field plate rotation and set the relative positions of the science fibres on the sky. Each of the 400 fibres used has a diameter of 0.14mm, corresponding to 2.1 arcseconds on the sky. To place the fibres on the plate, the 2dF fibre positioner, a multi-object fibre-feed to the spectrograph is used. Due to the large field of view of the 2dF, it is very sensitive to atmospheric effects. The system therefore includes an atmospheric dispersion corrector, as well as a wide-field corrector. A robotic arm positions optical fibres to within 0.3 arcseconds on the sky. Due to the shape and size of the fibres, the typical minimum separation between fibres is $\sim$ 2mm, corresponding to 30 - 40 arcseconds. The structure of the observations is shown in table 4.1, including the flat fields, arc lamp observations and flux calibrations needed to reduce the data.

The lines targeted in these observations are primarily the strong emission lines seen in star-forming systems, such as [O II] $\lambda\lambda$3727, 3729, Hβ λ4863, [O III] $\lambda\lambda 4959, 5007$, [NII]$\lambda 6549, 6583$, and H$\alpha$ λ6564. By determining the presence or absence, as well as velocity dispersion, of these lines, it should be possible to distinguish potential specLBAs from contaminating sources, such as broad- or narrow-line AGN, or white dwarves. Given the observed spectral range (up to 8500 Å), and assuming no significant losses in the red part of the spectrum, it would be possible to detect the Hα line to redshifts up $z \sim 0.3$, [O III] up to $z \sim 0.7$, Hβ up to $z \sim 0.75$, and [O II] up to $z \sim 1.3$ (though for an unambiguous redshift measurement, at least two lines should be well-detected).

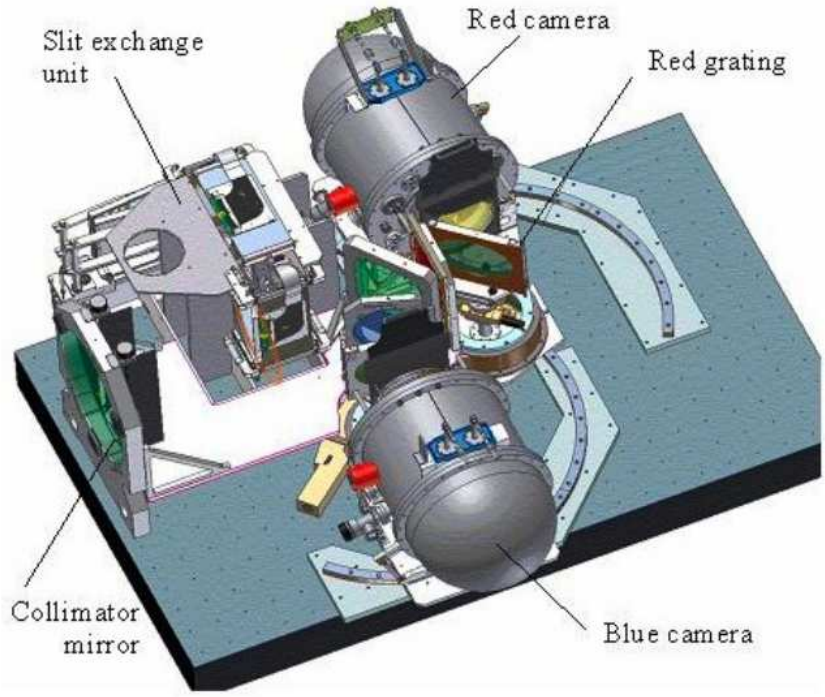

Figure 4.2: Layout of the AAOmega spectrograph used for the observations described in this chapter. Image from the 2dF-AAOmega Manual.https://www.aao.gov.au/get/document/2dF-AAOmega-obs-manual.pdf

4.2.3 Photometric Sample Selection for AAOmega Observations

The target field was chosen such that it was far enough South to be easily observable by the AAOmega spectrograph. Additionally, parts of the field had already been observed in the radio by ATCA, and is one of the fields which both contained a $z \sim 0.08$ LBA and showed a slight excess of radio sources relative to the background. A catalogue of target objects, providing data for the fibre placement algorithm, was submitted to the AAOmega spectrograph. The fibre placement algorithm modified both the target selection and field centre. Hence, potential targets were selected to lie within a one degree radius around two known LBA candidates, Obj27473 and Obj60392. In order to optimise fibre placement, a surplus of possible sources was submitted to the spectrograph. Not all of these targets were observed. Additional fibres were assigned to objects for which SDSS spectroscopy exists in order to serve as checks for wavelength and flux calibration. In order to quantify the spatial density and distribution of Lyman break analogue galaxies, this sample of photLBA objects will form the bulk of the analysis presented here. All photometric LBA candidate sources were required to have $17.5 < NUV < 23$ and $-0.5 < (FUV - NUV) < 0.5$, where NUV and FUV are the *GALEX* near- and far-ultraviolet filter bands centred at 2300Å and 1500Å respectively. Furthermore, the uncertainty on the NUV magnitude was restricted to be below ~ 0.36, in order to ensure a $\sim 3\sigma$ detection in that band. These selection criteria are identical to those used to select the pilot [Stanway & Davies, 2014] and Greis et al. [2016] samples, however without any spectroscopic classification or redshift indications. Using SDSS photometric measurements, the closest match between the SDSS and *GALEX* coordinates was chosen (since some *GALEX* sources produced more than one match in SDSS due to the larger beam size of the ultraviolet surveys). In order to mimic the compactness of distant Lyman break galaxies, the observed u-band radius was required to be < 4 arcseconds, and both the u- and g-band radii were restricted to be positive, i.e. to have meaningful measurements. All targets had to lie within 1.1 degree of the centre of the projected field-of-view at ra = 336.822 and dec = −9.089. Finally, the targets were given observational priorities in accordance with their ultraviolet-optical colours, such that the highest priority was given to sources with $-0.5 < NUV - r \leq 2$, and a lower priority to targets with $NUV - r \leq -0.5$. These selection criteria resulted in 305 photLBAs that were submitted to the AAOmega spectrograph.

While all photometric targets were selected to reproduce the Lyman break galaxy properties seen in the distant population, several potential contaminant sources are likely to be present in such a sample. In the initial LBA sample selection

described in chapter 2, many of the SDSS sources had originally been photometrically classified as QSOs due to their line strengths and ratios, indicating the similar colours between LBG analogues and this kind of contaminant, and raising the question of how well SDSS targets and classifies the types of objects constituting the Lyman break analogue population. An example of a QSO spectrum is shown in Fig. 4.3. White dwarves are another likely contaminant population in a photometrically selected Lyman break analogues sample due to their faintness and blue colour. A typical white dwarf spectrum is shown in Fig. 4.4. They are characterised by Balmer absorption lines in the blackbody spectrum, which are gravitationally broadened. The spectrum of a genuine LBA is characterised by its strong narrow emission lines, indicative of ongoing star formation. An example is shown in Fig. 4.5. All of these potential sources have similar colours because they have high temperature blackbody spectra (∼few $\times 10^4$ K). Their physical environments, however, are different, and need to be distinguished in order to correctly identify LBA candidates. A characteristic feature of AGN spectra is the presence of both high and low excitation emission lines, which can be either broad (with FWHM between 1500 - 30000 km/s) or narrow (FWHM $<$ 900km/s). Both broad-line AGN and narrow-line AGN exhibit similar line ratios, indicating that the physical conditions in the gas from which the lines are emitted are similar, and making it possible to define the parameter space into which AGN fall on the BPT diagram [Baldwin et al., 1981]. As mentioned in previous chapters, the ionization parameter in star-forming HII regions, in contrast, is less extreme, producing lower line ratios, and hence placing star-forming galaxies in a different region of the BPT diagram.

4.3 Reduction and Preliminary Analysis

Before a preliminary analysis of the data could be undertaken, I reduced the observations with the 2dfdr data reduction software[1], AAO's data reduction package for fibre-based spectrographs.

4.3.1 2dfdr Software

The reduction software requires at least three basic files to reduce AAOmega data:

- a multi-fibre flat field exposure, made using a quartz lamp. This provides a uniform spectrum which is used to flat-field the spectral response;

[1] 2dfdr data reduction software: https://www.aao.gov.au/science/software/2dfdr; see also Part IV of the 2dF-AAOmega Manual

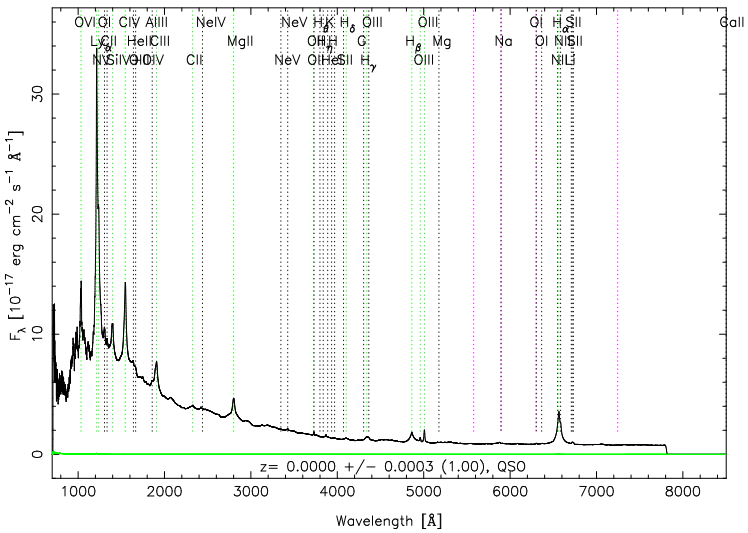

Figure 4.3: Example of a QSO spectrum; from SDSS spectroscopic templates #30 `http://classic.sdss.org/dr5/algorithms/spectemplates/`.

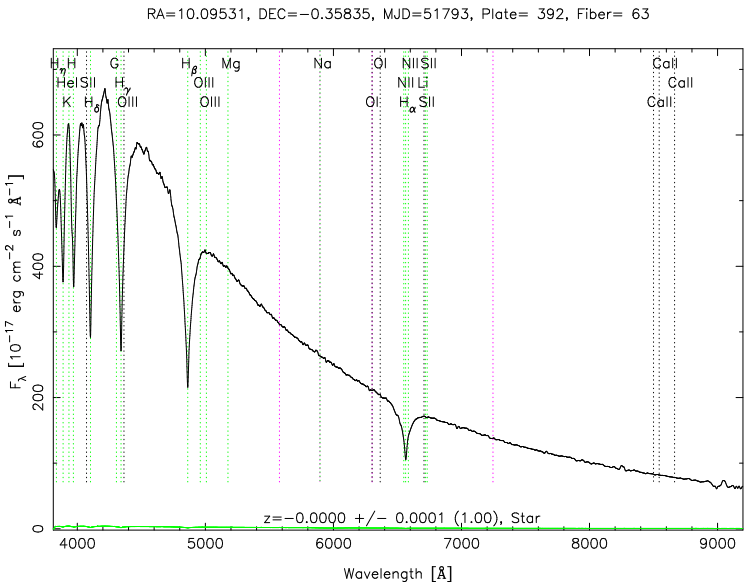

Figure 4.4: Example of a white dwarf spectrum; from SDSS spectroscopic templates #21 `http://classic.sdss.org/dr5/algorithms/spectemplates/`.

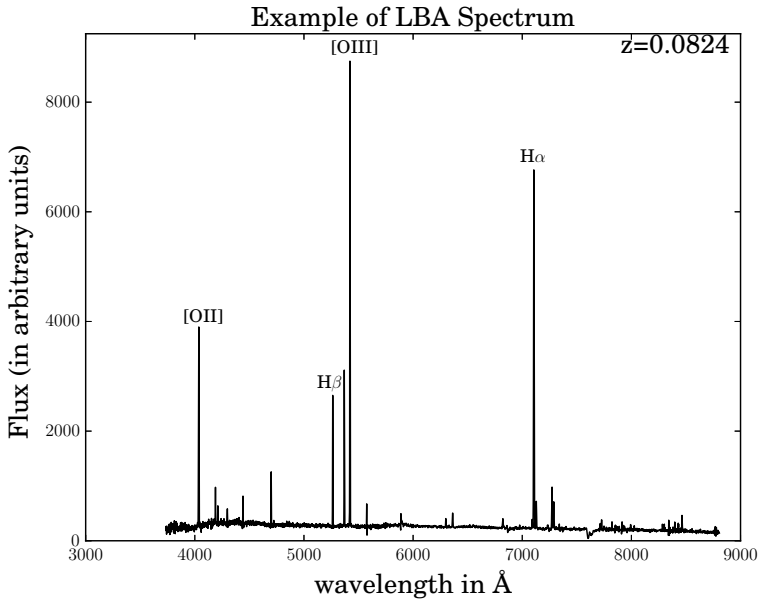

Figure 4.5: Example of a confirmed LBA spectrum.

- an arc exposure. For the observations described here the FeAr1, FeAr2, CuAr1, CuAr2, CuHe and CuNe arc lamps were used, whose various emission lines are well known and which can thus be used to calibrate the observed wavelengths and dispersion;

- one or more science frames which gives the science data to be reduced. These observations are required to have been taken with the same setup as the flat and arc frames.

The standard observing sequence shown in table 4.1 produces all these required frames.

The software can be used in 'Auto Reduction' mode, in order to reduce all the data in the current working directory. The reduction process then proceeds in the following way (see p.77 of the 2dF-AAOmega Manual):

1. Reduce any and all multi-fibre field frames.

2. Reduce any and all arc frames.

3. Re-reduce the flat field frames using the accurate wavelength solution obtained from the arc frame reduction to compute a better average illumination correction.

4. Reduce any and all science frames.

5. Combine the science frames, if desired.

In order to reduce the observations presented here, wavelength and flux calibration, as well as sky subtraction were performed by 2dfdr. Additionally, the software combined the red and blue arms of the observations to create one spectrum. Since the observed spectra overlap (the 580V grating produces an effective wavelength range of 3700 - 5800 Å , while the 385R grating gives 5600 - 8800Å), it is possible to combine the spectra. This is done by first combining the data from each camera separately before splicing the spectra into one continuous spectrum (using the blue arm, in this case, to calibrate the combined pixel scale).

For each individual frame, as well as for the combined frames, the 2dfdr reduction software produced a standard multi-extension FITS file. This includes the primary image extension with 400 AAOmega spectra (392 science fibres and 8 guide fibres), a variance extension, a FITS binary table providing RA, Dec, fibre number and other information for each fibre, as well as other extensions not required for the analysis described here.

4.3.2 Preliminary Classification and Redshift Estimates

The redshift and spectral type classification of the science targets was performed using an iterative process. Following the reduction with the 2dfdr software, I initially developed code to take each observed spectrum, display it on-screen, and request user input to indicate emission lines on the spectrum. Input for the OII λ3726, OIII λ5007 and Hα λ6563 emission features was accepted. Following the user's selection, the program would calculate the corresponding redshift and display a set of appropriately redshifted vertical lines overplotted onto the spectrum in the spectral regions where the above, as well as the Hβ λ4861 and NII λ6583 lines would be expected, allowing the user to input whether an acceptable redshift fit had been achieved. Since the entire spectrum was displayed during the process, only a rough estimate of the redshift could be made using this method. This process was additionally made more complicated by the presence of strong sky line residuals in the red optical part of the spectra. Additionally, this method was only able to provide redshift estimates for strong emission line sources, and was unable to to provide meaningful outputs for absorption spectra.

4.3.3 Final Redshift and Type Catalogue

Following my initial redshift estimation, a second independent classification and redshift-fitting was performed by Dr Stanway, in which strong emission-line galaxies were separated from other types of objects present. Following this, the two resultant classification and redshift catalogues were merged and a consensus was reached for each spectrum. For strong, and hence relatively easily identifiable, emission line galaxies, the consensus redshift was used to tune a program designed to fit Gaussian line profiles. The final redshift for objects classified as emission line galaxies was thus found. Similarly, for strong QSOs, absorption line systems, and white dwarves, the redshifts were determined by their strong spectral features. For some QSO spectra, it was not possible to fit a redshift since not enough lines were present in the spectral range observed. For lower signal-to-noise objects or where no consensus could be reached, the following approach was taken: the strongest sky lines were masked in order to avoid confusion. The observed spectra were then cross-correlated with SDSS templates for white dwarfs, QSO, emission line galaxies, absorption systems, and objects with both emission and absorption features. This cross-correlation provided an approximate redshift, which was subsequently refined by fitting Gaussian line profiles. Any objects which could not be fit in this way are marked as 'unknown' types. The presence of such 'unknown' objects in the sample and its implication for any conclusions drawn is discussed further in section 4.8. It should also be noted that objects classified as QSO or WD were not investigated further in this project as they could be excluded from a potential Lyman break analogue sample.

All final redshifts and line fluxes were confirmed by Gaussian fitting. These fits selected the best-fitting spectrum (i.e. the minimum χ^2 spectral template), and no extensive probability analysis was undertaken. The line fitting code took the following form: the fibre number, redshift, and approximate line width were read in, and a template spectrum was created with Gaussian lines and a constant continuum. For both the [OII] and [SII] doublets, the line ratios were allowed to vary freely, and the lines in each doublet were fit simultaneously. There was no overlap between the [OIII] and Hβ lines, and the Hβ line was fit freely, while the [OIII] doublet was fit in the 3-to-1 ratio required by quantum mechanical effects. In some objects one of the [OIII] doublet lines was covered by a sky line, and had to be masked; however, the 3-to-1 ratio in line strength was still applied in these cases. The Hα and [NII] spectral region was fit similarly. The line strength of Hα was allowed to vary freely, while the [NII] doublet was fit with a 3-to-1 ratio. In contrast to the [OIII] and Hβ region, Hα and [NII] were fit simultaneously since the wings of the two lines were not clearly distinct for particularly broad or high-redshift lines. The width of all

lines was permitted to vary by 50% from the original estimate.

A table of the results of all science targets can be found in appendix B of this thesis.

4.3.4 Flux Calibration

An initial spectral response calibration is done by the 2dfdr software, but this does not account for absolute flux or fibre losses. Since several white dwarves (WD) had been observed, I used their spectra to flux calibrate the science targets. For this, I used the SDSS WD templates[2] as well as the observed magnitudes of the white dwarves in the *g*- and *i*-band. Using the SDSS filter profiles, I adjusted the flux scaling of the templates such as to reproduce the observed magnitudes. Dividing this adjusted spectrum by the uncalibrated one observed by the AAOmega spectrograph, it was possible to determine the fibre-corrected flux per instrument count at each wavelength, and hence to apply this correction to the other science targets by multiplying the observed fluxes (in counts) at each wavelength by the true flux per instrument count at that wavelength.

4.4 How many photLBAs were observed?

Disregarding sky and empty fibres, a total of 360 objects were observed by the AAOmega '2dF' spectrograph. Of these, 2 sources were previously identified LBAs, while 227 sources were science targets, which constitute the focus of the analysis presented in this chapter. The remainder of the observed sources are disregarded for the purposes of this chapter (but will be listed in full in appendix B).

The driving question behind this investigation is to determine the likelihood of observing genuine local analogues to $z \sim 5$ Lyman break galaxies when selecting targets based on photometry only. Table 4.2 indicates the number of good photometric candidates and their selection criteria:

In order to reproduce the UV brightness seen in distant LBGs, their local analogues have to have observed NUV magnitudes such that $17.5 < NUV < 23$. All 227 sources satisfy this condition.

In order to reproduce the spectral slope of $z \sim 5$ LBGs, the sources are required to a $NUV - r$ colour such that $-0.5 < NUV - r \leq 2$. This criterion is fulfilled by 211 science targets, with the remainder having acceptable, though not ideal, colours such that NUV-r ≤ -0.5. The uncertainty on the NUV magnitude

[2]WD templates from SDSS spectroscopic templates #21 'White dwarf (Star)' `http://classic.sdss.org/dr5/algorithms/spectemplates/`, see Fig. 4.4.

Selection Criterion	Remaining (/227)
$17.5 < NUV < 23$	227
$-0.5 < NUV - r \leq 2$	211
Radius < 4 arcsec	211

Table 4.2: Selection criteria of photometric Lyman break analogue galaxies (photLBAs), and number of observed targets satisfying the conditions. The 16 targets not satisfying the $NUV - r$ constraint can be considered acceptable, though not ideal, photLBAs.

is less than 0.36 in all sources, hence indicating that a detection of at least 3σ was achieved in this filter band.

Finally, in order to mimic the compactness of $z \sim 5$ LBGs, good photometric LBA candidates are required to have projected Petrosian radii of 4 arcsec or less. All science targets fulfill this criterion.

Hence 211 (of 227) science targets make ideal photLBAs based on their apparent NUV magnitudes, colours, and projected radii. The remainder can be considered acceptable photLBAs, as they fulfill all photometric selection criteria, but have $NUV - r$ colours of $NUV - r < -0.5$.

4.5 Results of Spectroscopy

4.5.1 What Types of Objects Were Observed?

Fitting SDSS spectroscopic templates, the majority of observed sources could be classified. This identified most targets (151 of the 227 observed spectra) as arising from emission-line galaxies. For a large fraction (46+10 of 227 targets) it was either not possible to accurately constrain the object's spectral type or they showed unreliable spectroscopy. These sources were hence categories as 'Unknown' and 'Uncertain' targets, respectively. Additionally, small fractions of white dwarves (9/227), quasars (6/227), absorption systems (3/227), and absorption-and-emission galaxies (2/227) were identified (see Fig. 4.6). The sky positions of the emission line galaxies are shown in Fig. 4.7, colour-coded by the *GALEX* survey which observed them (AIS with black points, and MIS with red squares). Reaching a 5σ limiting depth m_{AB} of 22.6 (22.7) in the FUV (NUV), the MIS survey is deeper than the AIS one, which goes down to 19.9 (20.8) in the FUV (NUV).

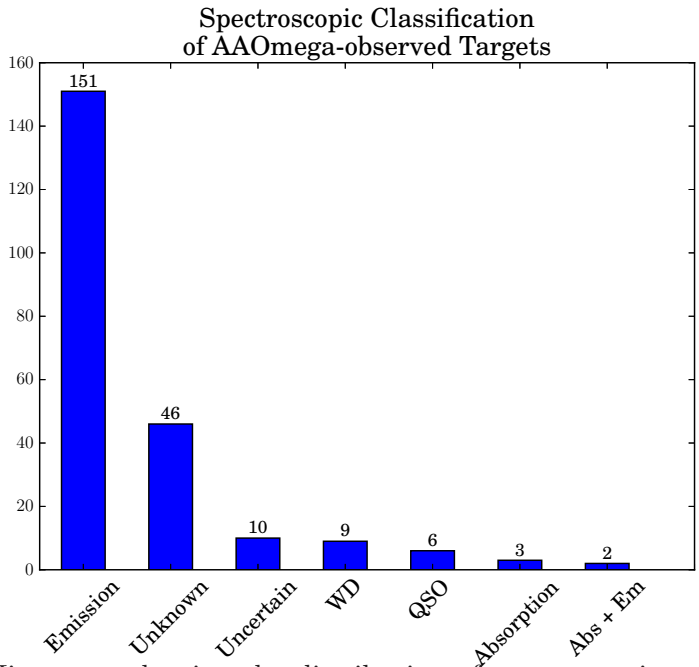

Figure 4.6: Histogram showing the distribution of spectroscopic types in the 227 observed AAOmega spectra. Emission-line galaxies constituted, by far, the largest fraction within the photometrically selected sample.

4.5.2 Redshifts

The redshifts of the observed sources could be determined for 179 (out of 227) objects, and ranged from $z = 0$ for the white dwarves to $z \sim 1.7$ for the most distant QSO. For some objects is was possible to determine their type, but not their redshift. For none of the unidentified targets ('Unknown' and 'Uncertain') could accurate redshifts be determined. Additionally, only in one of the three absorption-line systems was a redshift determination possible.

The mean, standard deviation, and range of redshifts for the different classes of objects in the AAOmega sample are shown in table 4.3. The redshift distribution of emission line galaxies is shown in Fig. 4.8.

4.5.3 Emission Line Strengths

The observed emission lines make it possible to plot the galaxies on the BPT diagram (Fig. 4.9). In addition to the emission line galaxies observed in the AAOmega observations (blue circles), the LBA sample presented in chapter 2 is indicated as black stars on the diagram. The black dashed line indicates the Kauffmann et al. [2003] line separating star-forming galaxies from AGN activity, while the solid black line shows the Kewley et al. [2001] maximal starburst line. Additionally, the red

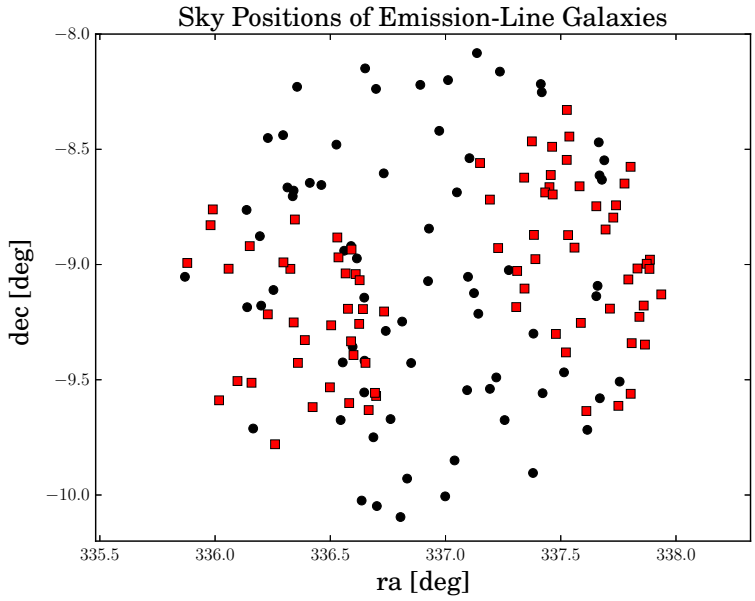

Figure 4.7: The distribution of emission line galaxies over the observed area. The targets are colour-coded by the *GALEX* survey (AIS with black points, and MIS with red squares) on which *FUV* and *NUV* measurements are based. MIS is deeper than AIS, reaching a 5σ limiting depth m_{AB} of 22.6 (22.7) in the *FUV* (*NUV*) (while AIS reaches 19.9 (20.8) in the *FUV* (*NUV*) band), and hence yields more candidate sources per unit area.

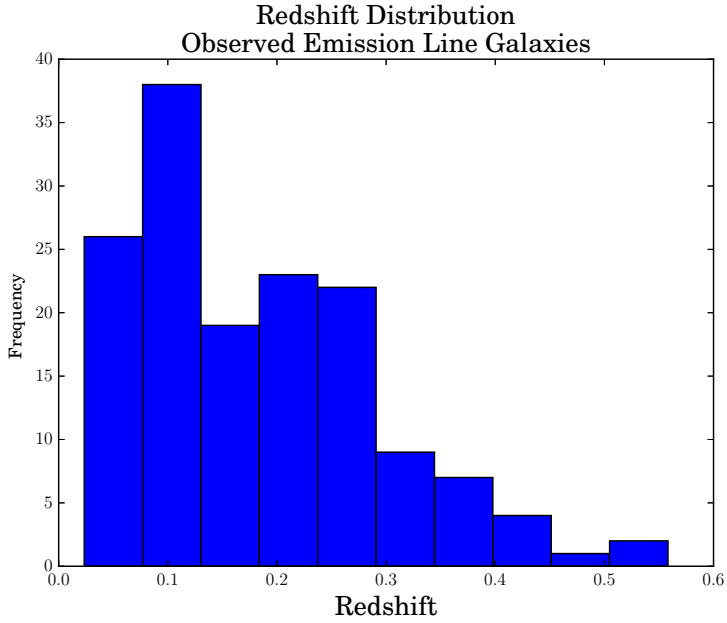

Figure 4.8: The redshift distribution of AAOmega-observed galaxies which were classified as emission line sources.

Classication	Min	Mean	σ	Max
Emission-line Galaxy	0.02	0.18	0.11	0.56
Absorption-line Galaxy†	-	0.197	-	-
Emission + Absorption	0.15	0.21	0.07	0.28
QSOs	0.18	0.93	0.48	1.66
Uncertain Sources	0.06	0.28	0.16	0.62

Table 4.3: The lowest, mean, standard deviation and highest values of the spectroscopically found redshifts for each of the types of objects observed. It should be noted that for absorption-line galaxies and the absorption-and-emission objects, this relies on very low number statistics.
†: only one of the three observed absorption-line galaxies had a reliable redshift estimate.

dotted line and the blue dash-dotted line indicate typical galaxies are $z \sim 2$ and 0 respectively [Steidel et al., 2014]. Some overlap between the sample established in chapter 2 and the AAOmega sample of emission line galaxies can be seen, suggesting that these sources are likely subject to similar physical processes within the galaxies as found within LBAs. There are, however, also many AAOmega-observed sources whose emission line ratios indicate lower ionisation parameters than found in the LBAs sources previously studied. The question thus becomes whether or not those sources which fulfill the additional spectroscopic selection criteria of LBAs also reproduce emission line strengths found within the LBA sample. This is commented on below in section 4.6.1.

The stacked spectra of all sources identified as emission-line galaxies are shown in Fig. 4.10, with redshift increasing upwards. Several strong emission lines can be clearly seen on the spectra, as well as the residuals of sky lines. An important point to note is that there is no significant loss of emission line visibilities for sources with redshifts in the $0.05 < z < 0.25$ range, suggesting that for galaxies at these redshifts (which forms one of the criteria for specLBAs) sufficient emission lines should be unobscured to determine the redshift and line strengths of these sources.

4.6 How many specLBAs were observed?

In order to determine the ratio of photometric LBA candidates to spectroscopic ones, the following selection criteria needed to be satisfied (summarised in table 4.4). Lyman break galaxies, and hence their local analogues, are emission-line galaxies whose emission is powered by recent star-formation events. Thus all observed

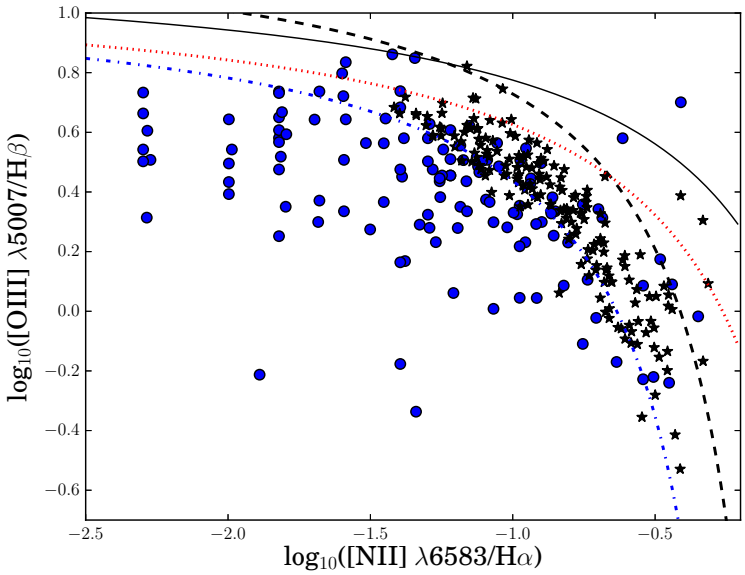

Figure 4.9: BPT diagram for those objects which were identified as emission line galaxies (blue circles), together with the confirmed LBA sample from chapter 2 (black stars). The line separating star-formation driven from AGN-driven galaxies is indicated by the black dashed line [Kauffmann et al., 2003], while the solid black line shows the maximum starburst line of Kewley et al. [2001]. The blue dash-dotted and red dashed line show the loci of typical local and $z \sim 2$ galaxies, respectively. While many emission-line galaxies observed by the AAOmega spectrograph show comparable line ratios to those found in the confirmed LBA sample of Greis et al. [2016], it can also be seen that a large fraction have significantly lower [NII]-to-Hα flux ratios than typically found in LBAs. It is worth noting, however, that all but one object identified as emission-line galaxies in the AAOmega observations fall within the potential star-formation driven region of the BPT diagram (by using the Kewley et al. [2001] maximal starburst criterion).

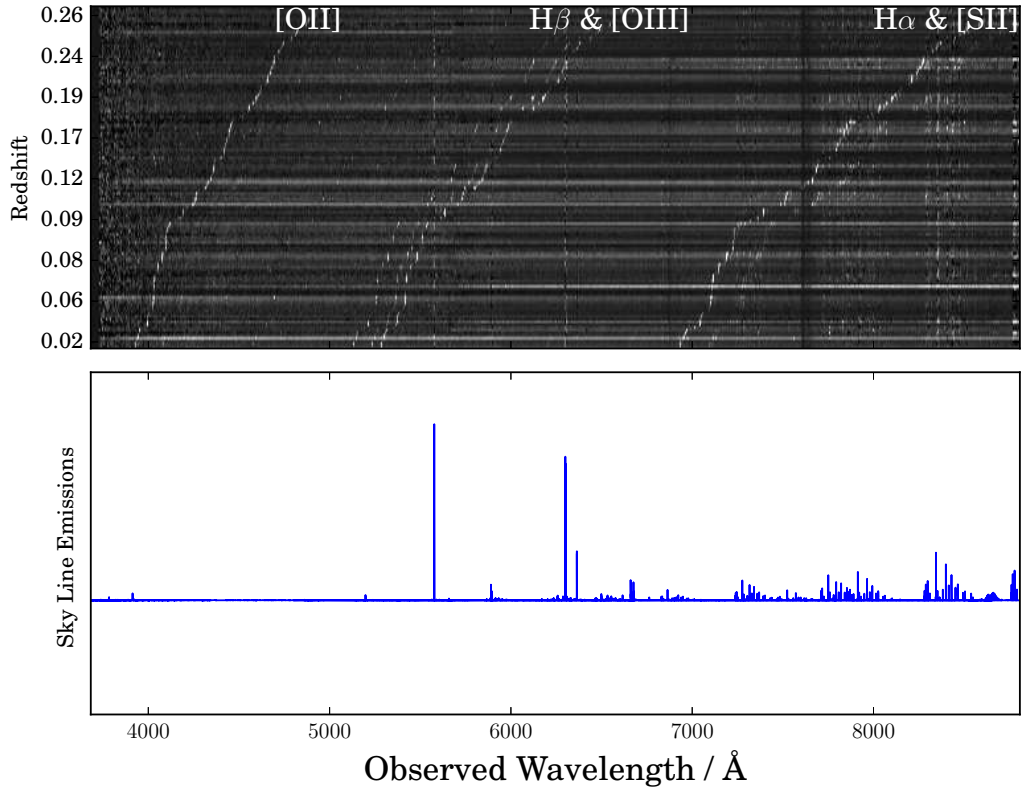

Figure 4.10: The spectra of all sources identified as emission-line galaxies in the AAOmega observations, stacked by their redshifts. Their strong emission lines can be clearly seen, as well as the redshifting of the lines. In addition to the emission lines present within the galaxies' spectra, the residuals of atmospheric emission and absorption line profiles can also be seen. From these stacked spectra is it apparent that emission line spectra of galaxies within the $0.05 < z < 0.25$ range do not suffer from significant loss of line visibility due to sky lines.

Cut Made	Remaining (/211)
Emission-line galaxy	144
$0.05 < z < 0.25$	99
absolute FUV mag < -16.5	74

Table 4.4: Selection criteria applied to good photometric LBA candidates (photLBAs) to determine what fraction of them are spectroscopic LBA candidates (specLBAs). The reasons for each cut are described in section 4.6.

spectra which did not yield an emission-line system were disregarded as potential Lyman break analogues. Among the 211 ideal photLBAs, 144 sources were classified as emission-line galaxies.

The local analogue sample established by Stanway & Davies [2014], expanded in Greis et al. [2016] and presented in chapter 2 requires LBA galaxies to lie within $0.05 < z < 0.25$. Applying this selection criteria to the emission-line galaxies leaves 99 potential specLBA sources.

The final selection criterion determines whether the absolute ultraviolet magnitude is such as to reproduce the strong UV luminosity seen in LBGs. The distribution of FUV absolute magnitudes is shown in Fig. 4.11 (adjusted to show the number of sources per unit area). Given the abrupt drop in frequency of observed galaxies with FUV apparent magnitudes > -17, it is likely that the sample is incomplete at fainter magnitudes. Accepting only those emission-line galaxies with FUV < -16.5, 74 good specLBAs remain, corresponding to 35% of the purely photometrically-selected sample. An absolute magnitude of -16.5 corresponds to apparent magnitudes of 20.2, 22.7, and 24.0 at $z \sim 0.05, 0.15$ and 0.25 respectively. Therefore, an important question to consider is whether the two *GALEX* surveys (AIS and MIS) affect how many genuine LBA sources are observed. Taking into account the different depths and spatial coverages of the two surveys, and adjusting for the fraction of genuine LBA per magnitude bin, the expected number of genuine LBA does not change significantly.

4.6.1 Star Formation Rates and Emission Lines in specLBAs

As described in previous chapters, the star formation rates within these sources can be calculated using a variety of conversion rates. In Fig. 4.12, the Hα inferred SFRs [Kennicutt, 1998] for the specLBA sample can be seen. In order to calculate this, I applied the flux calibration described above, which indicated that in the observed wavelength region of $\sim 6500 - 8500$ Å a conversion factor of $\sim 1 - 1.2 \times 10^{-18}$

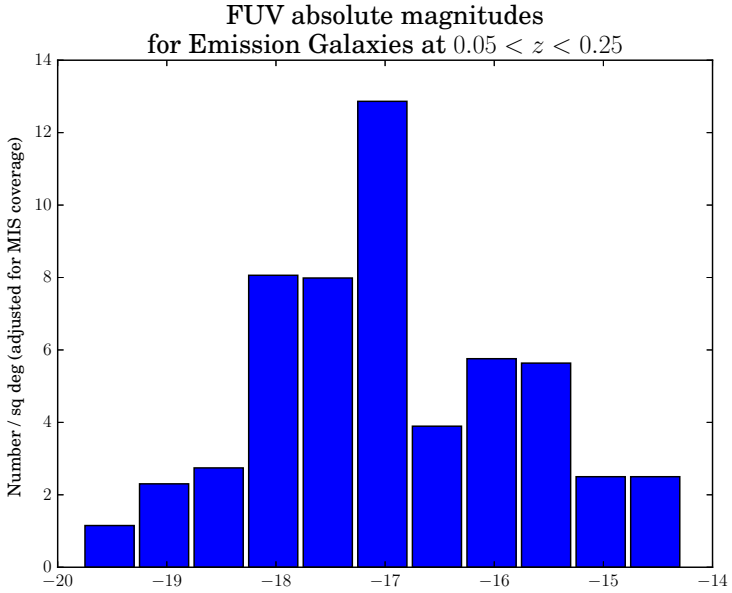

Figure 4.11: The distribution of FUV absolute magnitudes for photLBAs which are also emission-line galaxies in the redshift range $0.05 < z < 0.25$. Only galaxies with FUV < -16.5 are considered spectroscopic LBA candidates (specLBAs). If the luminosity function was fully sampled, more fainter galaxies would be expected to be present in this sample. Given the abrupt drop in frequency of observed galaxies with absolute FUV magnitudes > -17, it is likely that the sample is largely complete up to that magnitude, but that fainter galaxies are underrepresented.

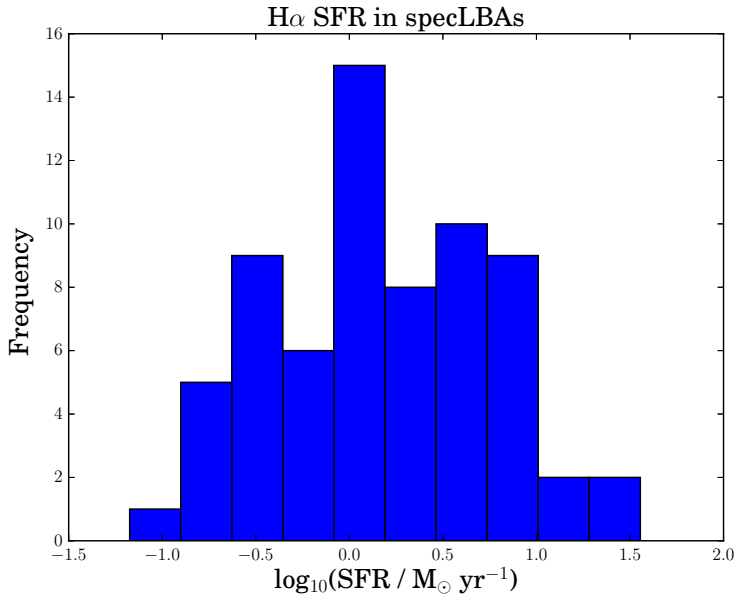

Figure 4.12: Hα-inferred SFRs (using the Kewley et al. [2004] conversion rate) for the specLBA observed.

ergs cm^{-2} s^{-1} Å^{-1} per instrument count needed to be applied. The mean SFR in the specLBA sample is found to be ~ 3.4 M$_\odot$ yr^{-1} (with a range between ~ 0.07 and ~ 36 M$_\odot$ yr^{-1}, and a standard deviation of ~ 5.5). This is in agreement with, though slightly lower than, the Hα SFRs of $\sim 5 - 20$ M$_\odot$ yr^{-1} derived for the LBA sample of Greis et al. [2016]. As noted in chapter 3, however, caution is advised when applying the standard star formation rate conversions to young stellar populations, as true SFR within the source is likely underestimated.

Plotting only the specLBA (together with those galaxies explored in chapter 2, Fig. 4.13), it can, again, be seen that these sources fall within the star-formation driven region, and not the AGN-dominated one, of the BPT diagram. Many sources reside in comparable regions to those of LBAs established in chapter 2, suggesting that similar physical processes are taking place within them. In those sources, which exhibit lower [NII]/Hα ratios, lower ionization parameters may be present. This may imply more dispersed (i.e. less concentrated) star formation, or a denser, more metal-rich ISM.

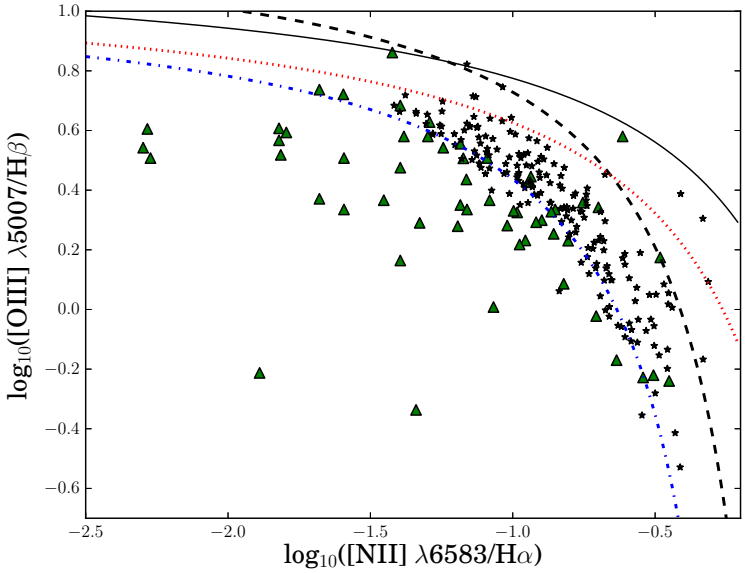

Figure 4.13: Similar to Fig. 4.9, but only showing those objects which were identified as specLBAs (green triangles), together with the confirmed LBA sample from chapter 2 and Greis et al. [2016] (black stars). Compared to the galaxies in Greis et al. [2016], the specLBAs identified from the AAOmega observations have lower [NII]-to-Hα ratios. Assuming that these sources contain similar amounts of [NII] as the Greis et al. [2016] sample, this would indicate significantly higher Hα (as well as Hβ) lines in the specLBA sample.

4.7 Contaminants and Marginal Sources

In order to establish a good photLBA sample, it would be ideal to exclude as many of the contaminants as possible. In the case of a photometric sample of local analogues to $z \sim 5$ LBGs, these contaminants are mostly white dwarfs, quasars, and a few absorption/emission-and-absorption systems. Since all of these sources are also faint blue compact objects, it is extremely difficult to make photometric cuts which exclude contaminants but do not compromise the likelihood of selecting genuine LBAs.

It was not possible to determine either magnitude or colour selections to exclude any significant fraction of either quasars or absorption/emission-and-absorption systems without also reducing the number of specLBA in the sample. However, excluding sources with a $g-i$ colour such that $g-i < 0.3$ was successful in excluding white dwarfs (apart from one system which was found to be a white dwarf - M star binary). This colour selection also excluded one (out of 74) specLBAs.

In section 4.4, I excluded 16/227 objects which have $NUV - r < -0.5$ from the photLBA sample. However, these sources can nevertheless be considered acceptable analogues, as some of the genuine LBAs examined in chapter 2 have comparable very blue colours. Including those acceptable photLBAs, the resulting number of specLBA changes in the following way. The number of emission-line galaxies increases from 144 to 151; the number of those which also fall within the $0.05 < z < 0.25$ redshift range increases from 99 to 104; and there are 78 galaxies whose FUV absolute magnitude satisfies $FUV < -16.5$, making them acceptable specLBAs. Thus, by increasing the number of allowable photLBA, the success rate for identifying specLBA has reduced slightly.

The photometric selection criteria described above are $\sim 35\%$ successful in identifying specLBAs. Since specLBA have a likelihood of between ~ 43 and 70% to be genuine LBAs, this indicates that the photometric criteria successfully identify genuine LBAs in between 15 and 25% of cases. In order to improve the photometric selection criteria, any photometric differences between the observed photLBA and observed specLBA samples had to be determined. This showed that no specLBA were observed with $FUV < 19$, $u > 23.5$, $g > 22.0$, $r > 21.3$, or $i > 21.2$ (as shown in Fig 4.14). Additionally, no specLBA had colours outside of the following: $-1 \leq FUV - u \leq 1.3$, $0 \leq FUV - g \leq 2.0$, $0.4 \leq FUV - i$, $3.0 \geq FUV - z$, $0 < u- < 2$, $0.5 < u - i < 2.4$, $u - z < 3$, $u - r < 2.2$, or $g - i < 0.3$ (Fig. 4.15). Applying these magnitude and colour cuts, 176 photLBAs satisfy the selection criteria, with all but one known specLBA recovered. The ratio of photometric to

spectroscopic LBA candidate thus improves to 47%. These magnitude and colour cuts, however, are very much instrument dependent, and hence only some of them can be physically motivated.

4.8 'Unknowns' in the Sample

The presence of 'unknown' sources in the sample poses several important questions: how many of the objects identified as 'unknown' should be included in or excluded from the analysis of potential LBA candidates? What fraction of 'unknown' sources might be specLBA which are too faint to be detected by these observations? Several possibilities exist why sources may be classified as 'unknowns'. The emission lines of the source may lie outside of the sensitivity range of the observations; this would indicate that these 'unknowns' lie at redshifts beyond the specLBAs range (and are likely QSO) and they can therefore be rejected from the specLBA analysis. Another possibility is that the sources do not contain emission lines, which, again, would indicate that they cannot be specLBAs, and these types of 'unknowns' can be considered contaminants in the photLBA sample (likely WDs or AGN). Two more intriguing and relevant possibilities are the following: the source could be a specLBA object and have emission lines, but these are missed due to sky residuals. Alternatively, the lines are present, but are too weak to be detected with enough confidence.

In section 4.5, and particularly in Fig. 4.10, it can be seen that sources in the $z \sim 0.05 - 0.25$ range do not suffer significant loss of emission lines due to sky line residuals. Approximately 5% of the observed sensitivity range had to be discarded due to sky lines. It is thus very unlikely that a source with strong enough emission lines in the relevant redshift range for specLBAs would be missed due to sky line residuals.

Measuring the typical noise in the spectral regions to which the Hα line would be redshifted makes it possible to put upper limits on the star formation rates within these sources (see Fig. 4.16). This suggests that it is unlikely that the 'unknown' sources have strong SFR, as even a relatively low rate of ~ 3 M$_\odot$ yr^{-1} in a galaxy at $z \sim 0.25$ should have produced a 10σ detection in Hα. Given that no strong emission lines were detected in these sources, it seems likely that their star formation rates are sufficiently low to exclude them as possible specLBAs.

To further illustrate that 'unknown' sources are unlikely to be specLBA, I show their stacked spectra (ordered by *FUV* apparent magnitude) in Fig. 4.17. While potential emission lines can be seen in these sources, no clear pattern emerges.

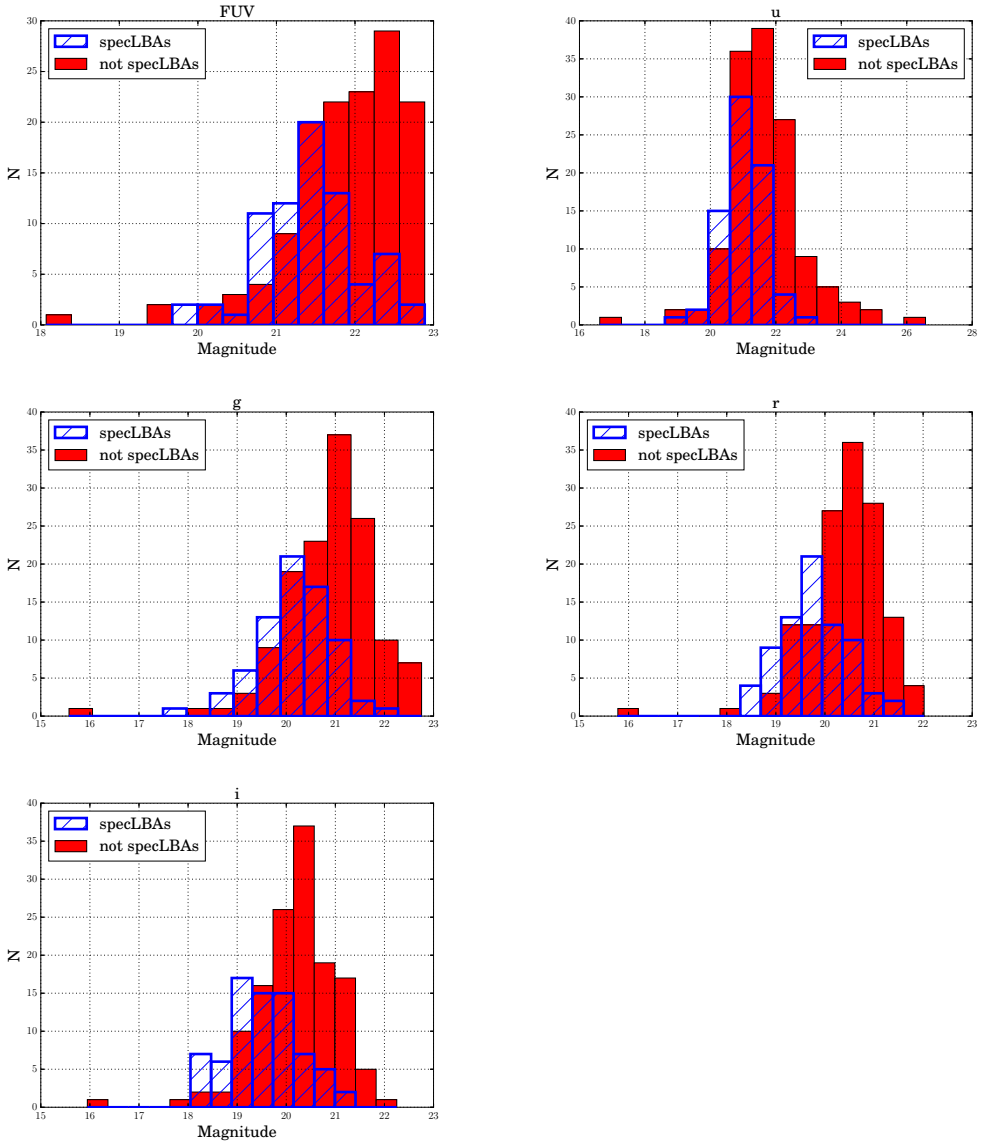

Figure 4.14: Histograms showing FUV, u, g, r, and i magnitude distributions of both those objects identified as specLBAs, and those which do not fulfill the spectroscopic selection criteria. These magnitude distributions were used to derive improved photometric selection criteria.

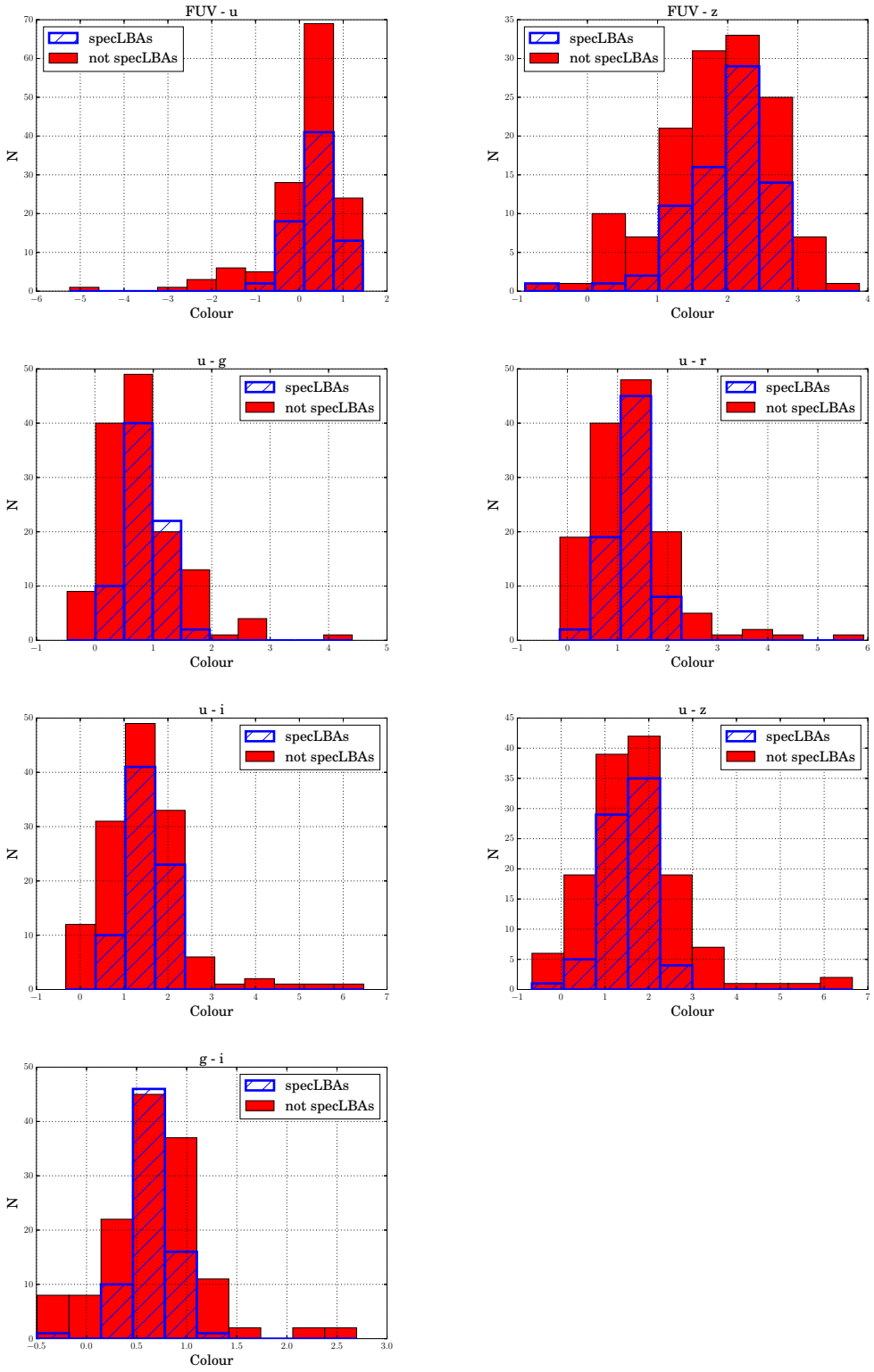

Figure 4.15: Histograms showing various colour distributions of both those objects identified as specLBAs, and those which do not fulfill the spectroscopic selection criteria. These colours were used to derive improved colour selection criteria.

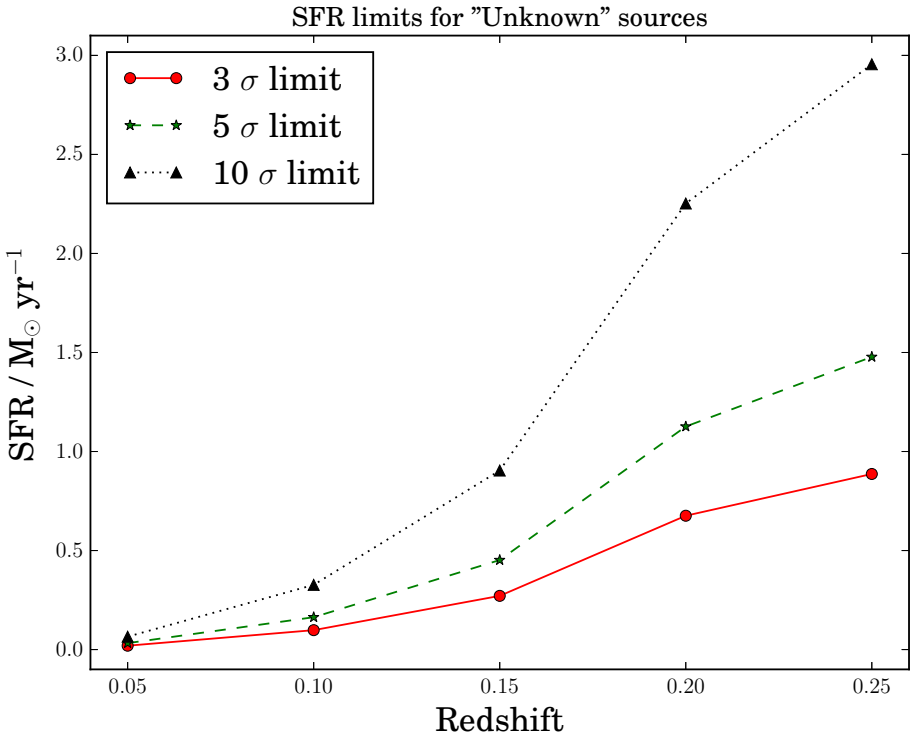

Figure 4.16: Inferred Hα star formation rate limits at 3, 5, and 10 σ above the noise level in the observed wavelength region into which the emission line would fall, for the 'unknown' objects in the sample. Since no emission lines were detected in the 'unknown' sources, their SFRs must be less still (or heavily dust-obscured), hence excluding them as potential specLBAs.

Additionally, the *NUV* apparent magnitude distribution of both the emission line galaxies and 'unknown' sources is shown in Fig. 4.19. From this, it is apparent that 'unknown' sources are generally fainter than emission line galaxies.

4.9 How many genuine LBAs are there?

In order to estimate the spatial density and total number of genuine Lyman break analogues, an estimate of the number of all possible photLBA within the field of view needs to be made. Applying the selection criteria discussed in section 4.4 (and summarised in table 4.2) to all *GALEX* and SDSS objects within a radius of 1.1 degrees around the central observed location at ra = 336.822 and dec = −9.089 degrees produces a sample of 538 potentially observable photLBA within the observed field of view. A small number of these are associated with the same *GALEX*

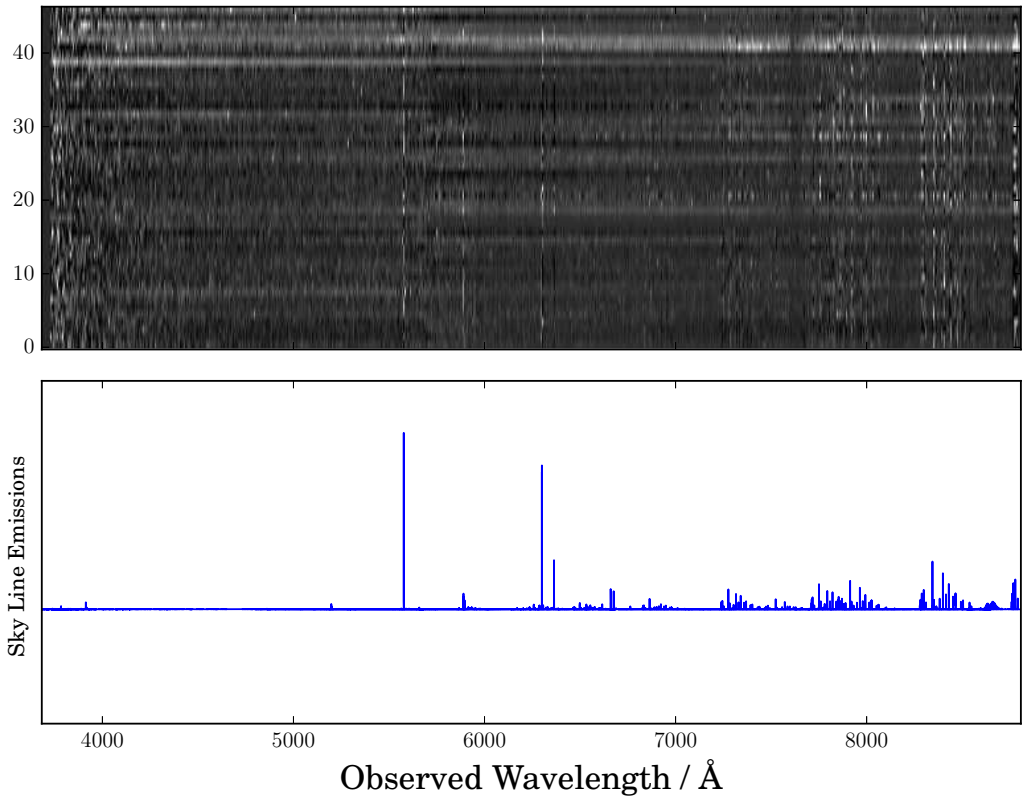

Figure 4.17: Stacked spectra of those objects classified as 'unknown' types. The spectra are stacked by FUV apparent magnitude. While the sky line residuals can be seen in the stacked spectra, no clear trend is visible among the 'unknown' spectra. Some emission lines can be seen in some spectra; however, these were not sufficient to unambiguously classify the sources or to determine their redshifts.

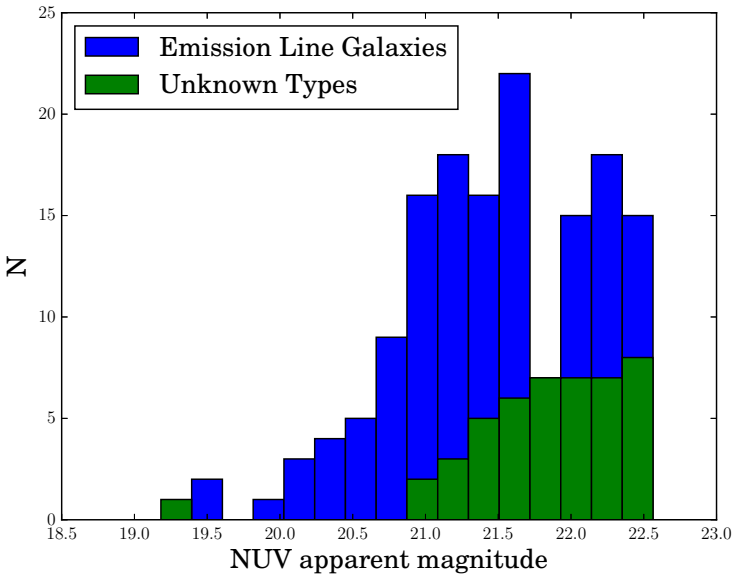

Figure 4.18: Near-ultraviolet apparent magnitudes of both the 'unknown' and emission line sample.

source, resulting in 508 unique *GALEX* identified objects within this sample. All of the photLBA observed in the AAOmega observations described above were recovered in this large photLBA sample. If it can be assumed that the observed field of view is representative of the sky distribution of LBA, the spatial density, and hence total number genuine LBAs, can be estimated in the following way. The ratio of AAOmega-observed photLBA to the number of potentially observable sources is $(211 \pm \sqrt{211})/508 = 42 \pm 3\%$. In section 4.6, I determined that $\sim 35\%$ of observed photLBA are specLBA. This implies that $(0.35) \times 508 \sim 180$ specLBAs are expected to be present within the field of view observed by AAOmega. In chapter 2 (section 2.9), I calculated that, depending on the age and mass cuts used, between ~ 43 and 70% of specLBA fulfill the physical selection criteria, making them genuine LBAs. Hence, it can be expected that there are between 77 and 130 genuine analogues to $z \sim 5$ Lyman break galaxies within the AAOmega's 2 degree diameter field of view. Extrapolating this to the whole sky suggests that the total number of genuine LBA on sky lies between $\sim 1 - 2 \times 10^6$, i.e. between $\sim 24 - 40$ per square degree.

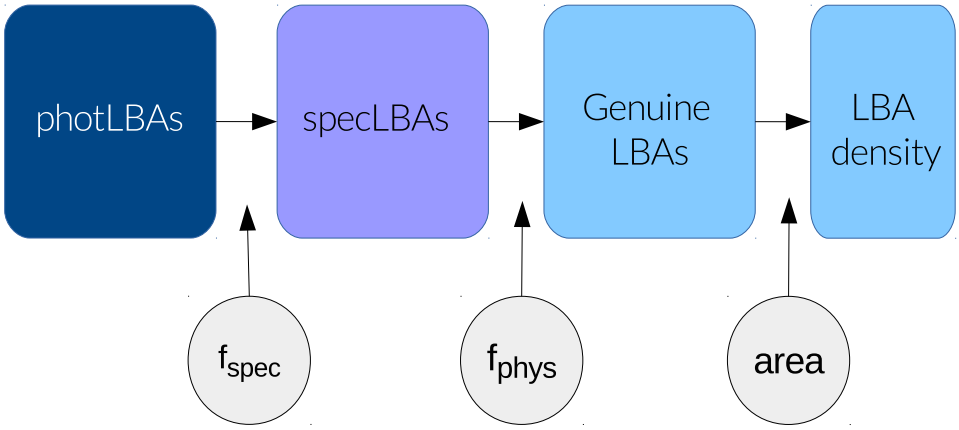

Figure 4.19: Visualisation of $N_{LBA} = N_{phot} \times f_{spec} \times f_{phys}$ where N_{phot} is the number of objects which satisfy the photometric criteria (termed 'photLBA'), f_{spec} is the fraction of those which fulfill the spectroscopic requirements (termed 'specLBA'), and f_{phys} indicates the fraction which additionally reproduces physical characteristics plausible for $z \sim 5$ LBGs. The fractions are given by $f_{spec} \sim 0.35$, and $f_{phys} \sim 0.4 - 0.7$, producing an estimated LBA density of between 24 and 40 per square degree.

4.10 Summary

- AAOmega 2dF spectrograph observations were undertaken, in order to determine the reliability of the photometric selection criteria used to find local Lyman break analogues. Strong emission lines (such as [O II] $\lambda\lambda$3727, 3729, Hβ λ4863, [O III] λ5007, [NII]λ6549, 6583, and Hα λ6564) were targeted. All of these lines lie within the sensitivity region of the spectrograph for sources in the relevant redshift range $0.05 < z < 0.25$.

- The total number of genuine LBAs per area is given by $N_{LBA} = N_{phot} \times f_{spec} \times f_{phys}$ where N_{phot} is the number of objects which satisfy the photometric criteria (termed 'photLBA'), f_{spec} is the fraction of those which fulfill the spectroscopic requirements (termed 'specLBA'), and f_{phys} indicates the fraction which additionally reproduces physical characteristics plausible for $z \sim 5$ LBGs.

- Likely contaminants to the specLBA sample, which nevertheless satisfy the photometric selection criteria are white dwarfs and QSO. Analysing the spectra, however, it was found that most sources (151 out of 227) were identified as emission-line galaxies.

- Applying the spectroscopic LBA selection criteria (i.e. that sources are emission line galaxies at $0.05 < z < 0.25$, and with absolute FUV mag < -16.5), 74 specLBA were identified, giving a success rate of $\sim$ 35% of identifying specLBA from photometry alone.

- Combining the results in this chapter with those found in chapter 2 which indicate that f_{phys} (i.e. the fraction of spectroscopic LBAs which additionally satisfy the physical characteristics of local analogues to $z \sim 5$ LBGs) is $\sim 43 - 70\%$ (depending on the mass and age cuts applied). The number of genuine LBAs consequently lies between 24 and 40 per square degree. This implies that e.g. the Hubble Deep Field (total area $\sim$ 7 square arcmin) should contain around 0.06 genuine LBAs, while the Hubble Ultra-Deep Field (with a total area of 11 square arcmin) should contain between 0.07 and 0.12. The Great Observatories Origins Deep Survey (GOODS) covers a total area of approximately 320 square arcmin with extremely deep observations in the ultraviolet, optical and infrared, is expected to contain between 2.1 and 3.6 genuine LBAs.

Chapter 5

Conclusions & Future Work

Gaining a deeper understanding of high-redshift galaxies allows us to answer important questions about the Universe, such as the evolution of galaxies within it, their role during the Epoch of Reionization, or to test models of galaxy formation. Alas, their great luminosity distances, and resulting small projected sizes on the sky and faint apparent magnitudes make it very difficult to study large numbers of high-redshift galaxies directly. However, as the dominant population of star-forming galaxies at high redshifts, the study of Lyman break galaxies is important in order to obtain a clear picture of the evolution of galaxies throughout cosmic time, and their role during the process of reionization. By establishing local analogue populations which mimic the observed physical characteristics of these distant sources, it becomes possible to gain insights into the mechanisms and processes taking place within the distant galaxies. Due to their relative nearness, the time needed to observe a significant number of these local analogues makes it more feasible to conduct statistically meaningful surveys of them.

Prior to beginning the work undertaken for this thesis, several local analogue populations had been established for intermediate ($z < 4$) and very high ($z \sim 8$) redshift Lyman break galaxies: using colour and luminosity cuts based on the observed photometry of the ~ 3 LBG population, Heckman et al. [2005] and Hoopes et al. [2007] established a sample of $z < 0.3$ UV-bright sources whose luminosities, masses, metallicities and star formation rates reproduce those found in $z \sim 3$ LBGs. A sample of local analogue galaxies which reproduce the strong emission lines and other physical properties seen in Lyman-α emitters (LAEs) was established by Cardamone et al. [2009]. Possible analogues to higher redshift galaxies can be found in the Blue Compact Dwarf (BCD) population whose very low metallicities of less than a tenth $Z_{\odot}$ make them some of the most metal-poor sources

and good candidates for $z \sim 8$ LBGs analogues. As described in the introductory chapter of this thesis, significant evolution occurs in the time between $z \sim 3$, $z \sim 5$ and $z \sim 8$ (corresponding to ages of the Universe of ~ 2, ~ 1, and ~ 0.6 Gyrs respectively), and hence no single population can serve as analogues to all these different redshifts. It thus becomes apparent that a dedicated analogue sample for $z \sim 5-7$ LBGs is needed, not only to form a bridge between our understanding of galaxy formation and evolution at redshifts $z \sim 3$ and $z \sim 8$, but also to shed light on the crucial period of the Epoch of Reionization which was mostly completed by $z \sim 6$. A pilot sample of potential Lyman break analogue galaxies was established by Stanway & Davies [2014], which formed the basis of the work undertaken in my PhD.

The primary goals of my PhD have thus been the establishment of such a dedicated $z \sim 5-7$ analogue population, the detailed study of the physical properties within these sources using multi-wavelength observations, as well as a quantitative assessment of the spatial density of such local analogue galaxies. Following on from this, the most significant result of this thesis is the establishment of the first confirmed sample of such local analogues, illustrating that there exist galaxies in the local Universe which are young, metal poor, moderately star-forming and with star formation rate densities comparable to those found in the distant Universe.

5.1 Summary of Results

5.1.1 Establishing a local Analogue Population to $z \sim 5$ LBGs via SED Fitting

In chapter 2, I made use of, and expanded upon, the pilot sample proposed by Stanway & Davies [2014] of UV-luminous blue compact sources at $0.05 < z < 0.25$. If shifted to $z \sim 5$, these sources would be identified as Lyman break galaxies. By obtaining UV (*GALEX*), optical (SDSS), as well as near-infrared (2MASS and *WISE*) observations of a sample of 180 potential LBA sources, I fit the spectral energy distribution of each source, hence determining the best-fitting age of the dominant stellar population, dust attenuation, stellar mass, star formation rate, star formation rate density ($\equiv$ SFR per unit projected area), and specific star formation rate ($\equiv$ SFR per unit mass) for each galaxy. Additionally, the gas-phase metallicity within the sources could be calculated from spectroscopic data. The median values found for the stellar mass ($\log(M_*/M_\odot) \sim 9.80 \pm 0.42$), metallicity ($\sim 0.4$ $Z_\odot$), star formation rates (between ~ 2.5 and 14 $M_\odot$ yr^{-1}, depending on SFR indicator), specific star formation rates ($\sim 10^{-9}$ yr^{-1}), and dust reddening ($E_{\rm cont}(B-V) \sim$

0.12 ± 0.07) all lie within the uncertainties of the values determined for $z \sim 5$ LBGs. The SED-derived age of the dominant stellar population in the LBA sample ($\log(\text{age/yr}) = 8.60 \pm 0.52$) indicates that, if the sample was redshifted to $z \sim 5$, their formation redshifts would be $z \sim 6-7$. These findings indicate that, excluding only the oldest and most massive sources within it, this sample can be used as a local laboratory to explore the physical properties and processes within the distant galaxy population. Depending on the mass and age cuts chosen, between $\sim 45-70\%$ of sources which satisfy the photometric and spectroscopic selection criteria are satisfactory local analogues. This work has been published in Greis et al. [2016].

5.1.2 Radio Observations confirm LBAs to be young, star-forming systems

Having confirmed that local analogues to $z \sim 5-7$ LBGs can be established using luminosity and colour cuts, a subsample of these local analogue galaxies was observed with the VLA at 1.5 GHz. Additionally, five LBA sources were observed in the sub-millimetre with the LABOCA instrument on APEX, but resulted in non-detections at the frequencies probed. These observations form the basis of chapter 3.

Out of 32 galaxies observed with the VLA, 27 were detected above 3σ. Comparing the inferred radio and Hα SFRs within the sources, a deficit in radio emission relative to Hα was observed, with the Hα-inferred SFR typically twice that found in the radio. This indicates that the sources do not contain strongly dust obscured regions of star formation; in agreement with the dust values found via the SED fitting described in chapter 2. More intriguingly, this apparent deficit in radio versus Hα SFRs implies that the observed sources are very young, having not yet established a strong supernova radio continuum. Star formation rate indicators are typically calibrated to stellar populations whose star formation has been continuous over the last 100 Myr. By contrast, the Hα flux traces only the stars formed within the last 10 Myr, while stars of a much larger age range contribute to the supernova rate within the galaxy and hence drive the radio synchrotron emission. This has two important implications: (1) a precise star formation rate conversion needs to take into account the stellar population age and past star formation history, and (2), for a given flux, the standard star formation rate indicators underestimate the true rate of star formation in stellar populations younger than a few hundred Myrs. Ten of the sources observed by VLA had previously been observed with ATCA, making it possible to constrain their radio spectral slopes, $F_\nu \propto \nu^\alpha$, between 1.5 and 5.5 GHz, and hence to evaluate the likelihood of the presence of an AGN. Since Lyman break galaxies are systems driven by star formation, the presence of an AGN would pre-

clude any source from being a potential local analogue. While normal star-forming galaxies with constant SFRs typically have radio spectral slopes of ~ -0.7 to -0.8, the slopes found in the local analogues are significantly shallower. This suggests that these sources have a high fraction of thermal radio flux, in agreement with a recent short-duration starburst which produced both thermal radio and Hα, but very little non-thermal synchrotron emission. Given both their radio luminosities and spectral slopes, we predict a total of $\sim$0.6 contaminating AGN sources in the sample of 32. This is consistent with their optical line ratios and the possibility that $\sim 1-2$ of our targets may show AGN-like characteristics. The radio observations additionally made it possible to place constraints on the phyical sizes of the sources, providing further evidence for their compactness. Combining this with the SFRs derived for the sources, it is apparent that the LBA sources have significantly higher star formation rate densities than typical (SDSS) star-forming galaxies at the same redshifts. It is possible that these high star formation rate densities may be driving galaxy-wide superwinds. Hence, if high-redshift LBGs mirror the properties inferred in the local population, such winds might have important consequences for the chemical enrichment of the intergalactic medium surrounding them. However, open questions remain as to how such winds might be driven, since the young stellar populations within the LBAs (and, at higher redshifts, the LBGs) preclude the existence of a strong AGB population. This work has been published in Greis et al. [2017].

5.1.3 Placing constraints on the total number of LBAs via Spectroscopic Observations

From the SED fitting described in chapter 2, I had determined that between $\sim 45-70\%$ of sources which fulfill the photometric and spectroscopic selection criteria, can be considered genuine local analogues to $z \sim 5$ LBGs, given their ages, masses, star formation rates, dust values, and metallicities. This led to an important question: how successfully would genuine LBAs be selected if only photometric selection criteria were used? And what implications does this have for the spatial density and total number of local analogues? In order to answer these questions, AAOmega 2dF spectrograph observations were undertaken, targeting strong emission lines (such as [O II] $\lambda\lambda$3727, 3729, Hβ λ4863, [O III] λ5007, [NII]λ6549, 6583, and Hα λ6564) in a sample of 227 purely photometrically selected potential LBAs. The total number of genuine LBAs per area is given by $N_{LBA} = N_{phot} \times f_{spec} \times f_{phys}$ where N_{phot} is the number of objects which satisfy the photometric criteria, f_{spec} is the fraction of those which fulfill the spectroscopic requirements, and f_{phys} indicates the fraction which

additionally reproduces physical characteristics plausible for $z \sim 5$ LBGs. Analysis of the observed spectra confirmed that likely contaminants, such as white dwarfs and QSO (which can satisfy the LBAs' photometric selection criteria), were present in the sample. Most observed sources (151 out of 227), however, were identified as emission-line galaxies. Applying the spectroscopic LBA selection criteria (redshift range $0.05 < z < 0.25$ and absolute FUV magnitudes of < -16.5) produced 74 sources which fulfill both the photometric and spectroscopic criteria, hence giving an overall success rate of $\sim 35\%$ of identifying LBA candidates from photometry alone. Combining the results of this spectroscopic analysis with the results found in chapter 2, and assuming that the observed field of view is representative of the whole sky, indicates that the number of genuine LBAs consequently lies between 24 and 40 per square degree. Publication of this work is currently in prep.

5.2 Future Work

Despite the progress made in establishing and beginning to probe a local analogue population to $z \sim 5$ Lyman break galaxies, many unresolved questions remain about the physical properties of these sources.

5.2.1 Molecular Gas

An approved ALMA project to target CO emission lines in the LBA sample will make it possible to constrain the available gas fraction within these galaxies. At the time of writing, there is very little information on the dynamic properties within the LBAs, with their velocity widths unresolved in existing observations. Given their stellar masses, it is likely that the velocity dispersions within them are ~ 50 km s^{-1}. The approved ALMA observations will target and spatially and spectrally resolve the CO(1-0) line in 5 LBA sources. Due to their low redshifts, these targets are expected to reach signal-to-noise ratios of ~ 50 within ~ 10 minutes. Interestingly, in intermediate-redshift ($z \sim 3 - 4$) LBGs, the CO lines were found to be a factor of $3 - 4$ weaker than expected based on the galaxies' infrared-to-CO luminosities of similarly massive galaxies at lower redshifts, suggesting lower metallicities within these sources [Tan et al., 2013]. However, this also indicates that detecting molecular gas in $z > 3$, and hence rather metal-poor, galaxies may remain challenging, even with ALMA, highlighting the value of local analogue studies. In addition to the CO measurements, these observations will also provide the first high-resolution sub-millimetre size measurements of these sources, making it possible to better constrain their star formation rate densities, and to investigate how the galaxies' gas

content and temperature are affected by their intense star formation. By measuring the luminosity in CO, L'$_{CO}$ (and applying a conversion factor between CO and hydrogen mass, known as the α_{CO} factor), and combining it with their known SFRs, metallicities, and sizes, it will be possible to calculate the molecular hydrogen gas masses within these galaxies. Even without knowing the exact conversion factor, it will be possible to determine a range of possible molecular gas masses within the galaxies. Measurements of intermediate-redshift LBGs suggest that these galaxies are relatively metal-poor, hence indicating higher α_{CO} factors. By comparing this with the inferred star formation rates within these objects, limits on the gas depletion timescales within the LBAs can be found, and hence it should be possible to determine whether their intense star formation is likely to continue throughout their evolution or is a transient phenomenon. If the latter case is found to be true, it would pose interesting questions, such as whether most galaxies undergo a comparable starburst phase, and what might act as the trigger for this. These ALMA observations will also make it possible to place the observed sources on (or off) the Schmidt-Kennicutt relation, hence giving insights into star formation driven gas feedback process which regulate the star formation in both low and high redshift systems. Lastly, it is likely that these observations might motivate not only observations of an increased sample, but also future excitation ladder programmes in which higher transitions of CO are observed. From these CO spectral line energy distributions (SLEDs) could be constructed which measure the relative strengths of higher order transitions. The shape of these SLEDs provides clues to the local thermal equilibrium within the system, as well as insights into their star formation rate density and gas density.

5.2.2 Outflows and Winds

As noted in chapter 3, spatially resolved morphological studies may provide insights into outflow structures and geometry. Such imaging, or resolved spectroscopy, of the LBA sources would shed further light on the question of outflows, particularly by probing for an excess of ionized gas along the galaxy's minor axis (along which outflows may be more likely to escape), or broader emission line profiles (higher wind velocities) along the minor axis than the major axis. By investigating the presence or absence of such winds or outflows, the galaxies' impact on their surround IGM can be calculated, providing clues to the impact of distant LBGs on the metallicity history of the Universe. In local analogues to $z \sim 2-3$ LBGs, very high velocity dispersions have been found, in some cases > 100 km s^{-1} (compared to more typical velocity dispersions in local galaxies of $\sim 5-15$ km s^{-1}), indicating strong random

components in the gas dynamics within these sources [Gonçalves et al., 2010]. The outflow velocities of local starburst-driven galaxies, most of which could be considered good analogues to $z \sim 3$ LBGs, were found to only weakly correlate with the stellar mass within the systems, but to strongly correlate with both the SFR and SFR per area [Heckman et al., 2015]. Interestingly, the latter correlation was found to 'saturate' at $v_{out} \sim 300 - 500$ km s^{-1} for SFR/area > 6 M$_\odot$ kpc^{-2}. Studying directly a subsample of the LBA sample described in my thesis, high [O III]/ Hβ emission line ratios were detected, with typical values of [O III]/ Hβ $= 3.36^{+0.14}_{-0.04}$ [Stanway et al., 2014], well above the norm for local star-forming galaxies. Since these line ratios depend on a combination of ionizing UV flux incident on the ISM and the ISM density, it is likely that such high line ratios are driving substantial winds and outflows in these systems.

5.2.3 Morphology

Currently, the highest resolution imaging of the LBA sample comes from SDSS and suggests that they have typical deconvolved projected sizes of $\sim 0.2-0.3$ arcseconds. Radio observations have, in some cases, been able to provide tighter constraints, but due to the systems' relatively low radio SNR, these size measurements are not very robust. High resolution imaging of the LBA sources (e.g. with HST) will thus place tighter constraints on their star formation rate densities, and will help answer such questions as: are LBAs galaxy-wide starbursts, or do they consist of multiple clumps of intense star formation? Morphological studies will additionally help to determine the merger fraction within this sample, thus allowing inferences about potentially merger-driven starbursts. Since such high-resolution studies are not currently possible in the very distant Universe, using local analogues remains the only method of gaining answers to these questions. In studies of local analogues to $z \sim 3$ LBGs, the galaxies have mostly been found to consist of several star-forming clumps exhibiting a range of sizes and luminosities, while a minority appear to contain only a single, highly compact (~ 100 kpc), massive ($\sim 10^9$ M$_\odot$) central source [Alexandroff et al., 2015]. Furthermore, such local analogues often display (optical) tidal features, suggesting a range of merger conditions and stages [Overzier et al., 2010]. These structures would not be recovered if these objects were observered at higher redshifts, underscoring again the importance of local analogue samples, and calling for caution when interpreting high-redshift observations.

5.2.4 Escape Fractions

In order to determine the possible impact of LBGs, or similar galaxies, to the process of reionization, the amount of ionizing radiation escaping the systems needs to be measured. While this would be near-impossible to undertake directly on the distant population, deep rest-frame far-ultraviolet measurements of a local analogue sample make it possible to constrain their escape fractions, and hence to make inferences about those of more distant systems. In local analogues to $z \sim 3$ LBGs, statistically significant correlations have been found between the escape fraction and the amount of residual intensity in the core of the Si II λ1260 ISM absorption line, the shape of the Lyα emission line profile, and the distance from the star-forming ridge line in the SII BPT diagram (in which the standard NII/Hα ratio is replace with the SII/Hα one) [Alexandroff et al., 2015]. For these sources it has also been found that those galaxies which have the highest SFR/area are the strongest candidates for high escape fractions. In Green Peas, which are good analogues to distant Lyman Alpha Emitters (LAEs), strong Lyα emission has been observed, with Lyα escape fractions between a few per cent and $\sim 60 - 70\%$ [Henry et al., 2015; Yang et al., 2016, 2017]. In particular, an increased Lyα escape fraction is correlated with lower dust reddening, lower metallicity (e.g. because a lower neutral hydrogen column density would allow more Lyα photons to escape), lower stellar mass, and higher [O III]/[O II]ratios (i.e. higher ionization fractions) [Yang et al., 2017]. Using the Cosmic Origins Spectrograph (COS) on board *Hubble*, with its G140L/B grating, it is possible to measure the flux shortwards of the (rest-frame) Lyman-limit for the LBA sample presented in this thesis. Since the grating's sensitivity improves by a factor of ~ 100 between the observed wavelengths of 1070 and 1150 Å, and despite their increased luminosity distances, it is significantly less time-consuming to observe the higher redshift LBAs (at $z \sim 0.2 - 0.25$) (see Fig. 5.1). Depending on the metallicity of the stellar population within these sources, the intrinsic flux ratio of Lyman continuum flux shortwards of the 912Å break compared to the flux longwards of it is expected to be ~ 0.5. The exposure times shown in Fig. 5.1 were calculated such as to yield a 20σ detection on the flux level longwards of the Lyman break. Hence, a SNR of 10 could be expected on the Lyman continuum shortwards of the break. Additionally, since the Lyman break observations utilise the B chip of the grating, measurements of the Lyα emission line can be undertaken simultaneously on the A chip, providing additional information on the escape fraction (e.g. by comparing the Hα and Lyα flux ratios). Given the young stellar populations - and hence large number of UV-emitting hot OB stars - in the LBAs presented here, it is likely that these sources will exhibit escape fractions which should be measurable

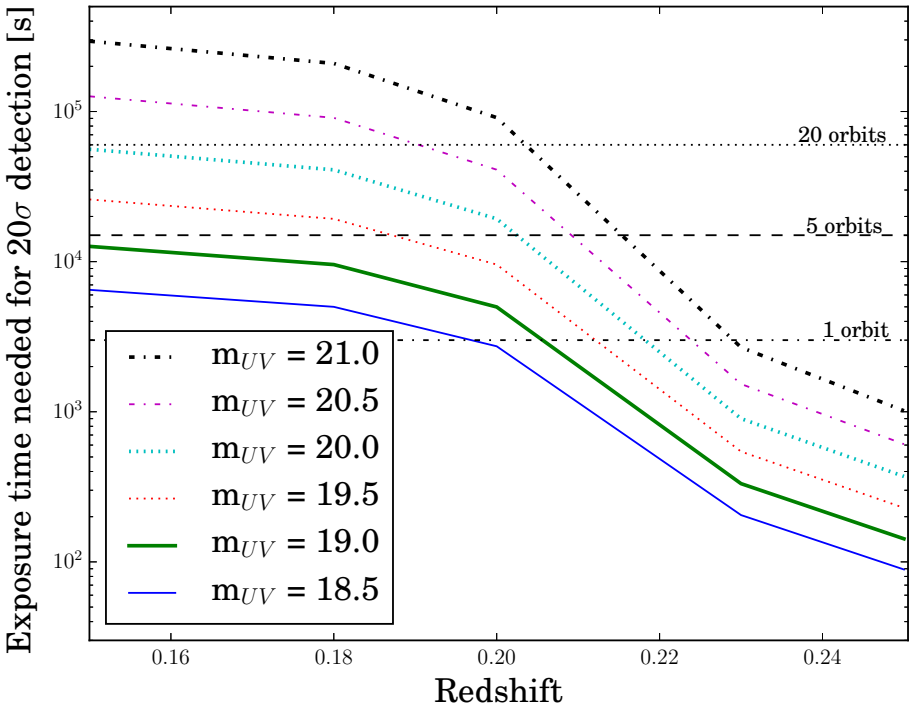

Figure 5.1: Exposure times needed to obtain SNR $\sim$ 20 on the Lyman continuum of an object with a given magnitude at 900 Å with HST's COS spectrograph at different redshifts, found by binning a 100Å rest-frame range. Imaging shortwards of the Lyman break is harder due to internal absorption of the flux, but may provide constraints on the escape fraction of these sources. An escape fraction of $\sim$ 10% should be detectable in $\sim$ 1 orbit for the brightest and highest redshift sources in the LBA sample, while future telescopes, such as LUVOIR, might be able to probe the fainter, nearer sources.

with a few orbits of *Hubble*.

5.2.5 Dust in LBAs

In the SED fitting described in chapter 2, I have assumed a Calzetti et al. [2000] dust law for the LBA galaxies. While this was justified by this law's calibration to local starbursts, it is possible that LBAs follow a different law. By obtaining and fitting rest-frame ultraviolet to infrared observations of these sources, their specific dust reddening curves could be determined, giving insights about the major constituents of the dust within these sources through the observed features in their dust curves. Alternatively, the dust laws within them can be constrained by using the Balmer

ratios, and fitting reddening curves to these.

5.2.6 LBAs in ultra-deep fields

The spatial densities determined in chapter 4 of between 24 and 40 genuine LBA per square degree suggest that e.g. the Hubble Deep Field (total area ~ 7 square arcmin) should contain around 0.06 genuine LBAs, while the Hubble Ultra-Deep Field (with a total area of 11 square arcmin) should contain between 0.07 and 0.12. With observations from *Spitzer*, *Herschel*, *Chandra*, *Hubble*, *XMM-Newton* and powerful ground-based telescopes, the Great Observatories Origins Deep Survey (GOODS) covers a total area of approximately 320 square arcmin with extremely deep observations in the ultraviolet, optical and infrared, and is expected to contain between 2.1 and 3.6 genuine LBAs. Using observations in these deep fields might make it possible to not only study their spectral energy distribution and star formation rates, but also to determine their clumpiness and asymmetry which, in turn, helps to distinguish a merger/interaction-triggered starburst event from an internally-driven one.

5.3 Future Surveys and Instruments

Several future surveys and instruments are being planned and built which will propel forward the study of high-redshift galaxies and their local analogues. Some of these upcoming opportunities, as well as some potential impacts to this field, are the following.

The James Webb Space Telescope (JWST) will be an infrared telescope with a 6.5-metre primary mirrors, to be launched from French Guiana in October 2018 [Gardner et al., 2006]. Made from 18 hexagonal mirror segments, the primary mirror is designed to unfold itself upon arrival at the second Lagrange point. One aim of *JWST*'s decade-long mission is to undertake ultra-deep, near-infrared surveys, which are followed up with low-resolution spectroscopy and mid-infrared photometry. Four instruments onboard the space telescope will make it possible to address questions such as when and how reionization occurred, and how the first galaxies formed and evolved. These will allow imaging and spectroscopy between 0.6 and 28.8 μm, making *JWST* ideal at identifying $z \sim 5 - 7$ LBGs (as well as higher redshift ones). Additionally, the telescope will undertake statistical surveys of galaxies to study their formation and evolution, with spectroscopic follow-up of hundreds of thousands of galaxies. Specifically two instruments onboard the *JWST* are likely to

prove invaluable in the study of high-redshift galaxies and their local analogues: The Near Infrared Camera (NIRCam[1]) will undertake imaging and spectroscopy of the 0.6 to 5 μm wavelength region, which is ideal for identifying high-redshift galaxies, while the Near Infrared Spectrograph[2]) will produce spectra over a region 3 arcsec square in the 0.6 to 5.3 μm wavelength range.

For the study of local analogues, the advent of *JWST* will provide near-infrared observations of these systems which will yield better constraints for one of the most difficult to constrain regions of their SED, providing even clearer insights into the stellar mass, dust and any potential older underlying stellar populations. In particular, the near-infrared Paschen and Brackett lines (at rest-frame $\sim 0.8 - 2\mu$m and $\sim 1.5 - 4\mu$m respectively) can be probed, from which the dust laws within the galaxies can be determined. Additionally, the PAH component of the LBAs' dust spectra (peaking in the mid-infrared at $\sim 5 - 10\mu$m) can be probed by *JWST*.

The Large Synoptic Survey Telescope (LSST) will be an optical to near-infrared telescope with *ugriz* filters akin to SDSS, as well as a redder y-band filter [Ivezic et al., 2008]. Its aim is to conduct a 10-year survey of the sky, starting in 2019, and delivering $\sim$ 200 petabytes of images and data. Since the process of galaxy formation is inherently stochastic, a large statistical sample is of particular importance to better understand galaxy formation and evolution. Using an 8.4-metre primary mirror, the telescope located in north-central Chile will provide a wide and deep survey of the sky. While not being the deepest or highest resolution survey, LSST will populate, by far, the largest database to date. With a limiting magnitude of ~ 27.5 (in the r-band), comparable to GOODS, and covering a solid angle of $\sim 20,000$ square degrees (greater than SDSS), a lookback time of ~ 12 billion years will be accessible to the telescope. This will provide photometry for 10^{10} galaxies, ranging in distance from the local group to $z > 6$. Scales of less than ~ 3 kpc will be resolvable up to this redshift, and the telescope is capable of detecting typical star-forming LBGs out to $z > 5.5$. Combining multi-band photometry with both wide area and deep imaging, it will be possible to detect some of the rarest high-redshift dropout galaxies. It is expected that hundreds of $z \sim 5 - 7$ Lyman break galaxies will be observed, illustrating that much of the power of LSST will come from its large statistical samples.

In addition to the wide and deep survey, several pointings will be observed

[1]NIRCam `https://jwst-docs.stsci.edu/display/JTI/Near+Infrared+Camera%2C+NIRCAM`
[2]NIRSpec `https:jwst-docs.stsci.edu/display/JTI/Near+Infrared+Spectrograph%2C+NIRSpec`

more frequently, making them 'deep drilling holes' which provide opportunities for coordinated multiwavelength follow-up with *JWST*, ALMA, and others. In summary, it seems likely that the field of study of $z \sim 5-7$ LBGs will undergo an explosion in the number of available sources over the coming decade, assuming that sufficiently large halos and bright galaxies have formed at these early times. Additionally, the number of potential local analogue sources to this distant galaxy population will also increase dramatically - though only if there is supporting UV data (e.g. from *LUVOIR*).

5.4 Final Conclusions

This thesis has identified the largest dedicated sample to date of local galaxies whose observed and inferred properties make them analogous to $z \sim 5$ Lyman break galaxies. This latter population is of particular importance in the history of the Universe as it is thought to have contributed significantly to the process of reionization, rendering a previously opaque intergalactic medium transparent at (rest-frame) $\lambda < 1216$ Å (and hence making the study of distant galaxies possible). From the research undertaken during my PhD I have not only confirmed that such local analogue galaxies exist and - akin to their distant cousins - are young (with SED-fitting derived ages of $\log(\mathrm{age/yrs}) \sim 8.6 \pm 0.5$), moderately massive (with SED-fitting derived stellar masses of $\log(\mathrm{M/M_{\odot}}) \sim 9.8 \pm 0.4$), and star formation driven (with SFRs ~ 14 $\mathrm{M_{\odot}\ yr^{-1}}$, as measured in the dust-corrected UV), but we have also learnt that they have low metallicities (with median metallicities < 0.5 $\mathrm{Z_{\odot}}$), are relatively dust-poor (typical $\mathrm{E(B\text{-}V)_{cont}} \sim 0.12 \pm 0.07$), unlikely to host an older underlying stellar population or AGN, and are potentially driving galaxy-wide superwinds due to their high star formation rate densities (though it is unclear whether these young galaxies actually have sufficiently large populations of e.g. Wolf-Rayet stars and/or supernovae which could be driving such winds). These findings have several important implications for the $z \sim 5$ LBG population:

- While it is very difficult, if not impossible, to break the age, dust and metallicity degeneracies seen in distant galaxies, this has been possible to do in the local analogue sample. In particular, it has been possible to derive these quantities using several independent methods (e.g. the ages were constrained using both SED fitting and radio observations, and the dust reddening was derived both from SED fitting and line ratio measurements).

- Local galaxies, selected for their high star formation rate densities, have been

shown to exhibit similar physical properties to those seen in high redshift galaxies, hence suggesting that galaxies with comparable star formation densities throughout cosmic time might have similar physical properties.

- Given that the vast majority of LBAs have consistently been found to have young stellar populations and to be actively star-forming, a bursty star formation history can be assumed in them, hence suggesting similarly bursty SFHs in the distant Lyman break galaxy populations. It is hence likely that all galaxies undergo one or more such phases of intense star formation, before potentially self-extinguishing by driving out their available gas through winds. Since successive generations of stars enrich the ISM within these systems, the interesting question remains whether such intense starbursts can only be sustained at low metallicities.

- The LBAs have been found to have higher ionization parameters than other typical local galaxies. Serving as local analogues to the distant galaxy population, predictions can thus be made about the line strengths expected in $z \sim 5$ LBGs, which may become observable in the near future with the advent of instruments such as the *JWST*.

For the first time, estimates of the projected spatial distribution and density of LBA galaxies have been achieved, indicating that there are $\sim 24 - 40$ genuine local analogues to $z \sim 5$ LBGs per square degree. Future studies of these local analogues will be able to quantify their escape fraction (and hence provide potential insights into the contribution which distant LBGs may have had on their surrounding neutral IGM), whether LBAs follow dust laws established in other nearby starburst galaxies, whether star formation within them occurs in clumps or galaxy-wide bursts, and what may be driving any winds or outflows from these sources. Additionally, by comparing the available hydrogen gas in these systems with their current rate of star formation, it will be possible to determine whether their current observed SFRs are indeed episodic starbursts or likely to be sustainable over a large fraction of the galaxies' lifespans.

It is, thus, clear that open questions remain in our understanding of high-redshift star-forming galaxies and their local analogues, many of which will likely be able to be explored with the next generation of both ground- and space-based telescopes. To end with the words of Edwin Hubble: "The search will continue. The urge is older than history."

Appendix A

SED Fitting Results

Table A.1: Spectrophotometric data for the 180 LBA candidate galaxies described in chapter 2. The object identified ('ObjID') is derived from the SDSS DR7 identifier. The Galactic foreground reddening ('MW dust') values were determined by Schlafly & Finkbeiner [2011]. The far- and near-ultraviolet AB magnitudes were measured by GALEX (with typical uncertainties of ~ 0.1 mag), while the *ugriz* AB magnitudes (with typical uncertainties of ~ 0.02 mag) come from SDSS measurements.

ObjID	ra	dec	redshift	MW dust	fuv	nuv	u	g	r	i	z
23734	1.16389	-10.15264	0.1085	0.032	19.8	19.44	19.8	19.6	19.57	18.94	19.8
58754	2.19214	-9.25568	0.2009	0.033	20.5	20.29	19.51	18.92	18.54	18.19	18.25
05815	8.65174	-9.57551	0.101	0.031	19.66	19.22	18.57	17.79	17.46	17.08	17.03
19220	14.6789	-9.68398	0.1883	0.034	21.26	21.27	20.65	20.09	19.42	19.02	18.78
92589	19.37123	-8.73437	0.1665	0.034	18.83	18.68	18.54	18.22	17.95	17.9	17.95
49226	20.59955	15.34222	0.153	0.067	20.3	19.98	19.51	19.1	18.59	18.56	18.84
02555	25.19056	13.88476	0.173	0.052	20.39	20.0	19.54	18.92	18.57	18.39	18.28
08755	25.58712	-8.76605	0.1636	0.031	20.41	20.06	19.47	18.92	18.58	18.33	18.34
32420	25.70536	-9.60746	0.1609	0.021	20.1	19.67	19.03	18.43	18.11	17.79	17.95
62100	26.84033	-9.27951	0.1356	0.022	19.98	19.86	19.71	19.43	19.1	18.97	19.3
51350	27.06657	-10.00187	0.2165	0.033	20.58	20.76	19.76	19.3	18.7	18.36	18.09
05083	27.9936	-9.38417	0.1457	0.021	20.36	20.03	19.61	19.01	18.61	18.38	18.56
04483	28.72465	13.12268	0.1189	0.047	20.34	20.05	19.72	19.25	19.08	18.77	18.88
45691	29.97112	-8.23027	0.1517	0.022	19.32	19.36	19.48	19.21	18.9	18.92	19.21
72856	33.14848	-9.63883	0.1499	0.022	20.06	19.88	19.6	19.09	18.8	18.58	18.66
24784	35.15693	-9.48536	0.1131	0.022	19.78	19.5	19.38	19.14	18.96	18.51	18.97
92239	37.28071	-8.95727	0.1828	0.024	20.0	19.76	19.43	18.95	18.65	18.64	18.82
27888	47.59977	-8.57579	0.0515	0.063	19.91	19.89	19.62	18.73	18.97	18.7	18.83
00364	57.10974	-6.09997	0.1637	0.068	20.88	20.56	20.02	19.37	19.01	18.74	18.74

Table A.1 Continued from previous page

ObjID	ra	dec	redshift	MW dust	fuv	nuv	u	g	r	i	z
78659	60.53695	-5.11169	0.1393	0.087	19.83	19.61	19.18	18.59	18.36	18.18	18.17
76428	111.6581	39.76609	0.1115	0.049	19.86	19.78	19.51	19.04	18.83	18.44	18.86
34524	112.65454	39.14399	0.1452	0.05	20.73	20.64	20.11	19.28	18.91	18.62	18.61
83073	115.62922	21.33423	0.1104	0.063	20.6	20.12	19.76	19.08	18.86	18.54	18.59
29921	121.91403	31.20504	0.1219	0.032	19.49	19.47	18.88	18.17	17.95	17.75	17.74
67086	122.2703	28.91937	0.1283	0.036	20.63	20.56	20.03	19.14	18.8	18.43	18.36
23117	123.59461	25.72017	0.1282	0.032	20.86	20.42	19.89	19.12	18.76	18.42	18.61
80920	125.31913	40.95998	0.1286	0.045	20.11	20.41	19.64	19.08	18.86	18.55	18.59
99943	126.02675	31.15663	0.1809	0.037	20.32	19.83	19.15	18.42	17.97	17.75	17.6
37625	126.46233	41.28621	0.1562	0.035	20.04	19.66	19.25	18.66	18.36	18.11	18.04
68579	128.32456	3.91666	0.1587	0.025	20.89	20.44	19.7	19.04	18.64	18.45	18.41
15004	128.45934	45.82598	0.1883	0.023	20.18	19.98	19.68	19.33	18.89	18.79	19.11
80573	128.92412	10.29985	0.1152	0.03	20.59	20.12	19.61	18.77	18.38	18.06	17.95
72555	129.2505	39.10582	0.128	0.033	19.44	19.07	18.9	18.33	18.15	17.92	17.9
14358	129.51555	44.98343	0.1432	0.022	19.23	19.18	19.2	18.93	18.73	18.59	18.76
71699	129.55936	46.0701	0.1235	0.022	19.81	19.61	19.05	18.35	18.06	17.69	17.64
67337	131.91766	23.40459	0.1389	0.026	21.31	20.91	20.32	19.47	18.96	18.58	18.55
95211	134.07263	4.84664	0.1742	0.04	21.54	21.07	20.46	19.7	19.31	19.0	18.87
19287	135.21178	40.20606	0.1353	0.016	19.73	19.5	19.2	18.54	18.28	18.02	17.97
52087	135.24699	40.61407	0.1382	0.017	20.31	20.01	19.51	18.9	18.64	18.25	18.29
31056	135.42306	8.69206	0.1256	0.05	19.89	19.75	19.14	18.36	18.05	17.75	17.72
11996	136.2786	22.64276	0.1256	0.029	19.5	19.19	19.24	18.94	18.59	18.47	19.01

Table A.1 Continued from previous page

ObjID	ra	dec	redshift	MW dust	fuv	nuv	u	g	r	i	z
41882	136.71599	41.36413	0.1353	0.015	20.33	20.07	19.54	18.83	18.53	18.29	18.39
38857	137.37213	6.55441	0.1808	0.041	19.73	19.48	19.19	18.72	18.4	18.18	18.32
49722	138.16125	8.42735	0.1593	0.062	19.86	19.58	19.08	18.69	18.39	18.37	18.4
05091	138.50597	7.34669	0.1824	0.035	20.32	19.96	19.45	18.83	18.44	18.13	18.17
42268	138.69192	13.10132	0.1505	0.022	20.06	19.65	19.33	18.62	18.29	18.03	18.22
19230	140.97096	7.85343	0.1851	0.038	20.69	20.24	19.9	19.31	18.9	18.57	18.67
76391	141.24336	16.6267	0.1787	0.023	20.63	20.31	19.61	18.99	18.52	18.09	18.14
47307	141.30575	32.07227	0.1397	0.018	20.48	20.15	19.9	19.24	18.91	18.62	18.52
86374	141.58014	46.93213	0.1849	0.014	20.3	19.87	19.22	18.67	18.31	18.03	18.05
57993	143.6293	26.28542	0.138	0.019	20.44	19.96	19.56	19.02	18.61	18.4	18.33
66254	144.25762	24.44382	0.1343	0.018	19.03	18.91	18.74	18.31	18.13	18.0	18.12
21702	147.18303	15.45254	0.1497	0.031	20.32	19.97	19.44	18.93	18.68	18.34	18.45
80781	148.35907	12.72934	0.1306	0.023	19.69	19.35	18.92	18.37	18.11	17.75	17.85
39595	149.84	31.96639	0.1214	0.013	19.63	19.35	19.09	18.47	18.25	18.0	18.05
41896	150.18236	5.08837	0.1402	0.018	20.01	19.66	19.2	18.48	18.2	17.94	17.9
17906	150.21726	38.51584	0.1474	0.013	20.11	19.86	19.49	19.12	18.82	18.61	18.91
46138	150.77536	20.79887	0.1329	0.022	19.09	18.64	18.48	17.9	17.74	17.61	17.62
88577	150.90098	47.8581	0.1194	0.009	19.65	19.75	19.03	18.36	18.14	17.92	17.9
72408	151.5014	44.66506	0.1393	0.007	19.48	19.32	19.31	18.83	18.59	18.46	18.63
43940	152.03788	46.19387	0.1749	0.008	20.43	20.17	19.56	18.97	18.55	18.23	18.23
72317	152.21954	21.45792	0.1488	0.023	19.89	19.96	19.64	19.1	18.79	18.6	18.86
59679	153.26224	34.271	0.1765	0.012	19.22	19.06	18.86	18.55	18.25	18.12	18.4

Table A.1 Continued from previous page

ObjID	ra	dec	redshift	MW dust	fuv	nuv	u	g	r	i	z
31771	154.7621	5.85705	0.1729	0.019	19.87	19.52	19.17	18.59	18.35	18.2	18.18
05793	154.92305	33.51315	0.1247	0.021	20.16	20.4	19.66	19.09	18.76	18.52	18.41
97155	154.97513	4.45409	0.1835	0.02	20.83	20.41	20.03	19.31	18.95	18.64	18.66
48854	155.35233	35.7748	0.1912	0.008	19.79	19.73	19.32	19.1	18.71	18.36	18.3
72523	156.45161	36.3829	0.1265	0.01	18.74	18.6	18.56	18.34	18.11	17.98	18.42
33387	157.35096	35.88161	0.1795	0.013	19.96	19.9	19.46	18.94	18.53	18.3	18.36
46300	158.52743	5.51848	0.1708	0.024	19.21	19.15	18.81	18.46	18.2	18.02	18.16
31994	159.05833	28.56038	0.1122	0.021	19.57	19.2	19.06	18.29	18.11	17.85	17.91
05800	159.09207	44.26913	0.1358	0.01	20.33	19.97	19.39	18.76	18.39	18.06	17.96
19777	159.8884	30.99103	0.1136	0.014	19.69	19.58	19.03	18.38	18.21	17.87	17.94
94468	162.42734	31.19139	0.1437	0.022	20.45	20.18	19.7	19.23	18.91	18.57	18.78
88629	162.62603	48.34874	0.1477	0.016	19.69	19.58	19.64	19.2	18.95	18.78	19.1
87146	164.36175	29.27005	0.1653	0.021	19.75	19.63	19.37	18.98	18.66	18.43	18.67
79737	167.30938	23.77849	0.1405	0.013	19.67	19.59	19.36	19.04	18.64	18.49	18.83
00205	168.53985	36.53985	0.1606	0.017	19.07	18.99	18.77	18.33	18.14	18.03	18.06
60185	169.23569	32.76928	0.1762	0.02	19.82	19.96	19.73	19.18	18.81	18.56	18.79
97269	170.57018	30.5129	0.1201	0.014	20.12	19.73	19.21	18.56	18.3	17.97	18.02
30847	171.13865	25.44768	0.1318	0.014	19.74	19.57	19.07	18.31	18.01	17.72	17.67
91891	171.31934	18.04925	0.1973	0.019	19.58	19.18	19.13	18.78	18.56	18.39	18.64
14657	171.32926	19.19115	0.1677	0.018	20.36	20.07	19.82	19.26	18.94	18.71	18.84
92876	171.44342	20.44942	0.1796	0.016	19.88	19.8	19.37	18.8	18.5	18.23	18.09
58757	173.39503	45.4643	0.1247	0.017	21.39	20.92	20.18	19.37	18.96	18.6	18.46

Table A.1 Continued from previous page

ObjID	ra	dec	redshift	MW dust	fuv	nuv	u	g	r	i	z
40416	174.01485	10.09028	0.1457	0.032	20.2	19.86	19.59	19.01	18.76	18.6	18.63
77424	174.03521	48.59255	0.1294	0.018	19.65	19.31	18.99	18.55	18.33	18.09	18.27
37518	174.90376	39.98296	0.1296	0.016	19.66	19.39	19.05	18.53	18.35	18.14	18.17
32360	175.40621	33.74326	0.1365	0.019	20.1	19.93	19.54	19.05	18.77	18.59	18.69
17599	175.61985	7.95264	0.1334	0.02	19.38	19.32	19.25	18.86	18.66	18.54	18.67
35368	176.59336	45.47085	0.1778	0.02	19.98	19.59	19.38	18.95	18.71	18.54	18.45
74772	177.93541	36.70623	0.1749	0.019	19.82	19.68	19.41	18.8	18.49	18.27	18.29
53150	178.63296	8.57709	0.1167	0.019	18.72	18.99	18.8	18.51	18.41	18.1	18.49
55849	179.62691	27.12393	0.1833	0.019	19.92	19.76	19.53	19.09	18.81	18.64	18.64
80172	180.03074	26.0872	0.189	0.019	19.19	19.07	18.92	18.58	18.38	18.21	18.29
97755	180.73719	48.20063	0.1949	0.024	19.94	19.76	19.34	18.95	18.61	18.56	18.9
05924	180.77237	8.86979	0.1818	0.018	19.4	19.22	18.87	18.4	18.11	17.91	17.97
41786	183.48457	6.39265	0.1899	0.014	19.75	19.69	19.18	18.59	18.3	17.98	18.13
82584	185.16857	47.72063	0.1567	0.012	20.27	19.79	19.35	18.69	18.32	18.08	18.13
99137	185.62116	38.45572	0.1274	0.012	20.61	20.15	19.46	18.8	18.48	18.16	18.14
06122	185.89012	15.57215	0.1327	0.023	20.18	19.76	19.58	19.12	18.9	18.77	18.89
71011	186.17401	14.96796	0.1398	0.02	19.57	19.43	19.22	18.77	18.48	18.4	18.62
61615	187.54429	46.97292	0.1642	0.011	19.9	19.64	19.14	18.49	18.19	17.98	17.93
14769	187.77879	22.8417	0.1341	0.013	18.93	18.76	18.82	18.54	18.42	18.16	18.4
76073	188.08861	29.98195	0.1228	0.019	19.28	19.21	18.74	17.94	17.74	17.53	17.6
95870	189.58464	6.13415	0.1189	0.018	20.47	20.0	19.75	19.02	18.8	18.53	18.53
43813	189.82162	14.8657	0.1774	0.027	19.31	18.84	18.98	18.62	18.55	18.39	18.45

Table A.1 Continued from previous page

ObjID	ra	dec	redshift	MW dust	fuv	nuv	u	g	r	i	z
74272	189.87282	37.19232	0.189	0.011	19.47	19.19	19.08	18.82	18.58	18.52	18.68
29942	189.89012	49.9099	0.1502	0.013	20.43	20.06	19.7	19.12	18.87	18.76	18.63
16982	190.22721	35.90026	0.1908	0.012	20.76	20.29	19.58	18.83	18.42	18.1	18.03
90130	190.30411	49.54553	0.1154	0.012	20.63	20.44	19.84	19.06	18.72	18.34	18.3
44692	191.08636	35.83436	0.1734	0.012	20.19	19.79	19.2	18.68	18.37	18.07	18.29
19697	193.11618	31.71308	0.1153	0.012	18.35	18.26	18.27	18.02	17.96	17.63	18.0
45022	193.66131	22.98316	0.122	0.024	20.07	19.68	19.36	18.68	18.52	18.37	18.34
53307	195.25666	40.07222	0.1444	0.014	19.82	19.49	19.38	18.94	18.71	18.47	18.45
04816	196.12796	31.89517	0.1805	0.012	20.0	19.59	19.2	18.61	18.3	18.09	18.11
37785	196.91194	32.16745	0.122	0.011	19.69	19.34	19.07	18.64	18.43	18.01	18.49
69378	196.91661	27.23722	0.1675	0.013	20.37	19.98	19.65	18.85	18.46	18.13	18.03
01656	197.50242	13.49651	0.1404	0.018	20.28	20.4	19.79	19.05	18.72	18.39	18.4
65988	198.38023	4.20842	0.1541	0.026	19.46	19.69	19.45	19.0	18.76	18.59	18.59
85709	198.56804	44.83602	0.1404	0.015	20.76	20.64	19.98	19.34	18.89	18.58	18.58
70623	199.06637	43.35536	0.1221	0.014	20.64	20.33	19.45	18.75	18.43	18.14	18.14
77967	201.26519	21.19272	0.176	0.023	19.63	19.15	18.75	18.31	18.05	17.67	17.88
98777	202.07039	12.42069	0.1131	0.029	19.25	18.83	18.7	18.34	18.27	18.06	18.08
15410	202.74064	32.63404	0.1116	0.009	19.42	19.44	19.24	19.09	19.03	18.73	19.05
92082	205.37167	13.53758	0.1358	0.02	18.9	18.83	18.58	18.22	18.13	17.98	17.95
57761	205.42495	39.37282	0.1238	0.007	20.22	20.04	19.69	19.03	18.75	18.49	18.43
38135	206.43421	19.60874	0.1932	0.022	19.93	19.73	19.3	18.76	18.4	18.18	18.4
27029	207.11579	21.48265	0.1141	0.018	19.41	19.04	19.59	19.06	18.98	18.65	18.8

Table A.1 Continued from previous page

ObjID	ra	dec	redshift	MW dust	fuv	nuv	u	g	r	i	z
31525	207.33599	37.68821	0.1265	0.009	19.71	19.23	18.67	17.92	17.65	17.42	17.45
52556	207.60085	21.13838	0.1856	0.021	19.98	19.56	19.33	18.94	18.61	18.44	18.7
65323	207.98294	3.42342	0.1296	0.028	19.22	19.13	18.98	18.79	18.6	18.38	18.87
88235	208.89063	32.53142	0.1666	0.011	18.63	18.65	18.43	18.2	18.01	17.89	18.14
13964	209.33999	5.75788	0.1764	0.022	19.48	19.26	19.03	18.55	18.32	18.13	18.12
74742	210.62136	6.05638	0.1118	0.023	21.12	20.71	20.0	19.08	18.71	18.42	18.29
36125	210.79584	43.90542	0.1218	0.006	20.15	20.37	19.47	19.18	18.79	18.31	18.32
23218	211.19882	40.64636	0.1452	0.013	20.08	19.7	19.34	18.76	18.45	18.24	18.32
37848	211.55951	19.82198	0.1328	0.025	19.71	19.62	19.21	18.66	18.43	18.27	18.3
56415	212.84126	47.48035	0.1445	0.015	19.73	19.65	19.41	18.93	18.66	18.52	18.76
02152	212.85968	12.34055	0.146	0.02	19.29	19.0	18.69	18.25	18.05	17.87	17.82
94209	212.94217	6.74853	0.1196	0.022	20.0	19.7	19.57	18.92	18.71	18.46	18.56
82365	213.56862	47.74157	0.1516	0.014	19.28	19.04	18.87	18.47	18.27	18.12	18.18
48839	214.93448	40.8057	0.1196	0.009	19.04	18.74	18.37	17.77	17.49	17.12	17.18
02547	215.87213	38.19445	0.1224	0.009	19.91	19.58	18.78	17.94	17.58	17.27	17.26
02494	216.29605	42.25727	0.141	0.01	20.87	20.54	20.06	19.36	18.84	18.44	18.32
49356	216.49678	41.20787	0.1529	0.007	19.95	19.61	19.09	18.39	18.1	17.83	17.82
46852	216.93997	14.028	0.1591	0.021	19.97	19.47	19.18	18.45	18.13	17.94	17.89
99418	217.16303	33.39596	0.1542	0.013	19.34	18.93	18.66	18.25	18.08	17.84	17.97
52057	218.97057	4.61712	0.1565	0.029	20.36	20.11	19.86	19.33	18.93	18.69	18.84
91412	221.73053	7.75607	0.1422	0.025	19.27	18.9	18.9	18.58	18.24	18.11	18.28
29786	224.25632	22.86286	0.1185	0.033	20.36	19.99	19.61	18.93	18.68	18.35	18.37

Table A.1 Continued from previous page

ObjID	ra	dec	redshift	MW dust	fuv	nuv	u	g	r	i	z
76856	224.62693	6.3341	0.1317	0.03	21.03	20.74	20.02	19.22	18.85	18.52	18.51
69711	228.6996	20.59306	0.1826	0.04	20.58	20.1	19.74	19.1	18.74	18.48	18.49
70402	229.10675	38.52991	0.128	0.017	20.67	20.22	19.5	18.71	18.35	18.03	17.95
30095	229.64305	36.27272	0.1504	0.015	19.36	18.96	18.7	18.11	17.85	17.58	17.6
08961	230.32268	37.09914	0.196	0.014	19.93	19.75	19.32	18.72	18.42	18.24	18.15
25783	231.61955	28.29079	0.117	0.024	20.29	20.66	19.73	19.55	19.18	18.58	18.6
76079	235.02877	24.51249	0.1216	0.038	19.46	19.13	18.87	18.31	18.15	17.9	18.03
75848	236.38473	40.96762	0.1933	0.018	19.35	18.88	18.62	18.18	17.94	17.76	17.75
95952	237.44271	7.92046	0.1976	0.031	20.18	20.02	19.76	19.3	18.97	18.87	18.9
08586	238.20283	16.98562	0.1488	0.041	20.48	20.17	19.28	18.8	18.49	18.28	18.36
43200	238.64018	28.68668	0.1896	0.04	19.94	19.61	19.32	18.95	18.74	18.56	18.66
16795	239.42926	34.55878	0.1571	0.024	19.39	19.32	19.21	18.8	18.59	18.53	18.48
83121	242.09655	12.54962	0.1887	0.043	20.29	19.96	19.3	18.52	18.12	17.87	17.91
30446	242.40841	4.75281	0.1378	0.043	20.4	19.96	19.3	18.57	18.22	17.92	17.91
28730	243.4572	14.11566	0.1237	0.041	19.75	19.53	19.28	18.97	18.84	18.6	18.72
54077	250.648	42.39715	0.1511	0.011	19.14	18.8	18.55	18.25	17.95	17.82	18.19
27825	251.40989	28.98597	0.1363	0.032	20.3	20.44	19.64	18.9	18.59	18.39	18.41
13995	316.63522	-7.5139	0.1357	0.084	20.24	19.96	19.45	18.88	18.64	18.48	18.63
08959	332.01197	13.22626	0.1164	0.061	19.55	19.5	18.95	18.62	18.5	18.18	18.59
54609	332.98331	-9.53977	0.2087	0.038	19.84	19.49	19.71	19.16	18.91	18.6	18.55
27473	336.64663	-9.68499	0.0831	0.04	20.39	19.99	19.79	19.1	18.99	18.63	18.62
60392	337.13304	-9.46809	0.1205	0.047	20.29	20.44	19.6	18.78	18.3	17.89	17.81

Table A.1 Continued from previous page

ObjID	ra	dec	redshift	MW dust	fuv	nuv	u	g	r	i	z
71294	340.88031	-9.44735	0.146	0.042	19.96	19.6	19.52	19.02	18.65	18.46	18.82
16911	344.79825	-8.77026	0.0974	0.032	19.31	18.88	18.6	18.09	17.79	17.39	17.38
77821	346.21707	-8.6318	0.1211	0.036	19.94	19.58	19.1	18.37	18.1	17.78	17.7
10045	349.66038	-10.50532	0.1373	0.024	20.28	19.95	19.74	19.28	18.95	18.76	18.9
54061	355.41867	-8.71988	0.0742	0.028	18.66	18.31	19.34	18.96	19.21	18.75	19.27
33326	358.81388	-10.97455	0.0638	0.03	19.93	19.63	19.92	19.01	18.9	18.71	18.35
10880	359.0195	-8.9065	0.1685	0.03	19.74	19.59	19.52	19.19	18.8	18.81	19.14

Table A.2: Infrared magnitudes of the 180 LBA candidate galaxies described in chapter 2. For a detailed description of how these magnitudes were determined, see section 2.3. Typical uncertainties on *JHK* were ~ 0.4 mag. In the *WISE* bands, *W1 - 3* magnitudes have typical uncertainties of ~ 0.2 mags, while *W4* has typical uncertainties of ~ 0.3.

ObjID	ra	dec	J	H	K	W1	W2	W3	W4
23734	1.16389	-10.15264	16.84	17.37	18.64	17.91	18.06	15.16	14.35
58754	2.19214	-9.25568	17.49	17.72	18.64	18.2	18.27	15.51	14.69
05815	8.65174	-9.57551	16.0	17.43	16.4	17.09	17.35	14.44	13.83
19220	14.6789	-9.68398	17.34	16.88	17.86	18.79	18.29	16.81	15.27
92589	19.37123	-8.73437	17.14	18.97	18.64	18.3	18.24	15.53	14.35
49226	20.59955	15.34222	17.28	18.97	17.27	18.96	17.63	15.33	14.03
02555	25.19056	13.88476	18.06	16.84	17.12	19.0	18.26	16.36	15.42
08755	25.58712	-8.76605	16.48	18.97	18.64	18.27	18.27	15.22	14.18
32420	25.70536	-9.60746	16.87	18.97	17.54	18.16	18.27	14.84	13.77
62100	26.84033	-9.27951	16.95	18.97	17.42	21.79	21.04	16.33	16.45
51350	27.06657	-10.00187	16.99	16.95	17.18	17.76	17.79	17.12	16.45
05083	27.9936	-9.38417	17.46	17.84	17.41	18.77	18.89	16.27	14.98
04483	28.72465	13.12268	19.19	18.97	18.64	18.21	18.16	18.72	16.45
45691	29.97112	-8.23027	19.19	17.85	18.64	20.03	19.42	16.68	15.56
72856	33.14848	-9.63883	19.19	17.33	16.94	18.26	18.18	15.83	15.61
24784	35.15693	-9.48536	18.12	18.97	17.21	19.05	18.69	15.25	13.99
92239	37.28071	-8.95727	19.19	18.97	18.64	19.2	19.29	16.82	16.45
27888	47.59977	-8.57579	17.76	17.06	17.27	19.57	19.4	16.93	14.92
00364	57.10974	-6.09997	19.19	18.97	18.64	19.21	18.84	16.67	16.45

Table A.2 Continued from previous page

ObjID	ra	dec	J	H	K	W1	W2	W3	W4
78659	60.53695	-5.11169	16.9	18.05	17.49	18.7	18.33	17.63	16.45
76428	111.6581	39.76609	17.69	18.08	18.64	17.61	16.36	14.6	14.13
34524	112.65454	39.14399	17.94	18.97	18.64	19.56	18.99	16.9	16.45
83073	115.62922	21.33423	17.25	18.97	17.75	19.02	18.97	17.44	15.24
29921	121.91403	31.20504	16.9	17.3	17.65	18.57	19.2	16.46	15.6
67086	122.2703	28.91937	17.9	17.7	17.67	18.52	18.24	16.21	15.69
23117	123.59461	25.72017	17.71	17.31	18.64	18.79	18.64	15.59	14.71
80920	125.31913	40.95998	17.77	17.46	18.64	19.36	18.81	16.49	16.45
99943	126.02675	31.15663	16.36	16.91	16.65	17.97	17.38	15.5	16.45
37625	126.46233	41.28621	16.43	18.97	17.32	18.16	17.93	15.82	15.18
68579	128.32456	3.91666	19.19	18.97	17.59	18.39	17.9	17.77	16.45
15004	128.45934	45.82598	17.66	18.97	18.64	19.12	17.84	15.32	13.98
80573	128.92412	10.29985	17.16	17.49	17.44	18.35	17.94	16.06	16.45
72555	129.2505	39.10582	16.78	17.8	17.38	18.4	17.93	16.44	15.66
14358	129.51555	44.98343	17.46	17.68	17.77	19.24	19.36	16.82	16.45
71699	129.55936	46.0701	16.45	17.12	17.0	18.08	17.83	15.09	14.66
67337	131.91766	23.40459	18.27	18.97	17.43	18.85	18.08	16.17	15.11
95211	134.07263	4.84664	19.19	17.59	18.64	18.91	18.3	16.46	16.45
19287	135.21178	40.20606	16.69	18.11	17.42	18.22	17.87	15.72	14.6
52087	135.24699	40.61407	16.86	18.03	17.86	18.53	17.74	15.42	14.59
31056	135.42306	8.69206	17.96	17.66	16.76	17.8	17.46	15.35	14.96
11996	136.2786	22.64276	16.96	17.49	18.64	19.51	19.04	16.97	14.26

Table A.2 Continued from previous page

ObjID	ra	dec	J	H	K	W1	W2	W3	W4
41882	136.71599	41.36413	17.93	17.86	18.64	18.85	18.33	15.92	14.94
38857	137.37213	6.55441	17.74	18.97	18.64	18.54	18.45	15.45	14.43
49722	138.16125	8.42735	16.88	18.97	17.87	18.3	17.62	15.17	14.22
05091	138.50597	7.34669	17.64	17.01	17.75	18.77	18.01	15.67	15.59
42268	138.69192	13.10132	16.62	17.61	18.64	18.96	18.92	15.72	14.47
19230	140.97096	7.85343	17.19	18.97	17.45	19.09	18.41	17.46	16.45
76391	141.24336	16.6267	19.19	17.27	17.25	17.86	16.95	14.55	13.94
47307	141.30575	32.07227	17.13	17.31	18.64	19.1	18.82	16.44	15.17
86374	141.58014	46.93213	17.3	17.02	17.29	18.18	17.87	15.23	14.34
57993	143.6293	26.28542	16.93	17.32	17.16	18.77	18.53	16.36	16.45
66254	144.25762	24.44382	19.19	18.97	17.36	18.96	18.6	15.91	14.98
21702	147.18303	15.45254	17.53	17.43	18.64	18.99	18.48	15.69	14.33
80781	148.35907	12.72934	17.13	17.15	16.75	18.19	17.12	14.59	13.7
39595	149.84	31.96639	16.63	16.89	18.64	18.47	18.21	16.25	15.11
41896	150.18236	5.08837	17.36	16.36	16.82	18.51	18.42	15.5	15.11
17906	150.21726	38.51584	19.19	18.97	18.64	19.03	18.16	16.05	14.63
46138	150.77536	20.79887	16.7	16.78	17.27	18.04	17.73	15.85	15.04
88577	150.90098	47.8581	16.8	17.49	17.16	18.4	18.01	16.07	15.26
72408	151.5014	44.66506	17.64	18.97	18.64	19.54	19.58	16.61	15.47
43940	152.03788	46.19387	17.42	18.97	18.64	21.79	21.04	18.72	16.45
72317	152.21954	21.45792	17.34	18.97	18.64	19.7	18.66	15.94	14.59
59679	153.26224	34.271	17.06	17.78	17.58	18.51	17.83	14.92	13.81

Table A.2 Continued from previous page

ObjID	ra	dec	J	H	K	W1	W2	W3	W4
31771	154.7621	5.85705	17.41	18.97	18.64	18.91	18.1	16.54	15.45
05793	154.92305	33.51315	17.13	17.54	18.64	18.99	19.48	16.87	16.45
97155	154.97513	4.45409	17.45	18.97	17.3	19.24	17.99	16.24	15.38
48854	155.35233	35.7748	17.95	17.59	17.34	17.49	16.73	15.66	14.86
72523	156.45161	36.3829	16.81	18.97	18.64	19.06	18.87	15.91	14.49
33387	157.35096	35.88161	17.52	18.97	18.64	18.78	17.96	15.94	15.14
46300	158.52743	5.51848	17.07	17.86	17.26	18.78	18.61	15.78	14.81
31994	159.05833	28.56038	16.99	18.17	17.84	18.62	18.48	15.62	14.5
05800	159.09207	44.26913	16.59	17.66	18.64	18.26	17.38	15.27	15.25
19777	159.8884	30.99103	17.27	16.86	18.64	18.32	18.54	15.84	15.13
94468	162.42734	31.19139	17.01	17.05	17.61	18.91	18.45	15.84	14.14
88629	162.62603	48.34874	16.97	18.97	18.64	20.24	19.29	16.96	15.42
87146	164.36175	29.27005	17.44	18.04	18.64	18.62	18.0	15.36	14.52
79737	167.30938	23.77849	17.13	18.97	17.64	18.3	17.39	14.89	13.59
00205	168.53985	36.53985	18.0	17.51	18.64	18.64	18.13	16.04	15.15
60185	169.23569	32.76928	17.91	17.42	18.64	19.34	18.01	15.69	14.52
97269	170.57018	30.5129	17.42	17.58	17.72	18.17	18.0	15.22	15.13
30847	171.13865	25.44768	17.33	18.97	17.26	18.04	18.12	15.44	15.39
91891	171.31934	18.04925	19.19	17.93	17.81	18.78	18.37	15.71	14.31
14657	171.32926	19.19115	17.23	18.13	17.26	18.79	18.18	15.11	13.49
92876	171.44342	20.44942	17.96	18.97	17.51	19.19	18.58	18.72	16.45
58757	173.39503	45.4643	16.72	18.97	17.45	18.46	18.21	15.75	15.68

Table A.2 Continued from previous page

ObjID	ra	dec	J	H	K	W1	W2	W3	W4
40416	174.01485	10.09028	16.9	18.97	17.77	19.37	19.3	16.9	16.45
77424	174.03521	48.59255	19.19	17.4	17.22	18.72	18.41	15.96	15.28
37518	174.90376	39.98296	17.71	17.62	18.64	18.66	18.4	16.04	15.68
32360	175.40621	33.74326	19.19	18.97	17.72	19.48	19.98	16.93	15.58
17599	175.61985	7.95264	18.01	18.97	17.46	19.5	18.72	17.63	15.38
35368	176.59336	45.47085	17.29	18.97	18.64	18.96	18.56	16.61	16.45
74772	177.93541	36.70623	17.41	17.74	17.87	18.77	18.29	15.97	15.33
53150	178.63296	8.57709	19.19	17.92	18.64	18.76	17.97	15.41	13.94
55849	179.62691	27.12393	17.03	18.11	18.64	19.48	19.59	16.73	16.45
80172	180.03074	26.0872	15.59	17.06	17.32	18.53	17.99	15.58	14.49
97755	180.73719	48.20063	18.36	18.97	18.64	19.5	19.59	16.32	14.88
05924	180.77237	8.86979	16.97	17.06	16.8	18.25	17.76	15.56	14.97
41786	183.48457	6.39265	17.04	18.97	18.64	18.4	17.28	14.69	13.54
82584	185.16857	47.72063	17.29	17.41	18.64	18.71	17.9	16.34	16.45
99137	185.62116	38.45572	17.06	17.93	18.64	18.48	18.78	15.75	15.18
06122	185.89012	15.57215	19.19	18.97	18.64	20.27	19.98	16.99	16.45
71011	186.17401	14.96796	16.61	17.07	18.64	19.5	19.28	17.02	16.45
61615	187.54429	46.97292	16.27	18.97	18.64	18.72	18.18	15.47	15.36
14769	187.77879	22.8417	19.19	18.97	18.64	18.87	18.5	15.75	14.52
76073	188.08861	29.98195	16.51	16.6	16.97	18.42	17.97	15.98	16.45
95870	189.58464	6.13415	17.6	18.09	18.64	19.48	18.98	17.4	16.45
43813	189.82162	14.8657	17.5	18.97	18.64	18.52	18.17	16.14	15.57

Table A.2 Continued from previous page

ObjID	ra	dec	J	H	K	W1	W2	W3	W4
74272	189.87282	37.19232	17.38	18.97	18.64	18.2	17.64	15.76	15.01
29942	189.89012	49.9099	19.19	18.97	17.78	19.73	18.65	18.72	16.45
16982	190.22721	35.90026	16.71	17.28	17.36	18.36	17.71	15.33	15.25
90130	190.30411	49.54553	17.29	18.97	18.64	18.7	18.4	15.72	15.68
44692	191.08636	35.83436	16.86	18.97	18.64	18.59	18.0	15.45	14.82
19697	193.11618	31.71308	17.14	17.51	17.73	18.38	17.76	15.35	13.92
45022	193.66131	22.98316	18.04	18.97	17.72	18.89	18.48	17.28	15.68
53307	195.25666	40.07222	17.4	18.97	17.67	18.62	18.25	16.2	16.45
04816	196.12796	31.89517	17.61	17.98	18.64	18.53	18.19	15.81	15.03
37785	196.91194	32.16745	16.68	17.98	17.41	18.74	17.66	14.52	13.22
69378	196.91661	27.23722	16.75	17.33	18.64	18.44	17.96	15.34	16.45
01656	197.50242	13.49651	18.16	17.96	17.0	18.58	18.22	15.78	15.18
65988	198.38023	4.20842	19.19	18.97	18.64	19.43	18.49	16.89	15.48
85709	198.56804	44.83602	17.13	18.97	17.04	18.74	18.38	16.16	14.8
70623	199.06637	43.35536	17.38	16.63	18.64	18.66	18.83	16.64	15.64
77967	201.26519	21.19272	17.08	17.12	17.55	17.69	16.74	13.57	12.22
98777	202.07039	12.42069	16.44	17.81	17.18	18.61	18.98	16.72	16.45
15410	202.74064	32.63404	17.41	17.56	18.64	20.08	20.24	17.24	14.98
92082	205.37167	13.53758	16.74	17.04	18.64	18.42	17.91	16.28	15.45
57761	205.42495	39.37282	17.82	18.03	18.64	18.97	18.57	16.07	16.45
38135	206.43421	19.60874	16.86	18.97	17.48	18.24	17.52	15.41	14.13
27029	207.11579	21.48265	19.19	17.53	18.64	18.62	18.35	15.56	14.1

Table A.2 Continued from previous page

ObjID	ra	dec	J	H	K	W1	W2	W3	W4
31525	207.33599	37.68821	16.39	17.68	17.41	18.1	17.89	15.39	15.58
52556	207.60085	21.13838	17.28	17.75	17.4	18.87	18.08	15.89	14.94
65323	207.98294	3.42342	19.19	18.97	17.78	21.79	21.04	18.72	15.65
88235	208.89063	32.53142	16.52	17.62	16.87	18.57	18.32	15.28	14.32
13964	209.33999	5.75788	18.21	16.98	18.64	18.61	18.38	16.11	16.45
74742	210.62136	6.05638	17.43	17.27	17.76	18.85	18.53	16.55	16.45
36125	210.79584	43.90542	17.2	17.76	17.76	17.17	16.25	14.84	13.67
23218	211.19882	40.64636	17.26	17.47	18.64	18.83	18.22	16.36	14.83
37848	211.55951	19.82198	17.09	17.31	17.56	19.04	18.63	16.87	16.45
56415	212.84126	47.48035	17.06	17.63	18.64	19.6	19.08	16.49	15.16
02152	212.85968	12.34055	16.57	18.97	18.64	18.35	18.08	16.65	15.56
94209	212.94217	6.74853	19.19	18.97	17.7	19.25	18.69	17.01	16.45
82365	213.56862	47.74157	17.41	18.16	18.64	21.79	18.89	18.72	16.45
48839	214.93448	40.8057	15.89	16.28	16.4	17.27	16.9	14.15	12.89
02547	215.87213	38.19445	16.25	16.68	17.22	17.69	17.18	14.75	14.75
02494	216.29605	42.25727	17.95	17.86	17.34	18.58	18.82	16.4	15.5
49356	216.49678	41.20787	16.97	17.52	18.64	18.12	17.7	15.53	14.43
46852	216.93997	14.028	17.97	18.97	18.64	18.38	17.9	15.75	15.66
99418	217.16303	33.39596	16.5	17.43	17.16	17.94	17.74	15.29	14.64
52057	218.97057	4.61712	17.19	18.97	18.64	19.27	18.22	15.92	14.72
91412	221.73053	7.75607	17.43	18.97	18.64	18.77	18.41	15.97	14.77
29786	224.25632	22.86286	17.39	18.97	17.13	18.87	18.64	16.35	15.39

Table A.2 Continued from previous page

ObjID	ra	dec	J	H	K	W1	W2	W3	W4
76856	224.62693	6.3341	17.38	18.97	18.64	18.77	18.42	16.04	16.45
69711	228.6996	20.59306	18.14	17.21	18.64	18.38	18.21	15.64	14.82
70402	229.10675	38.52991	17.05	17.64	17.86	17.76	17.21	15.54	16.45
30095	229.64305	36.27272	16.71	17.2	16.98	17.78	17.19	14.75	13.82
08961	230.32268	37.09914	16.97	17.51	17.46	21.79	21.04	18.72	16.45
25783	231.61955	28.29079	19.19	17.27	18.64	18.24	17.1	15.87	15.51
76079	235.02877	24.51249	16.27	17.21	17.23	18.3	17.98	15.64	14.43
75848	236.38473	40.96762	16.99	17.72	17.44	18.08	17.47	15.58	15.03
95952	237.44271	7.92046	19.19	18.97	17.66	19.81	18.68	16.47	15.18
08586	238.20283	16.98562	17.86	17.55	17.42	18.73	18.92	16.5	16.45
43200	238.64018	28.68668	16.89	17.89	18.64	18.84	17.97	16.24	15.21
16795	239.42926	34.55878	19.19	17.95	18.64	18.56	18.42	16.46	16.45
83121	242.09655	12.54962	16.86	17.73	16.76	18.42	18.2	15.47	15.54
30446	242.40841	4.75281	18.01	16.71	17.6	18.47	17.99	15.31	14.9
28730	243.4572	14.11566	17.15	17.4	17.47	19.32	17.93	16.67	15.51
54077	250.648	42.39715	17.3	18.97	16.42	18.38	17.78	15.39	14.16
27825	251.40989	28.98597	16.8	16.92	17.36	19.29	19.1	17.13	16.45
13995	316.63522	-7.5139	19.19	17.27	17.19	19.2	18.5	17.42	15.47
08959	332.01197	13.22626	19.19	18.97	18.64	18.87	17.83	15.52	14.85
54609	332.98331	-9.53977	16.17	16.74	16.4	17.18	17.14	14.52	14.18
27473	336.64663	-9.68499	17.92	18.97	18.64	19.35	19.3	16.97	15.64
60392	337.13304	-9.46809	17.16	18.09	18.64	17.54	18.07	15.94	15.19

Table A.2 Continued from previous page

ObjID	ra	dec	J	H	K	W1	W2	W3	W4
71294	340.88031	-9.44735	17.89	18.97	17.16	18.75	18.72	15.96	15.01
16911	344.79825	-8.77026	16.34	16.74	17.33	17.59	17.89	14.62	13.36
77821	346.21707	-8.6318	16.4	16.55	16.94	17.96	18.14	15.49	15.26
10045	349.66038	-10.50532	19.19	18.97	17.13	18.68	18.62	16.46	16.45
54061	355.41867	-8.71988	15.94	16.47	16.56	16.85	17.19	14.75	14.49
33326	358.81388	-10.97455	15.53	16.09	16.26	16.7	17.0	14.52	14.22
10880	359.0195	-8.9065	16.86	18.97	18.64	19.05	19.28	16.43	16.45

Table A.3: Results from the SED fitting described in chapter 2. Predictions of the W3 and W4 apparent magnitudes are included. The best-fitting values ('best') for mass (in $\log_{10}(M/M_{\odot})$), age (in $\log_{10}$(yrs)), and dust content (as $E(B-V)$) are shown. The upper ('max') and lower ('min') limits on these physical properties were derived by determining the maximum and minimum values which lie within 1σ of the lowest χ^2 value (the exact number for this interval depends on the degrees of freedom, which was taken as 6 in this case). All results are based on fitting the BPASS stellar population synthesis code.

ObjID	ra	dec	W3 (predict)	W4 (predict)	mass min	mass best	mass max	age min	age best	age max	dust min	dust best	dust max
23734	1.16389	-10.15264	16.9	15.91	6.8	7.2	10.0	8.1	8.3	9.4	0.00	0.1	0.2
58754	2.19214	-9.25568	16.36	15.77	6.6	8.7	10.0	9.1	10.2	10.5	0.05	0.15	0.3
05815	8.65174	-9.57551	15.41	14.31	8.4	10.0	10.0	10.0	10.4	10.4	0.15	0.15	0.25
19220	14.6789	-9.68398	16.54	15.9	6.3	9.6	10.0	8.7	10.1	10.3	0.15	0.25	0.4
92589	19.37123	-8.73437	16.78	16.1	6.6	8.3	10.0	9.0	9.9	10.3	0.00	0.05	0.15
49226	20.59955	15.34222	16.18	15.4	6.6	7.9	10.0	8.7	9.4	10.1	0.05	0.15	0.2
02555	25.19056	13.88476	16.33	15.63	7.3	8.5	10.0	9.3	10.0	10.3	0.10	0.15	0.25
08755	25.58712	-8.76605	15.85	15.12	6.8	8.1	10.0	9.0	9.7	10.3	0.10	0.2	0.3
32420	25.70536	-9.60746	16.0	15.26	6.5	8.7	10.0	9.1	10.2	10.5	0.10	0.15	0.3
62100	26.84033	-9.27951	16.44	15.59	6.8	7.3	10.0	8.4	8.7	9.7	0.00	0.15	0.2
51350	27.06657	-10.00187	15.2	14.65	6.8	7.9	10.0	9.3	10.0	10.6	0.15	0.3	0.35
05083	27.9936	-9.38417	16.59	15.78	7.4	8.7	10.0	9.2	9.9	10.2	0.10	0.15	0.25
04483	28.72465	13.12268	16.99	16.04	6.8	8.1	10.0	8.5	9.1	9.7	0.00	0.1	0.2
45691	29.97112	-8.23027	17.45	16.71	6.9	7.6	10.0	8.4	8.9	9.6	0.00	0.05	0.1
72856	33.14848	-9.63883	16.4	15.61	6.9	8.0	10.0	8.8	9.4	10.0	0.05	0.15	0.2
24784	35.15693	-9.48536	15.47	14.52	6.1	6.7	10.0	8.3	8.5	9.6	0.00	0.2	0.2
92239	37.28071	-8.95727	17.02	16.38	6.5	8.5	10.0	8.8	9.8	10.2	0.00	0.1	0.2

Table A.3 Continued from previous page

ObjID	ra	dec	W3 (predict)	W4 (predict)	mass min	mass best	mass max	age min	age best	age max	dust min	dust best	dust max
27888	47.59977	-8.57579	15.42	13.9	6.8	7.0	10.0	7.9	8.0	8.8	0.00	0.2	0.25
00364	57.10974	-6.09997	16.76	16.02	6.4	8.6	10.0	8.7	9.8	10.2	0.10	0.15	0.3
78659	60.53695	-5.11169	17.2	16.39	7.5	8.7	10.0	9.2	9.9	10.1	0.00	0.05	0.15
76428	111.6581	39.76609	17.63	16.67	6.5	8.6	10.0	8.5	9.4	9.8	0.00	0.05	0.2
34524	112.65454	39.14399	16.82	16.01	7.6	8.9	10.0	9.2	9.9	10.1	0.10	0.15	0.25
83073	115.62922	21.33423	17.06	16.05	6.7	8.8	10.0	8.6	9.6	9.8	0.05	0.1	0.3
29921	121.91403	31.20504	16.3	15.36	8.0	8.8	10.0	9.6	10.0	10.2	0.05	0.1	0.15
67086	122.2703	28.91937	16.76	15.85	7.9	9.9	10.0	9.4	10.0	10.1	0.10	0.15	0.25
23117	123.59461	25.72017	16.34	15.43	6.6	8.7	10.0	8.8	9.8	10.1	0.15	0.2	0.35
80920	125.31913	40.95998	17.04	16.15	7.4	8.6	10.0	9.0	9.6	9.9	0.00	0.1	0.2
99943	126.02675	31.15663	15.54	14.87	7.7	8.8	10.0	10.0	10.5	10.7	0.15	0.2	0.3
37625	126.46233	41.28621	16.67	15.9	7.6	8.8	10.0	9.4	10.1	10.3	0.05	0.1	0.2
68579	128.32456	3.91666	16.25	15.49	6.6	8.7	10.0	9.0	10.0	10.3	0.15	0.2	0.35
15004	128.45934	45.82598	17.1	16.48	6.5	8.3	10.0	8.6	9.6	10.1	0.00	0.1	0.2
80573	128.92412	10.29985	16.0	15.0	8.1	9.0	10.0	9.6	10.0	10.2	0.15	0.2	0.25
72555	129.2505	39.10582	17.06	16.2	7.8	8.7	10.0	9.4	9.8	10.1	0.00	0.05	0.15
14358	129.51555	44.98343	17.34	16.56	7.0	7.9	10.0	8.6	9.2	9.7	0.00	0.05	0.1
71699	129.55936	46.0701	15.99	15.06	8.2	9.0	10.0	9.8	10.2	10.3	0.15	0.15	0.2
67337	131.91766	23.40459	16.3	15.44	7.7	8.9	10.0	9.4	10.0	10.2	0.20	0.25	0.35
95211	134.07263	4.84664	16.83	16.13	7.3	8.8	10.0	9.2	9.9	10.2	0.15	0.2	0.3
19287	135.21178	40.20606	16.67	15.81	8.1	8.9	10.0	9.6	10.0	10.2	0.05	0.1	0.15

Table A.3 Continued from previous page

ObjID	ra	dec	W3 (predict)	W4 (predict)	mass min	mass best	mass max	age min	age best	age max	dust min	dust best	dust max
52087	135.24699	40.61407	16.45	15.6	7.7	8.6	10.0	9.3	9.8	10.1	0.10	0.15	0.25
31056	135.42306	8.69206	15.86	14.94	7.9	8.7	10.0	9.6	10.0	10.3	0.10	0.15	0.2
11996	136.2786	22.64276	17.33	16.47	6.9	8.1	10.0	8.5	9.2	9.8	0.00	0.05	0.15
41882	136.71599	41.36413	16.54	15.67	7.6	8.8	10.0	9.3	9.9	10.1	0.05	0.15	0.25
38857	137.37213	6.55441	15.94	15.29	6.7	8.0	10.0	9.0	9.7	10.3	0.05	0.15	0.2
49722	138.16125	8.42735	16.42	15.68	6.7	8.1	10.0	8.9	9.6	10.1	0.00	0.1	0.2 05091
138.50597	7.34669	15.83	15.17	7.5	8.4	10.0	9.6	10.1	10.5	0.15	0.2	0.25	
42268	138.69192	13.10132	16.76	15.97	7.8	9.0	10.0	9.6	10.1	10.2	0.05	0.1	0.2
19230	140.97096	7.85343	16.64	16.0	6.6	8.5	10.0	8.9	9.9	10.3	0.05	0.15	0.25
76391	141.24336	16.6267	16.01	15.33	6.7	8.7	10.0	9.2	10.2	10.5	0.15	0.2	0.35
47307	141.30575	32.07227	16.75	15.9	7.8	8.6	10.0	9.3	9.7	10.0	0.10	0.15	0.2
86374	141.58014	46.93213	15.66	15.01	7.0	8.2	10.0	9.3	10.0	10.5	0.10	0.2	0.3
57993	143.6293	26.28542	16.45	15.59	7.6	8.5	10.0	9.2	9.7	10.1	0.10	0.15	0.25
66254	144.25762	24.44382	19.15	18.73	7.5	8.8	10.0	9.2	9.8	10.0	0.00	0.0	0.1
21702	147.18303	15.45254	16.42	15.62	6.8	8.4	10.0	8.9	9.7	10.1	0.10	0.15	0.25
80781	148.35907	12.72934	15.94	15.05	7.8	8.6	10.0	9.5	10.0	10.2	0.10	0.15	0.2
39595	149.84	31.96639	16.53	15.6	7.8	8.6	10.0	9.3	9.7	10.1	0.05	0.1	0.2
41896	150.18236	5.08837	15.67	14.82	7.6	8.4	10.0	9.5	9.9	10.3	0.15	0.2	0.25
17906	150.21726	38.51584	16.94	16.15	6.5	8.1	10.0	8.5	9.3	9.9	0.00	0.1	0.2
46138	150.77536	20.79887	16.7	15.86	7.8	8.6	10.0	9.5	9.9	10.2	0.00	0.05	0.1
88577	150.90098	47.8581	16.56	15.61	7.8	8.9	10.0	9.4	9.9	10.1	0.05	0.1	0.2

Table A.3 Continued from previous page

ObjID	ra	dec	W3 (predict)	W4 (predict)	mass min	mass best	mass max	age min	age best	age max	dust min	dust best	dust max
72408	151.5014	44.66506	17.57	16.76	7.7	8.5	10.0	9.1	9.6	9.9	0.00	0.05	0.1
43940	152.03788	46.19387	16.05	15.35	7.5	8.5	10.0	9.5	10.0	10.4	0.10	0.2	0.3
72317	152.21954	21.45792	17.88	17.11	7.6	8.8	10.0	9.1	9.7	9.9	0.00	0.05	0.15
59679	153.26224	34.271	17.19	16.54	7.4	8.4	10.0	9.2	9.8	10.2	0.00	0.05	0.15
31771	154.7621	5.85705	16.76	16.06	7.4	8.8	10.0	9.4	10.1	10.3	0.05	0.1	0.2
05793	154.92305	33.51315	16.56	15.63	7.5	8.5	10.0	9.0	9.6	10.0	0.05	0.15	0.25
97155	154.97513	4.45409	16.42	15.76	6.8	8.5	10.0	9.0	9.9	10.3	0.15	0.2	0.3
48854	155.35233	35.7748	16.15	15.54	6.6	9.1	10.0	8.9	9.7	10.2	0.05	0.15	0.25
72523	156.45161	36.3829	16.76	15.91	6.5	7.9	10.0	8.6	9.3	9.8	0.00	0.05	0.1
33387	157.35096	35.88161	16.98	16.32	7.5	9.0	10.0	9.4	10.2	10.3	0.05	0.1	0.2
46300	158.52743	5.51848	17.01	16.33	7.4	8.3	10.0	9.3	9.8	10.2	0.00	0.05	0.1
31994	159.05833	28.56038	17.2	16.24	8.1	10.0	10.0	9.5	10.0	10.1	0.05	0.05	0.15
05800	159.09207	44.26913	15.87	15.0	7.6	8.5	10.0	9.4	9.9	10.3	0.10	0.2	0.3
19777	159.8884	30.99103	16.61	15.62	7.6	9.1	10.0	9.3	10.0	10.1	0.05	0.1	0.25
94468	162.42734	31.19139	16.06	15.24	6.9	7.8	10.0	8.8	9.3	10.0	0.10	0.2	0.25
88629	162.62603	48.34874	17.77	17.01	7.2	8.2	10.0	8.7	9.3	9.8	0.00	0.05	0.1
87146	164.36175	29.27005	17.66	16.97	6.7	8.7	10.0	8.8	9.8	10.1	0.00	0.05	0.2
79737	167.30938	23.77849	16.83	16.0	7.0	8.2	10.0	8.7	9.4	9.9	0.00	0.1	0.15
00205	168.53985	36.53985	19.2	18.84	6.7	8.9	10.0	8.9	10.0	10.2	0.00	0.0	0.15
60185	169.23569	32.76928	17.95	17.3	7.7	9.3	10.0	9.3	10.1	10.1	0.05	0.05	0.15
97269	170.57018	30.5129	16.19	15.23	7.7	8.7	10.0	9.4	9.9	10.1	0.10	0.15	0.25

Table A.3 Continued from previous page

ObjID	ra	dec	W3 (predict)	W4 (predict)	mass min	mass best	mass max	age min	age best	age max	dust min	dust best	dust max
30847	171.13865	25.44768	15.98	15.09	8.0	8.9	10.0	9.7	10.2	10.3	0.10	0.15	0.2
91891	171.31934	18.04925	17.33	16.78	6.8	8.2	10.0	8.8	9.7	10.2	0.00	0.05	0.15
14657	171.32926	19.19115	16.65	15.93	7.0	8.2	10.0	8.9	9.6	10.1	0.05	0.15	0.2
92876	171.44342	20.44942	16.89	16.23	6.7	9.1	10.0	9.0	10.2	10.3	0.05	0.1	0.25
58757	173.39503	45.4643	16.34	15.4	7.6	9.0	10.0	9.3	9.9	10.1	0.20	0.25	0.35
40416	174.01485	10.09028	17.02	16.22	6.8	8.5	10.0	8.7	9.6	10.0	0.00	0.1	0.2
77424	174.03521	48.59255	16.55	15.66	7.5	8.4	10.0	9.2	9.6	10.0	0.05	0.1	0.15
37518	174.90376	39.98296	17.37	16.51	7.6	8.8	10.0	9.2	9.8	10.0	0.00	0.05	0.15
32360	175.40621	33.74326	17.82	17.0	7.5	8.8	10.0	9.0	9.7	9.9	0.00	0.05	0.15
17599	175.61985	7.95264	17.42	16.58	7.3	8.2	10.0	8.8	9.3	9.8	0.00	0.05	0.1
35368	176.59336	45.47085	17.63	16.98	7.4	8.6	10.0	9.2	9.8	10.2	0.00	0.05	0.15
74772	177.93541	36.70623	16.82	16.14	7.7	8.7	10.0	9.5	10.0	10.3	0.05	0.1	0.2
53150	178.63296	8.57709	19.06	18.75	6.7	8.4	10.0	8.5	9.4	9.6	0.00	0.0	0.1
55849	179.62691	27.12393	17.01	16.37	6.9	8.4	10.0	8.9	9.7	10.1	0.05	0.1	0.2
80172	180.03074	26.0872	17.11	16.53	7.0	8.2	10.0	9.0	9.7	10.2	0.00	0.05	0.2
97755	180.73719	48.20063	17.61	17.05	6.5	8.5	10.0	8.7	9.8	10.2	0.00	0.05	0.2
05924	180.77237	8.86979	17.08	16.46	7.5	8.7	10.0	9.5	10.1	10.4	0.00	0.05	0.15
41786	183.48457	6.39265	16.64	16.02	7.5	8.8	10.0	9.5	10.2	10.5	0.05	0.1	0.2
82584	185.16857	47.72063	15.92	15.15	7.5	8.6	10.0	9.5	10.1	10.3	0.15	0.2	0.3
99137	185.62116	38.45572	16.49	15.58	7.7	9.1	10.0	9.3	10.0	10.2	0.10	0.15	0.25
06122	185.89012	15.57215	17.11	16.24	6.5	8.3	10.0	8.5	9.4	9.8	0.00	0.1	0.2

Table A.3 Continued from previous page

ObjID	ra	dec	W3 (predict)	W4 (predict)	mass min	mass best	mass max	age min	age best	age max	dust min	dust best	dust max
71011	186.17401	14.96796	17.42	16.62	7.3	8.4	10.0	8.9	9.5	10.0	0.00	0.05	0.15
61615	187.54429	46.97292	16.12	15.39	7.6	8.7	10.0	9.6	10.2	10.4	0.10	0.15	0.25
14769	187.77879	22.8417	17.04	16.21	6.8	8.0	10.0	8.6	9.3	9.8	0.00	0.05	0.1
76073	188.08861	29.98195	16.2	15.27	7.9	9.0	10.0	9.7	10.2	10.3	0.05	0.1	0.2
95870	189.58464	6.13415	16.66	15.69	7.5	8.6	10.0	9.1	9.6	9.9	0.10	0.15	0.25
43813	189.82162	14.8657	19.04	18.76	7.2	8.1	9.7	9.0	9.5	9.9	0.00	0.0	0.05
74272	189.87282	37.19232	17.4	16.83	6.8	8.2	10.0	8.8	9.6	10.1	0.00	0.05	0.15
29942	189.89012	49.9099	17.26	16.47	6.7	8.7	10.0	8.6	9.7	10.0	0.05	0.1	0.25
16982	190.22721	35.90026	16.0	15.37	7.6	8.8	10.0	9.8	10.3	10.6	0.15	0.2	0.3
90130	190.30411	49.54553	16.34	15.34	7.9	8.9	10.0	9.4	9.8	10.0	0.15	0.2	0.3
44692	191.08636	35.83436	16.23	15.53	6.6	8.5	10.0	9.0	10.0	10.4	0.05	0.15	0.25
19697	193.11618	31.71308	18.46	18.16	7.5	8.2	9.7	9.1	9.4	9.7	0.00	0.0	0.05
45022	193.66131	22.98316	17.62	16.73	7.7	9.1	10.0	9.2	9.8	10.0	0.00	0.05	0.15
53307	195.25666	40.07222	16.8	15.99	7.4	8.2	10.0	9.0	9.5	10.0	0.00	0.1	0.15
04816	196.12796	31.89517	16.69	16.03	7.5	8.8	10.0	9.5	10.2	10.4	0.05	0.1	0.2
37785	196.91194	32.16745	16.66	15.73	6.8	8.5	10.0	8.7	9.6	10.0	0.05	0.1	0.2
69378	196.91661	27.23722	16.04	15.32	8.0	8.8	10.0	9.8	10.2	10.5	0.15	0.2	0.25
01656	197.50242	13.49651	16.17	15.32	6.7	8.4	10.0	8.8	9.7	10.2	0.10	0.2	0.3
65988	198.38023	4.20842	19.82	19.38	7.6	9.0	10.0	9.1	9.8	9.9	0.00	0.0	0.1
85709	198.56804	44.83602	16.44	15.6	7.5	8.6	10.0	9.2	9.8	10.1	0.15	0.2	0.3
70623	199.06637	43.35536	16.0	15.05	7.6	8.6	10.0	9.3	9.8	10.2	0.10	0.2	0.3

Table A.3 Continued from previous page

ObjID	ra	dec	W3 (predict)	W4 (predict)	mass min	mass best	mass max	age min	age best	age max	dust min	dust best	dust max
77967	201.26519	21.19272	16.18	15.5	7.6	8.4	10.0	9.6	10.0	10.4	0.00	0.1	0.15
98777	202.07039	12.42069	16.77	15.84	7.4	8.0	10.0	8.9	9.3	9.8	0.00	0.05	0.1
15410	202.74064	32.63404	17.45	16.51	6.7	7.8	10.0	8.3	8.8	9.4	0.00	0.05	0.15
92082	205.37167	13.53758	18.99	18.57	7.6	8.6	10.0	9.2	9.7	10.0	0.00	0.0	0.1
57761	205.42495	39.37282	17.22	16.3	7.9	9.3	10.0	9.3	9.9	9.9	0.10	0.1	0.2
38135	206.43421	19.60874	16.75	16.15	7.4	8.7	10.0	9.4	10.1	10.4	0.05	0.1	0.2
27029	207.11579	21.48265	17.51	16.59	6.8	8.1	10.0	8.4	9.0	9.6	0.00	0.05	0.15
31525	207.33599	37.68821	15.31	14.39	7.9	8.7	10.0	9.8	10.2	10.5	0.15	0.2	0.25
52556	207.60085	21.13838	16.7	16.08	6.7	8.1	10.0	8.8	9.6	10.2	0.00	0.1	0.2
65323	207.98294	3.42342	17.24	16.4	6.8	8.0	10.0	8.5	9.2	9.6	0.00	0.05	0.15
88235	208.89063	32.53142	16.66	15.98	6.9	7.9	10.0	9.0	9.6	10.0	0.00	0.05	0.1
13964	209.33999	5.75788	17.24	16.59	7.4	8.6	10.0	9.3	10.0	10.3	0.00	0.05	0.15
74742	210.62136	6.05638	16.13	15.1	7.9	9.1	10.0	9.5	10.0	10.1	0.25	0.25	0.35
36125	210.79584	43.90542	14.84	13.94	6.4	6.7	10.0	8.6	8.7	9.9	0.15	0.3	0.35
23218	211.19882	40.64636	16.87	16.06	7.6	8.8	10.0	9.3	9.9	10.1	0.05	0.1	0.2
37848	211.55951	19.82198	17.46	16.62	7.7	8.8	10.0	9.3	9.8	10.0	0.00	0.05	0.15
56415	212.84126	47.48035	17.74	16.96	7.4	8.7	10.0	9.0	9.7	10.0	0.00	0.05	0.15
02152	212.85968	12.34055	16.16	15.36	7.0	8.2	10.0	9.0	9.7	10.2	0.00	0.1	0.2
94209	212.94217	6.74853	16.99	16.04	6.6	8.6	10.0	8.6	9.6	9.9	0.05	0.1	0.25
82365	213.56862	47.74157	17.21	16.46	7.5	8.5	10.0	9.2	9.8	10.1	0.00	0.05	0.1
48839	214.93448	40.8057	15.32	14.36	8.0	8.6	10.0	9.8	10.1	10.4	0.10	0.15	0.2

Table A.3 Continued from previous page

ObjID	ra	dec	W3 (predict)	W4 (predict)	mass min	mass best	mass max	age min	age best	age max	dust min	dust best	dust max
02547	215.87213	38.19445	15.29	14.34	8.3	9.0	10.0	10.1	10.4	10.5	0.15	0.2	0.25
02494	216.29605	42.25727	16.09	15.25	7.5	9.1	10.0	9.4	10.0	10.2	0.20	0.25	0.35
49356	216.49678	41.20787	16.58	15.8	7.9	9.3	10.0	9.7	10.3	10.4	0.05	0.1	0.2
46852	216.93997	14.028	16.58	15.84	7.8	9.1	10.0	9.7	10.3	10.4	0.05	0.1	0.2
99418	217.16303	33.39596	17.09	16.34	7.4	8.7	10.0	9.3	10.0	10.3	0.00	0.05	0.15
52057	218.97057	4.61712	16.61	15.85	7.3	8.2	10.0	9.0	9.5	10.0	0.05	0.15	0.2
91412	221.73053	7.75607	17.05	16.26	6.7	8.3	10.0	8.8	9.6	10.1	0.00	0.05	0.15
29786	224.25632	22.86286	16.52	15.55	6.7	8.7	10.0	8.8	9.7	10.0	0.10	0.15	0.3
76856	224.62693	6.3341	16.53	15.63	7.7	9.1	10.0	9.3	10.0	10.1	0.15	0.2	0.3
69711	228.6996	20.59306	16.45	15.8	7.2	8.4	10.0	9.2	9.9	10.3	0.05	0.15	0.25
70402	229.10675	38.52991	15.99	15.07	7.8	8.9	10.0	9.6	10.1	10.3	0.15	0.2	0.3
30095	229.64305	36.27272	16.18	15.39	8.0	8.7	10.0	9.8	10.1	10.4	0.05	0.1	0.15
08961	230.32268	37.09914	16.74	16.15	7.4	8.7	10.0	9.5	10.1	10.4	0.05	0.1	0.2
25783	231.61955	28.29079	15.52	14.56	6.7	7.2	9.7	8.6	8.8	9.4	0.15	0.25	0.3
76079	235.02877	24.51249	17.02	16.13	7.5	8.6	10.0	9.2	9.7	10.1	0.00	0.05	0.15
75848	236.38473	40.96762	16.86	16.29	7.4	8.6	10.0	9.6	10.2	10.5	0.00	0.05	0.15
95952	237.44271	7.92046	17.08	16.5	6.8	8.2	10.0	8.8	9.6	10.1	0.00	0.1	0.2
08586	238.20283	16.98562	16.81	16.02	6.7	8.7	10.0	8.8	9.9	10.2	0.00	0.1	0.25
43200	238.64018	28.68668	17.48	16.9	6.9	8.3	10.0	8.8	9.7	10.1	0.00	0.05	0.15
16795	239.42926	34.55878	17.41	16.68	7.3	8.3	10.0	9.0	9.6	10.0	0.00	0.05	0.1
83121	242.09655	12.54962	16.01	15.38	7.6	8.8	10.0	9.8	10.4	10.6	0.10	0.15	0.25

Table A.3 Continued from previous page

ObjID	ra	dec	W3 (predict)	W4 (predict)	mass min	mass best	mass max	age min	age best	age max	dust min	dust best	dust max
30446	242.40841	4.75281	15.72	14.86	7.8	8.6	10.0	9.6	10.0	10.4	0.15	0.2	0.25
28730	243.4572	14.11566	17.42	16.55	6.7	8.1	10.0	8.4	9.2	9.7	0.00	0.05	0.15
54077	250.648	42.39715	16.13	15.35	7.0	8.1	10.0	9.0	9.7	10.1	0.05	0.1	0.15
27825	251.40989	28.98597	16.52	15.66	7.3	8.7	10.0	9.1	9.8	10.2	0.05	0.15	0.3
13995	316.63522	-7.5139	17.48	16.66	6.5	8.6	10.0	8.6	9.6	10.0	0.00	0.05	0.2
08959	332.01197	13.22626	17.03	16.12	6.0	8.1	10.0	8.5	9.3	9.8	0.00	0.05	0.2
54609	332.98331	-9.53977	15.71	15.16	6.9	7.3	10.0	9.0	9.3	10.1	0.10	0.2	0.3
27473	336.64663	-9.68499	17.17	15.91	6.0	8.7	10.0	8.3	9.2	9.5	0.05	0.1	0.3
60392	337.13304	-9.46809	15.9	14.94	7.8	9.8	10.0	9.6	10.3	10.3	0.15	0.2	0.3
71294	340.88031	-9.44735	16.11	15.31	6.8	7.7	10.0	8.7	9.2	10.0	0.05	0.15	0.2
16911	344.79825	-8.77026	15.45	14.31	6.7	8.6	10.0	9.0	9.8	10.2	0.10	0.15	0.3
77821	346.21707	-8.6318	15.47	14.52	7.7	8.4	10.0	9.5	9.9	10.3	0.15	0.2	0.25
10045	349.66038	-10.50532	16.01	15.15	6.6	7.5	10.0	8.5	9.0	9.9	0.05	0.2	0.25
54061	355.41867	-8.71988	18.71	18.45	6.9	7.2	9.7	7.9	8.0	8.5	0.00	0.0	0.1
33326	358.81388	-10.97455	15.14	13.69	6.9	7.2	9.7	8.2	8.4	8.9	0.20	0.3	0.4
10880	359.0195	-8.9065	16.82	16.12	6.5	7.8	10.0	8.6	9.2	9.9	0.00	0.1	0.15

Table A.4: Additional results for the galaxies investigated in chapter 2, using spectroscopic measurements obtained from archival SDSS observations. The metallicities are derived using optical line ratios in the galaxies and applying the Dopita et al. [2016] metallicity diagnostics. They are converted to fractional Solar metallicities by assuming the local Galactic concordance value of 12+log(O/H)=8.77. The ultraviolet SFRs are derived using the Madau et al. [1998] prescription at 1500 Å for a Salpeter IMF. SFRs based on the SDSS *u*-band photometry are found using the calibration of Hopkins et al. [2003]. The star-formation rates inferred from the infrared bands were found using the empirical Lee et al. [2013] prescription for *W3* and *W4*. I also use the calibration of Cluver et al. [2014], which is based on the local GAMA galaxy survey, to calculate a further *W4* SFR. The star formation rates from Hα and [O II] fluxes are calculated using standard conversion factors (Kewley et al. [2004], see also Kennicutt [1998]). All but the *W3* and *W4* SFRs are dust-corrected using the Balmer-decrement derived dust reddening, for which an Hα/Hβ line ratio of 2.86 (for case B recombination, at a temperature of 10^4 K and an electron density of n_e= 10^2 cm^{-3}) is assumed. All SFRs are shown in $M_\odot$ yr^{-1}.

ObjID	ra	dec	Metallicity	$Z_\odot$	UV SFR	u SFR	W3 SFR	W4 (Lee) SFR	W4 (Cluver) SFR	Hα SFR	OII SFR	MPA SFR	dust Balmer
23734	1.16389	-10.15264	8.308	0.345	6.451	3.033	3.632	2.684	1.648	10.089	9.225	6.930	0.233
58754	2.19214	-9.25568	8.770	1.000	25.855	45.972	12.937	8.265	4.308	15.734	11.455	13.348	0.138
05815	8.65174	-9.57551	8.678	0.808	10.199	17.299	6.879	4.297	2.464	7.909	5.889	8.191	0.243
19220	14.6789	-9.68398	8.934	1.460	93.106	136.202	2.888	3.090	1.859	2.481	0.886	2.919	0.161
92589	19.37123	-8.73437	8.163	0.247	26.298	21.681	8.117	8.061	4.216	15.583	10.808	13.630	0.037
49226	20.59955	15.34222	8.471	0.502	20.171	23.737	7.674	9.002	4.633	13.859	7.192	5.697	0.091
02555	25.19056	13.88476	8.227	0.286	22.706	30.859	3.885	4.110	2.372	5.360	4.830	5.367	0.055
08755	25.58712	-8.76605	8.444	0.472	27.939	47.973	9.930	8.810	4.549	15.373	12.264	12.774	0.187
32420	25.70536	-9.60746	8.534	0.581	19.384	37.397	13.724	12.505	6.135	41.063	43.337	17.084	0.342
62100	26.84033	-9.27951	7.835	0.116	14.386	10.880	2.145	1.736	1.136	5.064	3.475	2.515	0.006
51350	27.06657	-10.00187	8.943	1.489	151.512	305.329	4.461	1.217	0.839	22.640	2.902	11.547	0.700
05083	27.9936	-9.38417	8.298	0.337	11.900	14.757	2.560	4.193	2.412	7.997	6.715	5.527	0.121

Table A.4 Continued from previous page

ObjID	ra	dec	Metallicity	$Z_\odot$	UV SFR	u SFR	W3 SFR	W4 (Lee) SFR	W4 (Cluver) SFR	Hα SFR	OII SFR	MPA SFR	dust Balmer
04483	28.72465	13.12268	7.888	0.131	5.450	4.603	0.241	0.521	0.406	3.497	3.257	2.219	0.073
45691	29.97112	-8.23027	8.036	0.184	12.186	5.607	2.135	3.052	1.839	6.953	3.656	4.305	0.010
72856	33.14848	-9.63883	8.156	0.243	16.916	16.411	4.722	2.317	1.454	4.853	4.418	3.678	0.089
24784	35.15693	-9.48536	8.314	0.350	6.661	5.104	4.044	4.942	2.776	6.674	3.178	3.349	0.040
92239	37.28071	-8.95727	7.990	0.166	17.667	19.125	2.751	1.633	1.078	9.532	6.419	6.036	0.035
27888	47.59977	-8.57579	8.039	0.186	3.841	1.963	0.037	0.331	0.276	0.852	0.475	0.656	-0.039
00364	57.10974	-6.09997	8.586	0.655	14.171	16.740	2.503	1.016	0.719	7.097	5.096	4.771	0.172
78659	60.53695	-5.11169	8.169	0.251	10.265	8.417	0.737	0.710	0.529	2.039	1.971	4.254	-0.035
76428	111.6581	39.76609	8.432	0.459	4.426	2.672	7.481	3.977	2.306	7.674	3.584	4.597	0.117
34524	112.65454	39.14399	8.413	0.439	10.497	9.851	0.385	0.778	0.572	2.727	2.545	2.791	0.096
83073	115.62922	21.33423	7.921	0.142	4.080	3.886	0.203	1.260	0.864	2.507	2.193	2.409	0.037
29921	121.91403	31.20504	8.042	0.187	11.316	11.475	1.450	1.237	0.850	4.593	4.235	4.783	0.101
67086	122.2703	28.91937	8.560	0.617	7.705	7.061	2.097	1.161	0.806	2.420	2.157	1.725	0.161
23117	123.59461	25.72017	8.249	0.302	10.014	14.684	3.876	2.877	1.749	6.225	4.817	4.466	0.118
80920	125.31913	40.95998	8.345	0.376	8.007	6.131	1.609	0.898	0.647	3.410	2.891	3.842	0.071
99943	126.02675	31.15663	8.879	1.284	41.027	94.882	9.519	2.934	1.778	2.720	1.237	4.646	0.197
37625	126.46233	41.28621	8.303	0.341	12.540	15.517	5.143	3.788	2.212	6.789	6.769	7.751	0.156
68579	128.32456	3.91666	8.428	0.455	15.801	32.984	0.712	0.948	0.678	6.917	7.017	5.537	0.190
15004	128.45934	45.82598	8.180	0.257	15.942	15.761	12.837	14.761	7.069	21.528	15.094	14.206	0.132
80573	128.92412	10.29985	8.604	0.682	9.761	14.563	1.989	0.642	0.485	1.782	1.396	2.789	0.114
72555	129.2505	39.10582	8.249	0.301	7.980	6.996	1.735	1.027	0.726	3.847	3.668	5.450	0.093

Table A.4 Continued from previous page

ObjID	ra	dec	Metallicity	$Z_\odot$	UV SFR	u SFR	W3 SFR	W4 (Lee) SFR	W4 (Cluver) SFR	Hα SFR	OII SFR	MPA SFR	dust Balmer
14358	129.51555	44.98343	8.093	0.210	11.551	6.470	1.531	1.345	0.913	5.874	4.212	3.473	0.023
71699	129.55936	46.0701	8.652	0.763	13.264	17.033	6.022	3.114	1.871	6.593	4.580	7.351	0.196
67337	131.91766	23.40459	8.869	1.257	12.954	20.941	2.834	3.157	1.893	2.939	1.839	2.486	0.162
95211	134.07263	4.84664	8.492	0.527	12.340	20.308	0.597	1.171	0.812	4.641	4.746	3.451	0.233
19287	135.21178	40.20606	8.395	0.421	10.161	9.981	3.921	5.223	2.910	5.562	5.117	5.505	0.166
52087	135.24699	40.61407	8.808	1.092	10.610	14.038	5.673	4.511	2.568	7.147	5.424	5.140	0.192
31056	135.42306	8.69206	8.395	0.422	16.156	18.811	4.666	2.801	1.709	5.628	5.257	5.592	0.171
11996	136.2786	22.64276	8.333	0.365	7.025	4.504	0.274	5.032	2.819	7.655	3.991	5.013	0.009
41882	136.71599	41.36413	8.198	0.268	9.818	12.610	3.222	3.140	1.885	5.244	5.178	3.067	0.110
38857	137.37213	6.55441	8.341	0.373	42.824	49.014	10.053	8.802	4.546	18.955	16.496	14.590	0.110
49722	138.16125	8.42735	8.611	0.694	19.300	22.478	9.997	9.008	4.636	14.749	7.920	25.716	0.108
05091	138.50597	7.34669	8.563	0.621	41.444	69.280	8.574	3.250	1.941	13.066	10.616	9.237	0.153
42268	138.69192	13.10132	8.495	0.531	10.241	12.058	5.238	5.378	2.984	7.952	5.892	7.340	0.116
19230	140.97096	7.85343	8.446	0.475	18.453	23.806	1.976	1.343	0.913	7.418	6.751	5.966	0.107
76391	141.24336	16.6267	8.666	0.788	26.858	51.506	23.850	13.440	6.525	27.352	22.089	15.601	0.313
47307	141.30575	32.07227	8.627	0.720	9.406	9.480	2.026	2.800	1.709	4.013	3.613	1.991	0.180
86374	141.58014	46.93213	8.831	1.150	37.147	83.725	13.609	10.106	5.115	11.449	8.221	8.881	0.232
57993	143.6293	26.28542	8.376	0.404	9.524	13.362	2.128	0.695	0.519	3.132	2.805	3.318	0.111
66254	144.25762	24.44382	7.990	0.166	6.926	4.759	3.247	2.866	1.743	7.017	5.405	6.266	0.068
21702	147.18303	15.45254	8.483	0.517	14.323	20.252	4.956	6.565	3.538	8.703	6.300	8.929	0.188
80781	148.35907	12.72934	8.941	1.482	17.131	23.180	10.030	8.285	4.317	7.539	4.593	11.275	0.140

Table A.4 Continued from previous page

ObjID	ra	dec	Metallicity	$Z_\odot$	UV SFR	u SFR	W3 SFR	W4 (Lee) SFR	W4 (Cluver) SFR	Hα SFR	OII SFR	MPA SFR	dust Balmer
39595	149.84	31.96639	8.169	0.251	8.450	8.120	1.707	1.959	1.260	3.880	3.316	4.207	0.109
41896	150.18236	5.08837	8.569	0.629	24.657	37.869	5.245	2.526	1.565	4.546	3.859	4.197	0.147
17906	150.21726	38.51584	8.301	0.340	8.654	9.151	3.425	5.403	2.996	8.185	5.845	7.477	0.055
46138	150.77536	20.79887	8.180	0.257	11.064	11.564	3.285	2.694	1.653	6.181	5.568	6.687	0.091
88577	150.90098	47.8581	8.347	0.378	7.748	8.143	2.113	1.566	1.040	2.975	2.719	3.808	0.146
72408	151.5014	44.66506	8.481	0.514	7.640	4.945	1.826	2.217	1.400	4.411	2.609	7.888	0.050
43940	152.03788	46.19387	8.712	0.874	15.962	25.230	0.391	0.303	0.256	8.987	6.755	6.206	0.208
72317	152.21954	21.45792	8.120	0.224	6.922	4.490	4.061	4.895	2.754	9.621	7.773	6.585	0.117
59679	153.26224	34.271	8.467	0.498	17.753	16.117	15.952	14.879	7.117	22.310	14.642	25.060	0.126
31771	154.7621	5.85705	8.207	0.273	16.622	21.057	0.586	3.617	2.126	3.773	3.873	4.910	0.079
05793	154.92305	33.51315	8.254	0.305	5.851	4.892	0.269	1.016	0.719	1.572	1.729	2.115	0.100
97155	154.97513	4.45409	8.432	0.459	23.411	34.901	5.049	2.479	1.540	8.758	8.976	5.994	0.197
72523	156.45161	36.3829	8.168	0.250	12.309	8.766	2.853	3.724	2.180	12.477	7.141	9.523	0.077
33387	157.35096	35.88161	8.468	0.499	16.059	16.552	6.182	4.333	2.481	12.539	9.289	11.124	0.181
46300	158.52743	5.51848	8.318	0.354	18.255	16.426	6.425	4.902	2.757	14.889	10.528	12.035	0.069
31994	159.05833	28.56038	8.290	0.331	4.742	3.880	2.740	3.240	1.936	4.657	3.491	6.553	0.128
05800	159.09207	44.26913	8.877	1.280	15.841	26.891	6.330	2.060	1.315	5.131	2.913	4.148	0.231
19777	159.8884	30.99103	8.554	0.608	11.526	13.406	2.328	1.420	0.957	4.536	3.527	6.379	0.123
94468	162.42734	31.19139	8.384	0.411	17.893	24.106	4.099	6.843	3.666	11.588	9.249	10.963	0.214
88629	162.62603	48.34874	8.108	0.218	7.827	4.272	1.483	2.171	1.375	8.726	7.468	5.091	0.181
87146	164.36175	29.27005	8.446	0.474	10.003	8.062	8.849	6.707	3.604	14.740	11.231	12.874	0.149

Table A.4 Continued from previous page

ObjID	ra	dec	Metallicity	$Z_\odot$	UV SFR	u SFR	W3 SFR	W4 (Lee) SFR	W4 (Cluver) SFR	Hα SFR	OII SFR	MPA SFR	dust Balmer
79737	167.30938	23.77849	8.461	0.491	11.619	9.197	9.736	10.789	5.409	11.948	7.271	21.299	0.138
00205	168.53985	36.53985	8.106	0.217	9.992	7.511	4.463	4.155	2.394	17.367	17.244	9.650	0.191
60185	169.23569	32.76928	8.598	0.673	10.834	6.463	7.581	7.658	4.036	11.023	7.183	10.253	0.110
97269	170.57018	30.5129	8.463	0.494	8.828	12.724	4.747	1.763	1.151	6.167	5.176	5.302	0.229
30847	171.13865	25.44768	8.683	0.819	15.643	19.391	5.094	1.724	1.129	4.590	3.531	3.675	0.116
91891	171.31934	18.04925	8.459	0.489	17.724	17.212	9.905	12.629	6.187	18.022	11.345	17.384	0.106
14657	171.32926	19.19115	8.408	0.435	16.571	17.641	12.184	17.600	8.215	11.194	9.772	8.686	0.151
92876	171.44342	20.44942	8.510	0.550	17.849	18.712	0.643	1.254	0.860	7.383	5.597	8.648	0.139
58757	173.39503	45.4643	8.535	0.582	8.564	16.843	3.016	1.507	1.007	2.222	1.605	1.794	0.228
40416	174.01485	10.09028	8.037	0.185	5.324	4.657	1.479	0.784	0.576	3.748	3.384	3.346	0.069
77424	174.03521	48.59255	8.323	0.358	9.983	11.078	2.756	1.870	1.210	7.928	5.453	8.909	0.099
37518	174.90376	39.98296	8.400	0.426	5.887	5.666	2.581	1.161	0.805	2.621	2.319	3.970	0.054
32360	175.40621	33.74326	7.979	0.162	4.547	3.877	0.333	1.718	1.126	5.270	4.057	3.697	0.096
17599	175.61985	7.95264	8.036	0.184	8.325	4.978	0.680	2.157	1.367	4.824	3.327	2.103	0.008
35368	176.59336	45.47085	8.465	0.495	9.585	9.779	3.185	3.099	1.864	2.817	2.013	4.079	0.028
74772	177.93541	36.70623	8.578	0.642	17.867	16.665	5.770	4.439	2.533	9.606	7.896	6.608	0.171
53150	178.63296	8.57709	8.313	0.349	6.731	3.077	3.789	5.216	2.907	10.690	6.998	8.580	0.095
55849	179.62691	27.12393	8.301	0.339	18.367	16.890	3.138	2.450	1.525	7.005	6.059	6.153	0.100
80172	180.03074	26.0872	8.484	0.518	22.888	19.165	10.139	10.148	5.133	14.810	10.399	12.989	0.108
97755	180.73719	48.20063	8.251	0.303	21.977	25.601	5.546	7.298	3.873	18.849	12.757	13.939	0.128
05924	180.77237	8.86979	8.595	0.669	16.877	17.934	9.376	6.166	3.354	14.311	9.463	14.868	0.174

Table A.4 Continued from previous page

ObjID	ra	dec	Metallicity	$Z_\odot$	UV SFR	u SFR	W3 SFR	W4 (Lee) SFR	W4 (Cluver) SFR	Hα SFR	OII SFR	MPA SFR	dust Balmer
41786	183.48457	6.39265	8.571	0.633	22.624	26.943	25.059	22.250	10.037	34.843	29.479	19.940	0.241
82584	185.16857	47.72063	8.662	0.779	24.285	43.346	3.186	0.922	0.661	14.599	13.171	10.077	0.245
99137	185.62116	38.45572	8.518	0.560	6.382	11.404	3.287	2.198	1.389	3.667	3.433	2.923	0.175
06122	185.89012	15.57215	7.999	0.169	6.842	6.475	1.121	1.716	1.125	2.936	2.106	2.453	0.003
71011	186.17401	14.96796	8.008	0.173	7.885	5.909	1.202	1.010	0.715	6.096	4.018	3.989	-0.025
61615	187.54429	46.97292	8.483	0.517	22.764	33.568	7.712	3.536	2.086	2.935	2.240	4.365	-0.062
14769	187.77879	22.8417	8.492	0.527	12.209	7.837	3.766	4.271	2.451	11.787	7.094	12.574	0.154
76073	188.08861	29.98195	8.331	0.364	12.628	12.700	2.364	1.556	1.034	2.232	2.095	3.324	-0.007
95870	189.58464	6.13415	8.076	0.202	6.469	7.041	0.611	0.695	0.520	2.577	2.579	2.380	0.131
43813	189.82162	14.8657	8.070	0.200	10.974	8.282	4.920	3.499	2.067	10.947	9.525	6.583	0.026
74272	189.87282	37.19232	8.327	0.361	16.530	15.374	8.384	4.888	2.750	13.022	10.151	12.716	0.101
29942	189.89012	49.9099	8.332	0.364	6.716	7.600	0.576	0.736	0.546	1.978	2.017	2.033	0.112
16982	190.22721	35.90026	8.806	1.085	25.820	62.155	13.031	5.827	3.196	10.593	6.196	10.263	0.259
90130	190.30411	49.54553	8.630	0.725	8.241	10.468	2.785	0.931	0.667	3.078	2.985	2.019	0.265
44692	191.08636	35.83436	8.413	0.440	20.060	37.340	9.295	5.367	2.979	16.325	12.879	15.315	0.199
19697	193.11618	31.71308	8.201	0.270	8.741	5.129	3.791	5.210	2.904	12.313	7.330	12.368	0.072
45022	193.66131	22.98316	8.023	0.179	3.712	3.550	0.694	1.614	1.067	1.383	1.467	2.107	0.047
53307	195.25666	40.07222	8.411	0.437	10.834	9.762	2.863	1.727	1.131	4.363	3.469	4.628	0.089
04816	196.12796	31.89517	8.355	0.384	15.489	22.274	7.423	5.780	3.174	14.847	12.316	13.406	0.188
37785	196.91194	32.16745	8.423	0.450	7.931	8.392	10.130	11.147	5.561	13.786	9.914	13.781	0.156
69378	196.91661	27.23722	8.615	0.700	26.518	38.636	9.192	2.556	1.581	7.797	6.821	6.819	0.223

Table A.4 Continued from previous page

ObjID	ra	dec	Metallicity	$Z_\odot$	UV SFR	u SFR	W3 SFR	W4 (Lee) SFR	W4 (Cluver) SFR	Hα SFR	OII SFR	MPA SFR	dust Balmer
01656	197.50242	13.49651	8.523	0.566	19.157	19.995	4.182	2.839	1.729	2.881	2.268	2.411	0.135
65988	198.38023	4.20842	8.372	0.400	6.815	3.337	1.795	2.113	1.343	4.141	3.359	3.978	0.068
85709	198.56804	44.83602	8.928	1.440	12.018	16.031	2.784	3.946	2.291	2.664	1.466	5.773	0.143
70623	199.06637	43.35536	8.356	0.386	9.443	18.941	1.222	1.222	0.841	3.752	3.809	3.211	0.197
77967	201.26519	21.19272	9.098	2.128	22.544	35.872	58.030	59.482	23.247	46.382	28.840	13.698	0.324
98777	202.07039	12.42069	8.164	0.248	4.158	3.318	0.967	0.796	0.584	2.649	2.115	3.339	0.025
15410	202.74064	32.63404	8.176	0.255	4.930	2.934	0.508	1.869	1.210	4.055	2.047	3.370	0.048
92082	205.37167	13.53758	8.207	0.273	8.088	5.920	2.330	2.075	1.323	4.326	3.046	5.032	0.067
57761	205.42495	39.37282	8.670	0.794	4.906	4.336	2.286	0.841	0.611	1.605	1.117	1.303	0.114
38135	206.43421	19.60874	8.440	0.468	21.371	25.775	12.578	14.833	7.099	27.982	20.708	21.427	0.135
27029	207.11579	21.48265	7.979	0.162	5.582	2.238	3.088	4.428	2.528	4.598	4.267	1.426	0.140
31525	207.33599	37.68821	8.504	0.541	23.364	47.868	4.594	1.500	1.003	7.176	6.285	6.603	0.189
52556	207.60085	21.13838	8.561	0.619	18.272	22.071	7.164	5.727	3.149	20.609	12.386	23.947	0.181
65323	207.98294	3.42342	8.433	0.461	9.672	6.463	0.294	1.929	1.243	9.522	4.752	18.352	0.059
88235	208.89063	32.53142	8.359	0.388	26.337	21.881	9.843	6.732	3.615	24.694	18.139	21.611	0.126
13964	209.33999	5.75788	8.340	0.372	15.039	14.089	5.314	2.326	1.459	7.889	6.493	9.172	0.086
74742	210.62136	6.05638	8.475	0.506	8.739	15.396	1.089	0.959	0.684	1.119	0.985	1.432	0.125
23218	211.19882	40.64636	8.182	0.258	8.499	10.244	2.492	3.719	2.178	6.531	4.491	5.750	0.085
37848	211.55951	19.82198	8.206	0.273	6.391	5.277	1.192	0.699	0.522	3.163	3.004	3.050	0.044
56415	212.84126	47.48035	7.987	0.165	7.061	5.142	2.194	2.732	1.673	7.532	5.897	5.294	0.071
02152	212.85968	12.34055	7.971	0.159	18.959	21.962	1.876	1.858	1.204	4.830	4.647	6.140	0.056

Table A.4 Continued from previous page

ObjID	ra	dec	Metallicity	$Z_\odot$	UV SFR	u SFR	W3 SFR	W4 (Lee) SFR	W4 (Cluver) SFR	Hα SFR	OII SFR	MPA SFR	dust Balmer
94209	212.94217	6.74853	8.229	0.288	6.217	4.873	0.862	0.990	0.703	2.256	2.225	2.172	0.070
82365	213.56862	47.74157	8.154	0.242	11.819	10.479	0.427	1.116	0.779	5.819	5.013	5.382	0.061
48839	214.93448	40.8057	8.923	1.423	22.712	31.108	14.285	14.006	6.759	17.976	11.100	30.749	0.264
02547	215.87213	38.19445	8.584	0.652	17.981	38.853	8.376	2.775	1.696	8.668	7.844	5.780	0.283
02494	216.29605	42.25727	8.853	1.210	17.702	26.715	2.282	2.618	1.614	3.509	2.500	2.631	0.197
49356	216.49678	41.20787	8.497	0.533	10.454	15.207	6.429	6.498	3.507	7.951	7.295	5.346	0.169
46852	216.93997	14.028	8.476	0.509	12.594	16.452	5.727	1.987	1.275	7.370	6.200	7.467	0.115
99418	217.16303	33.39596	8.351	0.381	11.530	13.775	8.427	5.266	2.931	12.109	11.674	11.295	0.162
52057	218.97057	4.61712	8.399	0.426	8.959	7.767	4.623	4.398	2.513	11.155	7.899	10.197	0.144
91412	221.73053	7.75607	8.154	0.242	11.171	8.944	3.525	3.276	1.954	9.324	7.036	5.522	0.028
29786	224.25632	22.86286	8.217	0.280	7.971	8.735	1.562	1.076	0.755	3.166	2.872	3.080	0.086
76856	224.62693	6.3341	8.625	0.715	9.029	13.641	2.704	0.453	0.361	2.743	2.204	2.011	0.134
69711	228.6996	20.59306	8.543	0.594	20.000	27.708	8.877	6.362	3.445	13.918	12.002	7.961	0.193
70402	229.10675	38.52991	8.493	0.528	10.532	20.759	4.161	1.472	0.987	2.644	2.038	2.764	0.146
30095	229.64305	36.27272	8.912	1.388	18.370	23.153	13.024	10.202	5.156	11.795	8.246	15.142	0.200
08961	230.32268	37.09914	8.424	0.451	20.748	25.340	0.518	1.531	1.020	5.857	5.427	6.461	0.128
76079	235.02877	24.51249	8.105	0.216	7.248	6.433	3.383	3.763	2.200	7.832	7.014	6.842	0.117
75848	236.38473	40.96762	8.445	0.473	20.786	28.265	10.860	5.745	3.157	10.776	9.481	10.584	0.122
95952	237.44271	7.92046	8.401	0.428	19.181	17.319	4.696	7.431	3.934	10.175	6.840	9.516	0.077
08586	238.20283	16.98562	8.196	0.267	7.742	13.393	2.482	1.467	0.984	5.049	4.103	5.519	0.063
43200	238.64018	28.68668	8.429	0.456	13.552	13.677	5.190	4.753	2.685	12.512	8.124	14.121	0.113

Table A.4 Continued from previous page

ObjID	ra	dec	Metallicity	$Z_{\odot}$	UV SFR	u SFR	W3 SFR	W4 (Lee) SFR	W4 (Cluver) SFR	Hα SFR	OII SFR	MPA SFR	dust Balmer
16795	239.42926	34.55878	8.140	0.234	12.644	8.378	2.582	2.145	1.361	3.522	3.069	4.293	0.057
83121	242.09655	12.54962	8.461	0.491	29.051	50.135	11.262	5.050	2.828	11.460	11.095	8.312	0.142
30446	242.40841	4.75281	8.453	0.482	20.092	36.468	6.078	3.274	1.953	5.977	5.729	6.054	0.171
28730	243.4572	14.11566	8.133	0.231	5.893	4.366	0.264	1.205	0.832	4.088	2.787	3.170	0.004
54077	250.648	42.39715	8.170	0.251	22.038	27.175	6.955	7.659	4.036	20.162	13.162	16.912	0.105
27825	251.40989	28.98597	8.162	0.246	11.599	12.530	1.001	0.677	0.508	3.716	3.467	3.192	0.142
13995	316.63522	-7.5139	8.053	0.192	6.510	5.786	0.328	2.014	1.289	4.165	3.680	3.895	-0.029
08959	332.01197	13.22626	8.036	0.184	7.181	5.833	3.370	2.304	1.447	7.273	4.339	6.270	0.055
54609	332.98331	-9.53977	8.473	0.504	94.447	80.741	37.263	19.081	8.802	12.496	10.714	10.209	0.224
27473	336.64663	-9.68499	8.015	0.176	2.169	1.556	0.357	0.521	0.407	1.255	1.016	1.527	0.014
60392	337.13304	-9.46809	8.714	0.880	16.301	18.120	2.898	2.667	1.639	3.834	2.621	2.434	0.162
71294	340.88031	-9.44735	7.978	0.161	20.474	18.266	3.387	1.733	1.134	8.042	5.499	7.313	0.078
16911	344.79825	-8.77026	8.979	1.618	13.116	15.205	5.043	6.124	3.334	4.990	2.228	3.871	0.155
77821	346.21707	-8.6318	8.421	0.448	21.097	30.390	3.674	2.055	1.312	3.803	3.707	4.764	0.075
10045	349.66038	-10.50532	8.124	0.226	19.144	20.333	2.370	1.138	0.792	3.159	2.285	2.428	0.026
54061	355.41867	-8.71988	8.134	0.231	2.802	0.548	2.536	1.222	0.842	3.031	2.882	1.520	0.104
33326	358.81388	-10.97455	8.345	0.376	12.380	6.669	2.236	1.192	0.824	1.093	1.166	0.429	0.161
10880	359.0195	-8.9065	7.943	0.149	19.246	14.043	4.110	1.936	1.247	11.982	7.249	6.823	0.129

Appendix B

AAOmega Results

Table B.1: Redshifts and line fluxes (in $\times 10^{-17}$ erg cm^{-2} s^{-1} Å^{-1}) measured in those galaxies identified as emission line galaxies.

ra	dec	redshift	[OII] 3727	[OII] 3729	Hβ	[OIII]	[NII]	Hα	[SII] 6718	[SII] 6732
337.93612	-9.12961	0.3064	85.76	166.96	51.52	207.85	18.83	266.87	140.50	37.46
337.65417	-9.13733	0.0725	204.82	331.25	197.91	1046.46	12.57	832.50	44.37	51.36
337.85996	-9.17805	0.0834	188.50	60.18	67.76	293.17	4.24	280.99	.00	16.33
337.71337	-9.19136	0.0603	99.07	79.57	113.03	297.26	3.47	345.21	31.36	16.39
337.84133	-9.22703	0.1931	351.68	360.89	151.49	555.64	202.61	833.05	128.21	97.08
337.12354	-9.12400	0.1064	312.80	485.71	182.29	388.06	163.98	820.59	188.12	143.17
337.30667	-9.18450	0.2737	145.19	199.17	86.87	256.30	35.42	395.80	56.16	29.10
337.58712	-9.25325	0.0351	74.30	13.64	41.37	217.38	1.29	256.44	15.95	10.29
337.86533	-9.34736	0.2548	98.14	159.71	51.97	183.20	7.39	209.68	48.56	.00
337.80779	-9.34114	0.3598	51.63	95.89	26.48	77.55	-	-	-	-
337.47892	-9.30111	0.0946	399.23	333.65	209.40	620.57	59.05	782.37	160.96	96.04
337.38150	-9.29991	0.1398	556.26	957.82	359.74	969.46	137.18	1185.11	169.54	141.52
337.52246	-9.38125	0.2226	91.22	140.47	66.83	38.79	123.82	396.62	73.72	43.47
337.75558	-9.50800	0.0583	1347.62	1584.05	825.98	2934.60	228.62	2596.17	322.52	230.80
337.14225	-9.21352	0.2496	117.28	166.87	61.52	106.31	45.63	327.50	69.94	23.69
337.80354	-9.56088	0.0585	203.48	223.69	79.84	218.83	9.15	224.16	46.16	33.66
337.51417	-9.46780	0.0528	72.84	65.98	33.74	124.74	3.47	230.00	48.51	10.78
337.75000	-9.61322	0.1980	-	165.84	4.74	82.39	607.78	2.99	3.29	86.86
337.66962	-9.58022	0.0824	53.91	115.86	49.85	59.41	233.07	642.76	149.40	103.78
337.61108	-9.63561	0.2593	-	-	65.64	4.15	10.49	50.73	48.07	15.41
337.61525	-9.71727	0.0302	393.65	290.88	513.12	2317.93	18.97	1226.87	59.84	41.71

Table B.1 Continued from previous page

ra	dec	redshift	[OII] 3727	[OII] 3729	Hβ	[OIII]	[NII]	Hα	[SII] 6718	[SII] 6732
337.42125	-9.55831	0.0553	293.22	355.30	253.92	1327.71	10.62	703.81	71.72	56.24
337.22021	-9.48994	0.1006	184.30	95.97	44.06	72.51	18.35	117.34	28.07	.77
337.19258	-9.53939	0.2474	16.44	65.08	17.78	17.46	6.29	73.51	2.48	.00
337.25646	-9.67489	0.0548	2412.43	2574.23	6772.11	47737.47	1438.50	38112.09	1697.71	1431.17
337.37962	-9.90447	0.1628	643.26	974.30	428.94	962.42	24.30	689.70	301.61	232.08
337.09362	-9.54511	0.3228	32.33	58.85	28.45	26.39	103.10	229.97	-	-
337.03917	-9.85006	0.1444	92.06	95.87	17.74	20.89	27.95	185.09	48.93	35.12
336.99854	-10.00589	0.3317	269.09	318.70	218.77	631.02	48.95	935.10	-	-
336.81179	-9.24750	0.1861	-	48.98	2.04	12.60	21.35	1.00	.69	4.65
336.83333	-9.92877	0.1440	446.87	640.51	256.09	796.18	76.97	946.68	119.65	103.37
336.80462	-10.09561	0.1480	46.55	62.92	12.08	85.10	.00	106.01	3.71	13.94
336.85075	-9.42728	0.1450	274.87	354.07	130.35	452.50	41.33	631.75	116.60	46.26
336.76142	-9.67063	0.0355	310.74	527.88	171.03	528.28	34.39	683.55	92.87	70.99
336.70192	-10.04800	0.1710	-	53.42	2.89	.00	64.91	1.71	1.83	.00
336.63600	-10.02419	0.1715	-	-	4.11	2.73	1.33	2.48	1.20	.68
336.68700	-9.74958	0.2387	103.58	192.68	29.04	103.32	1.13	74.56	12.01	3.92
336.69883	-9.57033	0.1864	198.85	256.07	92.18	237.48	36.42	316.22	43.02	29.87
336.66646	-9.63139	0.3106	93.15	87.11	28.76	35.38	16.04	87.46	.00	-
336.69383	-9.55688	0.0829	230.54	302.91	207.65	884.97	19.86	766.75	75.53	46.43
336.64717	-9.55500	0.1862	114.53	107.91	15.60	47.22	.00	24.62	.00	3.00
336.65267	-9.42678	0.5074	172.10	147.23	273.83	620.77	-	-	-	-
336.54492	-9.67480	0.4578	34.17	63.28	14.37	44.44	-	-	-	-

Table B.1 Continued from previous page

ra	dec	redshift	[OII] 3727	[OII] 3729	Hβ	[OIII]	[NII]	Hα	[SII] 6718	[SII] 6732
336.58187	-9.60113	0.1143	88.07	146.37	52.91	110.73	2.85	111.47	13.54	8.44
336.73329	-9.20380	0.1877	79.05	142.88	73.94	41.06	175.20	494.71	103.94	13.18
336.49825	-9.53275	0.3866	123.56	212.68	97.85	341.41	-	-	-	-
336.74058	-9.28802	0.2598	93.44	96.88	18.20	19.43	12.27	101.05	13.63	2.38
336.64846	-9.41725	0.2409	25.58	49.13	6.84	19.24	.00	24.93	1.75	2.08
336.42329	-9.61867	0.2908	94.82	123.06	17.42	24.74	3.70	88.26	9.13	11.89
336.26017	-9.77981	0.0325	-	65.63	7.69	28.90	57.16	1.62	.93	1.59
336.55392	-9.42475	0.3923	301.80	395.65	154.29	593.55	-	-	-	-
336.60062	-9.39275	0.2845	51.55	66.11	19.24	93.13	4.97	12.76	9.90	20.90
336.16525	-9.71158	0.3509	0.0	78.18	19.47	63.07	-	-	-	-
336.59000	-9.33308	0.1709	151.00	317.21	162.46	357.80	148.18	841.08	133.81	90.55
336.59671	-9.35666	0.0347	204.39	104.13	67.87	131.27	7.00	338.00	40.74	48.75
336.62529	-9.25763	0.2591	271.36	336.39	200.59	418.36	135.44	993.24	126.67	84.45
336.35942	-9.42678	0.1892	86.22	134.75	40.94	198.27	.00	136.49	8.30	24.04
336.15808	-9.51302	0.1253	212.36	132.53	65.75	241.73	11.45	227.56	47.62	29.75
336.01733	-9.58911	0.4263	45.37	63.13	6.62	157.42	-	-	-	-
336.09717	-9.50555	0.0833	185.53	215.38	73.42	202.85	12.47	206.44	54.98	29.79
336.38950	-9.32778	0.1252	56.08	80.03	49.66	221.12	.63	125.03	15.96	5.46
336.57667	-9.19213	0.2225	382.53	469.78	263.38	817.05	26.20	1025.54	133.35	82.84
336.64171	-9.19327	0.1578	258.32	302.08	212.80	831.95	1.57	104.00	27.91	21.19
336.34108	-9.25125	0.2582	63.50	66.69	44.75	49.67	12.19	196.88	11.22	36.27
336.64725	-9.14369	0.0557	253.36	386.22	515.34	2199.11	20.23	2010.69	107.25	74.50

Table B.1 Continued from previous page

ra	dec	redshift	[OII] 3727	[OII] 3729	Hβ	[OIII]	[NII]	Hα	[SII] 6718	[SII] 6732
336.50375	-9.26369	0.2856	104.55	135.80	49.13	112.16	17.34	215.09	41.73	6.68
336.22879	-9.21603	0.0884	192.46	323.03	142.30	557.97	40.68	673.78	80.50	44.64
336.13917	-9.18517	0.2286	209.38	235.92	77.61	149.04	45.81	362.14	52.41	37.22
336.20000	-9.17830	0.1868	-	92.98	3.47	15.40	154.95	2.06	1.66	30.33
336.61025	-9.04139	0.2567	213.13	221.71	173.79	378.29	108.48	1025.61	183.11	179.67
336.25321	-9.11050	0.2128	-	-	3.86	3.14	1.31	1.41	2.00	2.19
335.86921	-9.05325	0.0816	20.13	43.62	15.69	83.11	2.64	65.69	9.59	2.78
336.05862	-9.01828	0.0559	0.70	76.55	16.62	27.49	4.27	79.52	12.66	6.19
335.87929	-8.99322	0.2357	134.86	241.03	95.96	200.16	63.66	451.47	101.42	4.53
336.32658	-9.01875	0.0677	70.56	73.30	31.11	72.66	30.29	219.80	33.78	21.99
336.56654	-9.03850	0.2329	129.85	188.02	110.62	318.64	19.09	473.87	91.04	65.10
336.29658	-8.99066	0.2335	282.54	571.07	612.99	3224.30	47.44	2264.98	119.08	6.94
336.15046	-8.92011	0.1670	103.85	205.83	110.24	190.81	.00	136.72	17.61	17.65
336.62729	-9.06794	0.2716	169.88	.00	29.56	53.59	1.70	53.69	.00	.76
335.98037	-8.82930	0.0808	69.84	152.60	41.66	128.67	8.31	106.48	4.43	42.08
336.19433	-8.87700	0.0950	220.87	480.28	191.97	601.41	50.64	838.71	120.66	70.33
336.53542	-8.96889	0.1949	125.22	175.05	73.55	150.91	67.16	491.74	143.03	77.86
335.99012	-8.76081	0.0818	10.33	30.09	5.91	40.46	.97	21.35	.00	8.30
336.59012	-8.91975	0.0803	1.30	123.37	24.41	15.74	2.62	65.10	13.08	13.68
336.13671	-8.76302	0.0935	65.19	127.83	43.26	86.30	.43	83.21	3.98	16.60
336.59208	-8.93513	0.2700	63.83	119.40	58.19	205.46	8.73	286.22	57.66	11.32
336.34625	-8.80458	0.2404	91.69	123.50	14.67	49.28	.28	55.08	6.64	4.86

Table B.1 Continued from previous page

ra	dec	redshift	[OII] 3727	[OII] 3729	Hβ	[OIII]	[NII]	Hα	[SII] 6718	[SII] 6732
336.56012	-8.94011	0.1599	131.61	136.71	55.66	87.12	.00	72.26	51.76	41.88
336.53042	-8.88263	0.0555	106.75	101.70	29.62	69.33	5.29	95.08	28.40	18.36
336.61525	-8.97344	0.0731	49.37	244.70	60.89	168.27	10.30	170.53	31.44	22.69
336.33683	-8.70369	0.0816	124.49	204.88	39.20	133.62	14.07	126.47	27.42	12.88
336.31387	-8.66561	0.0816	1097.10	1252.44	1011.45	5156.71	73.12	2878.63	188.68	125.83
336.34067	-8.67924	0.0812	432.82	368.23	165.28	514.20	35.94	338.36	38.62	50.42
336.41100	-8.64569	0.0240	461.66	561.70	1051.02	6983.84	125.97	4864.82	181.57	142.18
336.22900	-8.45100	0.1988	-	65.07	2.95	5.16	102.29	1.67	2.46	8.03
336.46108	-8.65489	0.0743	165.59	106.61	52.64	126.02	.96	95.08	13.96	7.15
336.29512	-8.43855	0.2215	77.91	130.85	41.89	68.79	15.61	140.89	23.73	18.15
336.35587	-8.22889	0.0997	191.00	277.61	216.98	846.28	3.74	718.12	38.21	6.06
336.52646	-8.47978	0.0329	122.05	140.76	92.20	393.19	5.18	257.51	15.73	15.50
336.73187	-8.60430	0.1429	73.50	163.57	20.48	38.61	5.91	125.42	21.80	.64
336.65112	-8.14892	0.1002	166.03	157.46	42.11	196.74	7.00	174.00	37.94	34.06
336.69833	-8.23794	0.1313	0.0	106.37	25.31	51.73	3.97	38.36	.00	.00
336.89058	-8.22039	0.0945	263.22	477.48	217.29	450.40	57.17	568.11	84.08	42.47
336.92812	-8.84419	0.0999	82.71	80.70	3.30	67.64	.00	30.47	1.31	.00
336.97267	-8.41991	0.0821	55.21	69.37	43.52	75.26	1.29	85.24	22.85	.84
337.01083	-8.19975	0.1926	81.30	83.52	62.35	35.58	110.08	383.61	78.17	34.95
337.13625	-8.08250	0.0826	72.86	78.72	20.73	58.75	4.00	52.46	.46	6.35
337.04933	-8.68677	0.1255	88.25	135.58	105.27	432.31	33.70	659.96	85.28	65.02
337.23596	-8.16297	0.1011	120.83	135.98	40.14	74.25	8.94	93.50	25.69	16.70

Table B.1 Continued from previous page

ra	dec	redshift	[OII] 3727	[OII] 3729	Hβ	[OIII]	[NII]	Hα	[SII] 6718	[SII] 6732
337.10375	-8.53856	0.2537	143.95	282.41	57.86	159.08	13.40	237.31	36.51	18.52
337.14967	-8.55950	0.2161	35.17	44.77	15.40	28.23	4.96	77.41	14.02	5.57
337.41342	-8.21680	0.1695	207.00	170.65	61.18	205.87	14.30	250.86	40.97	29.60
337.41762	-8.25249	0.1015	103.59	170.99	59.77	54.95	33.38	170.10	41.22	36.33
337.19254	-8.71825	0.1047	339.23	343.65	144.16	312.46	11.68	178.53	43.07	28.30
337.37467	-8.46558	0.1696	277.74	270.29	116.00	260.22	25.80	311.18	52.23	28.36
337.52654	-8.32922	0.2668	193.58	239.03	44.92	135.84	27.62	219.35	30.59	17.33
337.46250	-8.48914	0.1926	87.82	191.52	34.46	106.99	.74	138.78	24.24	17.05
337.34125	-8.62300	0.1685	33.47	81.65	.00	41.45	6.04	40.02	.41	.41
337.53729	-8.44474	0.0721	280.86	351.21	252.16	1082.09	11.98	335.24	27.48	21.63
337.52596	-8.54591	0.0726	93.87	27.03	23.21	122.71	.00	125.59	10.81	5.24
337.45092	-8.66424	0.3655	210.14	248.88	64.09	231.40	-	-	-	-
337.45667	-8.61153	0.3887	64.39	110.71	55.06	187.98	-	-	-	-
337.66492	-8.46980	0.4225	0.0	317.84	76.62	201.97	-	-	-	-
337.43246	-8.68716	0.4321	24.11	67.35	32.31	123.10	-	-	-	-
337.46504	-8.69606	0.2495	350.30	494.96	114.65	420.25	24.38	587.76	103.64	64.10
337.68887	-8.54775	0.1811	159.76	265.25	31.10	117.68	2.45	152.69	30.29	9.89
337.58158	-8.66053	0.0795	31.49	92.80	8.76	53.27	1.13	45.08	7.20	8.24
337.66829	-8.61327	0.0995	74.34	37.91	28.32	64.40	2.65	126.64	13.54	3.19
337.67858	-8.63216	0.0554	82.01	328.18	63.86	168.98	11.74	212.18	67.65	41.96
337.80304	-8.57603	0.1005	109.26	140.52	49.67	79.38	9.16	86.64	27.51	18.26
337.77662	-8.64864	0.1005	212.73	283.74	123.66	357.62	1.93	127.55	16.60	9.91

Table B.1 Continued from previous page

ra	dec	redshift	[OII] 3727	[OII] 3729	Hβ	[OIII]	[NII]	Hα	[SII] 6718	[SII] 6732
337.65429	-8.74711	0.3205	86.99	88.04	25.15	84.59	1.29	124.76	-	-
337.38362	-8.87152	0.1205	146.93	208.03	75.00	232.93	21.90	326.74	51.36	35.03
337.73971	-8.74297	0.0879	0.0	79.35	26.75	72.32	6.76	122.15	24.58	21.34
337.22825	-8.92844	0.0293	222.84	190.08	206.00	626.07	4.05	402.54	25.48	23.70
337.72787	-8.79630	0.3060	-	.00	2.40	36.18	151.14	1.22	4.56	85.13
337.53187	-8.87230	0.1665	493.37	564.04	240.86	339.29	15.82	392.95	72.18	45.59
337.69450	-8.84794	0.2630	23.35	45.59	7.11	13.04	1.16	22.71	11.02	1.78
336.92412	-9.07208	0.2499	124.22	95.88	36.61	23.86	61.75	266.53	90.18	7.25
337.55967	-8.92667	0.0879	158.07	203.31	118.30	227.83	14.83	173.39	33.91	25.27
337.38987	-8.97661	0.1901	137.38	156.16	49.55	103.42	16.62	240.58	37.06	35.65
337.09754	-9.05328	0.2933	242.92	304.43	76.64	90.04	123.96	431.63	40.28	50.98
337.34275	-9.10431	0.2954	118.17	137.88	144.62	312.52	5.67	355.21	31.84	25.90
337.27458	-9.02436	0.3096	117.01	175.56	32.15	63.81	47.63	230.56	.00	-
337.31075	-9.02794	0.5583	63.57	78.52	41.49	144.01	-	-	-	-
337.88700	-8.97897	0.3585	49.64	100.26	45.33	134.54	-	-	-	-
337.87300	-8.99686	0.0234	0.0	116.60	127.16	392.99	1.82	362.16	6.93	4.85
337.83292	-9.01716	0.0879	79.31	125.93	44.12	90.06	7.94	157.74	29.48	15.36
337.88487	-9.01905	0.1953	222.44	310.26	115.41	218.29	50.22	415.66	95.83	58.48
337.79329	-9.06472	0.4284	159.66	213.69	94.80	204.58	-	-	-	-
337.65979	-9.09242	0.0610	98.89	234.40	89.93	287.62	5.97	389.75	76.14	45.98

Table B.2: Redshifts and line fluxes (in $\times 10^{-17}$ erg cm^{-2} s^{-1} Å^{-1}) measured in those galaxies which could not be clearly identified (i.e. those treated as 'uncertain').

ra	dec	redshift	[OII] 3727	[OII] 3729	Hβ	[OIII]	[NII]	Hα	[SII] 6718	[SII] 6732
336.62612	-9.50672	0.2216	-	14.44	2.49	9.21	38.62	1.28	3.17	5.47
336.64904	-9.53208	0.2683	32.56	39.08	10.00	26.31	5.92	52.34	5.58	3.04
336.16596	-9.75194	0.4374	0.89	26.61	32.92	31.30	-	-	-	-
336.08562	-9.75513	0.3281	-	23.24	2.37	15.66	48.15	1.44	-	-
335.98008	-9.49430	0.6232	-	54.88	1.34	62.61	-	-	-	-
336.43950	-9.21927	0.0557	-	-	2.37	5.26	1.55	1.89	0.94	1.18
336.06008	-8.51352	0.0855	-	-	5.01	15.80	24.45	1.65	0.90	6.71
337.38121	-8.55769	0.1690	12.32	143.75	22.82	42.98	22.59	151.78	5.92	16.89
337.19567	-8.90352	0.3232	20.19	27.99	21.17	10.99	15.26	73.21	-	-
337.41700	-8.81425	0.3042	30.94	57.17	7.48	11.72	7.60	48.67	0.00	6.26

Table B.3: The RA and dec of those AAOmega observations which could not be identied ('unknowns').

ra	dec	Class
337.788957771914	-9.0304164569466	U
337.266624808688	-8.9724388576573	U
337.268166638114	-8.8918294254604	U
337.634457983584	-8.6694988826378	U
337.604457913431	-8.5467999708105	U
337.533624860092	-8.3821089821781	U
337.574791304714	-8.2886366474805	U
337.214666131036	-8.6536909770701	U
337.311124721762	-8.4975828962088	U
337.294707762058	-8.3652181863777	U
337.249416594269	-8.4046090347929	U
336.059374659415	-8.5613874762746	U
336.490583268988	-8.8502498782677	U
336.493332893447	-8.8695814742754	U
336.388374473831	-8.8546903011800	U
336.089833095804	-8.7430265564869	U
336.211541363604	-8.8118330581042	U
336.428124566783	-8.9458020497617	U
335.972333203010	-8.7958589947760	U
336.166374527656	-8.9058840801749	U
336.074666330009	-8.8998565641702	U
335.847666181156	-9.1186347686629	U
335.934249844283	-9.2798593626348	U
336.310166307753	-9.2154417177282	U
336.371041354612	-9.2143588274954	U
335.912208157905	-9.4377206943492	U
336.552458127200	-9.2538012421122	U
335.972082820454	-9.4773292667266	U
336.027124584001	-9.5016341363961	U
336.087166550226	-9.4906906425091	U
336.190832950014	-9.4813571600264	U
335.984499961790	-9.6300225191290	U
336.437291318548	-9.3587728397581	U

Table B.3 Continued from previous page

ra	dec	Class
336.138999750120	-9.6019705054794	U
336.577874534992	-9.3199148420924	U
336.141499564980	-9.7419440948298	U
336.351124768696	-9.6136932219677	U
336.199999701779	-9.8348606604662	U
336.960249951686	-10.041440593500	U
337.116833014560	-9.8487720757320	U
336.821249817630	-9.1231897831342	U
337.296041607805	-9.4916360228710	U
337.657416402435	-9.3535818421343	U
337.661874587039	-9.2948307498215	U
337.754291533478	-9.3172448587671	U
337.805541462336	-9.2130811316123	U

Table B.4: The RA, dec, and redshifts (where possible) of those AAOmega spectra identified as white dwarves (WD), quasars (Q), emission and absorption systems (E+A), and absorption galaxies (A).

ra	dec	Redshift	Class
337.559499634120	-8.7779139566325	0.0	WD
337.167416593503	-8.5560818870917	0.0	WD
336.351458230133	-8.5050542658573	0.0	WD
336.096458206789	-9.0274714538796	0.0	WD
336.472708131696	-9.1658006543581	0.0	WD
336.398457958067	-9.2957474822937	0.0	WD
336.733791247950	-9.4876367774610	0.0	WD
337.208791594763	-9.4917219665403	0.0	WD
337.518749729815	-9.5877210451145	0.0	WD
337.205958318466	-9.0832202473459	0.176	Q
337.1606247518	-8.8768293903838	1.311	Q
337.173291129777	-8.2589688928486	1.66	Q
336.849124787321	-8.4240552223597	0.796	Q
336.588832925782	-8.9656378486291	1.046	Q
337.753416626924	-9.4156331713469	0.619	Q
336.619582997689	-9.5868329605320	0.2785	E+A
337.156166567196	-9.8048319424234	0.1452	E+A
337.703541223816	-8.7013610656250	-	A
337.123541204425	-8.5640803779117	0.197	A
336.734666154503	-8.7570239154220	-	A

Appendix C

Data Acknowledgements

C.1 Telescope Operators and Personnel

I would like to acknowledge and thank the operators and personnel working at the telescopes whose observations I used. Without their work and expertise, none of the analyses presented in this thesis would have been possible.

C.2 Software

In addition to the telescope-specific software mentioned within the main body of the thesis, I would also like to metion two pieces of software which have been invaluable to me during the course of my PhD:

- Ned Wright's very useful online cosmology calculator [Wright, 2006]; and
- the TOPCAT table operations software [Taylor, 2005].

C.3 Funding

I would like to thank the UK Science and Technology Facilities Council (STFC) for providing the research studentship which funded my PhD.

Bibliography

Abazajian K. N., et al., 2009, ApJS, 182, 543

Akiyama M., Minowa Y., Kobayashi N., Ohta K., Ando M., Iwata I., 2008, ApJS, 175, 1

Alexandroff R. M., Heckman T. M., Borthakur S., Overzier R., Leitherer C., 2015, ApJ, 810, 104

Allen C. W., 1976, Astrophysical Quantities

Allen R. J., et al., 2017, ApJL, 834, L11

Álvarez-Márquez J., et al., 2016, A&A, 587, A122

Amorín R., et al., 2015, A&A, 578, A105

Anders P., Fritze-v. Alvensleben U., 2003, A&A, 401, 1063

Baldwin J. A., Phillips M. M., Terlevich R., 1981, PASP, 93, 5

Barone-Nugent R. L., Wyithe J. S. B., Trenti M., Treu T., Oesch P., Bouwens R., Illingworth G. D., Schmidt K. B., 2015, MNRAS, 450, 1224

Best P. N., Heckman T. M., 2012, MNRAS, 421, 1569

Bian F., et al., 2010, ApJ, 725, 1877

Bian F., Kewley L. J., Dopita M. A., Juneau S., 2016, ApJ, 822, 62

Bianchi L., Herald J., Efremova B., Girardi L., Zabot A., Marigo P., Conti A., Shiao B., 2011, , 335, 161

Bonzini M., Padovani P., Mainieri V., Kellermann K. I., Miller N., Rosati P., Tozzi P., Vattakunnel S., 2013, MNRAS, 436, 3759

Boutsia K., et al., 2011, ApJ, 736, 41

Bouwens R. J., Illingworth G. D., Franx M., Ford H., 2007, ApJ, 670, 928

Bouwens R. J., et al., 2009, ApJ, 705, 936

Bouwens R. J., et al., 2011, ApJ, 737, 90

Bouwens R. J., et al., 2012a, ApJL, 752, L5

Bouwens R. J., et al., 2012b, ApJ, 754, 83

Bouwens R. J., et al., 2016, ApJ, 833, 72

Brinchmann J., Charlot S., White S. D. M., Tremonti C., Kauffmann G., Heckman T., Brinkmann J., 2004, MNRAS, 351, 1151

Bruzual A. G., 2007, in Vazdekis A., Peletier R., eds, IAU Symposium Vol. 241, Stellar Populations as Building Blocks of Galaxies. pp 125–132 (arXiv:astro-ph/0703052), doi:10.1017/S1743921307007624

Bruzual G., Charlot S., 2003, MNRAS, 344, 1000

Buat V., et al., 2012, A&A, 545, A141

Buitrago F., Trujillo I., Conselice C. J., Bouwens R. J., Dickinson M., Yan H., 2008, ApJL, 687, L61

Burgarella D., Buat V., Iglesias-Páramo J., 2005, MNRAS, 360, 1413

Calzetti D., Armus L., Bohlin R. C., Kinney A. L., Koornneef J., Storchi-Bergmann T., 2000, ApJ, 533, 682

Capak P. L., et al., 2015, Nature, 522, 455

Cardamone C., et al., 2009, MNRAS, 399, 1191

Carilli C. L., et al., 2001, in Hibbard J. E., Rupen M., van Gorkom J. H., eds, Astronomical Society of the Pacific Conference Series Vol. 240, Gas and Galaxy Evolution. p. 101 (arXiv:astro-ph/0008380)

Carilli C. L., et al., 2008, ApJ, 689, 883

Cassata P., et al., 2013, ApJ, 775, 106

Chabrier G., 2003, PASP, 115, 763

Chakraborti S., Yadav N., Cardamone C., Ray A., 2012, ApJL, 746, L6

Chevalier R. A., Clegg A. W., 1985, Nature, 317, 44

Cluver M. E., et al., 2014, ApJ, 782, 90

Cole S., Aragon-Salamanca A., Frenk C. S., Navarro J. F., Zepf S. E., 1994, MNRAS, 271, 781

Cole S., Lacey C. G., Baugh C. M., Frenk C. S., 2000, MNRAS, 319, 168

Condon J. J., Cotton W. D., Broderick J. J., 2002, , 124, 675

Conroy C., 2013, ARA&A, 51, 393

Conroy C., Gunn J. E., 2010, ApJ, 712, 833

Conselice C. J., 2014, ARA&A, 52, 291

Conselice C. J., Arnold J., 2009, MNRAS, 397, 208

Coppin K. E. K., et al., 2015, MNRAS, 446, 1293

Corbin M. R., Vacca W. D., Cid Fernandes R., Hibbard J. E., Somerville R. S., Windhorst R. A., 2006, ApJ, 651, 861

Daddi E., et al., 2005, ApJ, 626, 680

Daddi E., et al., 2007, ApJ, 670, 156

Dale D. A., Helou G., Magdis G. E., Armus L., Díaz-Santos T., Shi Y., 2014, ApJ, 784, 83

Davies L. J. M., et al., 2017, MNRAS, 466, 2312

Dayal P., Ferrara A., Dunlop J. S., Pacucci F., 2014, MNRAS, 445, 2545

Dopita M. A., Kewley L. J., Sutherland R. S., Nicholls D. C., 2016, , 361, 61

Douglas L. S., Bremer M. N., Stanway E. R., Lehnert M. D., 2007, MNRAS, 376, 1393

Douglas L. S., Bremer M. N., Lehnert M. D., Stanway E. R., Milvang-Jensen B., 2010, MNRAS, 409, 1155

Dwek E., 2005, in Popescu C. C., Tuffs R. J., eds, American Institute of Physics Conference Series Vol. 761, The Spectral Energy Distributions of Gas-Rich Galaxies: Confronting Models with Data. pp 103–122 (arXiv:astro-ph/0412344), doi:10.1063/1.1913921

Elbaz D., et al., 2007, A&A, 468, 33

Eldridge J. J., Stanway E. R., 2009, MNRAS, 400, 1019

Eldridge J. J., Stanway E. R., 2012, MNRAS, 419, 479

Ferguson H. C., et al., 2004, ApJL, 600, L107

Ferland G. J., Korista K. T., Verner D. A., Ferguson J. W., Kingdon J. B., Verner E. M., 1998, PASP, 110, 761

Ferland G. J., et al., 2013, , 49, 137

Fialkov A., Barkana R., Tseliakhovich D., Hirata C. M., 2012, MNRAS, 424, 1335

Finkelstein S. L., Rhoads J. E., Malhotra S., Grogin N., 2009, ApJ, 691, 465

Finkelstein S. L., et al., 2013, Nature, 502, 524

Franx M., van Dokkum P. G., Förster Schreiber N. M., Wuyts S., Labbé I., Toft S., 2008, ApJ, 688, 770

Fudamoto Y., et al., 2017, preprint, (arXiv:1705.01559)

Gardner J. P., et al., 2006, , 123, 485

Giallongo E., Cristiani S., D'Odorico S., Fontana A., 2002, ApJL, 568, L9

Gonçalves T. S., et al., 2010, ApJ, 724, 1373

González V., Labbé I., Bouwens R. J., Illingworth G., Franx M., Kriek M., Brammer G. B., 2010, ApJ, 713, 115

Greis S. M. L., Stanway E. R., Davies L. J. M., Levan A. J., 2016, MNRAS, 459, 2591

Greis S. M. L., Stanway E. R., Levan A. J., Davies L. J. M., Eldridge J. J., 2017, MNRAS, 470, 489

Hainline K. N., Shapley A. E., Kornei K. A., Pettini M., Buckley-Geer E., Allam S. S., Tucker D. L., 2009, ApJ, 701, 52

Heckman T. M., 2002, in Mulchaey J. S., Stocke J. T., eds, Astronomical Society of the Pacific Conference Series Vol. 254, Extragalactic Gas at Low Redshift. p. 292 (arXiv:astro-ph/0107438)

Heckman T. M., Armus L., Miley G. K., 1990, ApJS, 74, 833

Heckman T. M., et al., 2005, ApJL, 619, L35

Heckman T. M., Alexandroff R. M., Borthakur S., Overzier R., Leitherer C., 2015, ApJ, 809, 147

Henry A., Scarlata C., Martin C. L., Erb D., 2015, ApJ, 809, 19

Heyl J. S., Cole S., Frenk C. S., Navarro J. F., 1995, MNRAS, 274, 755

Ho I.-T., Wang W.-H., Morrison G. E., Miller N. A., 2010, ApJ, 722, 1051

Holden B. P., et al., 2016, ApJ, 820, 73

Hoopes C. G., et al., 2007, ApJS, 173, 441

Hopkins A. M., et al., 2003, ApJ, 599, 971

Huynh M. T., Hopkins A. M., Lenc E., Mao M. Y., Middelberg E., Norris R. P., Randall K. E., 2012, MNRAS, 426, 2342

Inoue A. K., Iwata I., Deharveng J.-M., Buat V., Burgarella D., 2005, A&A, 435, 471

Ivezic Z., et al., 2008, preprint, (`arXiv:0805.2366`)

Japelj J., et al., 2017, MNRAS, 468, 389

Jiang L., et al., 2013, ApJ, 772, 99

Juneau S., Dickinson M., Alexander D. M., Salim S., 2011, ApJ, 736, 104

Kaiser C. R., 2005, MNRAS, 360, 176

Kauffmann G., et al., 2003, MNRAS, 346, 1055

Kennicutt Jr. R. C., 1998, ARA&A, 36, 189

Kennicutt R. C., Evans N. J., 2012, ARA&A, 50, 531

Kennicutt R. C., et al., 2011, PASP, 123, 1347

Kewley L. J., Dopita M. A., Sutherland R. S., Heisler C. A., Trevena J., 2001, ApJ, 556, 121

Kewley L. J., Geller M. J., Jansen R. A., 2004, , 127, 2002

Kewley L. J., Groves B., Kauffmann G., Heckman T., 2006, MNRAS, 372, 961

Kewley L. J., Maier C., Yabe K., Ohta K., Akiyama M., Dopita M. A., Yuan T., 2013, ApJL, 774, L10

Kewley L. J., Zahid H. J., Geller M. J., Dopita M. A., Hwang H. S., Fabricant D., 2015, ApJL, 812, L20

Khaire V., Srianand R., Choudhury T. R., Gaikwad P., 2016, MNRAS, 457, 4051

Koprowski M. P., et al., 2016, ApJL, 828, L21

Kovács A., 2008, in Millimeter and Submillimeter Detectors and Instrumentation for Astronomy IV. p. 70201S (arXiv:0805.3928), doi:10.1117/12.790276

Kriek M., et al., 2010, ApJL, 722, L64

Kroupa P., 2001, MNRAS, 322, 231

Lacey C., Cole S., 1993, MNRAS, 262, 627

Lawrence A., et al., 2007, MNRAS, 379, 1599

Lee K.-S., et al., 2011, ApJ, 733, 99

Lee J. C., Hwang H. S., Ko J., 2013, ApJ, 774, 62

Lehnert M. D., Bremer M., Verma A., Douglas L., Forster Schreiber N., 2007, preprint, (arXiv:0708.3000)

Leitherer C., et al., 1999, ApJS, 123, 3

Leslie S. K., Kewley L. J., Sanders D. B., Lee N., 2016, MNRAS, 455, L82

Lilly S. J., Le Fevre O., Hammer F., Crampton D., 1996, ApJL, 460, L1

Liske J., et al., 2015, MNRAS, 452, 2087

Madau P., Dickinson M., 2014, ARA&A, 52, 415

Madau P., Ferguson H. C., Dickinson M. E., Giavalisco M., Steidel C. C., Fruchter A., 1996, MNRAS, 283, 1388

Madau P., Pozzetti L., Dickinson M., 1998, ApJ, 498, 106

Mannucci F., et al., 2009, MNRAS, 398, 1915

Maraston C., 2005, MNRAS, 362, 799

Martin D. C., et al., 2005, ApJL, 619, L1

Meurer G. R., Heckman T. M., Calzetti D., 1999, ApJ, 521, 64

Miller N. A., et al., 2013, ApJS, 205, 13

Mosleh M., et al., 2012, ApJL, 756, L12

Nandra K., Laird E. S., Steidel C. C., 2005, MNRAS, 360, L39

Naoz S., Noter S., Barkana R., 2006, MNRAS, 373, L98

Neistein E., van den Bosch F. C., Dekel A., 2006, MNRAS, 372, 933

Nieva M.-F., Przybilla N., 2012, A&A, 539, A143

Noeske K. G., et al., 2007, ApJL, 660, L43

Oesch P. A., et al., 2010, ApJL, 709, L21

Oesch P. A., et al., 2013, ApJ, 772, 136

Oesch P. A., et al., 2014, ApJ, 786, 108

Oesch P. A., et al., 2015, ApJL, 804, L30

Ono Y., et al., 2012, ApJ, 744, 83

Osterbrock D. E., 1989, Astrophysics of gaseous nebulae and active galactic nuclei

Ouchi M., et al., 2004, ApJ, 611, 660

Overzier R. A., Heckman T. M., Schiminovich D., Basu-Zych A., Gonçalves T., Martin D. C., Rich R. M., 2010, ApJ, 710, 979

Overzier R. A., et al., 2011, ApJL, 726, L7

Planck Collaboration et al., 2016a, preprint, (arXiv:1605.03507)

Planck Collaboration et al., 2016b, A&A, 594, A13

Press W. H., Schechter P., 1974, ApJ, 187, 425

Roehlly Y., Burgarella D., Buat V., Boquien M., Ciesla L., Heinis S., 2014, in Manset N., Forshay P., eds, Astronomical Society of the Pacific Conference Series Vol. 485, Astronomical Data Analysis Software and Systems XXIII. p. 347

Rubin K. H. R., Prochaska J. X., Koo D. C., Phillips A. C., Martin C. L., Winstrom L. O., 2014, ApJ, 794, 156

Sadler E. M., 2016, Astronomische Nachrichten, 337, 105

Salim S., et al., 2007, ApJS, 173, 267

Salim S., et al., 2016, ApJS, 227, 2

Salpeter E. E., 1955, ApJ, 121, 161

Sawicki M., 2012, MNRAS, 421, 2187

Scarlata C., et al., 2009, ApJL, 704, L98

Schenker M. A., et al., 2013, ApJ, 768, 196

Schlafly E. F., Finkbeiner D. P., 2011, ApJ, 737, 103

Schmidt M., 1959, ApJ, 129, 243

Schmidt K. B., et al., 2014, ApJL, 782, L36

Scoville N., et al., 2016, ApJ, 820, 83

Shapley A. E., 2011, ARA&A, 49, 525

Shapley A. E., Steidel C. C., Pettini M., Adelberger K. L., Erb D. K., 2006, ApJ, 651, 688

Shibuya T., Ouchi M., Harikane Y., 2015, ApJS, 219, 15

Skrutskie M. F., et al., 2006, , 131, 1163

Smith J. D. T., et al., 2007, ApJ, 656, 770

Song M., et al., 2016, ApJ, 825, 5

Songaila A., 2004, , 127, 2598

Stanway E. R., Davies L. J. M., 2014, MNRAS, 439, 2474

Stanway E. R., McMahon R. G., Bunker A. J., 2005, MNRAS, 359, 1184

Stanway E. R., Bremer M. N., Lehnert M. D., 2008, MNRAS, 385, 493

Stanway E. R., Bremer M. N., Davies L. J. M., Lehnert M. D., 2010, MNRAS, 407, L94

Stanway E. R., Eldridge J. J., Greis S. M. L., Davies L. J. M., Wilkins S. M., Bremer M. N., 2014, MNRAS, 444, 3466

Stanway E. R., Eldridge J. J., Becker G. D., 2016, MNRAS, 456, 485

Stark D. P., Ellis R. S., Bunker A., Bundy K., Targett T., Benson A., Lacy M., 2009, ApJ, 697, 1493

Steidel C. C., Giavalisco M., Pettini M., Dickinson M., Adelberger K. L., 1996, ApJL, 462, L17

Steidel C. C., Pettini M., Adelberger K. L., 2001, ApJ, 546, 665

Steidel C. C., Shapley A. E., Pettini M., Adelberger K. L., Erb D. K., Reddy N. A., Hunt M. P., 2004, ApJ, 604, 534

Steidel C. C., et al., 2014, ApJ, 795, 165

Tabatabaei F. S., et al., 2017, ApJ, 836, 185

Takeuchi T. T., Buat V., Heinis S., Giovannoli E., Yuan F.-T., Iglesias-Páramo J., Murata K. L., Burgarella D., 2010, A&A, 514, A4

Takeuchi T. T., Yuan F.-T., Ikeyama A., Murata K. L., Inoue A. K., 2012, ApJ, 755, 144

Tan Q., et al., 2013, ApJL, 776, L24

Tanner R., Cecil G., Heitsch F., 2016, preprint, (`arXiv:1608.05342`)

Taylor M. B., 2005, in Shopbell P., Britton M., Ebert R., eds, Astronomical Society of the Pacific Conference Series Vol. 347, Astronomical Data Analysis Software and Systems XIV. p. 29

Tilvi V., et al., 2016, ApJL, 827, L14

To C.-H., Wang W.-H., Owen F. N., 2014, ApJ, 792, 139

Trujillo I., Conselice C. J., Bundy K., Cooper M. C., Eisenhardt P., Ellis R. S., 2007, MNRAS, 382, 109

Vanzella E., et al., 2010, ApJ, 725, 1011

Verma A., Lehnert M. D., Förster Schreiber N. M., Bremer M. N., Douglas L., 2007, MNRAS, 377, 1024

Weinzirl T., et al., 2011, ApJ, 743, 87

Wilkins S. M., Stanway E., 2015, preprint, (arXiv:1510.01511)

Wilkins S. M., Bunker A. J., Stanway E., Lorenzoni S., Caruana J., 2011, MNRAS, 417, 717

Wilkins S. M., Bunker A., Coulton W., Croft R., Matteo T. D., Khandai N., Feng Y., 2013, MNRAS, 430, 2885

Williams C. C., et al., 2014, ApJ, 780, 1

Wofford A., et al., 2016, MNRAS, 457, 4296

Wright E. L., 2006, PASP, 118, 1711

Wright E. L., et al., 2010, , 140, 1868

Xu H., Wise J. H., Norman M. L., Ahn K., O'Shea B. W., 2016, ApJ, 833, 84

Yabe K., Ohta K., Iwata I., Sawicki M., Tamura N., Akiyama M., Aoki K., 2009, ApJ, 693, 507

Yang H., Malhotra S., Gronke M., Rhoads J. E., Dijkstra M., Jaskot A., Zheng Z., Wang J., 2016, ApJ, 820, 130

Yang H., et al., 2017, preprint, (arXiv:1701.01857)

Zhao Y., Gu Q., Gao Y., 2011, , 141, 68

Zwicky F., 1965, ApJ, 142, 1293

da Cunha E., Charlot S., Elbaz D., 2008, MNRAS, 388, 1595

de Barros S., Schaerer D., Stark D. P., 2014, A&A, 563, A81

van Dokkum P. G., et al., 2008, ApJL, 677, L5

van Dokkum P. G., et al., 2010, ApJ, 709, 1018

van der Burg R. F. J., Hildebrandt H., Erben T., 2010, A&A, 523, A74